Nuclear imaging: from the development of new production methods of terbium theragnostic isotopes, to the exploration of positron emission tomography for industrial applications.

By

Rebeckah Rachael Trinder

A thesis submitted to
the University of Birmingham
for the degree of
DOCTOR OF PHILOSOPHY

Nuclear Physics Research Group
School of Physics and Astronomy
College of Engineering and Physical Sciences
University of Birmingham
January 2022

ABSTRACT

Nuclear imaging has a wide range of applications in both medicine and in industry, such as diagnostic imaging in the former. The emerging field of theragnostics aims to use the two halves of nuclear medicine (therapy and diagnostic imaging) to tailor cancer treatments to each specific case. For optimal theragnostic treatment different isotopes of the same element should be used for the diagnostic imaging and therapy. A good candidate is terbium which has four medically-promising isotopes ^{149}Tb and ^{161}Tb for cancer therapy, and ^{152}Tb and ^{155}Tb for PET and SPECT nuclear imaging, respectively. The work discussed here looks at the production of the nuclear imaging isotopes ^{152}Tb and ^{155}Tb from α beams on Eu targets. To develop this new α+Eu production route, cross-sections of relevant nuclear reactions are needed. No previous nuclear reaction cross-sections for α+Eu have been measured for the production of these medical Tb isotopes. Therefore, the cross-section for the production of ^{152}Tb and ^{155}Tb and the contaminant Tb isotopes and isomers ^{151}Tb, ^{152}Tb^{m1}, ^{153}Tb, ^{154}Tb, ^{154}Tb^{m1}, ^{154}Tb^{m2} and ^{156}Tb from the α+Eu reactions were measured and are reported in this work. To enable this study, a method of measuring nuclear reaction cross-sections at the Birmingham Cyclotron Facility was developed and the details of each step are given in this thesis. In the process of measuring the cross-sections for each Tb isotope and isomeric state, new more precise half-life values for PET ^{152}Tb and SPECT ^{155}Tb isotopes were also measured. These are 17.07(7) hours and 5.25(1) days, respectively. Updated half-life values for the contaminant isotopes and isomeric states: ^{152}Tb^{m1}, ^{153}Tb, ^{154}Tb^{m1} and ^{154}Tb^{m2} were also measured, and found to be 4.22(2) minutes, 2.291(6) days 9.43(4) hours and 23.58(15) hours, respectively. Details on how these quantities were obtained, along with a comparison to previous half-life measurements are also discussed. Cross-section calculations using the

reaction code TALYS are also presented and compared to the experimental data.

Nuclear imaging can be performed using PET tracers and scanners. Although commonly used for medical applications, the work discussed in the latter part of this thesis details the development of novel techniques of using a former medical GE Discovery ST PET/CT scanner to explore the breadth of information that can be extracted from PET images taken of industrial machinery. Industrial PET imaging could provide alternative gas and liquid flow information in machinery that would not be obtainable using solid tracers in PEPT (a method of nuclear imaging which is currently used for industrial applications). Measuring the flow of gases and studying chemical reactions inside devices such as carbon absorbers and catalytic converters would be a desirable goal for industrial PET imaging, however, preliminary investigations were needed to develop the imaging techniques and analysis required. The first steps toward this goal were developed and are discussed in this work. Both qualitative and quantitative information about fluid flow through pipes with CALGAVIN inserts were measured. The final results included extracting dimensional information about the fluid flow and developing a technique using the voxel intensity data to measure residence time.

DEDICATION

Dedicated to my wonderful and most beloved parents, Chris and Sara Trinder

ACKNOWLEDGMENTS

When I started out on this road of research and writing this thesis, I never could have comprehended all the small and major bumps (Covid-19) that would add to the adventure and challenge that is carrying out post-graduate research. The completion of this chapter in my life would never have been possible without the wonderful, kind, and helpful people I have had the pleasure of knowing and working with throughout these four to five years.

Firstly, I wish to extend my many thanks and gratitude to my supervisors Professor Tzany Kokalova Wheldon and Professor David J Parker who initially provided me with this wonderful opportunity and since then have guided and supported me throughout my work. I also wish to thank Dr Ben Phoenix, Dr Carl Wheldon and the MC40 cyclotron team who were always so willing to offer their help and expertise. I also which to thank the Hawkesworth family who, through the Hawkesworth scholarship, funded my PhD research. It was also an honour to work with my colleagues and collaborators at NPL and CALGAVIN. An additional, official, and heart felt thank you is given to Tzany, David, Rachel Hindle (from Clear Links who read Chapters 1, 2, 3 and some of 4 and 7) and Chris Oliver who helped proofread sections of the thesis for spelling and grammar.

My experience and time spent in the nuclear group was made all the more special not only by its wonderful members of staff but also by the fun, caring and supportive atmosphere made by my fellow nuclear PhD students - Jack, Harry, Nima, Emily, Tony, Håkan, Stuart, Pedro, Jakub, Oliver, Yiming, Marianna, Ross, Angus, Dawid, Mark, Sammy, Stephen and honorary lunchtime and boardgame members Ellie, Chris Gill and Neil. The memories and friendships made with all of these people is something I will cherish forever. On a more

practical note, I wish to thank all those in the group who were always so willing to help on technical, coding, or logistical problems and always made sure we were enjoying work at the same time. So, thank you, to all of you, for being there and helping in your own way.

I would also like give a special mention and thank you to Tzany, David and Ross with whom I worked closely on the development of the cross-section measurement techniques. Subsequently I wish to thank Ross, Dawid, Pedro and Mark, who helped with the shift work needed for the data collection process of this work. I apologise for these many hours of your lives that you will not get back, but I will be forever grateful, and I personally enjoyed spending so much time with you all, so thank you.

Dealing with the effects of the pandemic and the loss of loved ones along with post-graduate-research did pose its unique challenges and I wish to thank my friends and family whose joy, love and emotional support were key to completing my PhD. A special thank you to Chris Oliver who has supported me and been there for me through the ups and downs of this work and life.

Finally, it cannot go unsaid that I have been blessed with the most supportive and caring parents and brother who always spurred me one at every point in my life believing that I can achieve even when I doubted myself. So, thank you for your unwavering support and love not only through this chapter of my life but for the whole story.

Tb or not Tb?

That is the Question

Adapted from William Shakespeare, "Hamlet"

Contents

List of Figures

List of Tables

Acronyms

AFOV	Axial Field Of View
CS	Compton Scatter
DSSD	Double-sided Silicon Strip Detector
FBP	Filtered Back Projection
FOV	Field Of View
FWHM	Full Width Half Maximum
HPGe	High Purity Germanium
IAEA	International Atomic Energy Agency
ISOLDE	Isotope Separator On Line DEtector
LOR	Line Of Response
LSF	Least Squares Fit
MEDICIS	Medical Isotopes Collected from ISOLDE
NDS	Nuclear Data Sheets
NEC	Noise Equivalent Counts
NNDC	National Nuclear Data Center
NPL	National Physical Laboratory
OSEM	Ordered Subset Expectation Maximisation
PE	Photoelectric Effect
PEPT	Positron Emission Particle Tracking
PET	Positron Emission Tomography
PIC	Positron Imaging Centre
PMT	Photo-Multiplier Tube
PP	Pair Production
ROI	Regions Of Interest
SNR	Signal to Noise Ratios
SPECT	Single Photon Emission Computed Tomography

Chapter One

Introduction

The number of cancer patients is growing year on year. In the UK, between 2015 and 2017, there were on average 1,000 new cases each day and between 2014 and 2035 the incident rate is expected to rise by 2% [1]. Therefore, the endeavour to find new and improve cancer treatments is an important and ever growing area of research.

Nuclear physics plays a large role in current methods of treatment. Over 27% of cancers are treated with various forms of external radio therapy [2]. In smaller use, but growing in interest [3], is the area of nuclear medicine, in which radionuclei are injected into the body and the radiation they emit is used for diagnostic imaging or cancer therapy. Nuclear medicine is more commonly used in diagnostics imaging, with hospitals utilising both PET-CT (Positron Emission Tomography combined with Computed Tomography) and SPECT-CT (Single Photon Emission Computed Tomography combined with Computed Tomography) for a variety of investigative and diagnostic work. For many years, nuclear medicine has also provided effective, niche internal ratiotherapy treatments such as thyroid cancer treatment using ^{131}I [3].

However, nuclear medicine could offer much more [4]. It's unique position to perform both diagnostic imaging and therapy could be used to personalise a patient's cancer treatment. In

the last two decades, the field has been looking to new, alternative radioisotopes to improve and expand the number of treatments. To enable this future, it is vital to be able to produce new medically useful isotopes using methods which are easily accessible to hospitals both physically and financially. The work covered in this thesis describes the initial investigations into the production of medically interesting terbium (Tb) isotopes using light ion cyclotrons, specifically using the MC40 cyclotron at Birmingham.

For production of isotopes to be understood and optimised, the cross-section of interaction (the likelihood of producing a product isotope given the initial reactant conditions) must be measured. A possible route for Tb production is to irradiate europium (Eu) with helium-4 (α) beams. Previously, only a small range of these cross-sections have been measured [5] and thus a more comprehensive measurement was needed. By using natural Eu targets and α-beams, the cross-section measurements for the production of Tb isotopes were carried out. Cross-section measurements of this type have never been performed at the MC40 facility and the work discussed here will detail how these measurements were carried out and the consequences of the final results for the future of medical Tb production.

One of the tools of nuclear medicine is Positron Emission Tomography (PET) imaging. This not only has applications in nuclear medicine but could also add to industry as an investigative tool. The Positron Imaging Centre (PIC) at the University of Birmingham has a long history of performing Positron Emission Particle Tracking (PEPT) imaging to investigate the inner workings of industrial machinery. In its simplest terms, PEPT uses a single (sometimes multiple) indivisible particles which emits positrons. This(these) particle(s) is(are) tracked around machines to look at the distribution and flow of the content.

The PIC obtained a GE Discovery ST PET/CT scanner from the Queen Elisabeth hospital, Birmingham. PET imaging offers the ability to image continuous distribution of radioactive fluids and gases instead of discrete particles used in PEPT. This difference in information

acquired could have impactful implications in industry. Therefore, the latter part of this thesis (chapters 7, 8 and 9) will look at work to investigate PET as an additional tool to PEPT in industrial imaging and the potential future for PET imaging in this area.

1.1 Uses of radioactive isotopes in medicine

1.1.1 Different types of decay and their uses in nuclear medicine

Unstable isotopes decay in order to reach stability. The means by which this happens depends on the nucleon balance of the nucleus. For the interest of this thesis, the four main roots of nuclear decay are as follows: neutron rich isotopes decay emitting a beta (β) particle (and anti-neutrino) whereas proton rich nuclei decay by electron capture (ϵ or ec) or emit a positron (β^+) (and neutrino), or the nucleus will emit an alpha (α) particle. Excess nuclear energy is also released via the emission of γ photons with energies specific to the nucleus.

These four types of decay have specific applications in nuclear medicine either for cancer treatment (therapy) or for diagnostic imaging. Isotopes emitting α and β particles are used in cancer therapy to cause double and single strand breaks to the DNA in order to kill the cancerous cells. Diagnostic imaging is a functional imaging tool and has a wide range of applications including the imaging of cancer cells and their metabolism but also in other areas of medicine, for example, looking at brain function or hypothyroidism. β^+emitters are used to produce PET images and γ emitting radionuclei are used to perform Single Photon Emission Computed Tomography (SPECT) imaging.

For a radioisotope to reach a desired location within the body or track a specific biological function, the isotopes are attached to biological targeting agents. Figure 1.1 depicts a few examples of different targeting agents. For instance, ^{18}F (a PET isotope) can be attached

to a glucose analogous, FDG (see figure 1.1 a). This can be used to track metabolism within the body. Areas of relatively high metabolism such as when the brain is active or where tumours are growing would use more glucose and thus produce a "hot spot" on a PET image. Hormones (figure 1.1 b) are a more specific targeting agent, however, highly specific and selective forms of biological targeting agents are proteins (peptides). Peptides are more commonly used for cancer therapy and imaging. A protein that is specific to the cancerous cells and is only expressed within or on the cancer cells is selected. A complementary targeting peptide can be produced which will solely attach to that cancer protein. An appropriate radioactive nuclide is then attached to this very specific peptide using a chelator (linker molecule) as shown in figure 1.1 c.

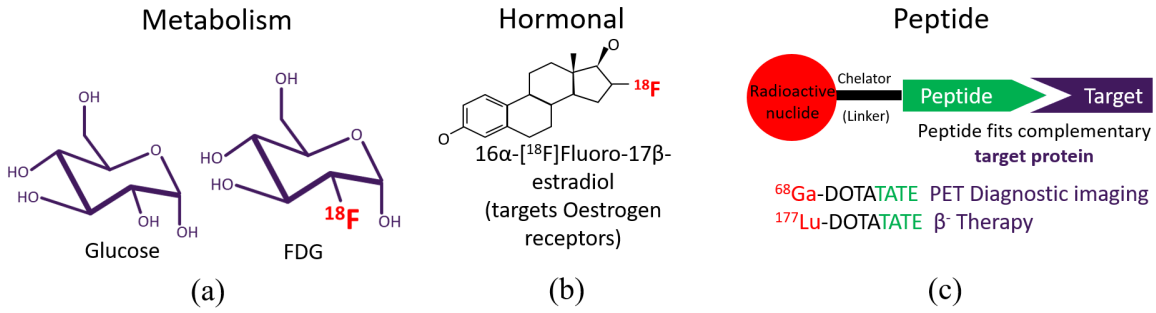

Figure 1.1: Three examples of biological targeting agents: (a) a glucose analogous, FDG (Fludeoxyglucose); (b) a hormonal vector with a ^{18}F attached; and (c) an example peptide molecule.

1.1.2 Selecting appropriate medical nuclei

Choosing the appropriate biological targeting agent to attach the radionuclide to is crucial to ensure the nuclide is taken to the desired location within the body and accurately achieve the goal of the therapy or imaging. It is equally important to select a radionuclide which optimises the imaging or treatment being performed. As well as knowing the type of decay the radionuclide undergoes and the likelihood (or branching ratio) of this type of decay

occurring, it is important to use isotopes whose radiation is emitted in a useful energy range. For example, SPECT imaging works best with isotopes that emit prominent γ's with energy around 100 keV to ensure optimal SPECT detector efficiency. For PET imaging, isotopes should emit positrons with energies usually less the 2 MeV [6] to ensure the average stopping distance of the positron before annihilation is less than or comparable to the spatial resolution of the PET scanner. If the positron range in the object (or patient) being imaged it too large then this will cause excessive blurring of the final PET images produced. For therapy isotopes, the energy of the β particle emitted will affect the range for which the isotopes will inflict damage within the patient, if this is too large then surrounding (non-cancerous tissues) will receive an unintended dose. Whereas, if the α particle energy is too large the nuclear recoil may cause the daughter nucleus to detach from the biological targeting agent. Moreover, if the daughter nuclear undergoes multiple α decays this could cause large unwanted damage to healthy tissues as the emitting nuclide is no longer attached to the biological targeting agent which keeps it next to the cancerous cells.

It is also important to select isotopes with appropriate half-lives. The half-life must be long enough for the isotope to be extracted from the production target, attached to the biological targeting agent, undergo quality and control checks and be administered to the patient with enough remaining activity to perform either therapy or diagnostic imaging. However, the half-life should not be too long else the patient and their surroundings will receive unnecessary and prolonged irradiation. Ideal medical isotopes possess half-lives which range from hours to days. Because of these short half-lives, production of these isotope should be ideally made at a local or on hospital site cyclotron or by milking longer lived isotope generators (e.g. ^{99}Mo generators produce the commonly used SPECT isotope ^{99m}Tc [7][8]).

It is also ideal to match the radionuclide half-life to the biological half-life of the targeting agent. For example, glucose is processed fairly quickly (a biological half-life of 16-20 minutes [9]) and thus the radionuclide half-life does not need to be particularly long (^{18}F used in FDG

has a half-life of 110 minutes). However, the biological half-life of proteins can be on the order of hours to days and thus a radionuclide of similar half-life would be ideal. This will allow the activity of the isotope to be high enough for when it reaches the point of interest in the body and will remain high to perform its function while at the point of interest.

Four isotopes of terbium have been found to fit these medical parameters: ^{149}Tb, ^{152}Tb, ^{155}Tb and ^{161}Tb. Not only this, but they have caused great excitement for future "theragnostic" cancer treatments. The next section will explain the term "theragnostics" and its medical application as well as demonstrate the significance of terbium and current medical studies which provide evidence for the future potential of these four isotopes.

1.2 Theragnostics

1.2.1 Aims of theragnostics

Improvements to cancer treatments have drastically improved the prospects of patient recovery and now, with people living longer, the likelihood of patients developing latent cancer from previous radiation treatment is growing. Therefore, there has been a movement within nuclear medicine to improve and develop treatment techniques that monitor and more accurately measure the dose to patients.

Theragnostics combines the two halves of nuclear medicine - therapy and diagnostic imaging - and aims to customise nuclear medicine cancer treatment. This treatment technique is designed to be cancer specific and thus radioactive nuclides are attached to protein biological targeting agents. The diagnostic imaging is used to monitor the cancer therapy so the treatment can be adjusted to ensure as low as possible dose is given to the patient while maintaining an effective treatment. Also if the therapy and diagnostic imaging isotopes share

similar length half-lives then more accurate dosimetry measurements of the patient can be calculated.

Unfortunately, at the moment separate elements are currently used for theragnostic treatment (see section 1.2.2). As well as being chemically different which may affect biological uptake in the body, the radiochemistry require to attach the radionuclide to the biological targeting agent may also differ. All these slight chemical differences between the tracer injected for therapy and tracer injected for imaging may affect how the therapy isotope and imaging isotope are distributed within the body and thus adds uncertainty when assuming that the imaging information is an accurate representation of the therapy distribution. To overcome this problem investigations over the last decade have been dedicated to identifying and producing elements which have more than one isotope with the desired properties for medical use. This is further discussed in section 1.2.3.

1.2.2 Current isotopes used in theragnostic treatments

For current theragnostic treatment, commonly ^{68}Ga is used for the diagnostic PET imaging. This can be paired with a relatively new β-therapy isotope, ^{177}Lu, which has a half-life more suitable for the protein targeting agent used (6.64 days). Numerous studies have proven the effectiveness of ^{177}Lu as a tool for prostate cancer metastasis treatment while causing minimal side effects to the patient [10]. Figure 1.2 [11] shows an example of such studies where the prostate cancer progression can be visually seen using the ^{68}Ga PET images where the size of tumours decrease over the ^{177}Lu treatment.

However, in some cases this type of therapy is not enough, either the cancer becomes resistant to the treatment (figure 1.3) or was never affected by the treatment in the first place (figure 1.4). More recently, a powerful α-therapy option in the form of ^{225}Ac (half-life of 10 days)

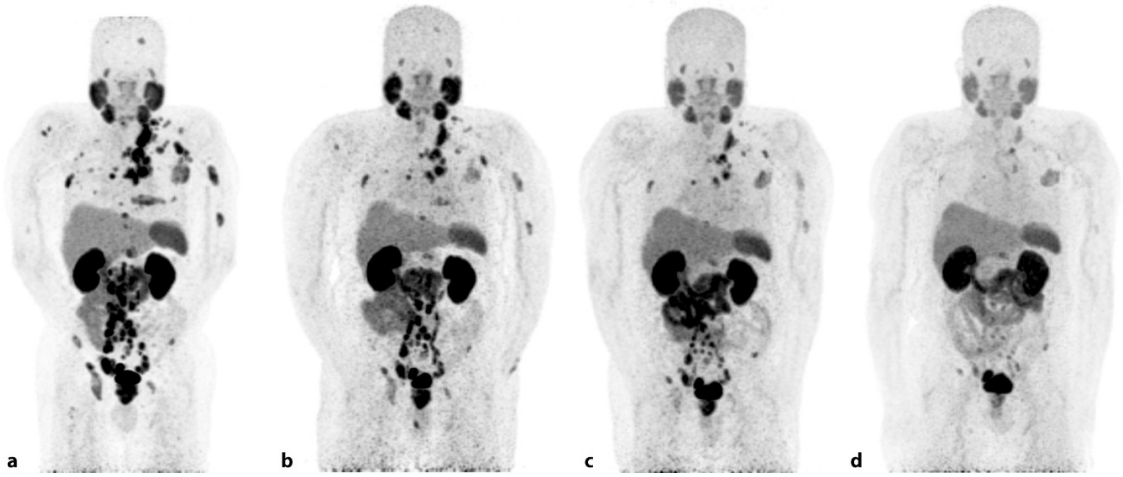

Figure 1.2: Baseline (a) and follow-up (b after 2 cycles; c after 4 cycles; d after 6 cycles) [68Ga]Ga-PSMA PET/CT of a patient with mCRPC, who was treated with 6.0GBq [177Lu]Lu-PSMA-617 (Novartis, Basel, Switserland). Prostate-specific antigen (PSA) response was as follows: 100ng/ml (baseline), 190ng/ml (after 2 cycles), 52ng/ml (after 4 cycles) and 19ng/ml (after 6 cycles) [11].

is in trial testing with prostate cancer patients and has proven to be a more potent therapy option as shown in figures 1.3 and 1.4 where the patients are also being monitored with ^{68}Ga PET imaging. This visual confirmation of the effectiveness of the ^{177}Lu and ^{225}Ac treatments are correlated with the prostate-specific antigen (PSA) values of the patients, which is used as a prostate cancer indicator.

Both of these α- and β- therapy options have proven to be valuable tools in treating cancer. However, to further theragnostics, the same element for therapy and imaging (a theragnostics pair) is required to access the full potential of using the images to monitor and quantify dose to the patient and tumour uptake.

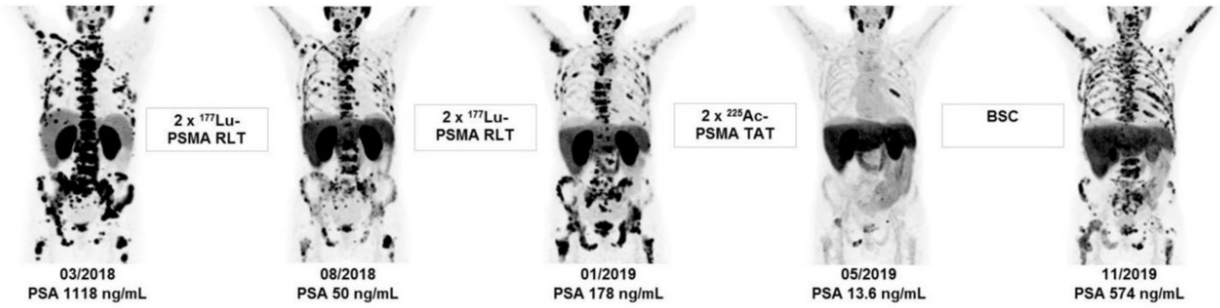

Figure 1.3: **^{68}Ga PET images of a patient's treatment progression using ^{177}Lu and then ^{225}Ac [12]. After this initial set of ^{177}Lu-PSMA treatment the tumours reduce in size and number. However, after an additional set of ^{177}Lu-PSMA treatment the remaining tumours had become resistant to the ^{177}Lu-PSMA treatment and continue to grow. This reduction and resurgence of tumours was reflected by the PSA values of the patient. The patient then received a set of ^{225}Ac-PSMA doses which dramatically reduced the number and size of the tumours and drastically reduced the PSA value. The last set of images were taken after the patient no longer received additional therapy doses and the remaining cancer left after the ^{225}Ac-PSMA treatment continued to grow.**

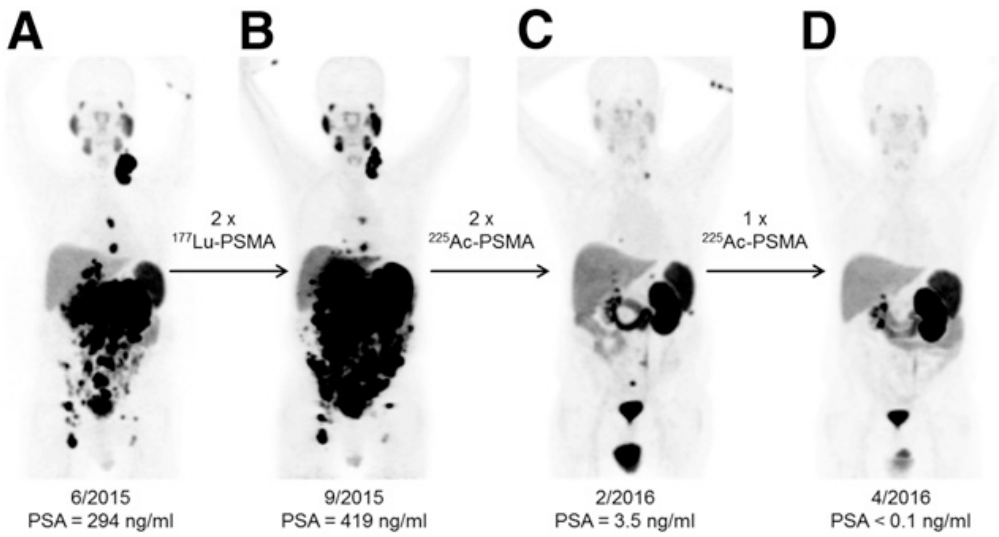

Figure 1.4: **^{68}Ga-PSMA-11 PET/CT scans of patient B. In comparison to initial tumour spread (A), restaging after 2 cycles of β-emitting ^{177}Lu-PSMA-617 presented progression (B). In contrast, restaging after second (C) and third (D) cycles of α -emitting ^{225}Ac-PSMA-617 presented impressive response. [13]**

1.2.3 Potential theragnostic elements

A paper promoting potential theragnostic elements was published in 2017 [14]. It discussed four elements of interest - scandium, copper, arsenic and terbium – and the type of cyclotron or reactor facilities needed to produce them. Table 1.1 shows the properties and uses for each isotope.

Table 1.1: Potential future theragnostic isotopes [14], their half-lives, decay modes and medical applications. The values for half-life and decay mode branching ratios were taken from NNDC [15] and the error on half-life is given in brackets.

Element	Isotope	Half-life	Decay mode	Medical application
Sc	43	3.891 (12) h	ec/β^+ 100 %	PET
	44	3.97 (4) h	ec/β^+ 100 %	PET/3y
	47	3.3492 (6) h	β^- 100 %	β^--therapy
Cu	61	3.336 (10) h	ec/β^+ 100 %	PET
	64	12.701 (2) h	ec/β^+ 61.8 % β^- 38.5 %	PET/ β^--therapy
	67	61.83 (12) h	β^- 100 %	β^--therapy/SPECT
As	72	26.0 (1) h	ec/β^+ 100 %	PET
	76	26.24 (9) h	β^- 100 %	β^--therapy
Tb	149	4.118 (25) h	α 16.7 % ec/β^+ 83.3 %	α-therapy/ PET
	152	17.5 (1) h	ec/β^+ 100 %	PET
	155	5.32 (6) d	ec 100%	SPECT
	161	6.89 (2) d	β^- 100 %	β^--therapy

Terbium is of particular interest because it has a quadruplet of isotopes which can be used in the four different types of nuclear medicine. It provides not only a β therapy option (^{161}Tb) but compared to the other suggested elements, terbium uniquely provides a potential α therapy option (^{149}Tb). An additional, favourable, property of ^{149}Tb is that it does not produce any α -emitting daughter nuclei. As mentioned previously, α emitting daughters can increase the dose to healthy cells, increasing patient toxicity [16]. Moreover, terbium exists in two theragnostic pairs (^{149}Tb is paired with ^{152}Tb (a PET isotope) and ^{161}Tb is paired with ^{155}Tb (a SPECT isotope)) where the half-life of the diagnostic imaging isotope

is comparable to the corresponding therapy isotope. Moreover, the SPECT (^{155}Tb) and β therapy pair have similar half-lives to the peptide targeting agents used (on the order of days). This will be discussed further in the next section along with preclinical studies proving the medical importance of these four terbium isotopes.

1.2.4 Terbium as a theragnostic element

Papers detailing studies of these four terbium isotopes' production and medical use go back as far as the early 2000's [17, 18, 19, 20, 21, 22, 23, 24]. However, a more recent series of papers published by Müller and her group at the Centre for Radiopharmaceutical Sciences ETH-PSI-USZ between 2012 and 2016 clearly demonstrate the medical potential of each isotope. In all of these studies, the isotopes ^{149}Tb, ^{152}Tb and ^{155}Tb were produced and extracted by the Isotope Separator On Line DEtector (ISOLDE) group, CERN and the ^{161}Tb isotope was produced via exposing enriched ^{160}Gd to a neutron flux outside a reactor at the Institute Laue-Langevin (ILL), France or a spallation-induced neutron source, SINQ at Paul Scherrer Institute (PSI), Switzerland and extracted using cation exchange chromatography [19].

The therapeutic properties of the α and β isotopes, ^{149}Tb and ^{161}Tb were investigated in mice with specifically grown tumours [25]. The survival curves of three mice for the ^{149}Tb and five mice for the ^{161}Tb experiments are compared in figure 1.5 against control sets of untreated mice. Unfortunately, the total activity of the ^{149}Tb available for this study in mice was lower than desired. However, even with this, there is a clear increase in mice survival for both the α- and β- therapy.

The imaging power of three of the Tb isotopes were also investigated, as shown in figure 1.6 [25]. Interestingly at therapeutic doses ^{161}Tb produced good quality SPECT images which is beneficial to monitor isotope distribution and compare to ^{155}Tb SPECT images. Importantly

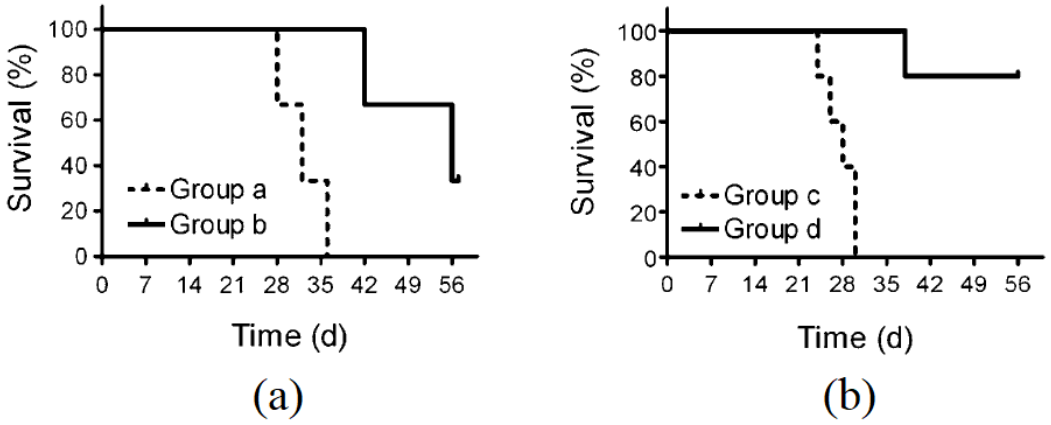

Figure 1.5: Survival curves of α-therapy and β-therapy studies. (a) α-therapy: Group a were the untreated control mice (n = 3) and Group b were mice treated with ^{149}Tb-cm09 (n = 3); (b) β-therapy: Group c were the untreated control mice (n = 5) and Group d were mice treated with ^{161}Tb-cm09 (n = 5). [25] (The cm09 was the targeting agent attached to the isotopes used in the treatment).

^{155}Tb produced very high quality SPECT image with only a small amount of activity.

A detailed investigation into the quality and potential of the SPECT ^{155}Tb isotope was carried out [26]. Part of the study compares ^{155}Tb to a currently used SPECT isotope, ^{111}In. As shown in in figure 1.7, 2.6 MBq of ^{155}Tb produced an excellent quality image of a Derenzo phantom. This image was comparable to that taken with almost double the activity of ^{111}In (4 MBq). The quality of the images produced and the half-life of ^{155}Tb (5.32 days) not only proved the suitability of the isotope as the complementary imaging isotopes for ^{161}Tb but with a reduced required activity for imaging it could also replace ^{111}In and be paired with other therapy isotopes including ^{177}Lu, ^{90}Y and ^{166}Ho.

Figure 1.8 was taken as part of a study investigating ^{152}Tb [27]. This work not only highlighted the good quality of the ^{152}Tb PET images, as seen in figure 1.8, but also the need for more regular and higher activity production of ^{152}Tb to further preclinical studies.

The therapeutic isotope ^{161}Tb has very similar properties to currently used ^{177}Lu, see ta-

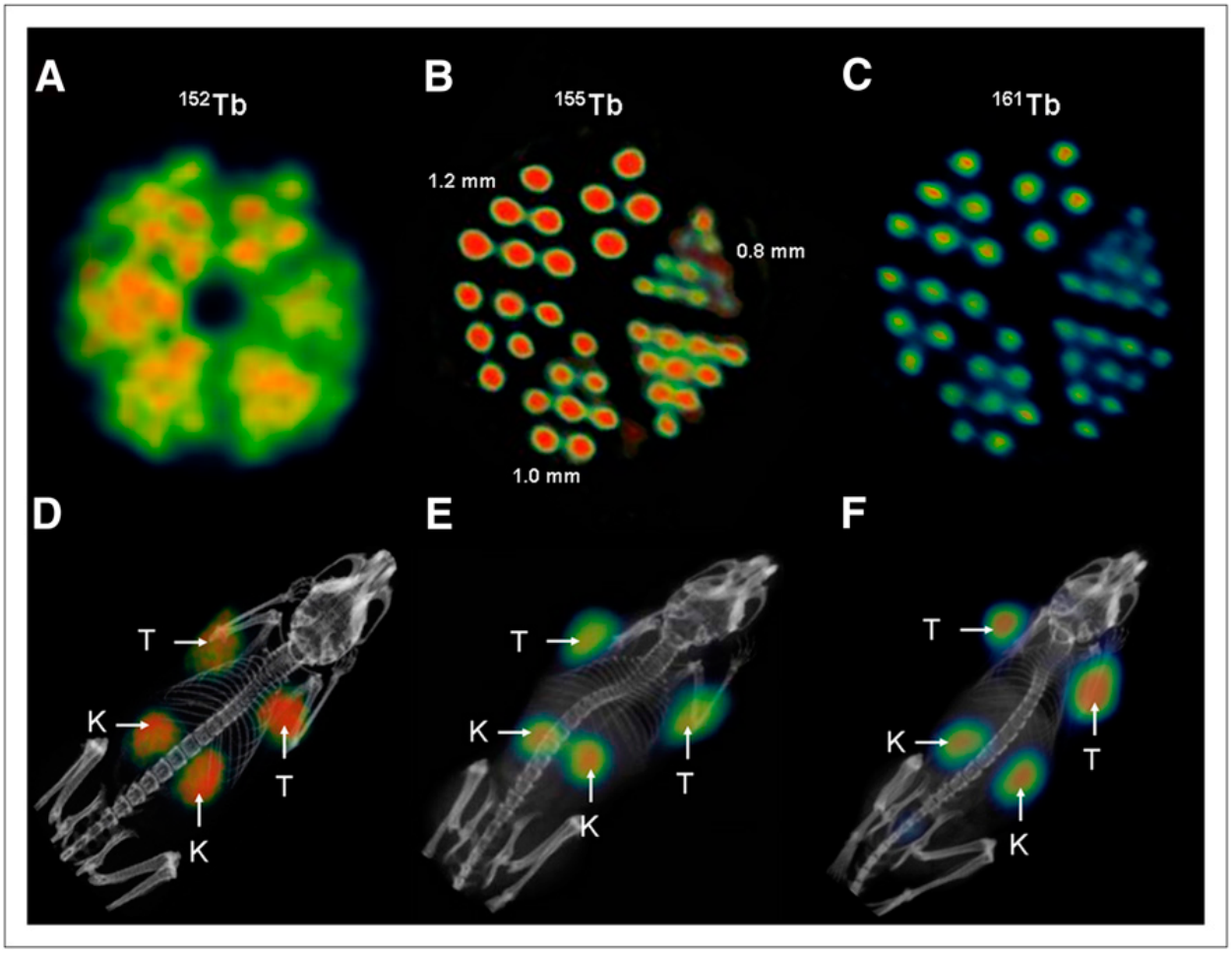

Figure 1.6: (A) PET image of Derenzo phantoms (1.9 MBq of ^{152}Tb). (B and C) SPECT images of Derenzo phantoms (0.6 MBq of ^{155}Tb and 50 MBq of ^{161}Tb, respectively). (D) PET/CT image of KB tumour–bearing mouse at 24 h after injection of ^{152}Tb-cm09, (E and F) SPECT/CT images of KB tumour–bearing mice at 24 h after injection of ^{155}Tb-cm09 (E) and ^{161}Tb-cm09 (F). K = kidney; T = tumour. [25](The cm09 was the targeting agent attached to the isotopes used in the imaging tumours in the mice).

ble 1.2. This has sparked studies comparing the effectiveness of the two isotopes [28, 29]. It is believed that because ^{161}Tb emits additional Auger electrons, this will increase the therapeutic power of the isotope.

Figure 1.9, taken from [28] compared Lu and Tb β-therapy in two different types of cancer tumours, KB tumours and IGROV-1 tumours. There was a clear increase in survival in KB

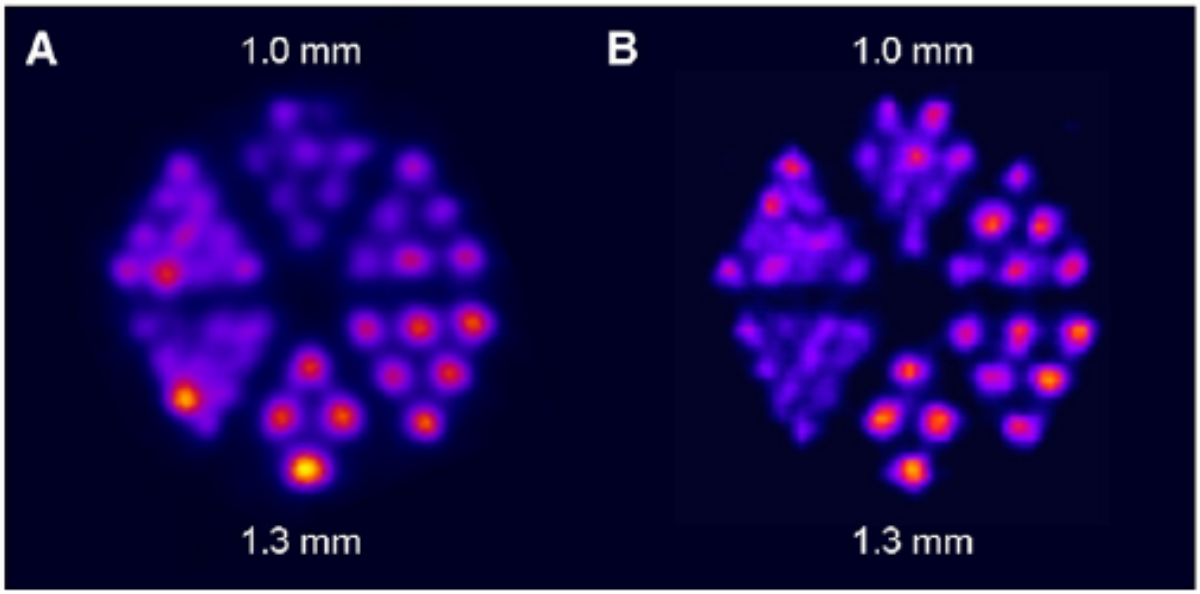

Figure 1.7: SPECT images of Derenzo phantoms filled with (A) ^{155}Tb (2.6 MBq) and (B) ^{111}In (4 MBq) [26].

Table 1.2: Comparison of ^{177}Lu and ^{161}Tb properties

	^{177}Lu	^{161}Tb
Half-life (days)	6.71	6.90
Average β energy (keV)	134	154

tumour-bearing mice when treated with Tb compared to Lu. However, there was only a marginal increase in survival for the IGROV-1 tumour-bearing mice (one mouse which may be statistical fluctuation). But an important point to note was that, for both tumours types, the Tb therapy reduced the size of the tumours more than the Lu treatment.

These and other studies are proving that ^{161}Tb may be a better treatment for certain cancers. In addition, the production and waste of ^{161}Tb compared to ^{177}Lu is much cleaner [30]. This is because the production processes for ^{177}Lu can also produce small quantities of ^{177}Lu in a metastable state which has a 160.44 day half-life. As these are the same isotope is makes separation impossible. ^{161}Tb does not exist in another isomeric form, thus does not suffer from these production and purification problems.

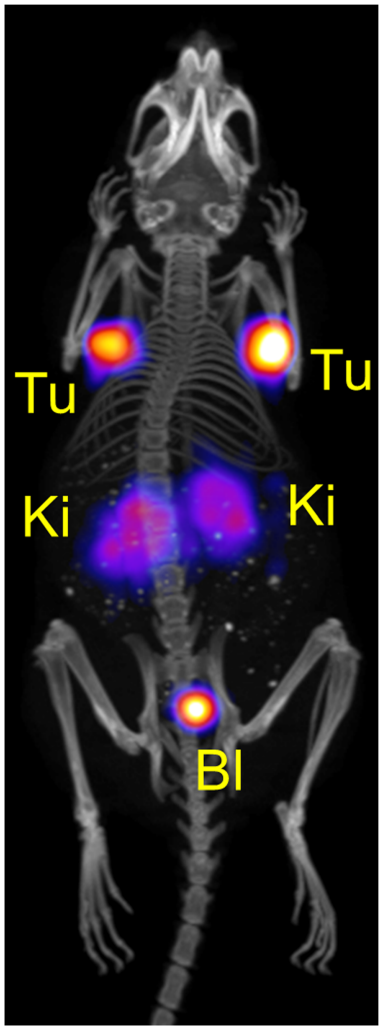

Figure 1.8: PET/CT of a tumour-bearing mouse 2 hours after being injected with 3.4MBq of ^{152}Tb -DOTANOC. The tumour (Tu), kidneys (Ki) and Bladder (Bl) are clearly visible [27]. (The DOTANOC was the targeting agent attached to the isotopes used in the PET imaging).

There is clear compelling medical evidence that this terbium theragnostic quadruplet has great potential for future medical use in customisable cancer treatments. The main drawback is the production, accessibility, and availability, in particular for the neutron-light isotopes (^{149}Tb, ^{152}Tb and ^{155}Tb). Current production of these isotopes is discussed in the next section and this thesis focuses on alternative production methods.

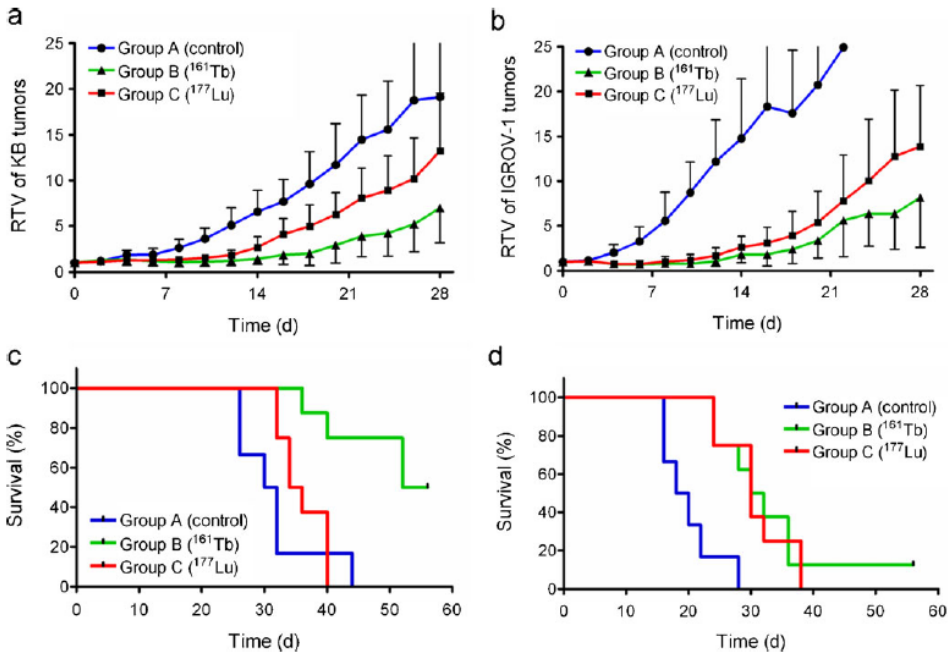

Figure 1.9: Tumour growth curves indicated as the relative tumour volumes (RTV) of KB tumour-bearing mice (a) and IGROV-1 tumour-bearing mice (b). Survival curves of KB tumour-bearing mice (c) and IGROV-1 tumour-bearing mice (d). Control mice (Group A) are shown in blue, mice treated with ^{161}Tb-cm09 (Group B) are shown in green and mice treated with ^{177}Lu-cm09 (Group C) are shown in red [28]. (The cm09 was the targeting agent attached to the isotopes used in the treatments).

1.3 Neutron light Tb production

1.3.1 Current production at CERN

As mentioned in the previous section ^{161}Tb is the only isotope of interest here not produced at CERN and is made via exposing a ^{160}Gd rich source to a high neutron flux [19]. Currently the other three isotopes (^{149}Tb, ^{152}Tb and ^{155}Tb) are produced exclusively at ISOLDE, CERN.

ISOLDE is a facility at CERN which produces different isotopes for various fundamental physics and materials experiments. A 1.4 GeV proton beam strikes a target, which results

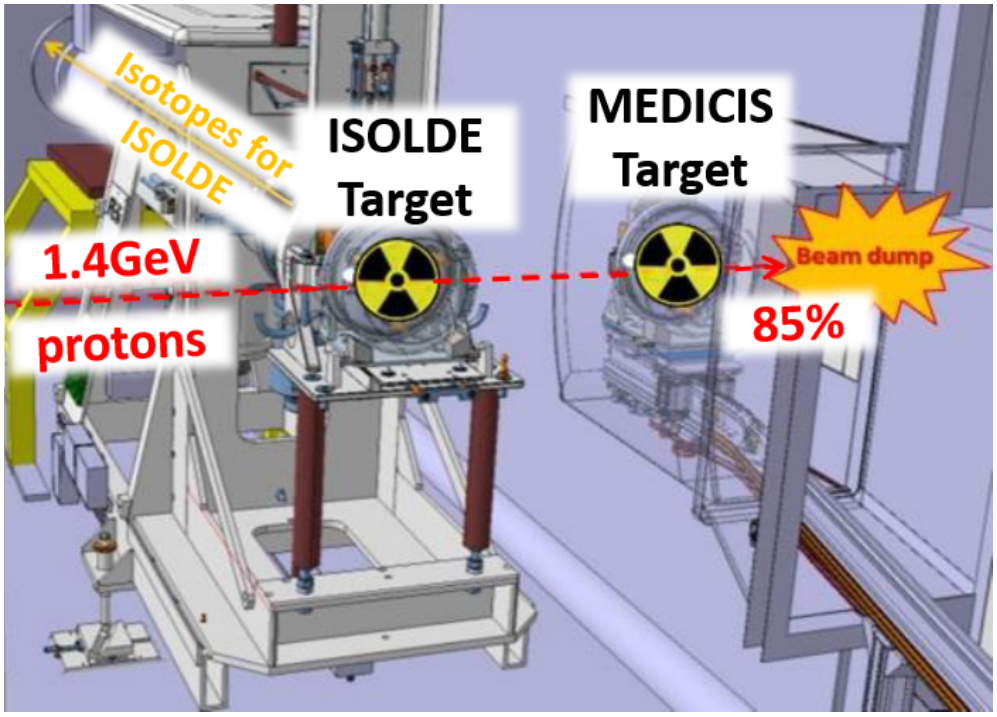

Figure 1.10: The MEDICS targets set-up behind the ISOLDE target [14].

in spallation reactions. This beam-line is connected to an on-line mass separator [14] which isolates the isotope of interest according to its mass. Unfortunately, there was limited beam time for the production of radioisotopes for medical use and research. However, the group Medical Isotopes Collected from ISOLDE (MEDICIS), founded in 2017 [31], hoped to resolve this beam time limitation by adding a secondary (tantalum) target behind the original ISOLDE target, see figure 1.10. This solution was deemed viable because 85% of the 1.4 GeV beam of protons pass straight through the ISOLDE target and can be used on the MEDICIS target.

Once a tantalum target has been irradiated and undergone proton induced spallation reactions [25], a multitude of isotopes are produced. The required isotopes are extracted by electromagnetic separation using an on-line mass spectrometer followed by chemical purification [32]. However, since autumn 2017 CERN has been on maintenance shut down, so there has been no proton beam. To overcome this, targets are irradiated at the 70 MeV cyclotron,

Table 1.3: ARRONAX C70 characteristics [33].

Beam	Extracted particles	Energy range (MeV)	Maximum current (μAe)	Duel beam
Proton	H +	35	<375	Yes
	H ++	35	<50	No
Deuteron	D +	15-35	<50	Yes
Alpha	He ++	70	<70	No

ARRONAX, Nantes, France, whose beam characteristics are given in table 1.3. The targets irradiated at ARRONAX are then shipped to MEDICIS to be separated.

1.3.2 Alternative production studies

The requirement for high energy proton-induced spallation reactions followed by electromagnetic separation for the production and extraction of the light-ion terbium reduces production possibilities to the CERN facility and hinders the element's future potential for world-wide hospital use. In 2012 and 2014 there was a push to look at using commercially available cyclotrons for production. The aim was to use stable isotope targets and irradiate them with light ions beams of protons (p), deuterons (d), helium-3 (^{3}He) or helium-4 (α) to produce the useful Tb isotopes.

Figure 1.11 depicts a small section of the nuclear chart which enables the reactions possible from stable isotopes (the black squares) near the desired Tb isotopes (highlighted in red) to be pictured. The information for each isotope is simplified to show the ground state, half-life and mode of decay or their natural abundance if the isotopes is stable. In order to know the likelihood of a selected reaction occurring given the energy of the beam, the cross-section of the reaction needs to be known. There are multiple nuclear reaction codes (e.g. TALYS [34], ALICE/ASH [35] and EMPIRE [36]) that will calculate cross-sections from nuclear theory, however, these must be verified by directly measuring the cross-sections.

Dy-150 7.17 M ε β⁺ α	Dy-151 17.9 M ε β⁺ α	Dy-152 2.38 H ε β⁺ α	Dy-153 6.4 H ε β⁺ (α)	Dy-154 3E+6 Y α	Dy-155 9.9 H ε β⁺	Dy-156 STABLE 0.06%	Dy-157 8.14 H ε β⁺	Dy-158 STABLE 0.10%	Dy-159 144.4 D ε	Dy-160 STABLE 2.33%	Dy-161 STABLE 18.89%	Dy-162 STABLE 25.48%
Tb-149 4.118 H ε β⁺ α	Tb-150 3.48 H ε β⁺ (α)	Tb-151 17.61 H ε β⁺ (α)	Tb-152 17.5 H ε β⁺ (α)	Tb-153 2.34 D ε β⁺	Tb-154 21.5 H ε β⁺ β⁻	Tb-155 5.32 D ε	Tb-156 5.35 D ε β⁺	Tb-157 71 Y ε	Tb-158 180 Y ε β⁺ β⁻	Tb-159 STABLE 100%	Tb-160 72.3 D β⁻	Tb-161 6.89 D β⁻
Gd-148 71.1Y α	Gd-149 9.28 D ε β⁺ (α)	Gd-150 2E+6Y α	Gd-151 123.9 D ε (α)	Gd-152 >1E+14Y α 0.20%	Gd-153 240.4 D ε	Gd-154 STABLE 2.18%	Gd-155 STABLE 14.80%	Gd-156 STABLE 20.47%	Gd-157 STABLE 15.65%	Gd-158 STABLE 24.84%	Gd-159 18.48 H β⁻	Gd-160 >3E+19Y 2β 21.86%
Eu-147 24.1 D ε (α)	Eu-148 54.5 D ε β⁺ (α)	Eu-149 93.1 D ε	Eu-150 36.9 Y ε β⁺	Eu-151 >1E+18Y α 47.81%	Eu-152 13.52 Y ε β⁺ β⁻	Eu-153 STABLE 52.19%	Eu-154 8.601 Y β⁻ (ε β⁺)	Eu-155 4.753 Y β⁻	Eu-156 15.19 D β⁻	Eu-157 15.18 H β⁻	Eu-158 45.9 M β⁻	Eu-159 18.1 M β⁻

Figure 1.11: A small section of the nuclear chart highlighting the medical Tb isotopes in red [15].

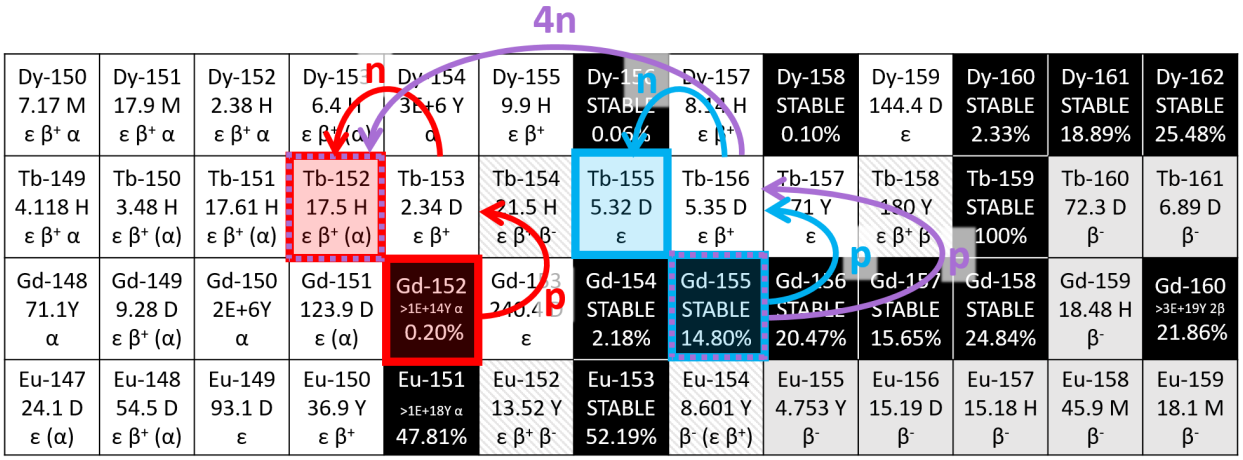

Figure 1.12: A small section of the nuclear chart depicting the reaction outlined in [37] ^{152}Gd(p,n)^{152}Tb in red, ^{155}Gd(p,n)^{155}Tb in blue and ^{155}Gd(p,4n)^{152}Tb in purple.

Initial research looked at production using commercial cyclotrons capable of producing 70 MeV protons. In 2012 ^{151,152,153,154m,155and156}Tb production cross-sections using ^{nat}Gd and protons were published [37]. The energy range of the protons covered 5.64 – 66.98 MeV. The cross-sections measured agreed with predicated cross-sections calculated using ALICE/ASH. The reactions of interest were ^{152}Gd(p,n)^{152}Tb, ^{155}Gd(p,n)^{155}Tb and ^{155}Gd(p,4n)^{152}Tb and are depicted as the red, blue and purple routes, respectively, in figure 1.12. Assuming a 100% enriched target is used, the yields of these reactions were calculated using ALICE/ASH pre-

dicted cross-section. High, clean yields of ^{152}Gd(p,n)^{152}Tb and ^{155}Gd(p,n)^{155}Tb are possible and are highlighted in red in figures 1.13 a and b respectively. Optimal yields of ^{152}Tb and ^{155}Tb with no contaminates were possible up to 12 and 11 MeV respectively. However, the production route of ^{155}Gd(p,4n)^{152}Tb contained many contaminants and shown in figure 1.13 c. Thus, if clean production without the need for electromagnetic separation is possible then only the ^{152}Gd(p,n)^{152}Tb and ^{155}Gd(p,n)^{155}Tb reactions are contenders. However, looking at the abundances of stable Gd isotopes in figure 1.11, ^{152}Gd only accounts for 0.2% abundance and ^{155}Gd 14.80% abundance. Gadolinium-155 can be enriched to >99% and so ^{155}Gd(p,n)^{155}Tb is possible without the need for electromagnetic separation but it is unclear whether ^{152}Gd can be enriched enough for viable ^{152}Tb production.

In 2014 additional cross-section measurements were published for alternative target-proton beam reactions for ^{149}Tb and ^{152}Tb production [38]. Again, Gd targets were used, however, instead of ^{nat}Gd, enriched targets of ^{152}Gd (30.60% enriched) and ^{155}Gd (99.82% enriched) were used to measure the cross-section for the reactions: ^{152}Gd(p,4n)^{149}Tb and ^{155}Gd(p,4n)^{152}Tb (red and purple routes, respectively, in figure 1.14).

This work also looked at the indirect production of ^{155}Tb via the production of ^{155}Dy which then decays to ^{155}Tb (the blue production route in figure 1.14). The excitation function (cross-sections) for ^{155}Dy production was measured after a proton beam irradiated a stack of ^{nat}Tb targets (which is monoisotopic ^{159}Tb). Taking all of the proton irradiation on Gd targets together, from these cross-section measurements, excellent production yields of ^{149,152,155}Tb are possible using a 70 MeV cyclotron. However, there is still a need for electromagnetic isotope separation.

As previously mentioned this is currently the case as these isotopes are being produced at ARRONAX (70 MeV cyclotron) followed by electromagnetic separation at MEDICIS, CERN.

Recent work published by Ulli et al. [39] successfully demonstrated a method of enriching Gd

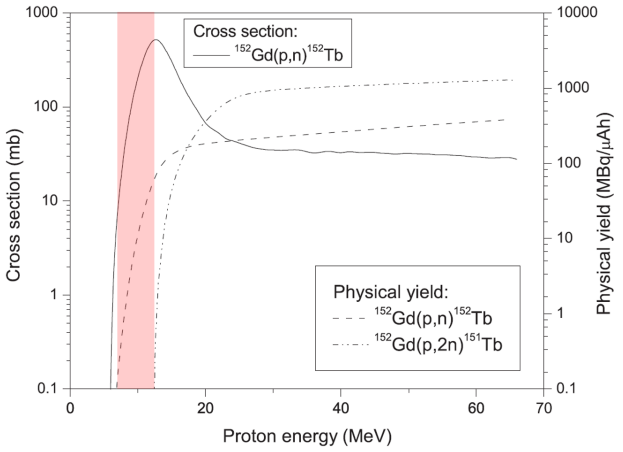

(a)

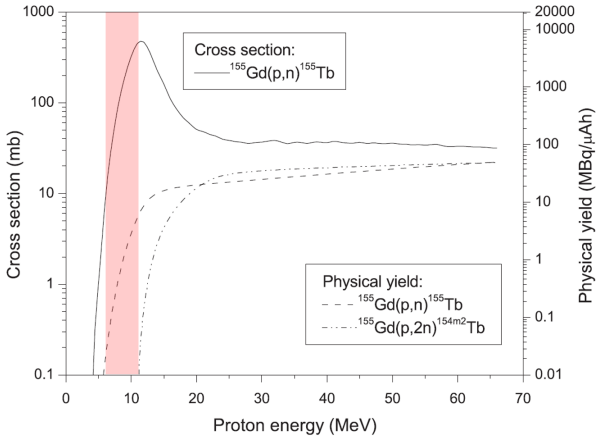

(b)

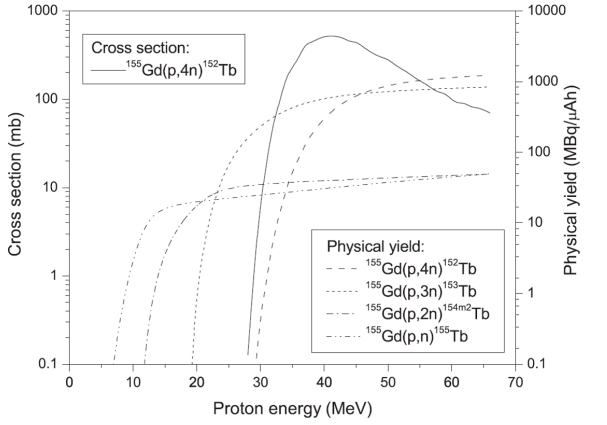

(c)

Figure 1.13: The cross-section and production yields of (a) ^{152}Gd(p,n)^{152}Tb, (b) ^{155}Gd(p,n)^{155}Tb and (c) ^{155}Gd(p,4n)^{152}Tb reactions [37].

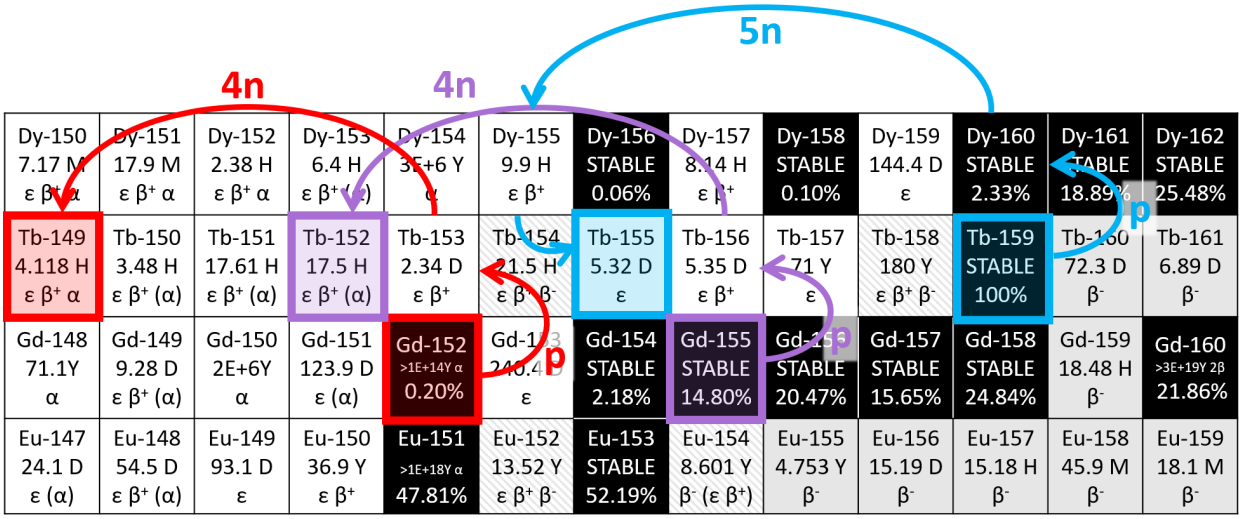

Figure 1.14: A small section of the nuclear chart depicting the reaction outlined in [38] ^{152}Gd(p,4n)^{149}Tb in red, ^{155}Gd(p,4n)^{152}Tb in purple and ^{159}Tb(p,5n)^{155}Dy $\rightarrow$ ^{155}Tb in blue.

targets using electromagnetic separation. This would be useful for ^{152,155}Tb production via the ^{152}Gd(p,n)^{152}Tb and ^{155}Gd(p,n)^{155}Tb reactions, particularly for the ^{152}Tb production as discussed previously [37]. Also, an historic, 99.9% enriched, ^{152}Gd target was used to demonstrate that ^{152}Tb could be produced with 12 MeV protons with medically acceptable levels of other Tb isotope contaminants. However, due to the need of a highly enriched target the main concern for commercial production using this route is the need for an efficient target recycling method.

1.3.3 Eu production

A production route option which has not been investigated till now is via the use of helium beams on europium targets. There are only two stable isotopes of Eu (^{151}Eu and ^{153}Eu) and they are naturally, approximately 50/50 split abundance. Compared to Gd, it is easier to produce >99% isotope enriched targets of europium oxide with fewer same-element, different-isotope contaminants.

By irradiating ^{nat}Eu with a ^{4}He (α) beam the ideal reactions would be ^{151}Eu(α,3n)^{152}Tb and ^{153}Eu(α,2n)^{155}Tb as depicted in the red and blue reaction flows in figure 1.15, respectively. However, compared to proton beams, α beams introduce more nuclides to the system, therefore a multitude of other isotopes can be produced (as there are more reaction channels open), including isotopes of other elements up to and including Tb.

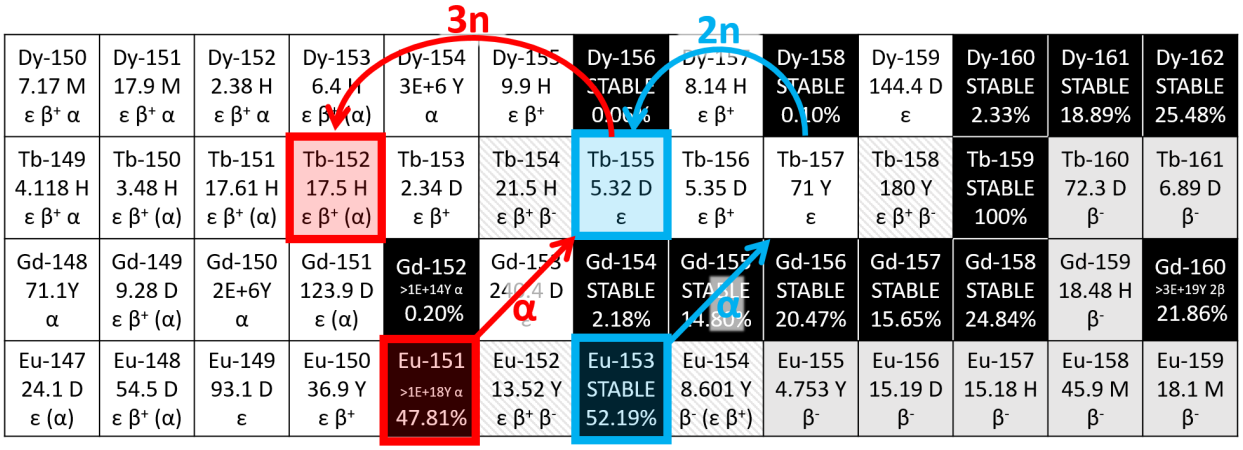

Figure 1.15: A small section of the nuclear chart depicting the reaction ^{151}Eu(α,3n)^{152}Tb in red, ^{153}Eu(α,2n)^{155}Tb in blue. The black squares indicate naturally occurring isotopes for which the natural atom-abundances are given as percentages. Other squares represent radioactive isotopes for which the half-life and primary decay modes are given.

Producing isotopes of elements other than Tb is not fundamentally a problem because the chemical difference between elements allows separation with relative ease. The work discussed in this thesis is part of a collaboration with radiochemists from the National Physical Laboratory (NPL) who have developed a chromatography technique using a commercial LN resin for lanthanide separation [40].

An irradiated target containing Eu, Gd and Tb is oxidised, mixed with the LN resin and placed in a chromatography extraction column. By pouring different concentrations of nitric acid (HNO_3) at different rates through the column (see figure 1.16) clean Tb separation can be achieved as shown by the black curve in figure 1.17. The success of this technique means

that the focus of production using Eu targets and α beams is now on the type and quantity of Tb isotopes produced in the interactions as other contaminant elements can be separated from the irradiated target.

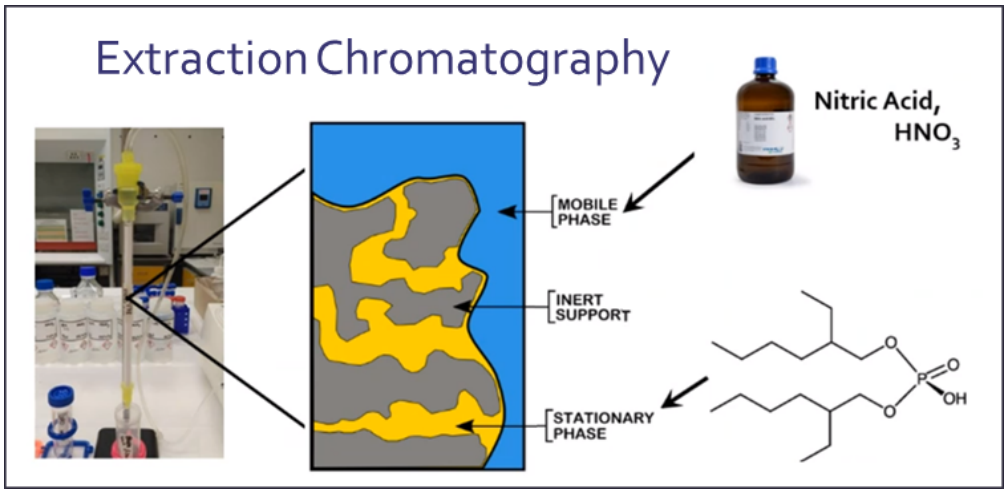

Figure 1.16: Photograph and diagram of chromatography column set-up [40].

As previously discussed, for ideal mass production for hospital use the process should not be reliant on electromagnetic separation of Tb isotopes from one another. Therefore, for Eu production to be a viable route there needs to be an α energy window where only a single terbium isotope of interest is produced. To quantify the other Tb contaminant isotopes produced and the production rate of the ^{152}Tb and ^{155}Tb , the cross-sections of ^{nat}Eu(α,xn)$^{nat+\alpha-xn}$Tb reactions need to be known.

Following the footsteps of previous investigations using Gd and Tb targets, the cross-section of the Eu and α beam will be measured. Until now, there has only been one measurement of this type which covered an α energy range of 12.59–16.00 MeV and only measured the cross-section of the ^{151}Eu(α,γ)^{155}Tb reaction and ^{151}Eu(α,n)^{154}Tb [5]. Therefore, the research endeavour of this PhD was to measure cross-sections for the full range of Tb isotopes produced when irradiating ^{nat}Eu with an α beam. From this the viability of this production route can be determined.

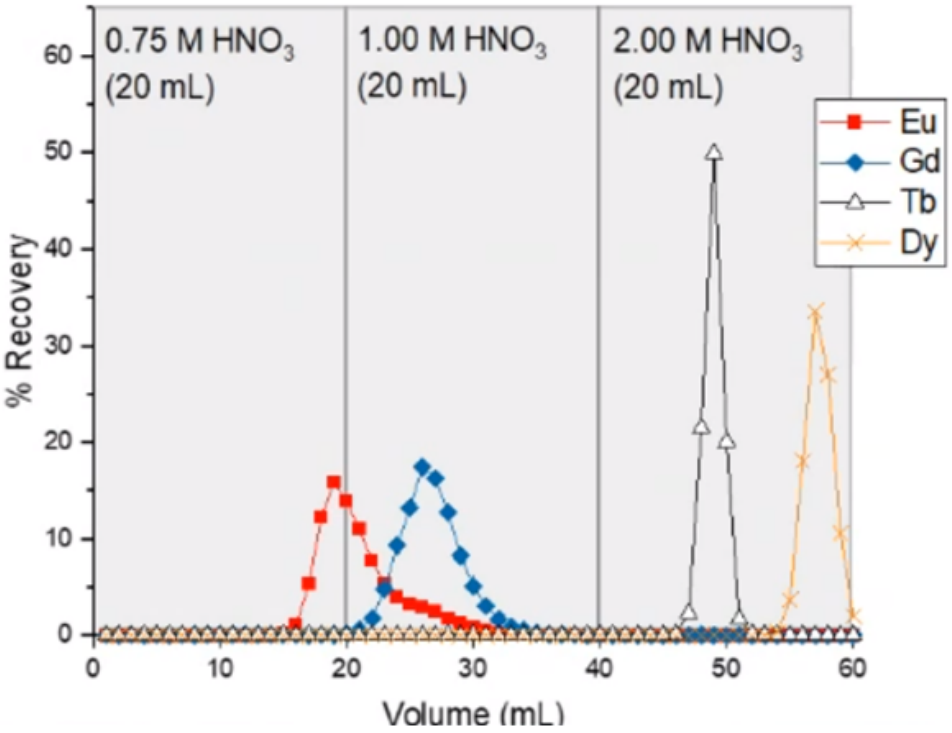

Figure 1.17: Graph of the lanthanide separation capable using the chromatography technique developed by NPL [40]. Three additions of 20 ml of nitric acid (HNO_3) were gradually poured into the chromatography extraction column. The graph is split into three section and labelled with the concentration for nitric acid used. The total volume of nitric acid added was monitored along the x-axis as the extraction (% Recovery) of elements Eu, Gd, Tb and Dy were recorded along the y-axis.

There were many measurements and factors that needed to be established before irradiation of the Eu targets took place. This included the measurement of α beam energy, Eu target thickness and method of foil stacking in the target. The method and analysis of the data from these steps are discussed in chapter 3 along with the α beam current measurement taken during target irradiation.

Once the Eu targets had been irradiated, the products of the reaction needed identifying and quantifying. Chapter 4 describes the γ spectra process identifying and extracting the activities of the isotopes produced. Then, chapter 5 discusses how the activities were used to

plot decay curves and extract half-life and cross-sections values. The process of measuring absolute cross-sections is intricate and prone to systematic errors. All the measurements taken at each step in the process need to be precise and accurate to ensure reliable cross-section measurements with reasonably sized error bars. A summary of the final cross-section and half-life measurement results and a discussion of future plans and potential areas of improvement are detailed in chapter 6.

However, firstly, the basic theory of nuclear reactions and cross-section measurement (both experimental and computer simulated) need to be discussed. These are explained in chapter 2 along with an overview of the experimental method of cross-section measurement used and derivations of the equations needed for each process in the quest for Eu+α cross-section measurements.

Chapter Two

Cross-section measurements

To investigate the viability of Tb production using Eu targets and α beams, the first step is to establish the cross-sections of the possible interactions. Theoretical calculations performed using nuclear reaction codes discussed in section 2.1 provide an approximate idea of the excitation functions of each possible interaction. However, for medical isotope production, accurate cross-section data are needed. Precise cross-sections are important for being able to select optimal energy windows for high yield production and are invaluable in determining quantities and types of contaminating isotopes. Therefore, the first step in producing medical isotopes is to measure the cross-sections.

This chapter discusses details of both the theory of nuclear reaction as relating to cross-section and theoretical calculations performed using TALYS, as well as the theory and outline of experimental cross-section measurements. As previously discussed, this work was part of a collaboration for which a chemical extraction process was produced by radiochemists at NPL which allows for clean extraction of Tb from a lanthanide target. This implies that, for medical Tb production with Eu targets and α beams, the isotopes that will provide contamination in the final product are other, non-medical, isotopes of Tb. Therefore, this research focused on measuring cross-sections for the production of Tb isotopes.

2.1 Theoretical calculation

2.1.1 Nuclear reaction mechanisms

When a piece of matter is exposed to particles from a source, for example, a reactor, cyclotron or even particles emitted by radioactive isotopes, it is possible for a nuclear reaction to take place within the material. The type and likelihood of the reaction depends on the target material and incident particle as well as the energy put into the reaction (i.e. the energy of the incident particle if the target material is stationary). The energy must overcome the Q-value of the reaction for it to take place. However, the type of interaction to achieve the same product nuclei will vary with the input energy.

Commonly, a light ion projectile, p, is incident on a heavier target, T. The products of the reaction will often consist of an altered target nucleus, U and a small ion , q, ejected from the target nucleus. This reaction can be represented as:

$$p + T \quad \rightarrow \quad U + q.$$

However, this is often written in a more compact format,

$$T(p, q)U.$$

The brackets of this compact form are used to describe the reaction taking place. For example, (p, n) reactions and (α, n) reactions where the resultant emitted projectile is the same for both (a neutron) and the reaction was initiated by a proton or alpha particle, respectively. There are many types of reaction that can be grouped depending on how the projectile interacts with the target nucleus. Some of the reaction types are shown in figure

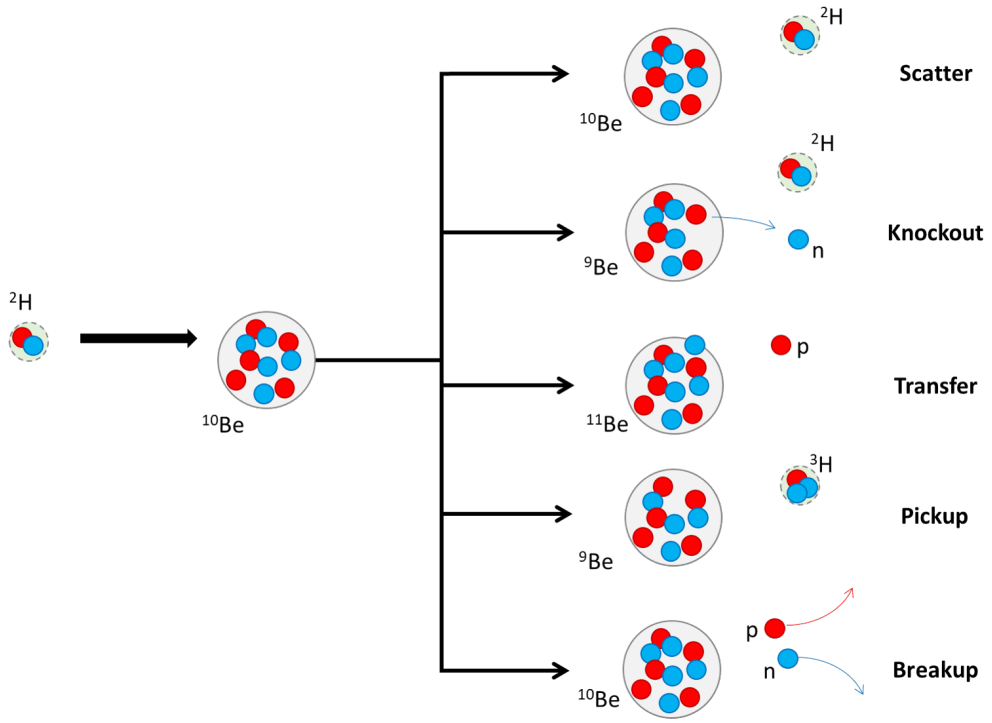

Figure 2.1: Examples of five different types of nuclear reactions that could occur when a deuteron consisting of a proton (red) and a neutron (blue) strikes a ^{10}Be target nucleus (adapted from [41]).

2.1 with examples to describe the processes. The scatter reaction shown in figure 2.1 can occur as either an elastic or inelastic collision. The incident and product nuclei and projectile remain the same but the product nucleus is in the ground state for elastic and in an excited state for inelastic collision.

The nuclear reactions can also be grouped under either direct, compound or quasibound (pre-equilibrium) reactions [42]. In essence, the categorisation of the reaction depends on how much of the nucleus the projectile interacts with.

Direct reactions

When the projectile hits the target nucleus with energies greater than 5 MeV per nucleon [43] (i.e. 20 MeV for an α projectile) then a direct reaction is more likely. This is where the

projectile interacts with only one nucleon within the target nucleus. Direct reactions occur in the shortest time frame compared to the other two reaction classifications outlined in the subsequent sections.

Compound reactions

Often occurring at lower projectile energies, compound reactions are where the projectile is fully absorbed within the target nucleus. The formation of this compound nucleus is brief. The energy is distributed among the nucleons of the compound nucleus, before a smaller projectile, q, is emitted from the compound nucleus leaving the product nucleus, U.

Due to the brief formation of the compound nucleus, compound reactions occur slower than direct reactions. Although compound reactions occur at lower projectile energies, the projectile must have enough energy to overcome the Coulomb barrier. For α+Eu compound reactions the energy of the α particle must be 19 MeV or greater (see appendix A for details).

Moreover, the compound nucleus has no memory of its previous state, i.e. there are multiple reactions which can form the same compound nucleus which could then separate to a variety of the final products. There would be no way to identify the original reactants from the products. Figure 2.2 provides an example of this to form a ^{157}Tb compound nucleus using either Eu or Gd target nuclei and α or proton projectiles, respectively.

Quasibound reactions

As the name suggests, this classification of reaction is where the projectile interacts with only a smaller selection of nucleons within the target nucleus. However, the information is not uniformly dissipated through the nucleus as a whole.

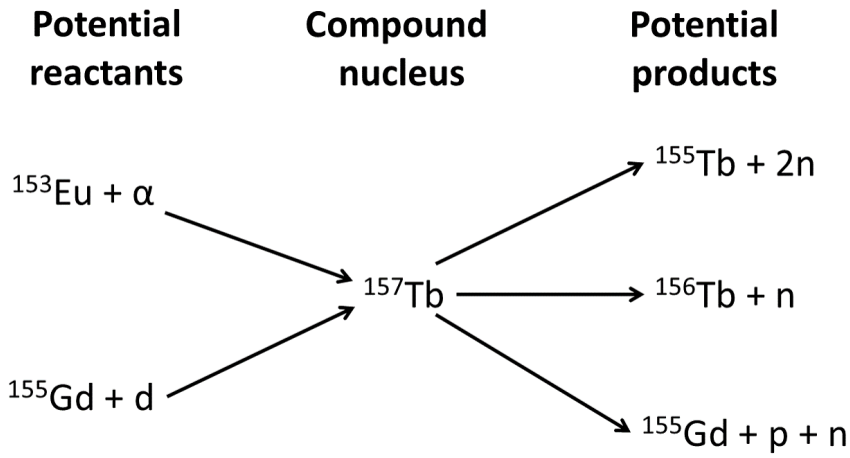

Figure 2.2: Examples of reactants and products that could form and be formed from the compound nucleus, ^{157}Tb.

The cross-section contributions for all these possible types of reactions need to be accounted for when calculating a total cross-section for production of a specific isotope. This is too complex to solve directly, thus, multiple models have been produced to calculate the likelihood of the different interactions which will contribute to the overall cross-section. These models are used in nuclear reaction codes such as TALYS and EMPIRE to calculate cross-sections.

2.1.2 Predicted cross-sections from nuclear reaction codes

Nuclear reactions codes like TALYS and EMPIRE use models to calculate theoretical cross-sections. Where measured nuclear cross-section data exist, these are incorporated into the models. More information about the models used for each code can be found in Refs. [34] and [36].

UoB-TIP is a data extraction code that has been developed at the University of Birmingham [44, 45] to interact with either the TALYS or EMPIRE reaction codes and use their data outputs. Among many of its features, UoB-TIP can be used to extract csv files of total

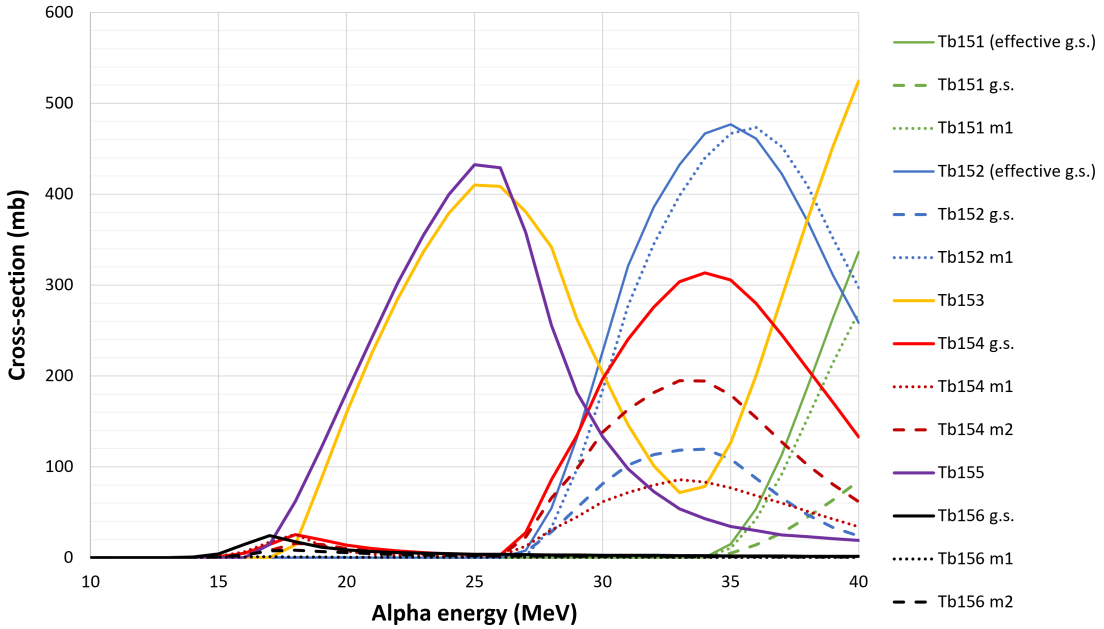

Figure 2.3: TALYS predicted cross-sections against α energy for the production of Tb isotopes and isomers from α+^{nat}Eu reactions. The ground state of the isotopes are represented by g.s. and the excited meta-stable state isomers are denoted as m1 or m2. The "effective g.s." is the cross-section for the ground state accounting for the decay of meta-stable states into the ground state. Effective g.s. has been calculated for ^{151}Tb and ^{152}Tb because the half-life of their isomers are 25 seconds and 4.2 minutes, respectively. Therefore, most/all of these isomers will have decayed away adding to the cross-section measurement of the ground state.

cross-sections for product isotopes and isomers for a specified nuclear reaction as a function of projectile energy.

Figure 2.3 shows the TALYS predicted cross-section for the production of Tb isotopes and isomers from α+^{nat}Eu reactions. There are very limited measured cross-section data for the nuclear reaction codes to use to calculate the cross-sections. Therefore, only nuclear models were used.

Looking at the TALYS predicted cross-sections for α+^{nat}Eu reactions (see figure 2.3), it would seem impossible to be able to produce either ^{152}Tb or ^{155}Tb without another Tb

isotope produced in large quantities as well. When the cross-section for ^{155}Tb is high, the cross-section for ^{153}Tb also follows a similar trend. Likewise, the cross-section of the contaminant ^{154}Tb isotope also follows a similar pattern to the medical isotope ^{152}Tb .

A solution to this could be to produce ^{152}Tb and ^{155}Tb using targets of enriched ^{151}Eu or ^{153}Eu, respectively. The predicted TALYS cross-sections for the separate α+^{151}Eu and α+^{153}Eu reactions are presented in figures 2.4 and 2.5, respectively. These predicted cross-sections would suggest the possibility of a relatively high yield and clean production window for ^{152}Tb between 33 and 37 MeV and optimally at 35 MeV. Additionally, a high yield and very clean ^{155}Tb production window could be achieved between 20 and 27 MeV with optimal production at 25 MeV.

Europium exists naturally as a 47.81/52.19% mix of 151/153 isotopes. Therefore, it would be relatively easy to produce highly enriched targets of either isotope. This is especially significant for the production of ^{152}Tb where previously performed methods of production require highly enriched ^{152}Gd which has a natural abundance of only 0.2%. Therefore, if a high yield, low-Tb-isotope-contaminant production of medical Tb isotopes can be performed with enriched Eu targets then this could prove to be a more suitable production avenue than Gd targets.

However, these are only predicted cross-sections and as stated above, there are very few experimental cross-section measurements (see the beginning of section 2.2 for more details). There are also no relevant cross-section measurements for the production of medical Tb isotopes from α +Eu reactions. Therefore, these predicted cross-sections need to be verified experimentally.

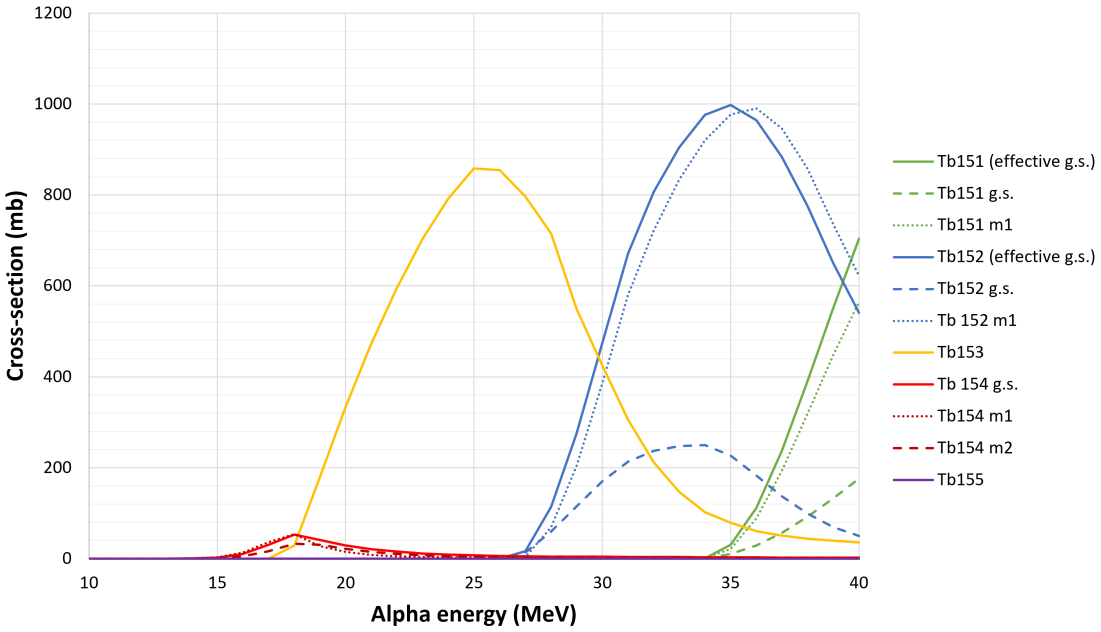

Figure 2.4: TALYS predicted cross-sections against α energy for the production of Tb isotopes and isomers from α+^{151}Eu reactions.

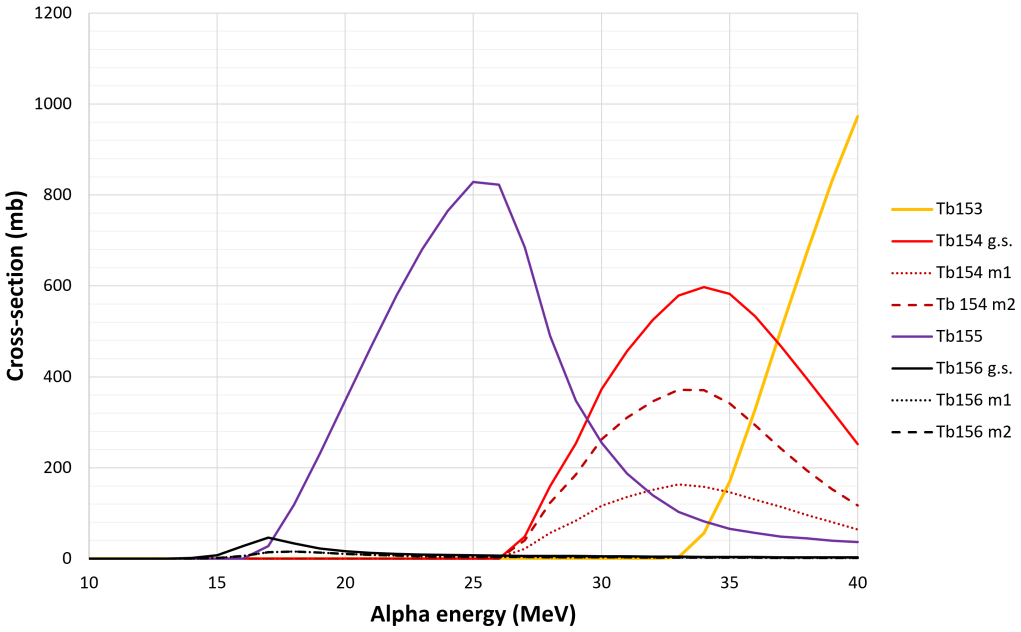

Figure 2.5: TALYS predicted cross-sections against α energy for the production of Tb isotopes and isomers from α+^{153}Eu reactions.

2.2 Experimental measurement

As mentioned previously, there are limited experimental results [5] for α+Eu cross-sections. The excitation functions for the production of ^{155}Tb and the two isomers and ground state of ^{154}Tb from α beams and ^{151}Eu targets were examined over an energy range of 11.30–17.09 MeV. The data points are compared to TALYS in figure 2.6. Looking at TALYS cross-sections in section 2.1, it is clear that this energy range and the ^{151}Eu(α,γ)^{155}Tb production route are not optimal for medical isotope production nor does this set of data provide information about ^{152}Tb production. Therefore, cross-sections for a higher and wider range of α energies, as well as alternative production routes, i.e. ^{151}Eu(α,3n)^{152}Tb and ^{153}Eu(α,2n)^{155}Tb, need to be measured for medical Tb isotope production.

2.2.1 Parameters required for experimental cross-section measurement

If a stationary foil target with N_{target} number of nuclei per cm^2 is irradiated for time, t_{irrad}, by a beam of particles with constant current Φ (number of beam particles per second), the total activity (A_T) of an isotope produced (with decay constant, λ) is given by

$$A_T = \Phi N_{target} \sigma \left(1 - e^{-\lambda t_{irrad}}\right), \tag{2.1}$$

where σ is the cross-section of interaction for the production of this isotope, given the beam energy and reactants. For an α beam, Φ can be expressed as $N_\alpha I$ where N_α is the number of α particles per μA of beam current and I is the measured beam current in μA. Therefore, equation 2.1 can be expressed as,

$$A_T = N_\alpha I N_{target} \sigma \left(1 - e^{-\lambda t_{irrad}}\right), \tag{2.2}$$

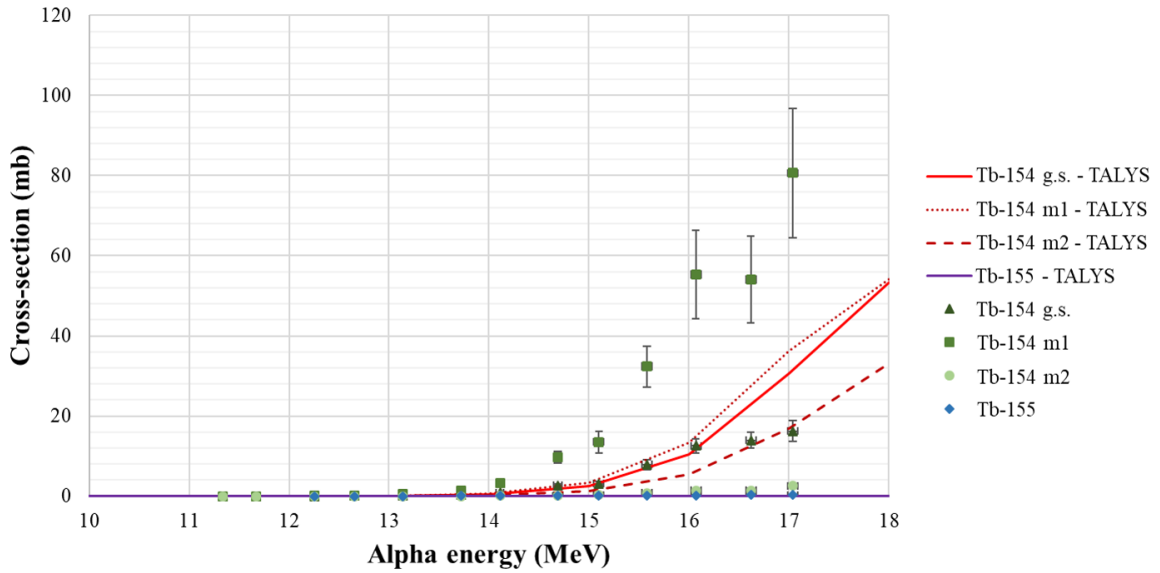

Figure 2.6: The measured cross-sections of α+^{151}Eu reactions against α energy in MeV. The blue data points are the measured ^{151}Eu(α, γ)^{155}Tb reaction cross-sections and varying shades of green data points are the measured ^{151}Eu(α, n)^{154}Tb reaction cross-sections. The triangle points are the measurement of ^{154}Tb ground state (g.s) production; the square data points are for the ^{154}Tb first excited state (m1) production; and the circular data points are for the ^{154}Tb second excited state (m2) production. The data points were taken over and α energy range of 11.30 – 17.09 MeV and are published in Ref [5]. The TALYS predicted cross-section given by the four different lines (see key for more details) are compared to these measured values. Although the order in which the isotopes and isomers are most likely to be produced follows the same pattern, in many cases, the measured values are wildly different to the predicted ones. This highlights the need to measure the cross-sections rather than using TALYS predictions at face value.

for which a derivation can be found in appendix B. For longer lived nuclides, the activity of the isotope produced is limited by the irradiation time and the beam current. However, the activity of shorter lived isotopes plateaus during the irradiation and is, therefore, only limited by the current. In such cases, increasing the production time will not increase the

total short-lived isotopes production. Equation 2.2 can be rearranged to give

$$\sigma = \frac{A_T}{N_\alpha I N_{target}\left(1 - e^{-\lambda t_{irrad}}\right)}. \tag{2.3}$$

This equation provides the framework of parameters that need to be measured in order to calculate cross-sections. The decay constant, $\lambda = \frac{\ln 2}{T_{1/2}}$, is calculated from half-life values, $T_{1/2}$, of each product isotope, and are taken from the National Nuclear Data Center (NNDC) and the International Atomic Energy Agency (IAEA) [15] [46] (see table 4.2). The irradiation time was recorded for each α beam exposure. Knowledge of the target foil thickness is required as

$$N_{target} = \frac{\rho N_A}{A_r} x \ , \tag{2.4}$$

where ρ is the density of the target in gcm^{-3}, N_A is Avogadro's number, A_r is the atomic weight of the target and x is the target thickness in cm. Therefore, accurate and precise foil thicknesses were measured as described in section 3.1.

The total activity of the isotope produced by the end of target irradiation required multiple measurement steps. First, multiple γ spectra of the irradiated targets were taken over a time period of 5-6 half-lives of the isotope under investigation. After identifying the most intense γ peaks emitted by the isotope of interest, the area under the peaks would be corrected for count-rate changing over each spectrum due to the isotope decaying while the spectra are being recorded. In addition, these count-corrected activities for each peak in each spectrum, A_C, were then corrected for detector and geometric efficiency.

Once these corrections have been applied, the activity of the isotope at the start of each γ spectrum, A_E, is produced for each γ peak measured. Decay curve graphs, of $\ln(A_E)$ against time since the end of the irradiation, were then plotted. The gradient of these decay curves is $\frac{\ln 2}{T_{1/2}}$ and the intercept, $\ln(A_T)$, provides the total activity of the isotope at the end of α irradiation.

The number of α particles per 1 μA, N_α, is

$$N_\alpha = \frac{1 \times 10^{-6}}{2 \times 1.60218 \times 10^{-19}} = 3.12075 \times 10^{12}. \tag{2.5}$$

The beam current is measured by the collection of charge in a Faraday cup as described in section 3.4. The counts of the Faraday cup were recorded by a Brookhaven model 1000c charge integrator, using a full scale of 60 nC. The conversion to current is given by,

$$I(\text{nA}) = \frac{\text{counts} \times 60 \text{ nC}}{\text{time (minutes)} \times 60}. \tag{2.6}$$

However, if the current varies over the irradiation time and the length of irradiation is less than or comparable to the half-life of the isotope, then the activity of the isotope produced can be given by

$$A_T = \sigma N_{target} \sum_{i=1}^{n} \Phi_i \left(1 - e^{-\lambda\tau}\right) \cdot e^{\lambda\tau(n-i)}. \tag{2.7}$$

Here, the irradiation time is divided into, n, smaller sections (periods), of length $\tau = t_{irrad}/n$ and $\Phi_i (= N_\alpha I)_i$ is the beam flux for the i^{th} period of irradiation time [47].

2.2.2 Multiple foil cross-section measurement

To measure cross-sections for multiple α energies the standard thin foil stacking method was employed. Several thin (10s of microns thick) Eu foil were laid over each other and then irradiated as one target. As the α beam travels through the target the beam energy degrades. This energy degradation and the energy range covered by each foil can be calculated using the Monte-Carlo Code, SRIM (the Stopping and Range of Ions in Matter) [48] which utilised the Bethe-Bloch formula [49] for dE/dx (the instantaneous energy loss per unit distance) of a light ion in a material.

To extend the energy range of α beam as it travels through the target, thin layers of materials such as Al foils can be added in between the Eu foils to further degrade the energy of the beam. Therefore, it was imperative to measure the thickness of the Eu and Al foils and the initial α – beam energy used to a high degree of accuracy and precision.

A couple of preliminary studies were performed to look at the feasibility of this cross-section measurement. An initial cross-section measurement experiment with a different foil stacking arrangement was also conducted and will be commented on. However, all of these previous studies were used to improve and develop the technique for the final cross-section measurement. The experimental set-up and data for this last study will be the main focus for the remaining chapters on cross-section measurements.

Chapter Three

Experimental methods for α+Eu cross-sections

This chapter will expand on the experimental set-up and analysis performed to measure the parameters outlined in equation 2.3, chapter 2 which are used for the extraction of cross-sections from the experimental data. The foil thickness measurements and foil target stacking will be discussed along with beam parameterisation. However, the γ spectroscopy measurement set-up and initial analysis for decay and efficiency corrections are described in chapter 4 and the final decay curves and cross-section extraction can be found in chapter 5.

3.1 Foil thickness

3.1.1 Theory

As charged particles travel through a medium they lose energy according to the Bethe-Block formula. The energy loss per unit length ($\frac{dE}{dx}$) and the range of an α particle traveling through different elements can be calculated using a Monte-Carlo code like SRIM (the Stopping and

Range of Ions in Matter) [48]. Figure 3.1 shows the range of α particles through Eu calculated using SRIM.

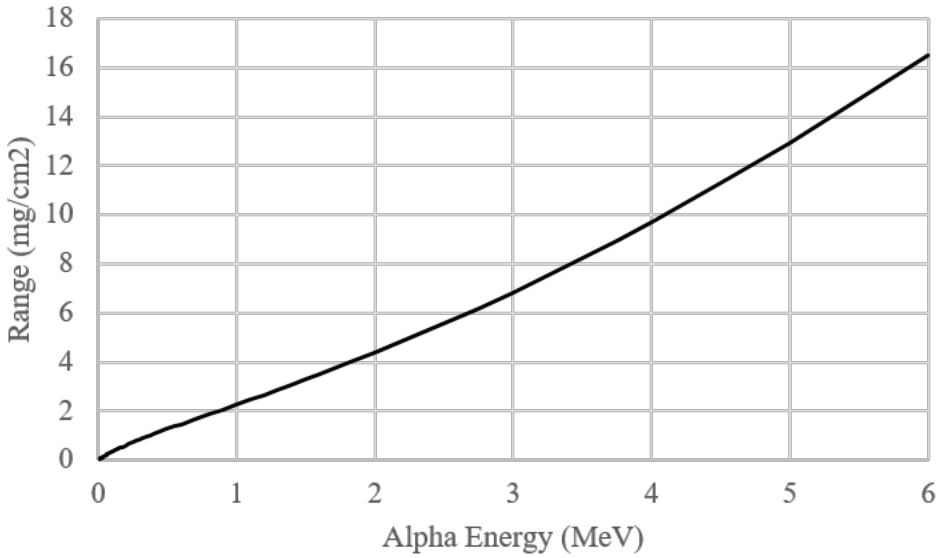

Figure 3.1: The range of α particles travelling through Eu as a function of the α energy.

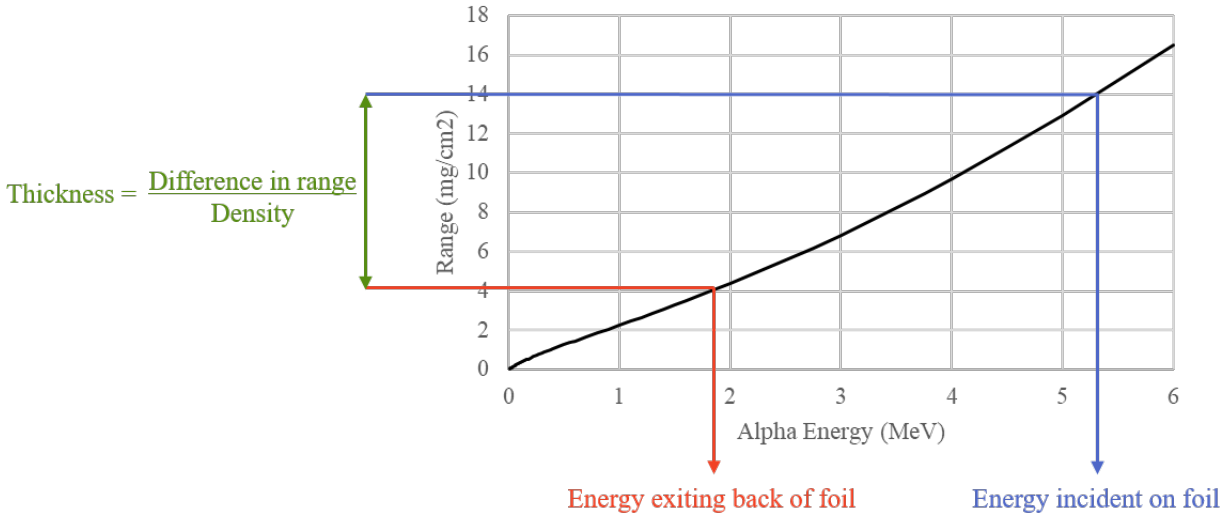

Figure 3.2: Calculating the thickness of the foil using a range of monoenergetic α particles in Eu. One α energy is shown on the graph as an example.

If a mono-energetic α source is incident on the front of a foil then the transmitted α energy can be used to determine the thickness of the foil. This is shown graphically in figure 3.2.

Table 3.1: Table of energies and intensities of the most prominent α energies emitted by the triple α source containing ^{239}Pu, ^{241}Am, ^{244}Cm. An intensity weighted average of the two energies emits by ^{239}Pu was calculated as the detector resolution could not distinguish between these values. The α source was coated in 100 μm/cm^2 of gold. Therefore, the final prominent energies emitted by the source were degraded a small amount. The energy degradation was calculated and the final triple α source calibration energies used for DSSD calibration are shown in the final column.

Isotope	Energy (error) (MeV)	Intensity (error) (%)	Energies used for DSSD calibration (MeV)
^{239}Pu	5.1443 (8)	17.11 (14)	**5.13079**
^{239}Pu	5.15659 (14)	70.77 (14)	
^{241}Am	5.48556 (12)	84.8 (5)	**5.46223**
^{244}Cm	5.80477 (5)	76.90 (10)	**5.78226**

Instead of a single α energy emitting source, a triple α source (containing ^{239}Pu, ^{241}Am, ^{244}Cm) was used. Table 3.1 shows the α energies which were emitted with the highest intensity by each isotope. The energy resolution of the Double-sided Silicon Strip Detector (DSSD) used to detect the α particles could not resolve the two most intense peaks of ^{239}Pu, 5.14430 MeV and 5.15659 MeV. Therefore, a weighted average of these energies was taken. The triple α source was also covered in a thin, protective, gold coating, 100 μm/cm^2 thick. Knowing the initial α energies emitted by the source and the thickness of the gold coating, SRIM was used to determine the exit energy of the α particles. From the SRIM calculations it was found that the gold coating degraded the main α energy peaks of ^{239}Pu and ^{241}Am by 23.33 keV and the main ^{244}Cm α peak was degraded by 22.51 keV. Both the ^{239}Pu and ^{241}Am α energies being degraded by the same amount of energy was initially unexpected. However, the reason for this was due to energy resolution limitations of SRIM. For this energy range (5 to 6 MeV) SRIM only outputs particle ranges in material every 0.5 MeV (i.e. at 5, 5.5 and 6 MeV). To determine range values for particle energies between these, a linear extrapolation between the SRIM data points was taken. Therefore, the energy change for the ^{239}Pu and ^{241}Am α energies were the same as they both lay within the same 5 to 5.5 MeV window.

This is a limitation of the SRIM code and is an area that could be improved in future work. The final α energy values used for the triple α source spectrum when calibrating the DSSDs are shown in the last column of table 3.1.

3.1.2 Experimental method

A DSSD, a semiconductor detector, was used to detect the charged α particles under vacuum. The DSSDs used each consisted of a solid silicon detector where the electronic read-out signal of each detector was split into 16 vertical strips on the front and 16 horizontal strips across the back. This design acts as a pixelated detector allowing for identification of particle location. The 32 strips output separate signals and each of the 32 channels can be connected to an electronic detection set-up. When the front and back detector strips are connected to the electronic set-up shown in figure 3.3, the 16 front detector channel strips are used to trigger coincidence windows via the use of a LED (leading edge discriminator), FiFo (Fan-in Fan-out), Gate & Delay Generator and Trigger SAC electronics. As the charged particle passes through the detector a signal from the front vertical strips triggers the Gate & Delay Generator to produce a 5 ms coincidence window in which the signal from the back horizontal strip arrives. It is the coincidence from the front and back strip that allows for α particle location.

To measure the thickness of the Eu and Al foils used in the target, a triple α source was collimated using disks of lead with a 2 mm pin hole. A foil could be placed in between the two disks and this set of apparatus was placed in front of a DSSD as shown in figure 3.4.

Each of the three α energy peaks forms a Gaussian shape. However, if the α particles travel through the foil at angles not perpendicular to the foil then they will travel farther through the foil than the foil's thickness. This affects the shape of the Gaussian's such that they are

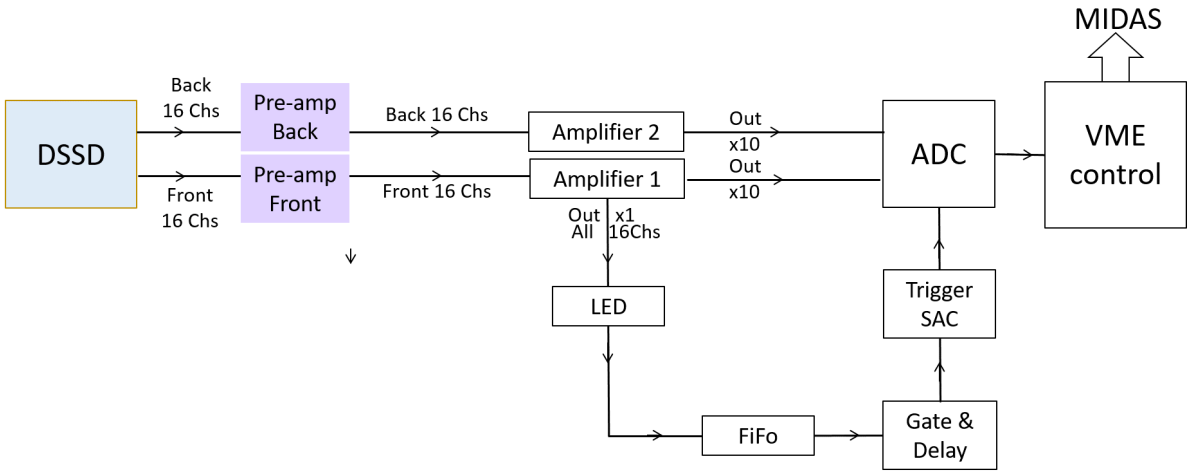

Figure 3.3: DSSD and electronic diagram for foil thickness measurement. See text for details.

skewed in shape at lower energies and the peak is broadened . Therefore, it is important to collimate the α source before and after the foil and to only look at data on the DSSD pixel which is directly opposite the collimator to reduce the Full Width Half Maximum (FWHM) of the Gaussian's and ensure they are not skewed in shape.

With this in mind, only data from the pixel directly in front of the collimated source was used. As shown in figure 3.5, the collimator hole lines up with the 14^{th} horizontal back strip and boarded the 8^{th} and 9^{th} vertical front strips.

Firstly, an approximately 6 μm thick piece of Al foil was placed between the collimators and an α spectrum (alsix1_0) was collected over a weekend. Then, a calibration of the DSSD with no foil in between the two collimator discs was taken (alsix2_0 and alsix3_0). After this, a section of approximately 25 ($\pm$ 25%) μm thick >99.9% pure ^{nat}Eu foil bought from ESPI Metals, USA [50] was placed between the two discs and the spectra were collected over 8 days. The reason for this long collection period was because the statistics were low due to the thickness of the Eu foil. Then an additional calibration was taken (alsix5_0 and alsix6_0) to see if the DSSD calibration had shifted over a week.

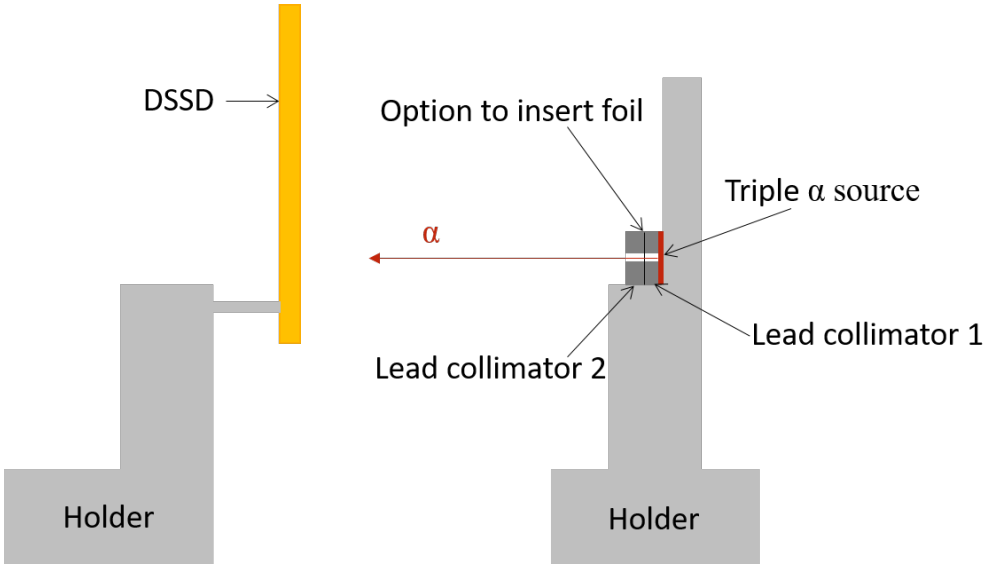

Figure 3.4: Diagram of the α source collimated by two lead collimators with a 2 mm hole in the centre. A foil, the thickness of which is to be measured, can be placed between the two collimators and the DSSD detects the α particles transmitted.

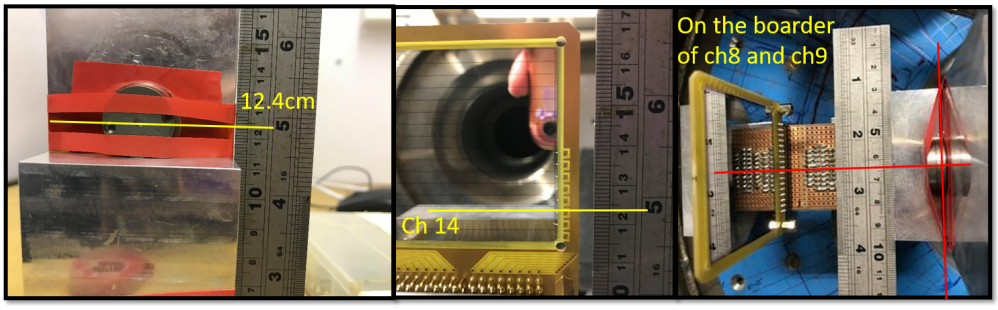

Figure 3.5: The left two images show the height of the collimator hole lies at 12.4 cm. This lines up with the 14^{th} horizontal strip on the back of the DSSD. The right image shows the 8^{th} and 9^{th} vertical, strips on the front of the DSSD align with the collimator.

3.1.3 Data analysis and results

Gating spectra

As depicted in the diagram in figure 3.3, the data were collected through MIDAS (Multi Instance Data Acquisition System). This is a nuclear electronics data handling software created by Nuclear Physics Group (NPG) at STFC (Science & Technology Facilities Council) [51]. The data were then processed using a sort-code. For the foil thickness measurement only the α energy spectrum of the pixel directly in front of the collimator was needed. Therefore, in the sort-code the spectra from strips 8 and 9 on the front of the DSSD were gated by the 14^{th} strip on the back. Thus, these gated energy spectra for strips 8 and 9 on the front of the DSSD only show events that occurred at the height of the 14^{th} strip across the back of the DSSD.

Calibration

Calibration spectra alsix2_0, alsix3_0, alsix5_0 and alsix6_0 are overlaid on top of each other in figure 3.6. Red is alsix2_0; blue is alsix3_0; pink is alsix5_0; and purple is alsix6_0. The calibration spectra alsix2_0 and alsix3_0 were taken after the Al foil thickness measurement and before the Eu foil thickness measurement and the calibration spectra alsix5_0 and alsix6_0 were taken after the Eu foil thickness measurement.

Red and blue overlay each other and pink and purple overlay each other but are shifted slightly to the right, as shown in figure 3.7. The shift in the centroid values of the peaks was less than 3 channels. Therefore, for the calibration for the Eu thickness measurement all these spectra were summated and a Gaussian fit of the three peaks was used to find the centroids of the three peaks.

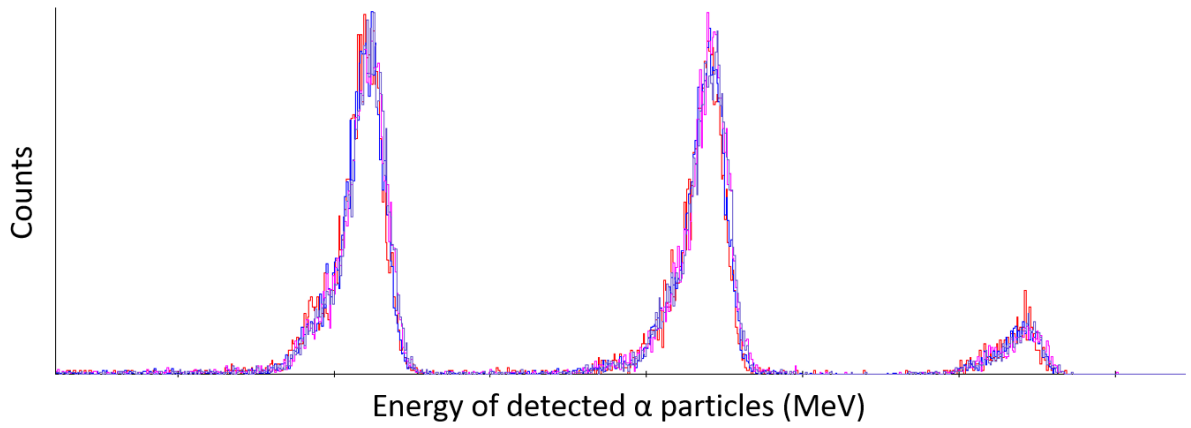

Figure 3.6: Triple α source calibration spectra: alsix2_0 (Red); alsix3_0 (Blue); alsix5_0 (Pink); and alsix6_0 (Purple).

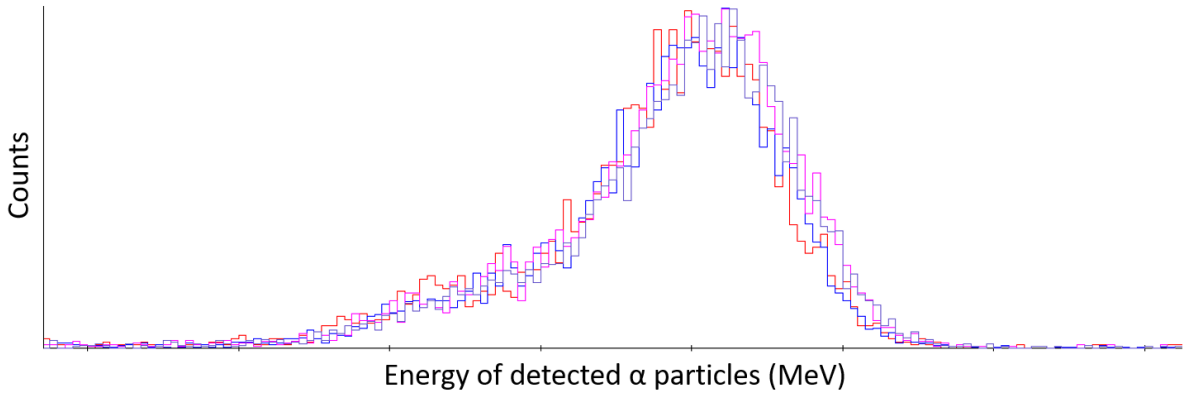

Figure 3.7: Zoomed-in view of the first α peak of the triple α source calibration spectra: alsix2_0 (Red); alsix3_0 (Blue); alsix5_0 (Pink); and alsix6_0 (Purple).

In figure 3.6, the three peaks appear skewed with lower energy tails. This, in part, may have been due to some irradiation damage to the detectors from previous experiments. However, the main cause for this shape was due to the presence of less intense lower α energies being emitted by the source. Unfortunately, when attempting to fit these peaks as well, the areas under the peaks did not reflect the well established intensity ratios of the α energies. Therefore, only Gaussian fits were made of the main three peaks. A Gaussian fit was chosen over a skewed Gaussian for these data as it followed the form of the peaks better and the

Table 3.2: The gradient and intercept values used for the energy calibration of the Eu foil thickness measurement. The values for the gated strip-8 and strip-9 are given and the errors are shown in the brackets.

Strip	Gradient	Intercept
8	0.6425 (99)	109 (55)
9	0.6295 (266)	291 (146)

centroid of the normal Gaussian better reflected the position of the centroid of each peak.

The error on the centroid values provided by the fitting code were too small to accurately portray the size of the error of the thickness measurements that were taken. As shown later in figure 3.8, the foil attenuation of the α particles caused a broadening of the α energy peaks. Therefore, to reflect on this and account for the broadening affect, the FWHM of these Gaussian fits were used to find the standard deviation ($\sigma = \frac{\text{FWHM}}{2\sqrt{2\ln(2)}}$) on these centroids values. An LSF (Least Squares Fit) of the centroid (with σ as the error) and the energies given in the last column of table 3.1 was made for each of the strip-8 and strip-9 gated spectra. Table 3.2 shows the gradient (m_{Eu}) and intercept (c_{Eu}) of these LSF fits which will be used for calibration.

However, the calibration used for the thickness of Al measurement only summated the channel 8 alsix2_0 and alsix3_0 spectra, as these were taken just after the Al foil measurement and were most likely to reflect the energy calibration for their measurement. These energy calibration LSF fit parameters for this case were $\text{m}_{Al} = 0.6430 \pm 0.0094$ and $\text{c}_{Al} = 105 \pm 52$.

Eu foil thickness

All the spectra taken across the 8 days for the Eu foil thickness measurement were summated and three Gaussian peaks were fitted to the spectrum, see figure 3.8. The centroid values were converted from channel number to energy (in keV) using the calibration parameters, m

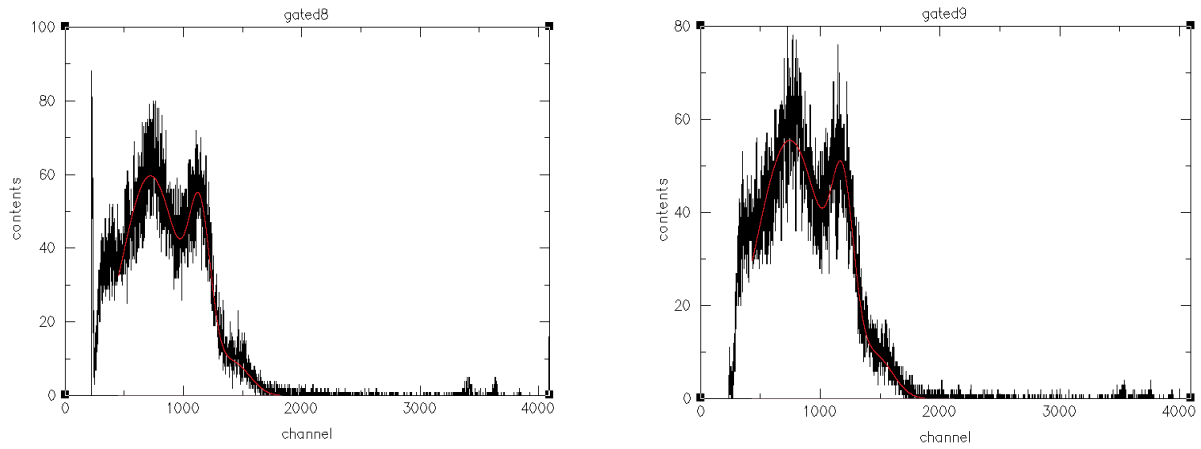

(a) Strip 8 **(b) Strip 9**

Figure 3.8: Triple Gaussian peak fitted to Eu foil thickness spectrum.

and c (depending on the foil and detector strip):

$$\text{centroid (keV)} = \frac{\text{centroid (Ch. no.)} - c}{m}. \tag{3.1}$$

As explained previously, the error (Σ) on the centroid (Ch. no.) values extracted from the Gaussian fits in figure 3.8 were calculated using the FWHM of the fits by calculating $\Sigma = \frac{\text{FWHM}}{2\sqrt{2\ln(2)}}$. In addition to Σ, the errors on the gradient and intercept values, σ_m and σ_c, respectively, were used in the error calculation for the error (σ_E) on the energy (centroid (keV)) for each attenuated α peak,

$$\sigma_E = \sqrt{\left(\frac{\Sigma}{m}\right)^2 + \left(\frac{\sigma_c}{m}\right)^2 + \left(\frac{\sigma_m(centroid(ch) - c)}{m^2}\right)^2}. \tag{3.2}$$

From the Gaussian fits of these gated spectra, the energy of the three transmitted α peaks (from the centroids of the fit) were known. For each of the three α peaks, the range (in mg/cm^2) of an α particle in Eu with the energy of the centroid values (before and after passing through the foil) were calculated using SRIM. As depicted in figure 3.2, for each of

Table 3.3: Table of Eu foil thickness measurements with the upper and lower errors of each measurement for channel 8.

Isotope of α peak	Thickness (μm)	Upper error on thickness (μm)	Lower error on thickness (μm)
^{239}Pu	21.50	1.48	1.50
^{241}Am	21.17	0.68	0.70
^{244}Cm	21.49	1.01	1.05

Table 3.4: Table of Eu foil thickness measurements with the upper and lower errors of each measurement for channel 9.

Isotope of α peak	Thickness (μm)	Upper error on thickness (μm)	Lower error on thickness (μm)
^{239}Pu	22.37	2.06	1.92
^{241}Am	21.89	1.11	1.15
^{244}Cm	22.20	1.37	1.45

the α peaks, the range of an α with an attenuated energy was subtracted from the range of the original α energy. This provided three separate measurements for the thickness of the foil in mg/cm^2. To convert the thickness from mg/cm^2 to μm the result is divided by the density of the Eu, 5.24 g/cm^3 [48].

Tables 3.3 and 3.4 show the thickness measurements for each α peak with the upper and lower error bars. The upper and lower thickness measurements were calculated using the same method as above. However, instead of using the centroid energy values of the attenuated α energy peaks, the centroid energy value minus σ_E was used to calculated the upper error on thickness and the centroid energy value plus σ_E was used to calculated the lower error on thickness. The difference between the lower or upper thickness measurement and the thickness measurement calculated using the centroid attenuated energy values provided the upper and lower errors on the foil thickness measurement for each α energy.

The larger of the errors for each peak was used to perform a weighted average of the three measurements. The measurement from strip 8 resulted in a Eu foil thickness to be 21.3 $\pm$ 0.5 μm and for strip 9, 22.1 $\pm$ 0.8 μm. These agree within errors of each other, however,

the data from strip 9 were less precise most likely due to strip 9 not being directly in front of the collimator. Thus, the α particle would be travelling at a slight angle through the foil, broadening the peak and the final error margins. Therefore, the thickness of the Eu foil was taken to be 21.3 $\pm$ 0.5 μm.

Al foil thickness

The thickness of the Al foil used in the target stack with the Eu foil pieces was measured before the Eu foil with the same set-up as described above. As the Al was a much thinner foil (approximately 6 μm) only one spectrum, taken over a weekend, was needed to have enough statistics for the Gaussian fitting. This spectrum was alsix1_0.

The same analysis steps used to calculate the Eu foil thickness were used to obtain the Al foil thickness. However, as mentioned previously the m_{Al} and c_{Al} calibration parameters were used and, drawing from the previous analysis, only the strip 8 data was analysed. In addition, the range of α particles through Al was calculated for each α energy rather than through Eu.

With this in mind, table 3.5 displays the thickness measurement results for each of the three α peaks. Similarly to the Eu analysis, the larger errors of the upper and lower error in table 3.5 were used to perform a weighted average of the thickness. The final result was the Al foil had a thickness of 6.6 $\pm$ 0.4 μm.

Table 3.5: Table of Al foil thickness measurements with the upper and lower errors of each measurement (using strip 8).

Isotope of α peak	Thickness (μm)	Upper error on thickness (μm)	Lower error on thickness (μm)
^{239}Pu	6.66	0.66	0.67
^{241}Am	6.60	0.70	0.71
^{244}Cm	6.56	0.74	0.75

3.2 Beam energy

3.2.1 Theory

To determine the energy of the α beam used to irradiate the stacked foil target, the beam was first scattered through a thin gold (Au) foil. The nuclear interaction of interest was the elastic scatter of the α particles off the Au nuclei. Figure 3.9 depicts how each α particle in the beam may scatter off a Au nucleus. The mass of the Au nucleus is denoted by m_A and m_C, and the mass of the α particle by m_B and m_D. The incident energy of the α particle beam is E_B; E_A is the energy of the stationary Au target; E_C is the energy of the scattered Au nucleus as it travels at an angle ϕ to the beam axis; and E_D is the energy of the α particle scattered by angle, θ from the beam axis.

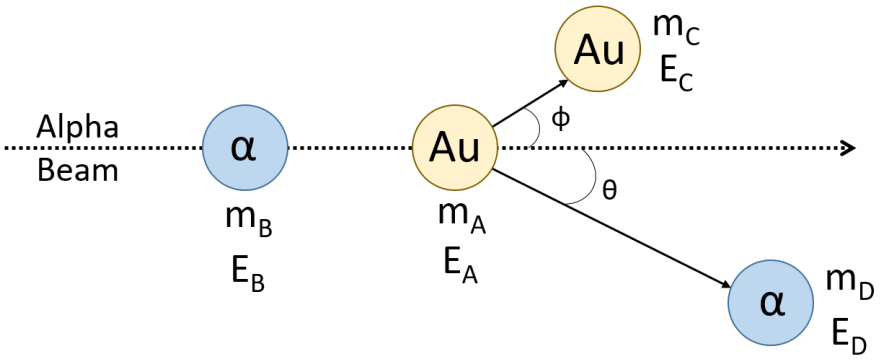

Figure 3.9: Diagram showing the α beam scattering off a gold target.

By the conservation of energy and momentum,

$$\left(1-\frac{m_C}{m_B}\right)E_B - 2cos(\theta)\sqrt{E_D}\sqrt{E_B} + \left(1+\frac{m_C}{m_B}\right)E_D = 0 \tag{3.3}$$

is found to be true and a full derivation can be found in appendix D. Therefore, by solving

the quadratic equation

$$x = \frac{-b \pm \sqrt{b^2 - 4ac}}{2a}$$

where

$$\begin{aligned} x &= \sqrt{E_B} \\ a &= 1 - \frac{m_C}{m_B} \\ b &= -2cos(\theta)\sqrt{E_D} \\ c &= \left(1 + \frac{m_C}{m_B}\right) E_D \end{aligned}$$

the beam energy can be determined by measuring the energy of the scattered α particles and the angle through which they have scattered.

3.2.2 Experimental method

Two DSSDs were used to measure the α beam energy. The beam energy to be measured was between 38 - 40 MeV. In order to measure the energy of the scattered α particles the silicon of the DSSD needed to be thick enough to fully stop up to 40 MeV α particles. Thus DSSDs of $\sim$ 1000 μm thickness were used.

Each DSSD was connected to an electronic set-up similar to that used for the foil thickness measurement, a full schematic is given in figure 3.10. The DSSDs were calibrated using the triple α source and checks were carried out to ensure that the position of each pixel was known. This was achieved by placing a mask over the DSSD with the letter "R" cut-out. The triple α source was place in front of the DSSD covered by the mask. The order of the

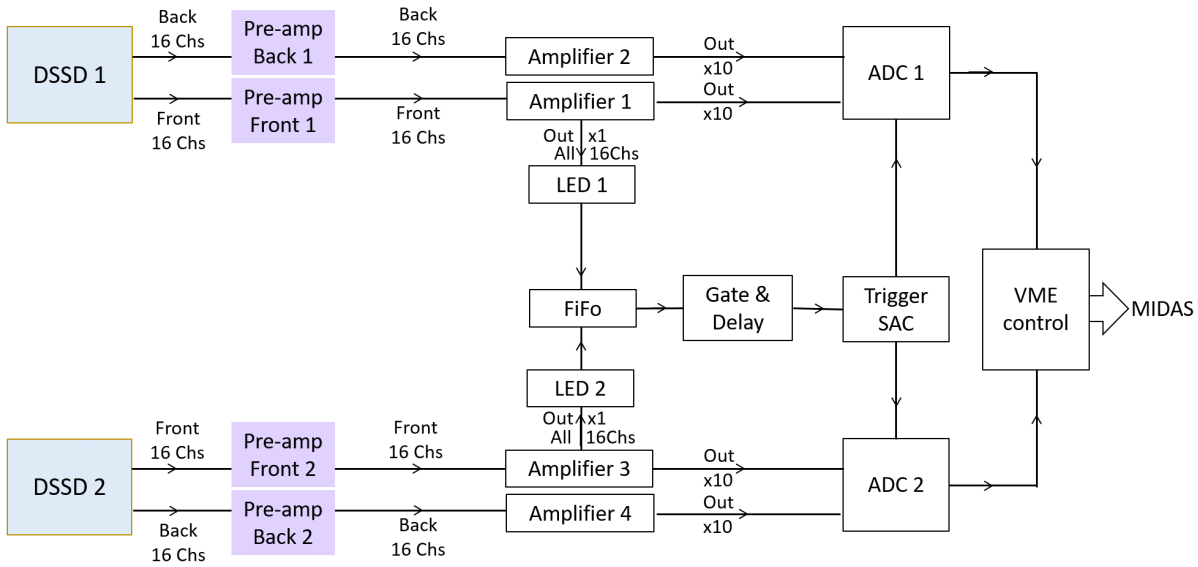

Figure 3.10: Diagram showing the electronics set-up for the two DSSD detectors.

DSSD channel outputs were altered in the sort code until a clear image of the "R" could be seen as demonstrated in figure 3.11. The re-ordered channel number for each DSSD was carried forward to the rest of the code.

The DSSDs were then placed in a scattering chamber at the end of the beam line as shown in figure 3.12. The Au foil in this figure consisted of a target ladder with two Au foils, shown in figure 3.13. The α beam was then directed down this beam line to measure the α beam's energy before being directed on to the Eu/Al target using a dipole magnet. Three data sets were collected for the beam-energy measurement. One with a 300 μg/cm^2 thick Au foil and two using a Au foil with a thickness of 200 μg/cm^2, the first of these was taken with a lower beam current.

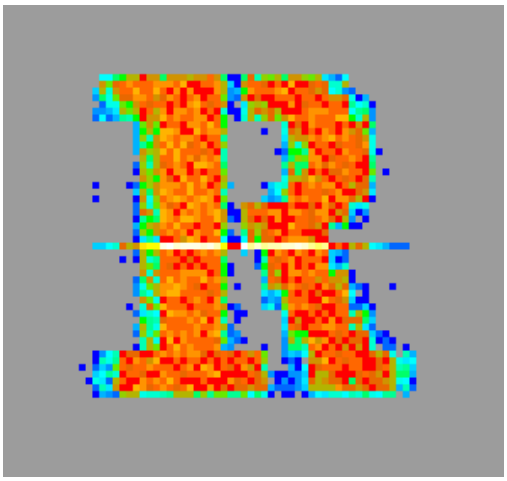

Figure 3.11: A uniformly irradiated DSSD covered by a mask with the letter "R" cut-out. The image was formed after the output channels of the DSSD were re-ordered in the sort code to ensure a clear image of the "R".

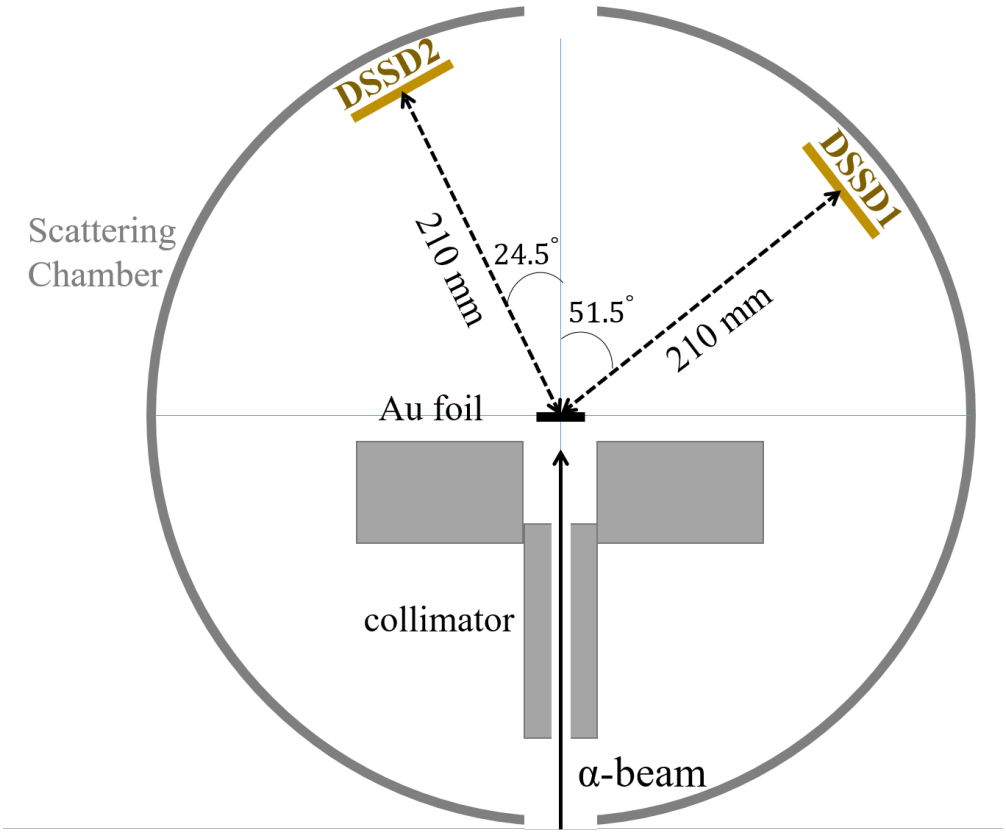

Figure 3.12: Diagram showing the scattering chamber set-up used to measure the energy of the beam by scattering α beams off a gold target.

Figure 3.13: Target ladder with two gold foils the top is 300 μg/cm^2 thick and the second one below is 200 μg/cm^2 thick.

3.2.3 Data analysis and results

Calibration

Compared to the calibration performed for the foil thickness measurement, the amplification of the DSSDs were decreased to ensure the maximum cyclotron α energy (40 MeV) was within the top few channel numbers of each of the 64 DSSD energy histograms. The impact of this was that the triple α calibration peaks were compressed to within the first 600 channels, as shown in figure 3.14. For accurate calibration, knowledge of the channel number for the centroid of each peak needed to be determined. Both the Gaussian and skewed Gaussian functions were fitted to the calibration data. For the compressed α calibration spectra, the centroids of the skewed Gaussian fits better reflected the centroid position of the three peaks

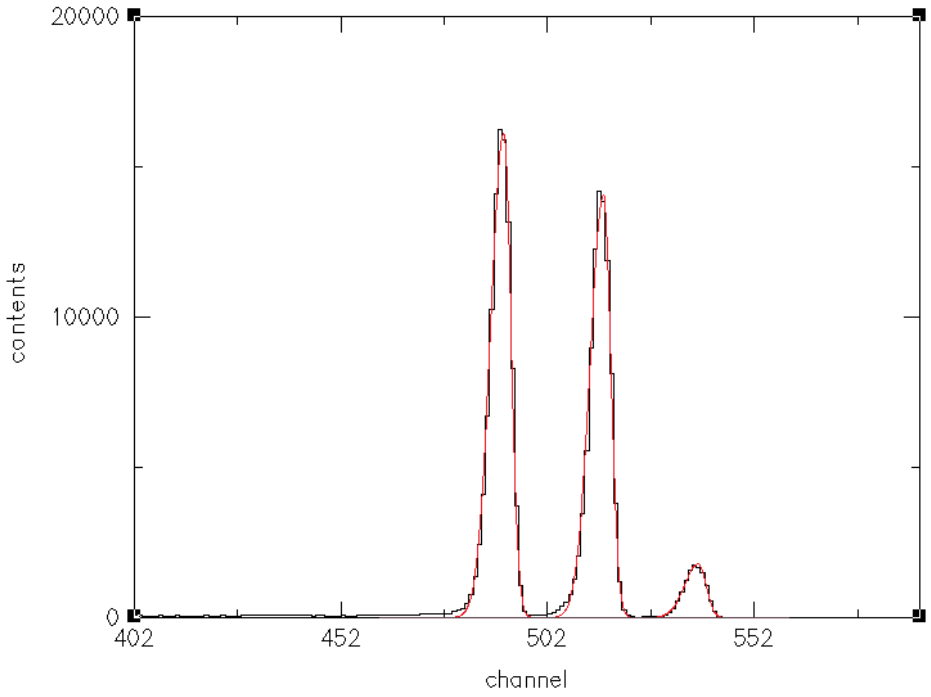

Figure 3.14: Triple α calibration energy histogram (data in black) fitted with three skewed Gaussians (in red).

in the spectra data. Therefore, the skewed Gaussian function was used for the beam energy DSSD calibration process.

Each of the 64 detector strips were calibrated by fitting 3 skewed Gaussians to the α energy histogram, as shown in figure 3.14. The centroid values were then used to convert the energy channel number of the histogram to the physical energy of the α particles in MeV. A skewed Gaussian fit was used because, unlike the collimated calibration performed for the foil thickness measurement, the triple α source was not collimated. This was to allow the calibration of the entire detector face and not just one or two pixels. As mentioned previously, the triple α source is coated in a thin gold foil layer. Therefore, some of the α particles reaching the detector face will have travelled through a larger angle of this coating (and the source itself) thus will be slightly attenuated to lower energies. This caused the energy of the Gaussian peaks to be skewed in shape.

The LSF calibrations were produced for each of the 64 channels using the centroid values from the skewed Gaussian fits and the error on the centroids and plotting them against the energies of the α emissions given in the last column of table 3.1. The 1/gradient and intercept/gradient of the calibration LSF plots were listed in a calibration text file and incorporated into the sort-code to calibrate the DSSDs (converting the integer channel number of each signal in received in each strip to energy in MeV).

Beam Energy

To process the data collected for α beam energy measurements a sort-code was used. For each α particle detected its location on the DSSD was found by using the coincidence between the front and back strip detection. The physical location of the detectors within the scattering chamber, shown in figure 3.12, were also imbedded in the sortcode to calculate the angle of the detection from the original beam, θ.

The front strips of the DSSDs provide a more precise and higher statistical measurement of the beam energy. Therefore, the information about the energy of the scattered α particle was taken from the front strips. The calibration conversion for each DSSD strip from channel number to α energy (in MeV) was incorporated in the code. Assuming, on average, the α particle in the beam will interact in the middle of the foil target, then the scattered α particle with energy E_D will lose energy in the remainder of the target before exiting and striking a DSSD with the detected energy. To obtain the original scattered α energy, each detected energy is corrected for the dE/dx loss of an α particle through the remainder of the gold foil.

The average thickness of gold foil travelled through was calculated for each detection by using $\frac{\text{half thickness of Au foil}}{\cos\theta}$ as shown in figure 3.15. The detected α energy and the distance travelled through the Au foil provided enough information to perform the reverse process

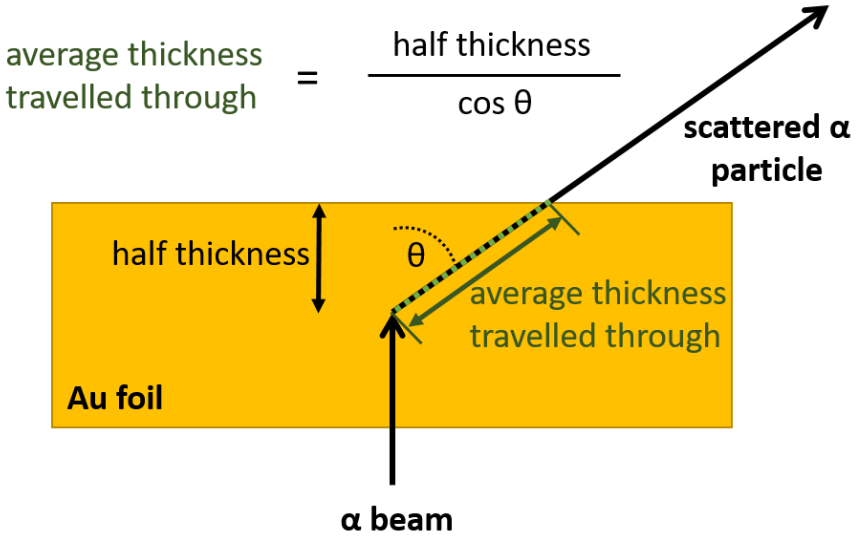

Figure 3.15: Diagram showing the average distance of Au foil the scattered α particle travels through.

used to determine Eu and Al foil thickness in section 3.1. By using dE/dx range values for α particles in Au calculated using SRIM, the original energy (E_D) of the scattered α particle was determined.

As the mass of the α particle is known and the E_D and θ are measured with the DSSDs, for each detection, the energy of the α beam (E_B) was calculated using equation 3.3. These values of E_B were used to build energy histograms of the α beam.

For each of the three data sets two beam energy spectra were produced, one with the right DSSD and one with the left DSSD. A Gaussian was fitted to each spectrum (see example in figure 3.16). The centroid value provided the beam energy and the error was given by $\frac{\text{FWHM}}{2\sqrt{2\ln 2}}$. All of the six beam energy readings produced beam energy values within error of each other as shown in table 3.6. However, the first set of data taken with the thicker (300 μg/cm^2) Au foil produced a beam energy peak with ten times fewer statistics. Across all the data sets, the left detector (DSSD2 in figure 3.12) consistently contained at least 100

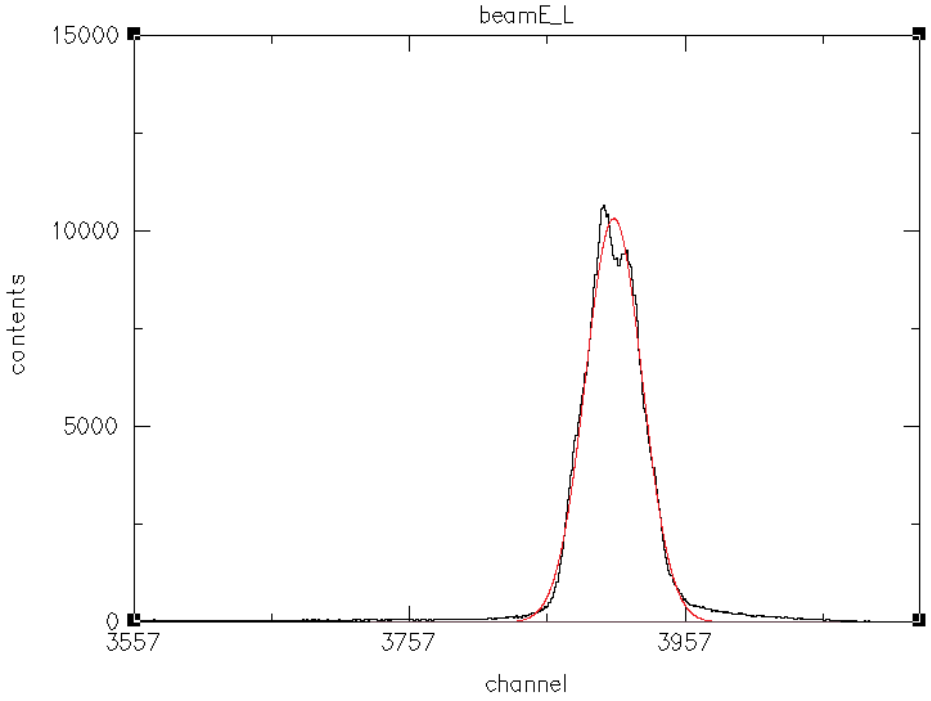

Figure 3.16: A single Gaussian (red) fitted to the beam energy histogram (black) of the left DSSD of the low current 200 μg/cm^2 thick Au foil data set.

Table 3.6: Table showing the fit parameters for the single Gaussian fits of each data set for each detector.

Data set	Beam energy (MeV)	Error on beam energy (MeV)
300 μg/cm^2 Au foil DSSD 1	38.79	0.18
300 μg/cm^2 Au foil DSSD 2	39.07	0.21
200 μg/cm^2 Au foil DSSD 1 - low current	38.76	0.17
200 μg/cm^2 Au foil DSSD 2 - low current	39.06	0.21
200 μg/cm^2 Au foil DSSD 1 - high current	38.78	0.17
200 μg/cm^2 Au foil DSSD 2 - high current	39.06	0.21

times more statistics than the right (DSSD1) due to its closer proximity to the beam line. Therefore, the final beam energy measurement was taken from the higher statistics beam energy peaks produced from the left DSSD of the thin (200 μg/cm^2) Au foil data sets. The α beam energy was measured to be 39.06 $\pm$ 0.21 MeV.

3.3 Foil stacking

3.3.1 Handling thin europium foils

Europium is the most reactive lanthanide. It reacts with air and water swiftly such that once the foil has been unsealed from its container it should be handled quickly and be placed under vacuum or in an argon atmosphere as quickly as possible. The thickness measurement using α particles was carried out under vacuum and the irradiation of the stacked Eu and Al target was also carried out under vacuum. Once irradiated, each foil was sealed separately within two plastic bags, however, within 24 hrs the Eu foil had completely oxidised to a powder.

Europium's relatively high reactivity posed many logistical and practical problems that had to be considered when designing and assembling the stacked target to be irradiated. An initial cross-section measurement was made where the Eu and Al foils (30 μm and 25 μm, respectively) were stacked as shown in figure 3.17. A 3 $\times$ 3 cm^2 Eu foil was cut in to nine 1 cm^2 pieces under argon in a glove box. However, assembling the stacked target with the Al foils within a glove box proved impossible as this was intricate work. Thus the 12 foils were stacked relatively quickly on a clean bench top using tweezers while wearing gloves to prevent any moisture and oil from the skin transferring to the foil.

Unfortunately, Eu is a poor conductor of heat and during irradiation each Eu foil fused with

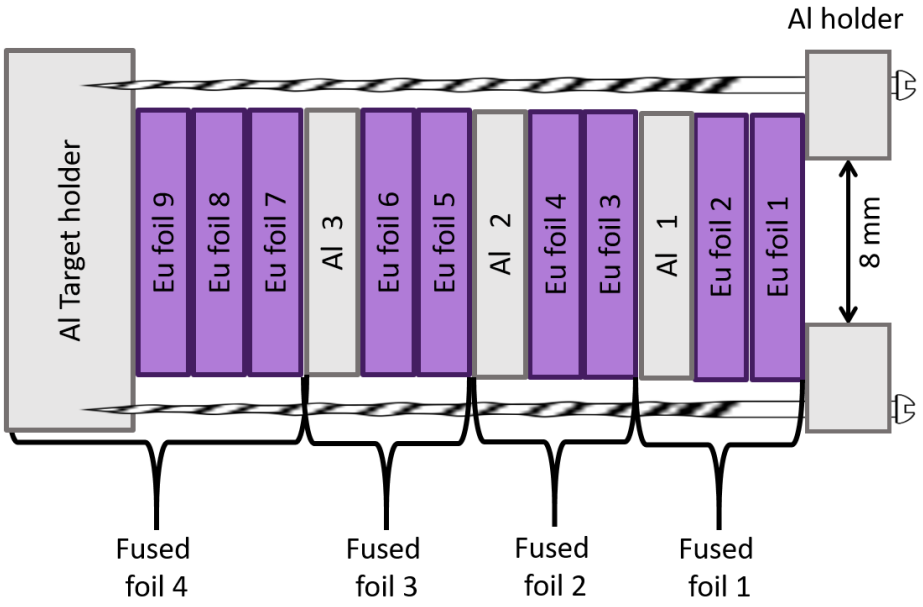

Figure 3.17: Initial design for Eu/Al foil stacking. The beam enters from the right side of the image towards the left through the 8 mm gap in the target holder.

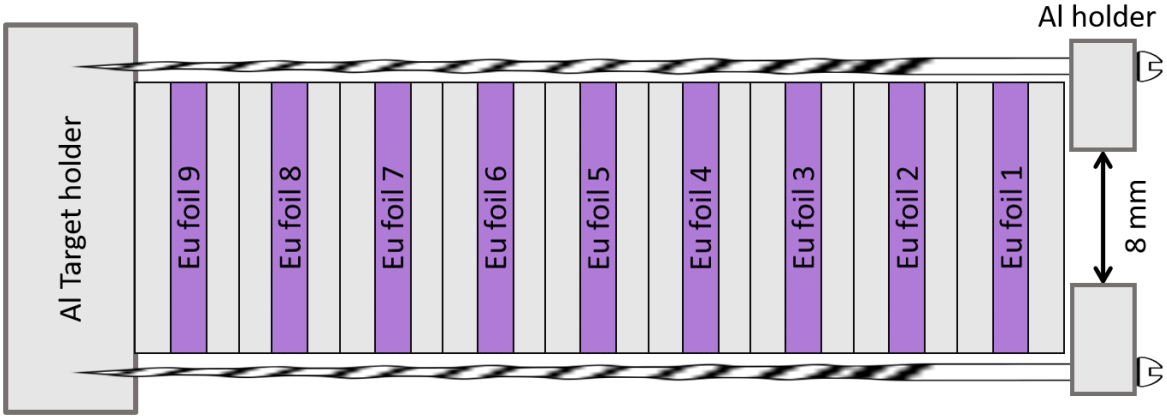

Figure 3.18: Target stack design of 27 Eu and Al foils to prevent Eu foils fusing with other Eu foils. The beam enters from the right side of the image towards the left through the 8 mm gap in the target holder.

(a) **1 cm^2 Eu foils on the left and 1×2 cm^2 pieces of Al foil on the right.**

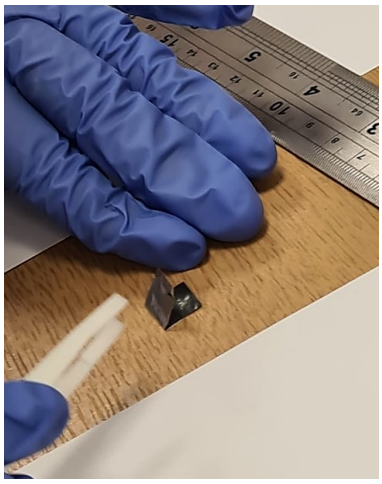

(b) **Folding the Al foil around the Eu foils.**

(c) **Final stack of foils in target holder.**

Figure 3.19: Foil stacking process.

the foil behind it. The Al foils did not fuse with the foils behind them, because Al is better at dissipating heat due to a higher thermal conductivity (235 $\mathrm{Wm^{-1}K^{-1}}$ compare to Eu's thermal conductivity of 14 $\mathrm{Wm^{-1}K^{-1}}$ [52]). Therefore, after irradiation there were effectively four Eu foils of double to triple the original thickness as shown in figure 3.17.

For the final measurement it was imperative to overcome this problem of the Eu foils fusing to their neighbour. To mitigate this, 6.6 μm thick Al foils were placed before and after each 21.3 μm thick Eu foil such that the target stack consisted of 27 foils as shown in figure 3.18. However, stacking 27 separate 1 cm^2 thin foils proved impossible. Instead of cutting the Al foil into 18, 1 cm^2 pieces, the solution was the cut nine 1 × 2 cm^2 pieces of Al foil as seen in figure 3.19 (a). Each Al foil could then be folded in half with a 1 cm^2 piece of Eu foil inside, securely containing the Eu for stacking as captured in figure 3.19 (b). Therefore, only nine

foil envelopes were required to be stacked as shown in figure 3.20 and placed into the target holder seen in figure 3.19 (c).

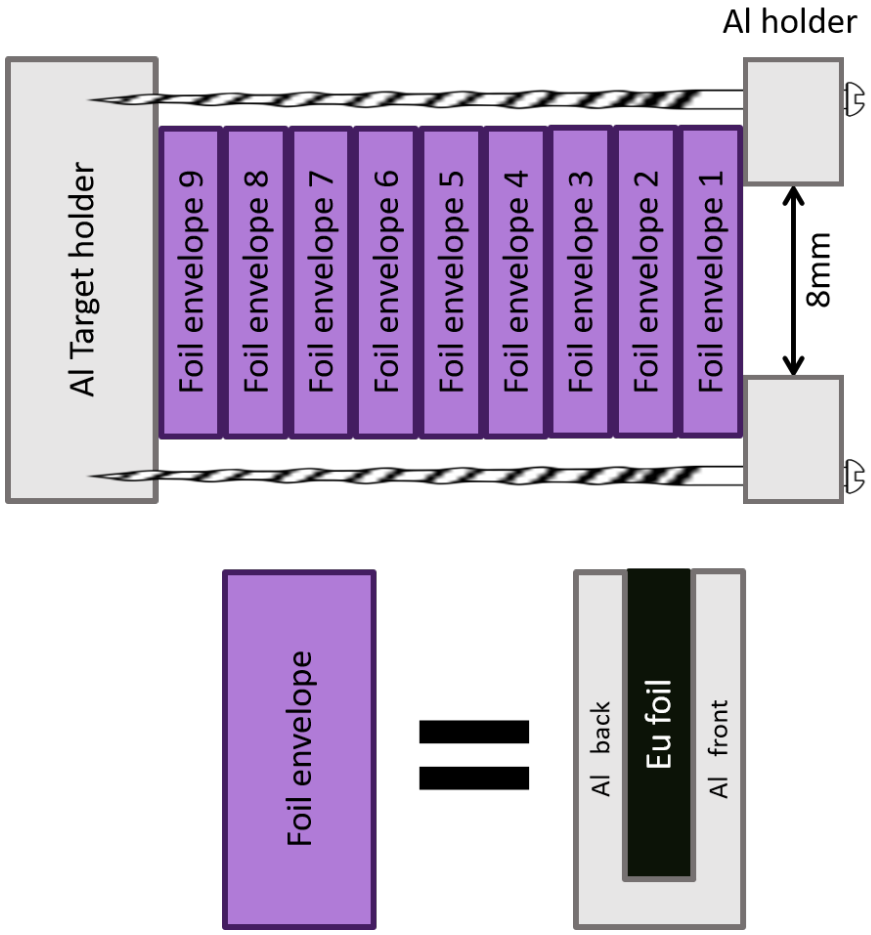

Figure 3.20: Final stacking of Eu and Al foils by forming and stacking nine foil envelopes. The beam enters from the right side of the image towards the left through the 8 mm gap in the target holder.

3.3.2 Energy distribution across each Eu foil

From sections 3.1 and 3.2 the thickness of the foils in the target and the initial α beam energy were known. As the α beam travels through the stack of foils its energy decreases. The energy of the α beam before and after each foil was calculated using SRIM [48]. In figure 3.21 the α energy range covered by each Eu foil has been highlighted in purple and

overlaid on TALYS predicted cross-sections.

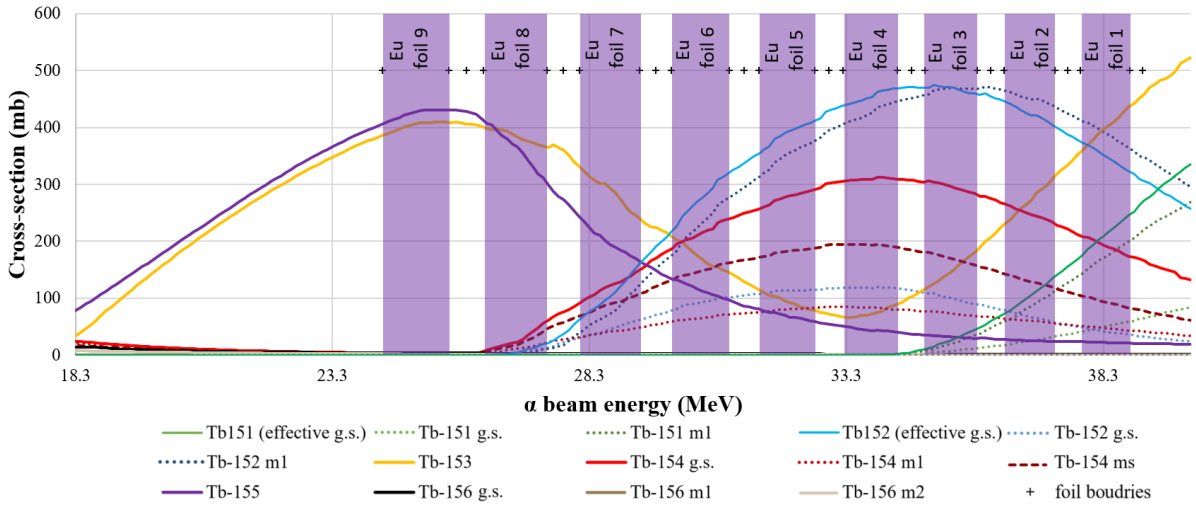

Figure 3.21: The energy range covered by the nine Eu foils in the target stack (highlighted in purple) overlaid on TALYS predicted cross-sections.

However, these values were calculated using the Eu thickness of 21.3 μm, Al thickness of 6.6 μm and initial beam energy of 39.06 MeV. These three values all have known error on their measurement. Thus to obtain the maximum α energy the Eu foils cover, the α energy degradation was calculated using the thickness of the foils minus their error (20.8 μm and 6.2 μm for Eu and Al foil, respectively) and the initial energy of the beam plus its error (i.e. 39.27 MeV). To obtain the minimum α energy of each Eu foil, the α energy degradation was calculated using the thickness of the foils plus their error (21.8 μm and 7.0 μm for Eu and Al foil, respectively) and the initial energy of the beam minus its error (i.e. 38.85 MeV).

The energy of the α beam at the centre of each foil was calculated using the Eu foil thickness of 21.3 μm, Al thickness of 6.6 μm and initial beam energy of 39.06 MeV. These values are quoted as the "Average foil energy". These and the maximum and minimum values of each foil are recorded in table 3.7

Table 3.7: The mean α energy of each Eu foil in the stack and the maximum and minimum α energy at the front and back of each foil.

Eu Foil	Lowest energy at the back of foil (MeV)	Average foil energy (MeV)	Highest energy at the front of foil (MeV)
1	37.62	**38.34**	39.04
2	36.06	**36.86**	37.64
3	34.46	**35.35**	36.19
4	32.81	**33.77**	34.71
5	31.08	**32.16**	33.18
6	29.30	**30.47**	31.59
7	27.45	**28.72**	29.97
8	25.48	**26.90**	28.25
9	23.40	**25.00**	26.46

3.4 Target irradiation

3.4.1 Charge collection

The stacked Eu/Al foil target was placed at the end of the beam line and the tube was evacuated. The α beam was collimated using two tantalum (Ta) collimators, positioned in the beam line as shown in figure 3.22. The end of the beam line was designed to act as a Faraday cup by inserting an electrically insulating material to isolate the last 14 cm of the pipe and end-cap. The end of the beam line was connected via a wire to a Brookhaven model 1000c which recorded the current. As the α particles strike the target the addition of the positive charge draws electrons from the wire (i.e. two electrons per α particle). This current flow was then recorded on the Brookhaven model 1000c which was on the 60 nC setting, i.e. a count is recorded for every 60 nC of charge accumulated. Therefore, as explained in section 2.2, the current of α particles (I) can be calculated by

$$I\ (\text{nA}) = \frac{\text{counts} \times 60\ \text{nC}}{\text{time (minutes)} \times 60}, \tag{3.4}$$

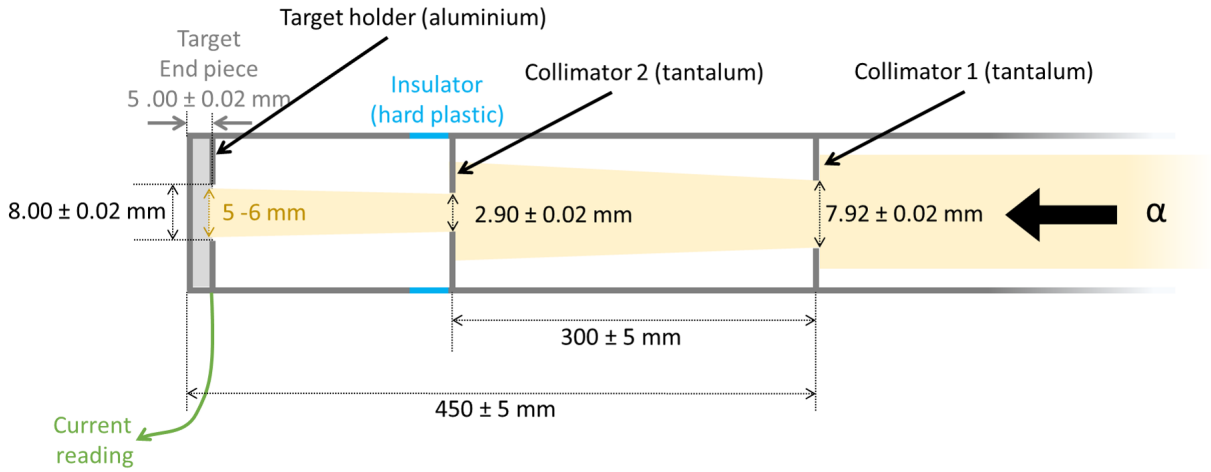

Figure 3.22: Diagram of the end of target irradiation beam line including α beam collimation and Faraday Cup for measuring beam current.

which is defined in chapter 2 as equation 2.6, can be simplified to

$$I\ (\text{nA}) = \frac{\text{counts}}{\text{time (minutes)}}. \tag{3.5}$$

This equation could be used when the α beam was irradiated in the target with a constant current. In this case Coulomb count recorded would increase linearly with time, however, this was not the case when the target stack of Eu/Al foils was irradiated as shown in figure 3.23.

3.4.2 Target irradiation and current measurement

The target was irradiated for 25 minutes 33 seconds, beginning and ending at 17:03:27 and 17:29:00, respectively. The time and Coulomb count of the Brookhaven model 1000c charge integrator, using a full scale of 60 nC, were recorded at regular intervals during irradiation (approximately every minute). These are plotted in figure 3.23. A straight line fit has been

added to the graph to highlight the non-linearity of the Coulomb count.

Unfortunately, on the day of irradiation the cyclotron's α beam was unstable and the ion filament broke. The initial plan was to irradiate the target for 1 hr with a beam current of 50 nA. However, using the total Coulomb count of 567 and the irradiation time of 25.55 minutes in equation 3.5, the average current achieved was only 22 nA. Irradiating the target for under half the planned time and current meant that under a quarter of the planned activity for the longer lived (days half-life) isotopes were produced and approximately half the activity of the planned short lived (minutes half-life) isotopes were produced. The effect of these reduced expected activities on the collection of γ spectra will be explained in section 4.6.

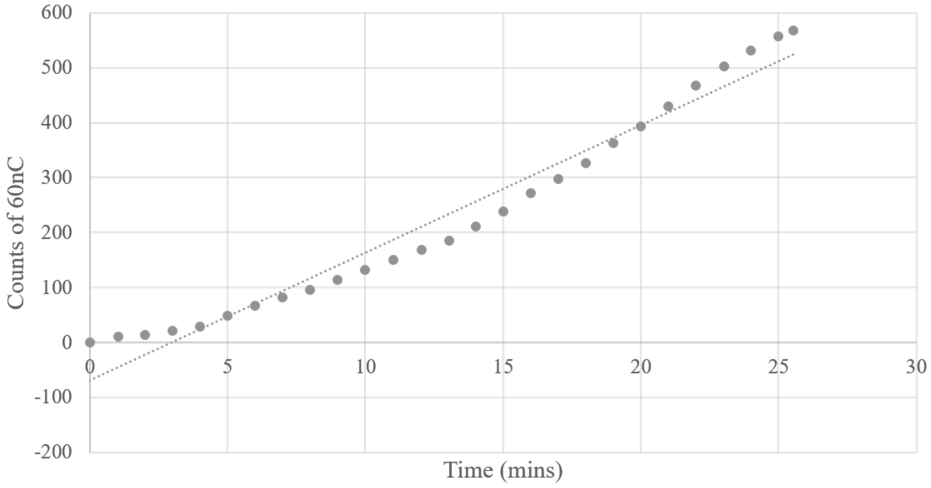

Figure 3.23: Coulomb count of the Brookhaven model 1000c on the 60nC setting while the Eu/Al target was irradiated. The larger dots are the data points taken approximately every minute and the fine dotted line is a liner fit of the data to demonstrate the non-linear behaviour of the data points.

As explained in section 2.2, the inconsistent current will have a greater effect on the production of short lived isotopes and isotopes with comparable half-lives to the irradiation time. Therefore the effect of the inconsistent current needed to be accounted for. This was achieved by using equation 3.6 which was originally defined in chapter 2 as equation 2.7.

$$A_T = \sigma N_{target} \sum_{i=1}^{n} \Phi_i \left(1 - e^{-\lambda\tau}\right) \cdot e^{\lambda\tau(n-i)}, \tag{3.6}$$

where A_T is the activity of the isotope produced and N_{target} is defined in equation 2.4. The current data is then split into n sections equal sections of time. The average current, I_i for each (i^{th}) segment is used to calculate $\Phi_i = N_\alpha I_i$ for each section of the data (where N_α is defined in equation 2.5). The calculation for each segment of the sum also contains the parameters λ (the decay constant of the isotope produced) and τ which is the length of time for each data segment.

The total irradiation time was 25 minutes 33 seconds = 1533 s. Therefore, the total irradiation time can be split into 1533 segments (i.e. n = 1533 and τ = 1 second). Focusing on the summation part (Y) of equation 2.7, Y can be written as

$$Y = \sum_{i=1}^{n=1533} \Phi_i \left(1 - e^{-\lambda}\right) \cdot e^{\lambda(n-i)}, \tag{3.7}$$

where λ has units, s^{-1}. The parameter $\Phi_i (= N_\alpha I_i)$ for each second needed to be determined. The Coulomb count was recorded every minute and equation 3.5 was used to determine the average beam current for each minute. The average beam current for a particular minute was then used as the current, I_i, for each second in that minute. I_i was then multiplied by constant N_α (see equation 2.5) to give Φ_i for each second.

As Y is λ dependent, separate values of Y were then calculated for each isotope produced by summating each segment with the appropriate Φ_i and λ. These values of Y were then used to calculate the cross-section,

$$\sigma = \frac{A_T}{Y \cdot N_{target}}, \tag{3.8}$$

as discussed in chapter 5. Appendix C derives the error calculated for Φ_i, Y and cross-section.

After α irradiation of the Eu/Al foil stack, the amount of each Tb isotope and isomeric state produced needed to be quantified. Gamma spectroscopy was used to measure this in each Eu foil. Chapter 4 discusses the method and initial γ spectra analysis in more detail.

Chapter Four

Gamma spectroscopy

Once the stack of Eu/Al foils had been irradiated the products of the irradiation needed to be identified and quantified. Each radioactive nuclide emits it own specific set of γ energy photons. The energies of these photons work much like a fingerprint, and are used to identify the nuclide that emitted them. The process of collecting energy spectra of sources and identifying the energies of the peaks, and thus the nuclides, is known as γ spectroscopy. Moreover, these spectra can be used to calculate the activity of the radioactive isotopes produced; A_T in equation 2.3.

This chapter will discuss the detector and experimental set-up required to perform the necessary γ spectroscopy. The selection of specific γ energies for identification and activity calculation of the produced isotopes will be explained along with the initial spectra analysis and correction processes. The final steps of using these data to produce decay curves and then calculate cross-section of production will be covered in chapter 5.

4.1 HPGe Detectors

4.1.1 Theory of HPGe Detectors

There are several families of γ detectors, organic and inorganic scintillating detectors, proportional counters that use a counting gas, and semiconductor detectors. For precise γ spectroscopy the superior resolving power of semiconducting detectors is needed. More specifically, High Purity Germanium (HPGe) detectors were used.

Types of γ interactions with detectors

In order for the detectors to record information about the γ rays the photons must interact within the detectors. There are three main types of interactions a γ photon will have within a detector and the probability of each depends on the energy of the photon and the material of the detector.

The first type of interaction occurs by Compton scatter (CS). This is where the γ photon interacts with an electron within the detector. The photon transfers some of its energy to the (recoil) electron and leaves at an angle (θ) compared to the original trajectory of the photon. The energy of the photon ($E_p{}'$) after the collision is given by

$$E_p{}' = \frac{E_p}{1 + \frac{E_p}{m_0 c^2}(1 - \cos\theta)}, \tag{4.1}$$

where $m_0 c$ is the rest mass energy of the electron (511 keV). The probability of the reaction depends linearly on the number of electrons [53]. Therefore, the probability of interaction increases linearly with detector material atomic number (Z). Interaction probability falls off as energy increases as shown in figure 4.1.

The second type of γ interaction is the photoelectric effect (PE). This is where all of the photon's energy is transferred to a bound electron of an atom in the detector, ionising the atom. The energy of the ionised electron (E_{e^-})is given by

$$E_{e^-} = h\nu - E_b, \tag{4.2}$$

where h is Plank's constant, ν is the frequency of the γ photon and E_b is the binding energy of the electron. The probability of this interaction mechanism occurring increases with Z of the detector material but decreases as the energy of the photon (E_γ) increases. The approximate dependence is given by

$$constant \times \frac{Z^n}{E_\gamma^{3.5}}, \tag{4.3}$$

where n varies between 4 and 5 depending on the energy of the γ ray [53].

The third interaction between γ rays and the detector is pair production (PP). PP is only possible for γ rays with energies greater than 1022 keV. As 511 keV is the mass of an electron (or positron), then 1022 keV is the minimum energy required to produce an electron positron pair. The γ photon travels close to a nucleus within the detector and the interaction causes the photon to transform into an electron and positron. The probability of a PP interaction is proportional to Z^2 and increases with energy above 1022 keV [53].

Figure 4.1 is a plot of atomic number against γ photon energy. The three sections are labelled to show the dominant interaction mechanism for that region of atomic number and photon energy.

When a γ ray interacts only by the PE effect, all the energy information of the photon will be transformed to an electrical pulse and passed to the electronics. On an energy spectrum this gives rise to the "photopeak" of equivalent energy to the original γ ray. For photons that

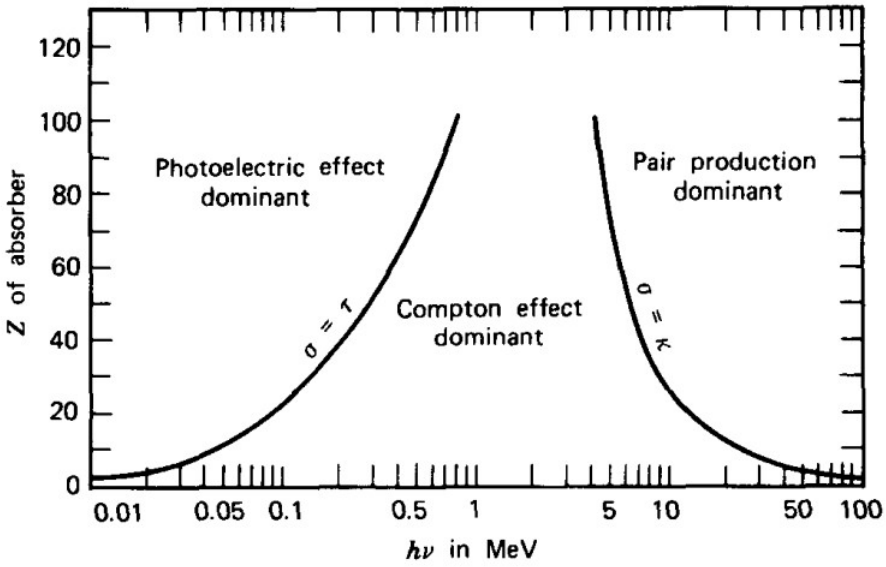

Figure 4.1: A plot of atomic number (Z) of detector material against the energy of the radiation photon (in MeV). The three areas of the graph show the dominant interaction that takes place [53].

interact by CS, the energy transferred to the electron is collected by the detector, however, this is not all the energy of the original photon. The scattered photon either continues to CS until it interacts photo-electrically or the photon may escape. In the latter case some of the energy information is lost and this gives rise to the Compton continuum as shown in figure 4.2.

After PP, the subsequent interaction of the newly created leptons gives rise to other spectrum features. The energy of the electron will be transferred to and translated by the detector. The positron produced will lose energy to the detector till it comes to rest (or near rest) and then annihilate with a detector electron. This produces two back-to-back annihilation photons of 511 keV each. These photons may escape the detector, CS, or lose their energy by the PE effect. If both photons leave there will be a "double escape peak" at the energy of the original γ photon minus the rest mass of two electrons. If only one of the photons escapes there will be a "single escape peak" at an energy equal to that of the original γ photon minus the rest mass of one electron. These features can be seen in figure 4.3.

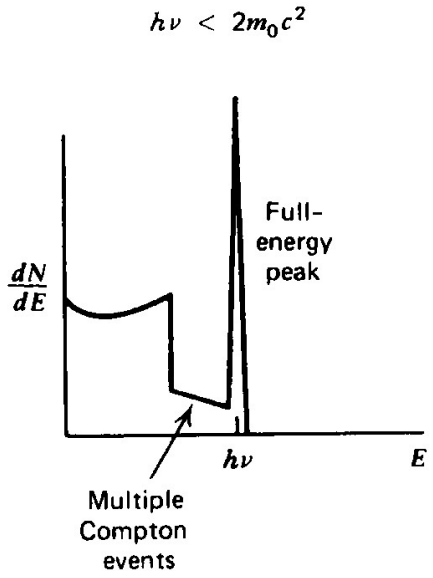

Figure 4.2: A simplified plot of counts against photon energy for lower energy photon interactions. Some features to be expected such as Compton continuum from CS interactions and a full energy peak from PE absorption are labelled [53].

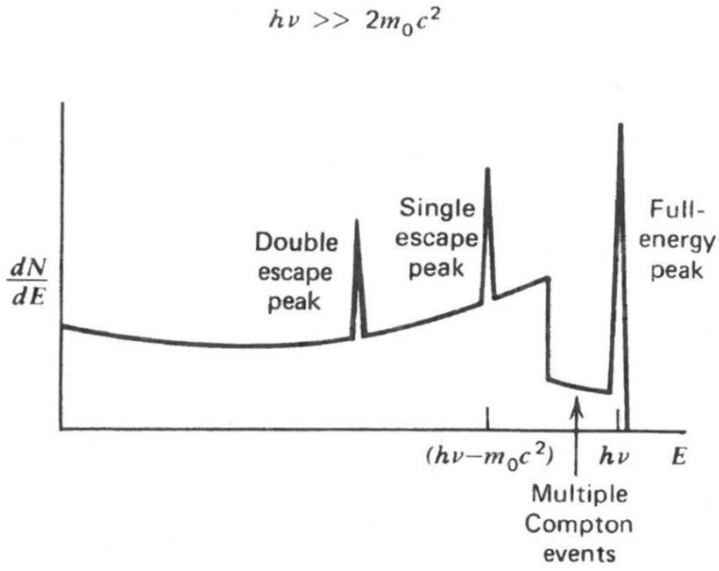

Figure 4.3: A simplified plot of counts against photon energy for high energy photons. Some features of the interactions are labelled, such as the full energy peak, and single and double escape peaks. The latter two are the result of PP interactions where one or both of the 511 keV photons produced escape the detector, respectively. [53].

The simplified example spectra above considers a mono-energetic γ source, however, when collecting γ spectra from irradiated Eu foils there are multiple γ rays. If these features overlap, identifying the nuclide from the γ rays increases in difficulty.

If a detector was large enough or dense enough, all the energy of the photon would be absorbed (either in one interaction or in multiple), therefore, the spectra would only contain photopeaks.

HPGe detectors

Standard semiconductor detectors work by applying a reverse bias across an n-p junction [53]. This forms a depleted region of no free charge. When ionising radiation interacts within the depleted region, electrons are excited from the valence band to the conduction band creating electron-hole pairs. Under the voltage applied to the detector, the electrons and holes produced are attracted and drawn to the positive and negative electrodes respectively. When they reach the terminals they produce a voltage pulse proportional to the radiation energy deposited in the detector.

Standard semiconductor detectors only produce depleted regions of 2-3 mm which is too small to be an efficient γ ray detector. The achievable thickness of a germanium detector's depletion region increases the purer the germanium used. For 1000 V of applied voltage, 100 mm of depletion is possible when impurity levels are less than 1 part in 10^{12}. Therefore, high-purity germanium detectors are used as efficient γ detectors.

The band gap between valence and conduction bands is 0.7 eV. Unfortunately, at room temperature this small energy gap is easily bridged by electrons leading to thermal noise. Therefore, to reduce thermal noise the HPGe detectors are cooled with liquid nitrogen to 77 K. This very small band gap results in detectors with excellent energy resolution, making

them ideal for γ ray spectroscopy.

Germanium is also a semiconductor with a high Z value. Reflecting on equation 4.3, the high Z value increases the likelihood of γ photons interacting by PE effect. This increases the photopeak-to-Compton ratio which is also desirable for γ spectroscopy.

4.1.2 Experimental set-up

To ensure enough spectra data could be collected for each of the nine irradiated Eu foils (see section 4.6), two HPGe detector set-ups were used. In both cases, the detectors were each connected to an electronics set-up as shown in figure 4.4. The electronic voltage signal produced by the HPGe detector, which is proportional to the energy deposited by the γ interaction, is passed through a pre-amplifier. The pre-amplifier matches the high detector output impedance and the low amplifier input impedance and generates a voltage pulse. The pre-amplifier also separates the detector electronics from the rest of the electronics to ensure changes to the subsequent electronics do not impact the signal production in the detector. After the pre-amplifier, the signal is then shaped and amplified using an amplifier. The voltage of this final signal is still proportional to the original energy deposited by the photon and the Analogue-to-Digital Converter (ADC) discretizes these signals and bins them into channel numbers proportional to the peak voltage and thus γ energy. The final spectra of counts against channel number were collected using MAESTRO software [54].

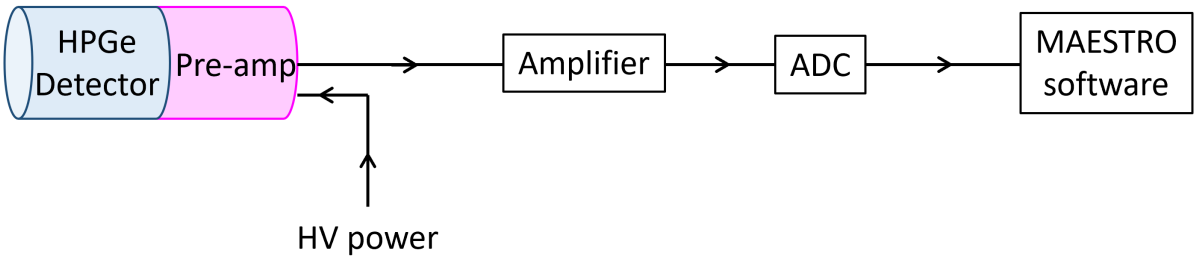

Figure 4.4: Diagram showing the electronics set-up of a HPGe detector.

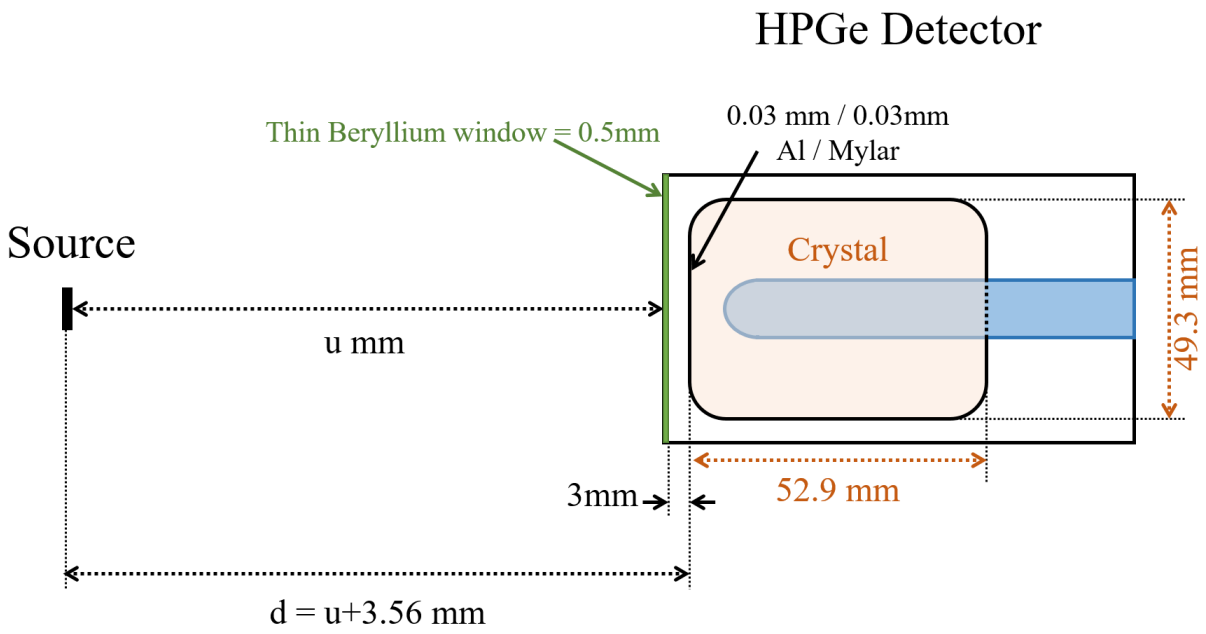

Figure 4.5: Diagram showing the separation between the irradiated Eu foils and the G11 HPGe detector (not to scale).

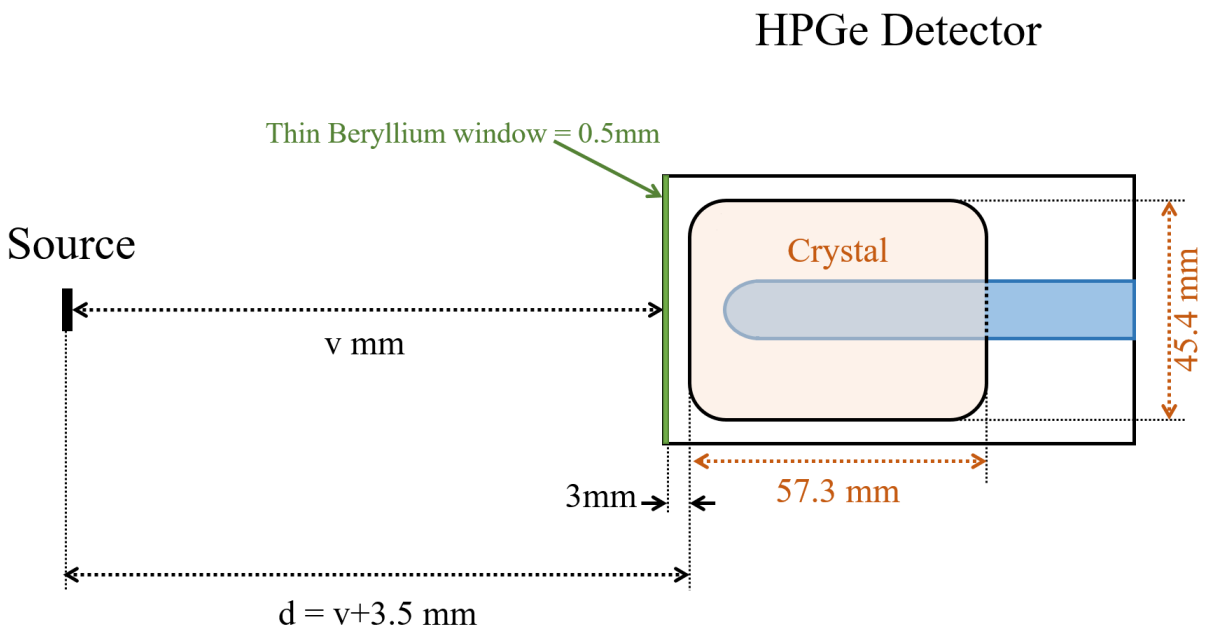

Figure 4.6: Diagram showing the separation between the irradiated Eu foils and the HPC HPGe detector (not to scale).

For notation purposes, the two detectors will be referred to by the name of the rooms they were in; "G11" and "HPC". Detailed diagrams of these HPGe detector dimensions can be found in appendix E. Figures 4.5 and 4.6 show simplified diagrams of the crystal and casing of the detectors, as well as the distance of the sources (u and v) from the detector face. The sources were either the irradiated Eu foils or calibration sources.

4.2 Calibration

As explained in section 4.1 the energy transferred from the γ photon to the detector is converted by the ADC into discrete channel numbers and recorded in a histogram such that the channel number is proportional to the energy deposited. Each nucleus emits a specific set of γ photons thus, the photopeaks of the spectrum can be used to identify the nuclei. However, in order to achieve this, the channel numbers need to be converted back into energy values (in keV). In other words, a calibration of the channel number to energy value needs to be carried out.

Known radioactive sources can be used to determine the relationship between photon energy and channel number. Looking at the photon energies of interest in the irradiated Eu foils (see section 4.5), the calibration of channels needed to be carried out over the energy range of 80-2200 keV. An excellent HPGe calibration source is ^{152}Eu. When this isotope decays to either ^{152}Gd or ^{152}Sm, a multitude of γ energies ranging from 30 keV to 1500 keV are produced due to the large decay Q-value and it's electron capture and β^- branches. Figure 4.7 shows a ^{152}Eu spectrum with the 16 energy peaks used for calibration labelled.

However, in order to obtain a higher energy calibration point, a ^{60}Co source was used. If the 1173.228 keV and 1332.492 keV coincidence γ's emitted by the ^{60}Co source arrived at the detector within a very short time window (i.e. less than a few hundred nanoseconds) then

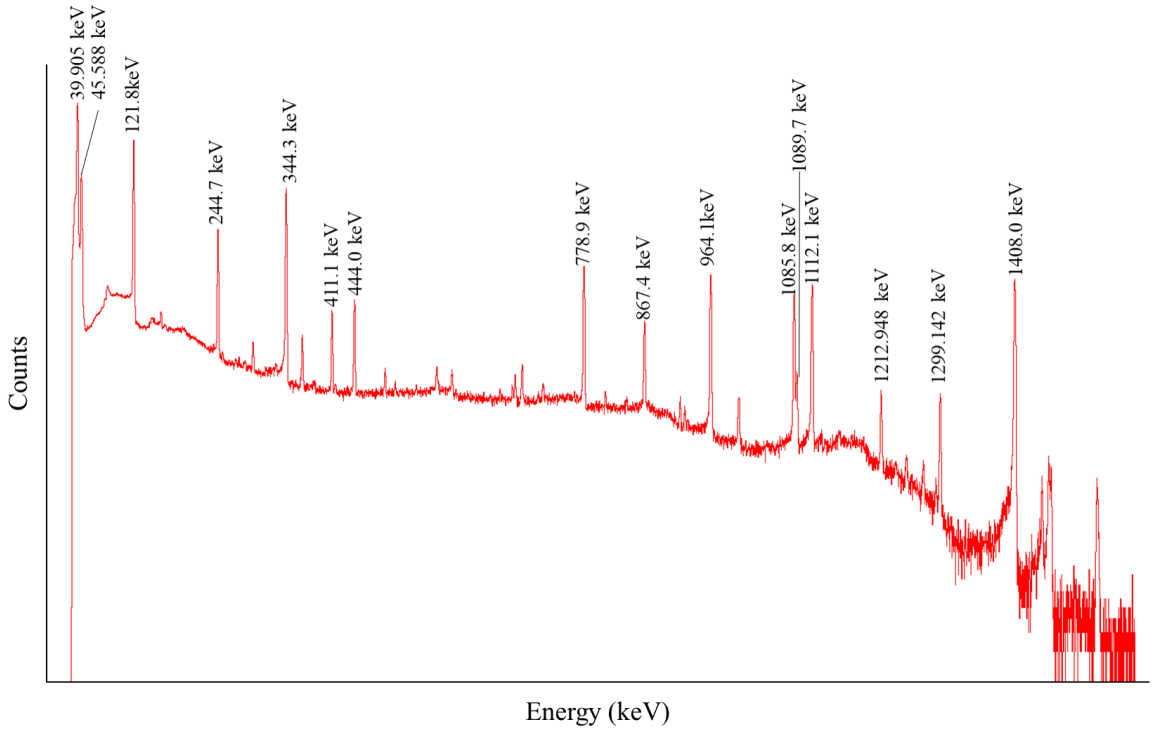

Figure 4.7: ^{152}Eu calibration spectrum. The 16 peaks labelled were used for energy calibration.

this produces a summation peak at 2505.72 keV. To increase the counts in the summation peak the ^{60}Co source was placed very close to the face of the detector.

The two calibration spectra (^{152}Eu and ^{60}Co) were taken twice a day to monitor any shift in the gain. Each of the 19 peaks were fitted with a Gaussian using the "gf3" fitting function in the RadWare software package [55]. The centroid values and the NNDC [15] peak energy values extracted from the latest nuclear data sheet [56] were then used in the "encal" function of RadWare to calculate the calibration fitting parameters. A quadratic calibration from channel number to energy was used. These calibration parameters were then applied to the irradiated Eu spectra collected to enable peak identification.

4.3 Resolution

4.3.1 Theory

HPGe detectors have excellent energy resolution making them ideal for γ spectroscopy. However, it is important to know how the ability of the detectors, to resolve two neighbouring peaks from one another, changes with energy.

If the number, N, of electron-hole (e-h) pairs produced when a γ photon deposits energy, E, within the HPGe detector were simply dependent on the average energy, ω, to produce a single e-h pair then $N = E/\omega$. Moreover, if the production of these e-h pairs were completely independent of each other then the statistical fluctuation in N would follow Poisson statistics. In other words, the error on N, $\sigma(N) = \sqrt{N}$.

For large N, Poisson distribution tends to a Gaussian distribution where the FWHM $= 2.35\sigma(N)$. Resolution, R is given by

$$R = \frac{FWHM(N)}{N}, \tag{4.4}$$

therefore,

$$R = \frac{2.35\sqrt{N}}{N} = 2.35N^{-1/2}. \tag{4.5}$$

However, the production of each e-h pair is not independent of every other e-h pair. Although a full theoretical model for the effects of this does not currently exist, it is experimentally seen that for semiconductor detectors, such as germanium, the observed statistical variance is smaller than Poisson statistics would predict. Because of this, the Fano factor, F ($= \frac{\text{observed statistical variance}}{E/\omega}$), is added to equation 4.5 to give,

$$R = \frac{2.35\sqrt{FN}}{N} = 2.35F^{1/2}N^{-1/2}. \tag{4.6}$$

For germanium, F can range from 0.057 to 0.129 [53]. The energy deposited by the photon, E, is proportional to the number of electron hole pairs produced. Therefore,

$$R \propto 2.35 F^{1/2} E^{-1/2}, \tag{4.7}$$

i.e.

$$R \propto E^{-1/2}. \tag{4.8}$$

4.3.2 Measurement

A set of calibration ^{152}Eu and ^{60}Co spectra taken for each HPGe detector were recorded as described in section 4.2. The peaks in each spectra were fitted to provide the centroid values and FWHM in channel number. Each detector was calibrated and the FHWM values for each peak were converted into energy units, keV, see figure 4.8. Resolution for each peak was calculated using $R = \frac{FWHM(E)}{E}$. Subsequently, R against E was plotted, as shown in figure 4.9. During the irradiated Eu spectrum collection, the shaping time of the HPC HPGe detector was changed from 1 μs to 3 μs. This improved the resolution as shown in figure 4.9 where the orange points (HPC at 1 μs) lie above the G11 (blue) and HPC with 3 μs shaping time (grey).

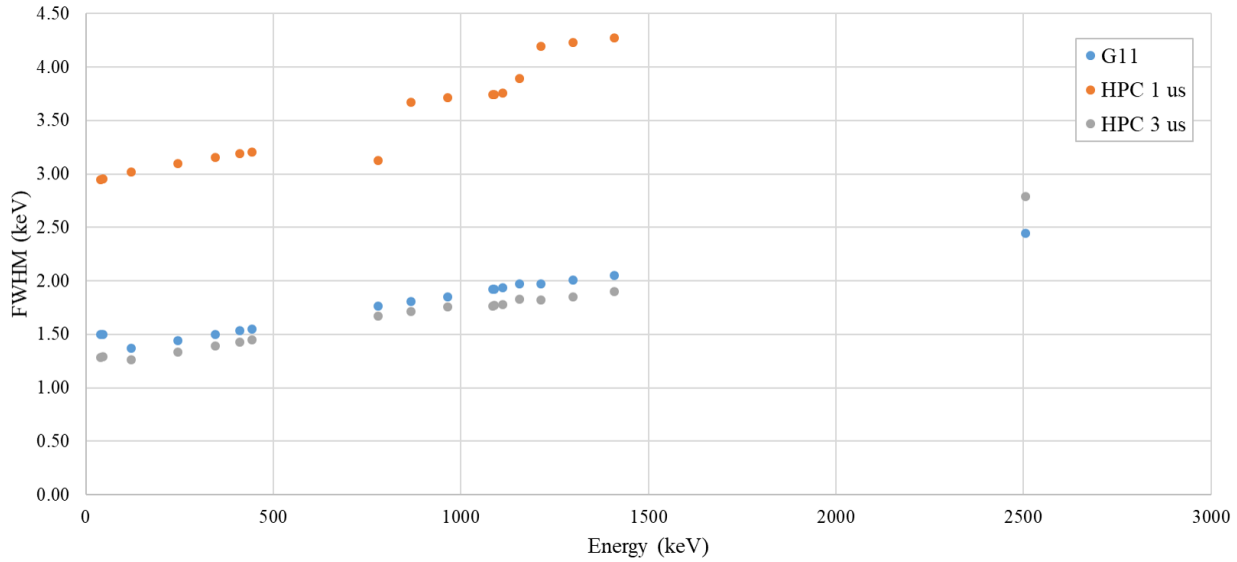

Figure 4.8: The change of FHWM in keV of a photopeak with energy for the G11 and HPC HPGe detectors. The orange points are the resolution of the HPC detector when the shaping time of the amplifiers was 1 μs and the grey when it was 3 μs.

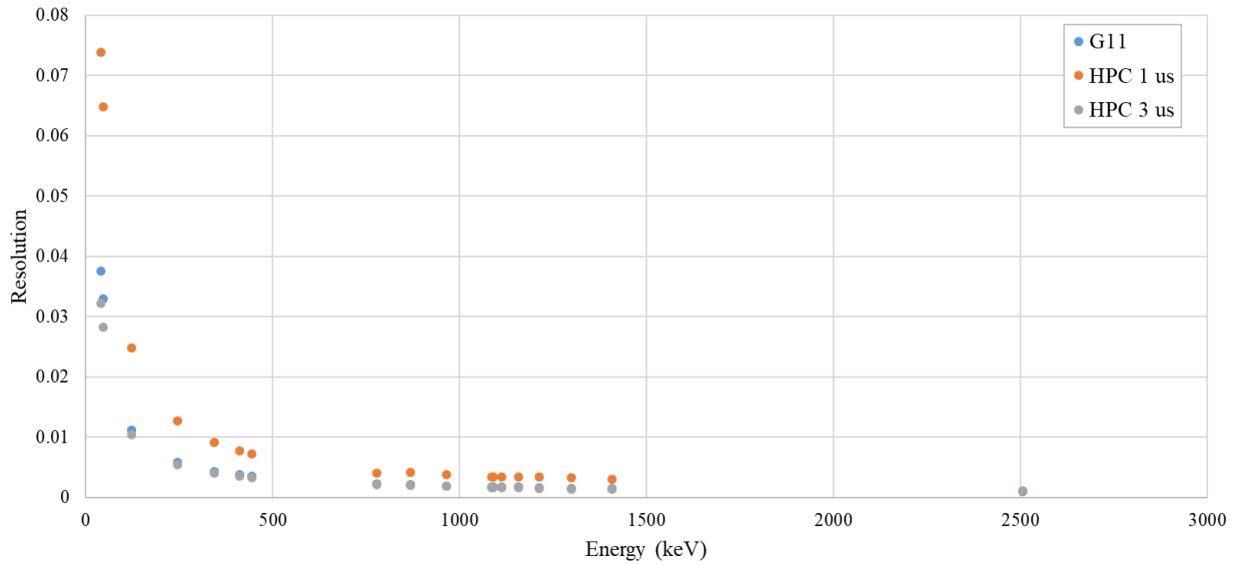

Figure 4.9: Resolution change with photon energy for the G11 (blue) and HPC (grey and orange) HPGe detectors. The orange points are the resolution of the HPC detector when the shaping time of the amplifiers was 1 μs and the grey when it was 3 μs.

4.4 Efficiency

4.4.1 Efficiency theory

Not all the radiation quanta will cause the detector to produce a signal pulse, this is particularly true for γ photons. Due to the low ionising power of photons it is not guaranteed that a photon will interact within the detector triggering a signal pulse. This causes the detector to be less than 100% efficient at detecting photons. It can be said [53] that absolute efficiency, ϵ_a, is defined as

$$\epsilon_a = \frac{\text{number of detected pulses recorded}}{\text{number of radiation quanta emitted by the source}}. \tag{4.9}$$

If coincidence detections of γ rays in a cascade were were being recorded then a consideration of the effect of angular distribution would need to be considered. However, for this work only singles data were recorded it can be assumed that the emission of γ rays from a source is isotropic and no adjustment is needed for detector angle. However, as radiation is emitted isotropically from a source not all the radiation quanta will reach the detector. Therefore, intrinsic efficiency, ϵ_i, which is defined as [53],

$$\epsilon_i = \frac{\text{number of detected pulses recorded}}{\text{number of radiation quanta incident on the detector}}, \tag{4.10}$$

may be necessary to account for any geometric differences between experimental set-ups. Equation 4.10 implies that a geometry efficiency factor, or fractional area of sphere covered by the detector, f_A, is incorporated into total efficiency. Geometry efficiency corrections will be discussed further in section 4.4.2.

For γ spectroscopy the photo peak is the point of interest in the spectra. Thus, it is important

to know the efficiency of detecting a photopeak contributing signal. If a source of activity, A, is placed in front of a detector and a spectrum is collected for a set time, then a photopeak from a γ photon produced by the source with intensity, I_γ, will have N counts under the peak. Therefore, absolute and intrinsic efficiency can be written as

$$\epsilon_a = \frac{N/\text{time}}{AI_\gamma}, \tag{4.11}$$

and

$$\epsilon_i = \frac{N/\text{time}}{AI_\gamma f_A}, \tag{4.12}$$

respectively. It is important to note that the 'time' used for efficiency calculations and all subsequent γ spectra corrections mentioned in this chapter was the live time of the spectra. This was because live time accounted for the variation in dead-time of the detector (between 0.1 and 6.1%) due to the variation in source activity and distance from the detector.

4.4.2 Geometric efficiency correction

Geometric efficiency is equivalent to knowing the fraction of the radiation emitted that reaches the detector. For a point source distance, d, from a detector with radius, R, (see figure 4.10) the fractional area of a sphere of radius, d, covered by the detector is given by the solid angle, Ω, divided by the total solid angle, 4π, i.e. $\frac{\Omega}{4\pi}$. If a point source is aligned axially with the detector (like in figure 4.10) then the fractional area (f_A) is given by [53],

$$f_A = \frac{1}{2}\left(1 - \frac{d}{\sqrt{d^2 + R^2}}\right). \tag{4.13}$$

This calculation for fractional area in equation 4.13 was valid when measuring the known sources to obtain the calibration, resolution and efficiency of each detector. This was because

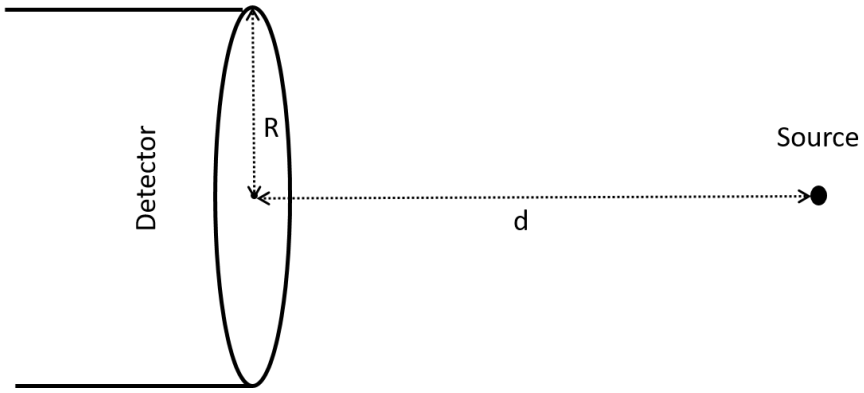

Figure 4.10: A point source placed *d* cm in front of a detector of diameter *R*.

these known sources were very small (point-like). However, for most of the irradiated Eu target γ spectra collected, the distance of the source from the detector, d, was not much greater that than R as the source was often less then 5 cm from a detector of radius $\sim$2.5 cm. In addition, the irradiated foils had a finite size and thus the area of the source could not be considered to be negligible.

The irradiated targets were disc shaped with a radius of r. The diameter of the beam spot of the irradiated Eu foil was 5.5$\pm$0.5 mm therefore the original radius of the irradiated foil sources, r = 0.275$\pm$0.025 cm. However, this r value was only valid for the first day of γ measurement. After this, the foil pieces had oxidised into a powder and each foil was collected into the corner of the plastic bag for which it was contained. The oxidised targets formed approximate disc shapes which repeat measurements using a vernier caliper were taken. The radius of the oxidised targets were 0.292$\pm$0.019 cm.

Figure 4.11 provides a schematic of a disc source and detector set-up. Ruby [57] derived that the fractional area (f_A) of a disk shape source could be found using an integral containing Bessel functions, where

$$f_A = \frac{R}{r}\int_0^\infty \frac{e^{-kd}J_1(rk)J_1(Rk)}{k}\,dk. \tag{4.14}$$

Equation 4.14 does not have an analytical solution but can be approximated numerically. A

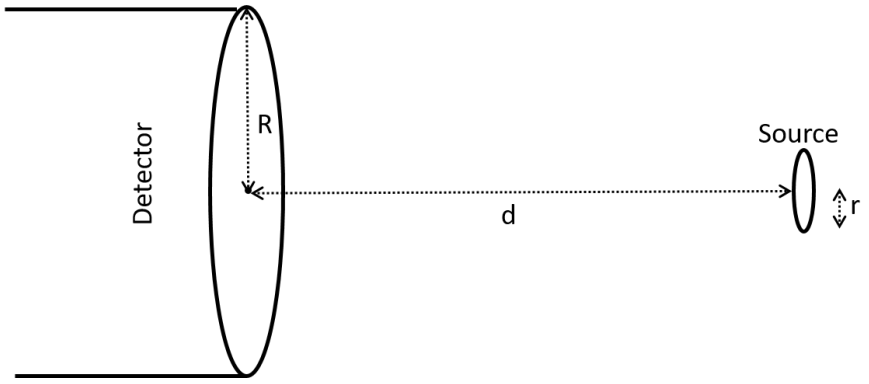

Figure 4.11: A disc shaped source, diameter, r, placed d cm in front of a detector of diameter R.

python script was written to find numerical solutions to equation 4.14 with the appropriate R, r and d input parameters. These were then compared to the point source f_A values, calculated using equation 4.13. A comparison of the two f_A values is shown in table 4.1.

The point source and disc source f_A values calculated for the different geometric set-ups used during spectra collection were the same to at least two significant figures. However, the disc f_A values had a larger uncertainty (error) so this value was incorporated into the efficiency correction.

Table 4.1: A comparison of the fractional area (f_A) calculated using a point source assumption and the numerically evaluated disc source solutions. The r (disc radius), R (radius of detector) and d (distance from detector crystal to source) parameters that were used throughout the experiment are also shown.

Detector	r (cm)	r error (cm)	d (cm)	d error (cm)	R (cm)	R error (cm)	Point source aprox. f_A	Point source aprox. f_A error	Disc source aprox. f_A	Disc source aprox. f_A error
G11	0.2750	0.0250	15.36	0.2	2.465	0.01	0.0063	0.0002	0.0063	0.0002
	0.2920	0.0190	15.36	0.2	2.465	0.01	0.0063	0.0002	0.0063	0.0002
			4.806	0.1	2.465	0.01	0.055	0.002	0.055	0.002
			4.906	0.05	2.465	0.01	0.053	0.001	0.053	0.001
			5.656	0.05	2.465	0.01	0.0416	0.0007	0.0416	0.0010
			4.956	0.05	2.465	0.01	0.0523	0.0010	0.0522	0.0013
HPC	0.2750	0.0250	13.85	0.1	2.27	0.01	0.0066	0.0001	0.0066	0.0002
	0.2920	0.0190	13.85	0.1	2.27	0.01	0.0066	0.0001	0.0066	0.0002
			5.65	0.05	2.27	0.01	0.0360	0.0006	0.0360	0.0009
			5.45	0.05	2.27	0.01	0.0384	0.0007	0.0384	0.0009
			5.4	0.05	2.27	0.01	0.0391	0.0007	0.0390	0.0010

4.4.3 HPGe efficiency measurement

The efficiencies of the two HPGe detectors, G11 and HPC, were found by placing several known sources, one at a time, at known distances from the face of each detector. The number of counts (N) or area under each γ energy peak were found by fitting Gaussian functions and a quadratic background shape. The efficiency spectra for the HPC detector were collected twice because the shaping time of the amplifier was changed during irradiated Eu target spectrum collection. The change in shaping time affected the resolution and efficiency of the spectra collected. Therefore, efficiency data were needed for both shaping-time scenarios.

The known sources used for the efficiency measurements were ^{152}Eu, ^{44}Ti, ^{60}Co and, for two out of the three efficiency measurements, a ^{133}Ba source was also used. For each spectra, N was extracted for the major peaks and used in the "effit" fitting function in the RadWare software package [54]. This piece of software was specifically design to fit efficiency curves of HPGe detectors. The "effit" program was initially fed the ^{152}Eu peak area and I_γ data, and a relative efficiency curve was fitted with

$$\text{RadWare relative efficiency} = e^{\left[(A+Bx+Cx^2)^{-G}+(D+Ex+Fx^2)^{-G}\right]^{-1/G}}, \tag{4.15}$$

where A, B, C, D, E, F and G are fitting parameters. RadWare relative efficiency is a function of γ energy (E_γ) and, in equation 4.15, x and y are defined as,

$$x = ln\left(\frac{E_\gamma}{E_1}\right) \tag{4.16}$$

and

$$y = ln\left(\frac{E_\gamma}{E_2}\right) \tag{4.17}$$

where $E_1 = 100$ keV and $E_2 = 1$ MeV.

To improve the fit, the area and I_γ data for each major peak in the ^{44}Ti, ^{60}Co and ^{133}Ba spectra were then scaled by the RadWare "effit" software and added to the ^{152}Eu data points. After the addition of each isotope data set, the efficiency curve was refitted to fine-tune the parameters A, B, C, D, E, F and G. The best efficiency curve fits occurred when parameter C was set to zero and G was set to 15. The final RadWare relative efficiency fits for each detector including all the 3-4 isotope data sets and the fit parameters are displayed in figures 4.12 to 4.14.

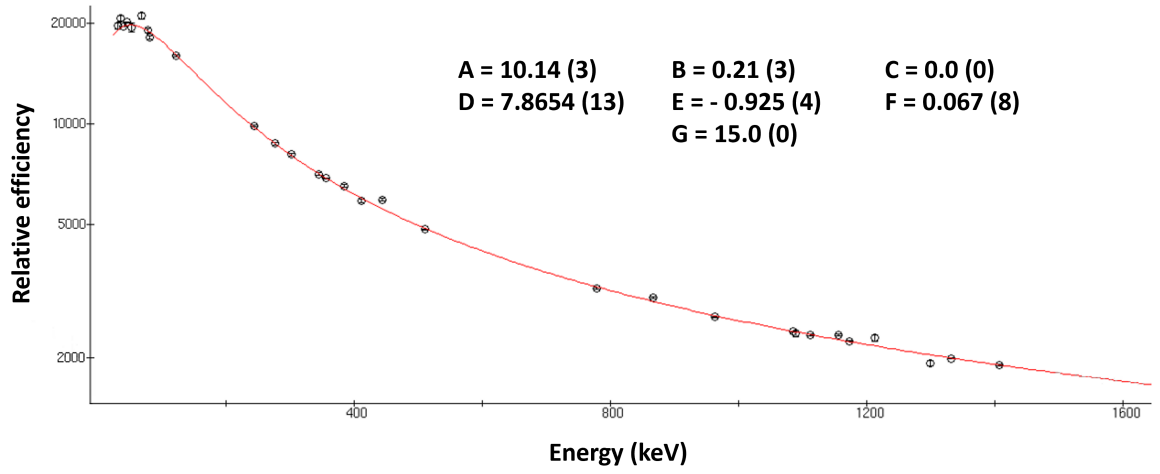

Figure 4.12: A plot of relative efficiency against γ energy. The RadWare relative efficiency fit is shown in red and was produced from using the γ peak data (black circular data points) of known ^{152}Eu, ^{44}Ti, ^{60}Co and ^{133}Ba sources measured using the G11 HPGe detector. The parameters *A* to *G* of the fit are also display on the graph. The error for each parameter is given in brackets.

In order for the efficiency fit of the detectors to be usable in the analysis of the irradiated Eu foil data collected, the relative efficiency produced by RadWare subsequently needed to be scaled to the intrinsic efficiency of the detector. Therefore, the intrinsic efficiency for each of the major fifteen ^{152}Eu γ peaks was calculated using equations 4.12 and 4.13 for each of the three detector scenarios. The RadWare relative efficiency was also calculated using equation 4.15 and the parameters A to G given in figures 4.12 to 4.14. For each of the 15 peaks, a ratio

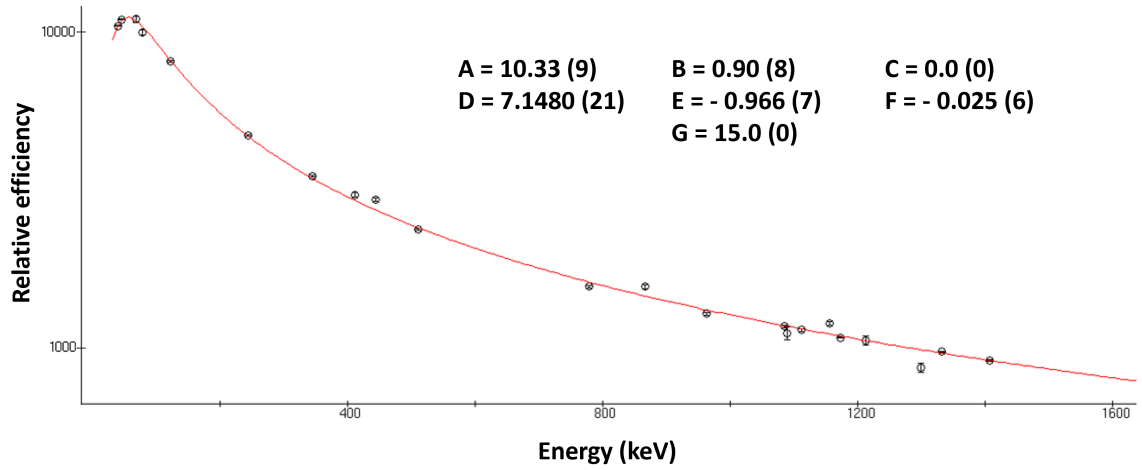

Figure 4.13: A plot of relative efficiency against γ energy. The RadWare relative efficiency fit is shown in red and was produced from using the γ peak data (black circular data points) of known ^{152}Eu, ^{44}Ti and ^{60}Co sources measured using the HPC HPGe detector with a shaping time of 1 μs. The parameters *A* to *G* of the fit are also display on the graph. The error for each parameter is given in brackets.

of $\frac{\text{intrinsic efficiency}}{\text{Radware relative efficiency}}$ was calculated and a weighted average of these was taken to provide a scaling ratio for the RadWare relative efficiency, S_R. For the G11 detector $S_R = (4.193 \pm 0.064) \times 10^{-5}$; for the HPC (1 μs shaping time) detector $S_R = (8.71 \pm 0.13) \times 10^{-5}$; and for the HPC (3 μs shaping time) detector $S_R = (19.41 \pm 0.29) \times 10^{-5}$.

Therefore, the intrinsic efficiency for a particular Tb isotope or isomer γ energy was calculated using equation 4.15. This value was then multiplied by S_R to obtain the intrinsic efficiency of the HPGe detector for that energy. The error associated with this process is discussed in appendix F.

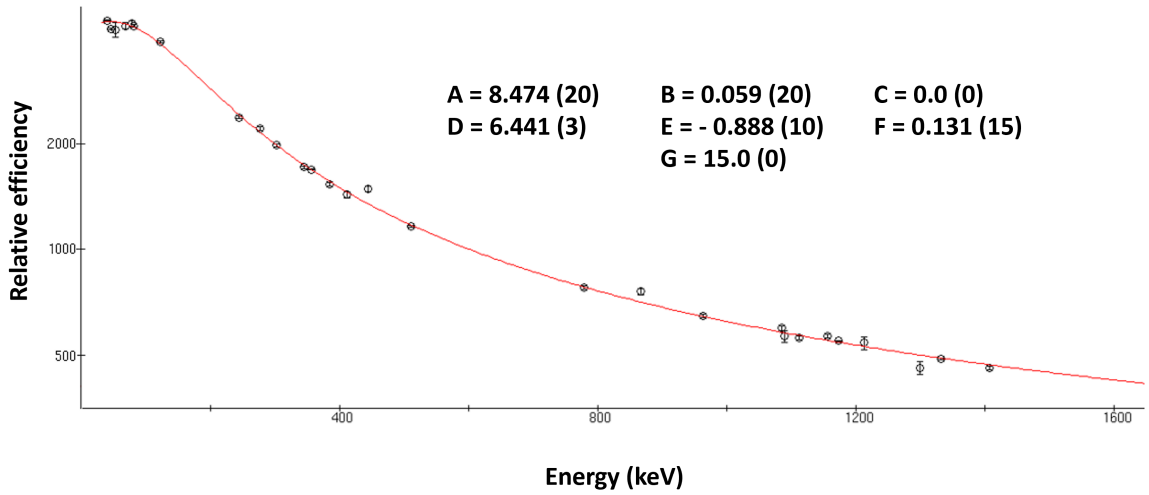

Figure 4.14: A plot of relative efficiency against γ energy. The RadWare relative efficiency fit is shown in red and was produced from using the γ peak data (black circular data points) of known ^{152}Eu, ^{44}Ti, ^{60}Co and ^{133}Ba sources measured using the HPC HPGe detector with a shaping time of 3 μs. The parameters *A* to *G* of the fit are also display on the graph. The error for each parameter is given in brackets.

4.5 Gamma energy selection

The predicted TALYS cross-sections for the Tb production from irradiating ^{nat}Eu with an α beam were discussed in section 2.1. In order to measure the cross-section for each isotope at different α energies, the total activity of each isotope needed to be measured. Measuring each activity was carried out by selecting specific γ energies emitted by each isotope as it decays and measuring the area under each peak and how these changed over time as the isotope decayed.

Each of the Tb isotopes and isomers produced in the α+^{nat}Eu reactions (^{151}Tb^{m1}, ^{151}Tb, ^{152}Tb^{m1}, ^{152}Tb, ^{153}Tb, ^{154}Tb^{m2}, ^{154}Tb^{m1}, ^{154}Tb, ^{155}Tb, and ^{156}Tb) are neutron light. Therefore, these Tb nuclei will eventually decay to their respective Gd isobar nuclei. The Gd nuclei then subsequently emit γ rays with energy specific to the nucleus. It is these γ en-

ergies which were selected and used for cross-section and half-life analysis. Most of the Gd isotopes produced from the Tb decays are stable or very long lived (^{152}Gd). However, the ^{151}Gd and ^{153}Gd will then undergo subsequent decays to the stable isotopes of Eu.

The nuances of the decays of several Tb isomeric states were also considered. The ^{152}Tb^{m1} isomer decays by internal conversion (IT) to the ground state of ^{152}Tb in 78.9(6)% of the decays that occur and the remaining 21.1(6)% of ^{152}Tb^{m1}, decays by electron capture (ec) or β^+ to ^{152}Gd. TALYS calculated cross-sections also predict the production of the ^{151}Tb^{m1} isomer. This decays by IT to the ground state of ^{151}Tb in 93.4(20)% of the decays that occur and the remaining 6.6(20)% of ^{151}Tb^{m1} decays by ec or β^+ to ^{151}Gd. The ^{151}Tb^{m1} isomer state has a half-life of 25(3) seconds and was too short to be recorded using the set-up described in this chapter, therefore, only the ^{151}Tb ground state decays were measured. Terbium 154 production and decay is slightly more complected due to the presence of two excited isomer states. Figure 4.15 depicts a simplified decay diagram of how the three states of ^{154}Tb decay. The importance of isomers decaying by internal conversion is discussed further in chapters 5 and 6.

Where possible, a few γ energies were selected for each Tb isotope and isomer decay. For the best results the γ energies emitted with the highest intensities were selected. However, many different isotopes were present at once in each irradiated Eu foil, therefore, the γ energies selected must also be distinguishable from any other γ rays emitted by the foil. Consequently, it was important to understand the resolution limitations of each detector as discussed in section 4.3.

Table 4.2 lists the energies of the γ rays (E_γ) and their intensities (I_γ) used to determine the activity of each isotope. The Q-values for the production of each isotope are also shown. Much of the γ energy and intensity information for each isotope was taken from NNDC [15]. However in a few cases the experimental data for this information was limited. For all of the

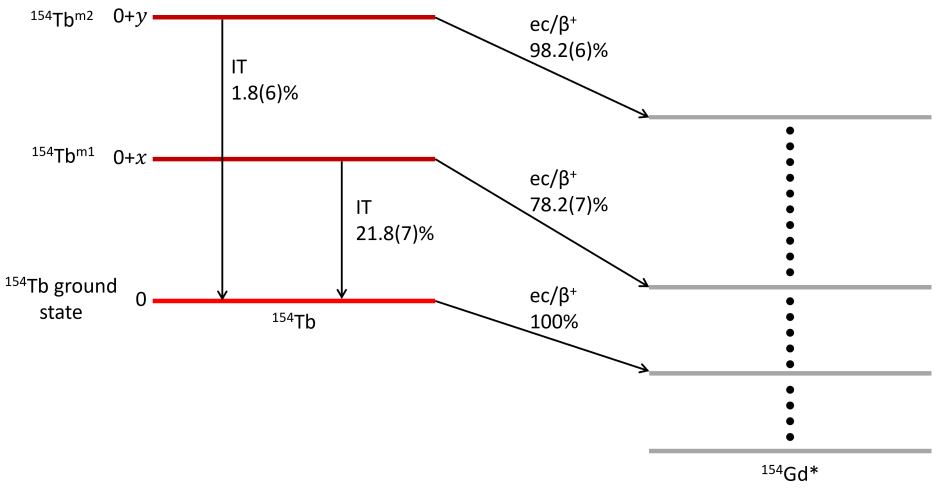

Figure 4.15: A simplified decay diagram of how the three states of ^{154}Tb decay. The values were extracted from the NDS for A=154 [58]. The nuclear energy levels of the isomeric state have not been measured which is why they are labelled $0+x$ and $0+y$. Note that the ec/β^+ decays by do not immediately decay to the ground state of ^{154}Gd but a variety of excited states of ^{154}Gd. The de-excitation of ^{154}Gd^m produces the γ rays detected.

^{154}Tb isomers the γ information was taken from IAEA [46]. The Nuclear Data Sheet (NDS) sources used for these values are cited in the last column of table 4.2.

Note that the 586.27(7) keV γ emitted following the decay of the ^{152}Tb ground state was only used after the excited state of ^{152}Tb had decayed away as the excited state emitted a γ of 586.2(2) keV.

It is also important to note that the 160.51 and 161.29 keV γ emissions from ^{155}Tb could not be distinguished from each other in the spectra. Thus a weighted average of the two γ energies and the sum of their intensities were used. Therefore, this peak was located at 161.118(83) keV and its intensity was 3.54(16)%.

The γ energies selected and listed in table 4.2 were checked against the NNDC and IAEA databases for γ emissions of energies within the FWHM resolution of the detectors from

the decay of Tb, Gd and Eu isotopes, as all these elements were likely to be made in the irradiation process. The selected γ energies were also checked against γ emissions from the potential products of α+Al interactions that would have occurred in the degrader foils. Background spectra were also recorded and the energies of these peaks were measured and compared to the selected energies in table 4.2 to ensure there was no overlap.

Table 4.2: The isotopes and isomers of Tb produced by irradiating ^{nat}Eu with an α beam. The Q-value for the production of each isotope and the prominent γ rays used for determining the activity of the isotopes are also detailed here. All the γ energies listed here were monitored and measured, however, the ones in grey were not used for cross-section calculations, the reasons for this are discussed in chapter 5.

Terbium isotope/isomer	Half-life	Decay mode	E_γ (keV)	I_γ (%)	Contributing reactions	Q-value (MeV)	NDS reference
151	17.609(14) h	ε β^+ : 99.99 %	251.863(10) 287.357(10)	26.3(11) 28.3(12)	151Eu(α,4n)151Tb 153Eu(α,6n)151Tb	-32.8884 -47.7448	[59]
		(α : 9.5E-3 %)					
152	17.5(1) h	ε β^+ : 100%	271.09(7) 764.89(7) 778.9045(24) 586.27(7)	9.53(21) 2.74(7) 5.54(13) 9.21(21)	151Eu(α,3n)152Tb 153Eu(α,5n)152Tb	-25.724 -40.5804	[56]
152m	4.2(1) m	IT : 78.9 (6) %	159.59(10) 235.4(1) 277.2(1) 283.29(5)	16.6(8) 4.2(3) 8.5(4) 59.8(5)	151Eu(α,3n)152mTb 153Eu(α,5n)152mTb	-26.2257 -41.0821	[56]
		ε β^+ : 21.1(6) %	385.9(1) 471.9(1) 526.8(2) 647.4(2) 1166.9(2)	3.27(20) 11.8(7) 1.64(13) 4.3(3) 3.7(3)			
153	2.34(1) d	ε β^+ : 100 %	82.86(2) 109.758(15) 212.00(2)	5.4(7) 6.2(4) 28.5(19)	151Eu(α,2n)153Tb 153Eu(α,4n)153Tb	-17.0566 -31.913	[60]
154	21.5(4) h	ε β^+ : 100 %	704.90(11) 2064.11(10) 2187.10(16)	4.8(3) 7.1(3) 9.9(8)	151Eu(α,n)154Tb 153Eu(α,3n)154Tb	-10.1426 -24.999	[58]
154m1	9.4(4) h	ε β^+ : 78.2(7) %	540.18(6) 1208.06(14) 1229.42(20) 1288.39(14) 1490.37(22)	20(3) 0.51(9) 0.59(14) 1.4(3) 1.04(18)	151Eu(α,n)154Tb 153Eu(α,3n)154Tb	-10.1426 + x -24.999 + x	[58]
		IT : 21.8(7) %					
154m2	22.7(5) h	ε β^+ : 98.2(6) %	225.94(3) 426.78(7) 1061.39(9)	27(3) 17.3(12) 4.1(7)	151Eu(α,n)154Tb 153Eu(α,3n)154Tb	-10.1426 + y -24.999 + y	[58]
		IT : 1.8(6) %					
155	5.32(6) d	ε : 100 %	105.318(3) 148.64(1) 160.51(10) 161.29(1) 163.28(1)	25.1(13) 2.65(14) 0.78(4) 2.76(15) 4.44(23)	151Eu(α,γ)155Tb 153Eu(α,2n)155Tb	-0.9779 -15.8343	[61]
156	5.35d(10)	ε β^+ : 100 %	534.29(6) 1065.11(14) 1154.07(15) 1222.44(9) 1421.67(9)	67(6) 10.8(10) 10.4(10) 31(3) 12.2(12)	153Eu(α,n)156Tb	-8.9226	[62]

4.6 Spectra collection

Once the stack of Eu/Al target foils had been irradiated with an α beam the nine Eu/Al envelopes were placed in separate resealable bags. Two HPGe detectors, in separate rooms, were used to collect the γ spectra of the nine foil envelopes. The schematic of these detectors are shown in figures 4.5 and 4.6. A spectrum of a foil envelope was taken by a single plastic bag containing a single foil envelope which was placed within a plastic holder at a distance (u or v) from either of the HPGe detectors. The remaining seven foil envelopes were placed away from the detector behind lead shielding to prevent any of the other foils affecting the spectra being taken.

In order to produce decay curves and accurately determine the total activity of each isotope at the point the α beam irradiation stopped, several measurements of the area under the selected γ peaks needed to be measured. For this to be possible, several spectra must contain peaks with significant statistical counts for each isotope. Thus several spectra must be taken within 5-6 half-lives of the isotope being measured. As seen in table 4.2, the half-lives of the isotopes and isomers of interest vary from 4.2 minutes to 5.35 days. Therefore, the measurement time and number of spectra taken in a day was varied.

On the same day of irradiation many spectra were taken initially starting with 1 minute measurement duration to monitor the decay of the $^{152}\mathrm{Tb}^{m1}$ isomer (4.2 minute half-life). Due to the short time window and only two HPGe detectors available, only four irradiated Eu foils could be monitored in this initial stage and still achieve enough data points to form decay curves. Looking at TALYS predicted cross-sections and the energy ranges covered by each Eu foil shown in figure 3.21, it seemed that the first few foils were likely to produce larger numbers of the $^{152}\mathrm{Tb}^{m1}$ isomer. Therefore, the first four foils were chosen for the initial 1 minute spectra monitoring. Foil 1 was placed in front of the G11 HPGe detector and 20 one minute spectra were taken. Foils 2, 3 and 4 were rotated in front of the HPC

HPGe detector and six 1 minute spectra were taken of each of the three foils. Thus, a total of 38 spectra were collected to measure the decay of the ^{152}Tb^{m1} isomer.

After this, all nine Eu foils were monitored separately between the two HPGe detectors. A 15 minute spectrum was taken of each foil followed by a set of 30 minute spectra. The following day an additional three 30 minute spectra were recorded for each foil and two sets of 1 hour spectra were collected in the subsequent two days. Predominately, these spectra were to monitor the decay of the isotopes and isomers with half-lives of less than a day (^{151}Tb, ^{152}Tb and the ^{154}Tb isomers).

Following this, a 2 hour, 5 hour and two 7 hour spectra were collected for each foil to ensure enough data points were available for the ^{153}Tb isotope with a 2.34 day half-life. Afterwards, spectra of each foil were then collected 9-11 times over a period of 29 days after irradiation. Each spectrum was taken for 10 -11 hours at a time to ensure the γ peaks of the ^{155}Tb and ^{156}Tb isotopes contained a significant number of counts. Therefore, after a period of 29 days, a total of 209 spectra were collected to measure the decay of the isotopes and isomers (other than the ^{152}Tb^{m1} isomer).

Initially, the distance of the sources were approximately 13 to 15 cm from the face of the detectors. This was to reduce the percentage error of the measured distance of the source from the detector. However, due to a reduced length in planned irradiation time and current, the statistics of each isotope was lower than planned and two days after irradiation the foils had to be placed 4 to 5 cm from the detector. The plastic foil holder was fixed to the table, but the distance from the foils to the detectors was measured regularly (with a ruler) in case the detectors were accidentally knocked out of place. The distances were recorded and were used in the geometric efficiency correction. The d parameter in table 4.1 lists all the distances measured over the course of the data collection.

4.7 Peak fitting

The cross-section values for the production of each isotope changes with α beam energy, therefore, the ratio of the areas under the peaks of the different isotopes and isomers in the spectra will change from foil to foil. In addition, the isotopes and isomers have differing half-lives, thus, the ratios between the different isotope/isomer peaks will change with time for the same foil. These differences will cause the spectra to look slightly different from one another. However, in general, the same γ peak fitting principles were applied to all the spectra. This section will discuss the fitting of the spectra collected as described in section 4.6.

A set of ^{60}Co and ^{152}Eu calibration spectra were taken on each detector at both the start and end of the day to track any detector energy gain shifts. As described in section 4.2, these calibration spectra were used to transform the channel numbers of the spectra of each foil into their equivalent energy values.

As with the calibration spectra, the "gf3" fitting function of RadWare [55] was used to fit skewed Gaussians to each of the peaks of interest given in table 4.2. There were a total of 247 spectra taken of the nine foils. The first 38 spectra were collected for the monitoring of the nine γ peaks emitted by the short lived ^{152}Tb^{m1} isomer, meaning a total of 342 peaks were fitted for this isomer measurement over the four foils monitored. The remaining 209 spectra collected as described in section 4.6 were to measure the other isotopes and isomers given in table 4.2. This involved the monitoring and fitting of up to 30 different energy peaks of interest depending on which isotopes were present in the foil and on the time since irradiation.

Figure 4.16 shows an example of a spectrum taken of foil 5, one day after the foil was irradiated. The peaks of interest have been labelled with their isotope/isomer and energy

values. Note that the isotopes ^{151}Tb and ^{156}Tb were not present in this foil and are thus not labelled. Figure 4.17 is the labelled spectrum of foil 1 taken 10 minutes and 50 seconds after α irradiation ceased. Here the nine ^{152}Tb^{m1} isomer peaks are labelled.

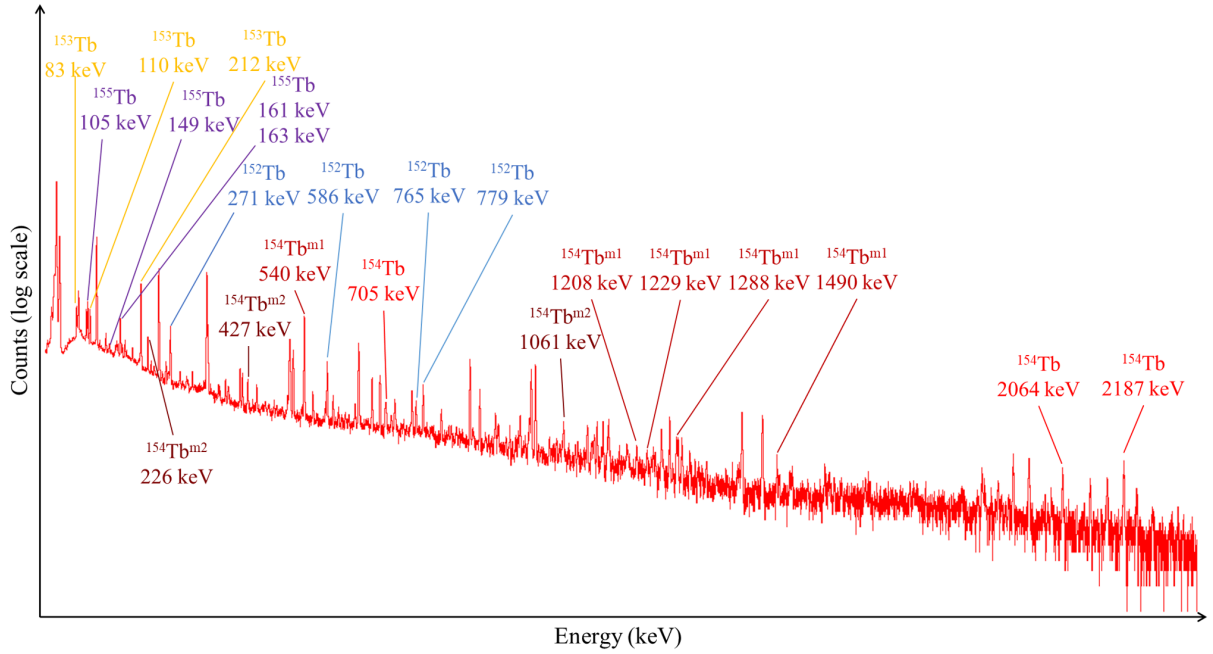

Figure 4.16: Spectrum taken of foil 5 one day after the foil was irradiated. The spectrum was collected for 30 minutes. The counts are given in a log scale to enable the visibility of the high energy, lower statistics peaks. The peaks belonging to the isotopes/isomers of interest are labelled accordingly. The other peaks in the spectrum are either background peaks or other energies emitted by the irradiated Eu or Al foil.

With up to 30 peaks of interest stretching over a wide range of energies where the background is affected by the Compton edged of other peaks in the spectrum, only small energy ranges were fitted at a time. Figures 4.18 to 4.35 show example Gaussian fits for each of the 39 peaks of interest.

From each fit the width and area under each peak of interest were recorded along with the associated errors. The areas were then corrected as discussed in sections 4.8 and used to determine the activity of the isotopes/isomers. The widths (FWHM) of the peaks were used

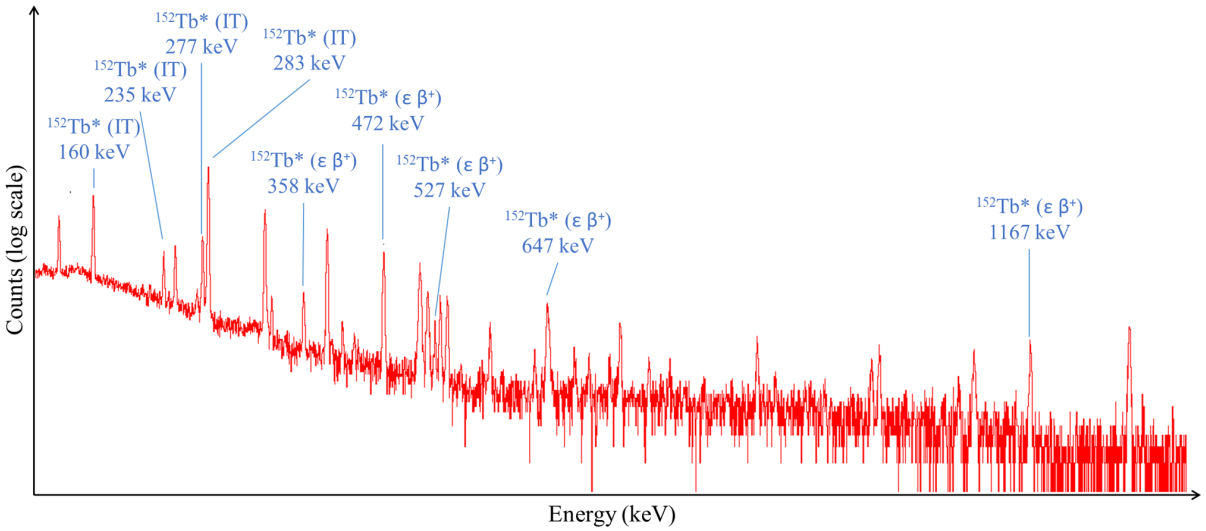

Figure 4.17: Spectrum taken of foil 1, 10 minutes 50 seconds after the foil was irradiated. The spectrum was collected for 1 minute and is zoomed in on a smaller energy range to enable the visibility of all nine labelled γ peaks emitted by the ^{152}Tb^{m1} isomer (labelled as 152Tb*). The type of decay which the isomer undergoes when emitting these γ photons is also included in the label.

to determine if the fit of each peak was appropriate and in agreement with the resolution of each detector.

4.7.1 Short-lived isomer peaks

The following set of figures show example skewed Gaussian fits for each of the nine peaks of interest emitted by the ^{152}Tb^{m1} isomer. This excited state decays 78.9% of the time to the ground state by internal conversion (IT). Otherwise, 21.1% of the time the ^{152}Tb^{m1} isomer decays by electron capture (ε) or β^+ decay to ^{152}Gd. The distinction between these two decays are also denoted in the figures. In each figure the red line represents the spectrum data and the black line is the fit.

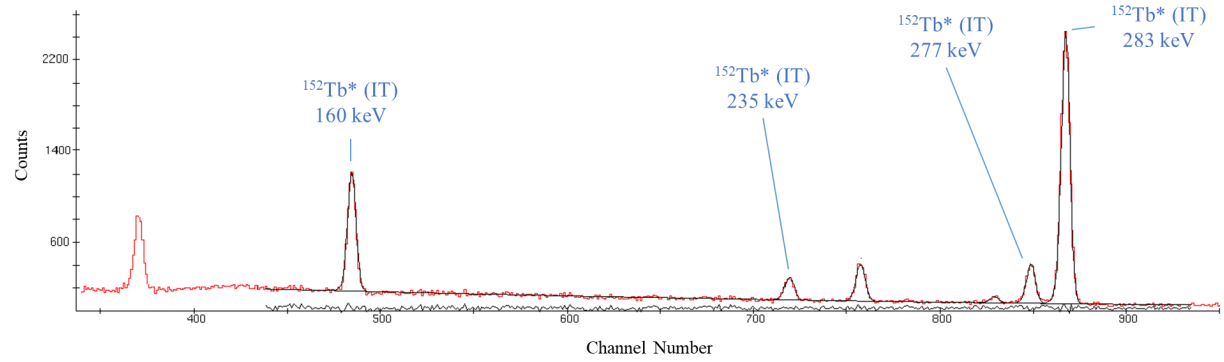

Figure 4.18: Fitting skewed Gaussians to the four lower energy ^{152}Tb^{m1} isomer decay peaks.

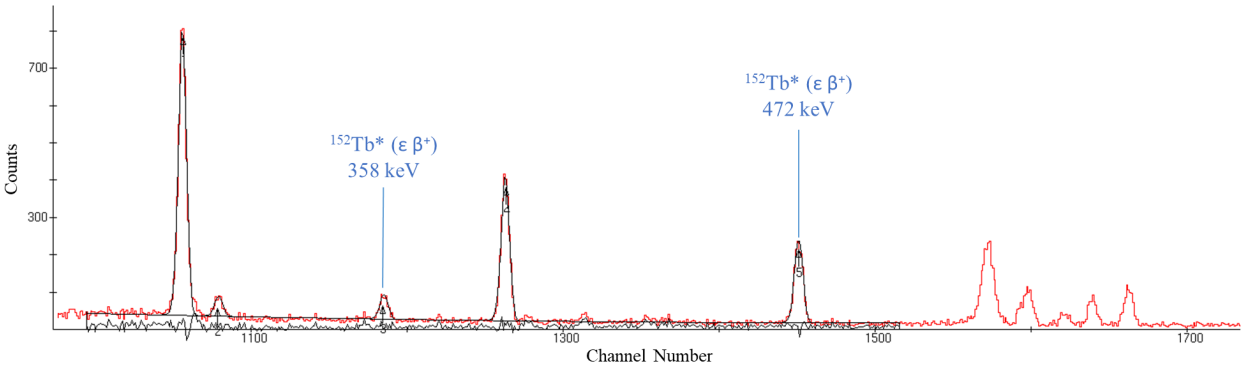

Figure 4.19: Fitting skewed Gaussians to the 358 and 472 keV ^{152}Tb^{m1} isomer decay peaks.

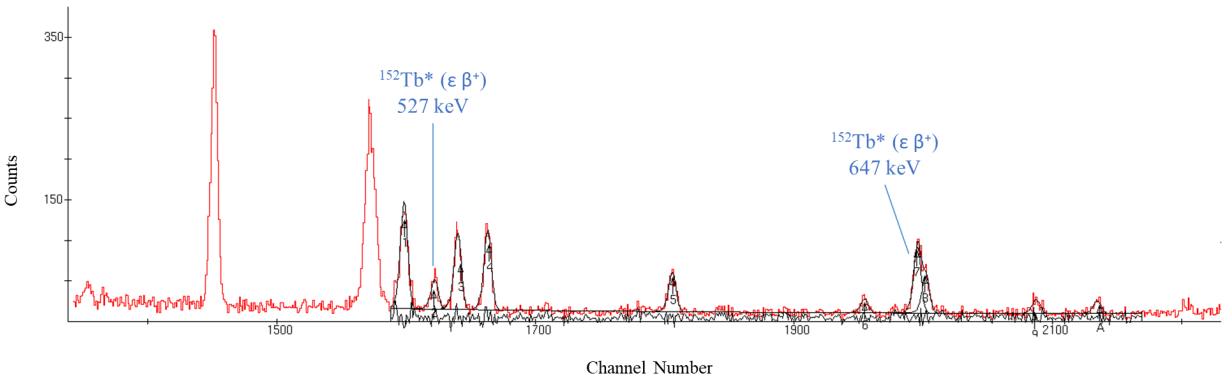

Figure 4.20: Fitting skewed Gaussians to the 527 and 647 keV ^{152}Tb^{m1} isomer decay peaks.

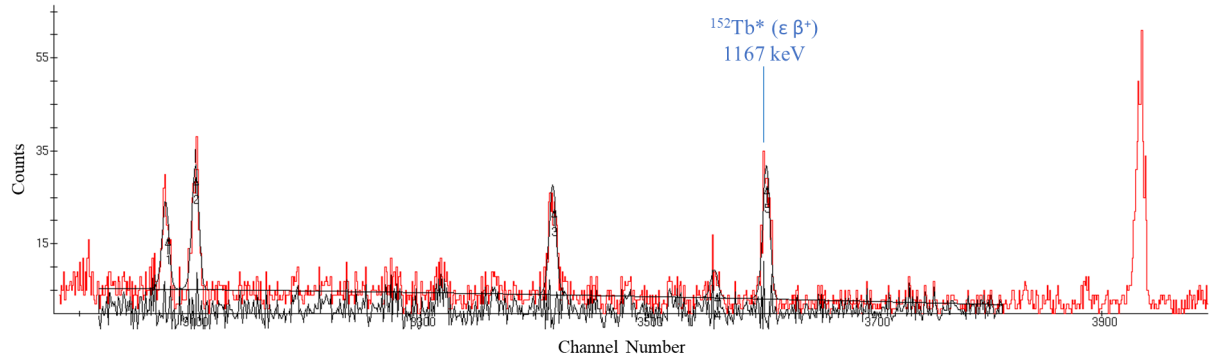

Figure 4.21: Fitting skewed Gaussians to the 1167 keV ^{152}Tb^{m1} isomer decay peak.

4.7.2 Other isotope and isomers

The following set of figures show example skewed Gaussian fits for each of the 30 peaks of interest emitted by the ^{151}Tb, ^{152}Tb, ^{153}Tb, ^{154}Tb, ^{154}Tb^{m1}, ^{154}Tb^{m2}, ^{155}Tb, and ^{156}Tb isotopes and isomers. In each figure the red line is the spectrum datum and the black is the fit.

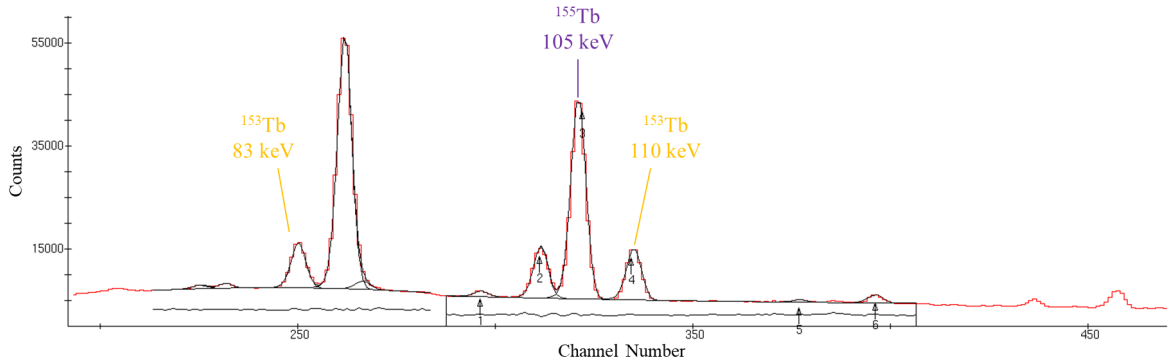

Figure 4.22: Skewed Gaussians fitted to the 83 and 110 keV peaks from the decay of the ^{153}Tb isotope and the 105 peak from the decay of the ^{155}Tb isotope in a spectrum of foil 9 taken on day 5. The peaks were fitted in two separate sections to allow the background to be fitted accurately.

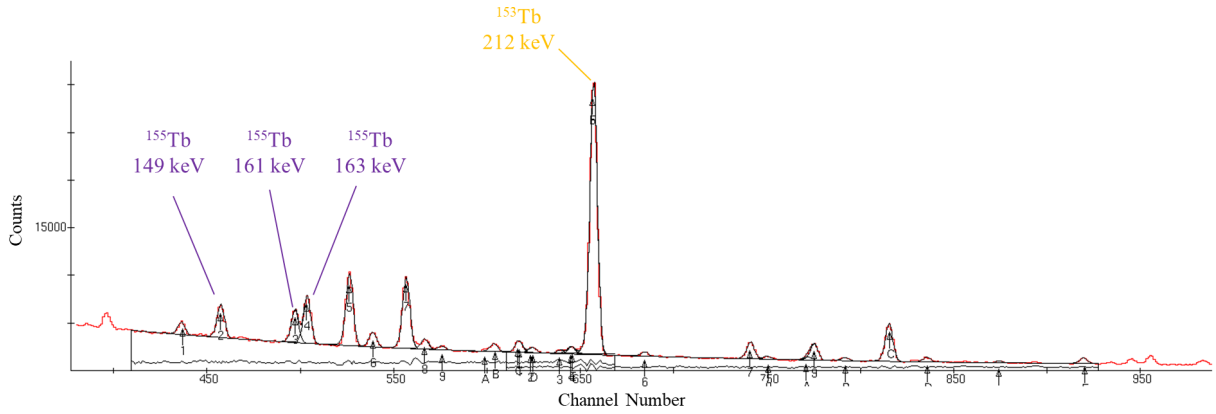

Figure 4.23: Skewed Gaussians fitted in the 120 keV to 300 keV range of a foil 9 spectrum taken on day 5. This section was often fitted in two parts to achieve a good background fit for each peak. In some spectra the 212 keV peak emitted by the decay of ^{153}Tb isotope was fitted with the first set of peaks and in others the second.

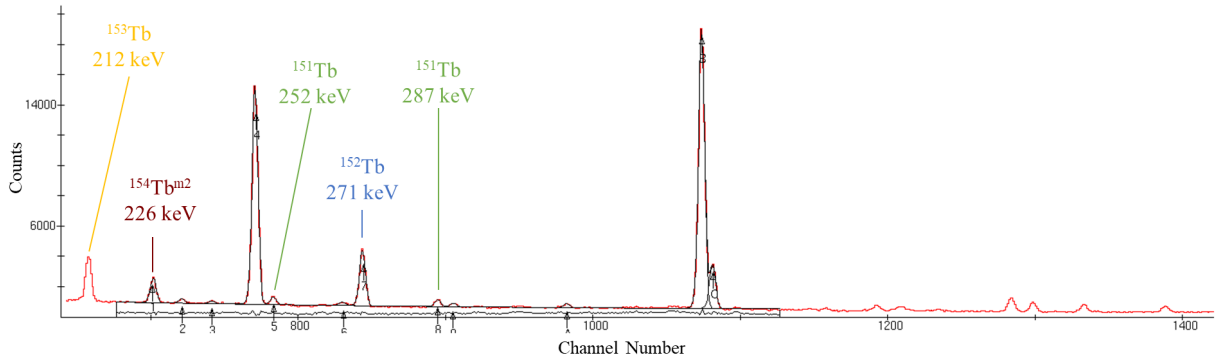

Figure 4.24: Skewed Gaussians fitted in the 220 keV to 300 keV range of a foil 1 spectrum taken on day 2. In this spectrum (taken earlier than figure 4.23), due to the higher energies of the α particles in this foil, the ^{151}Tb isotope and ^{154}Tb^{m2} isomer decay peaks are visible.

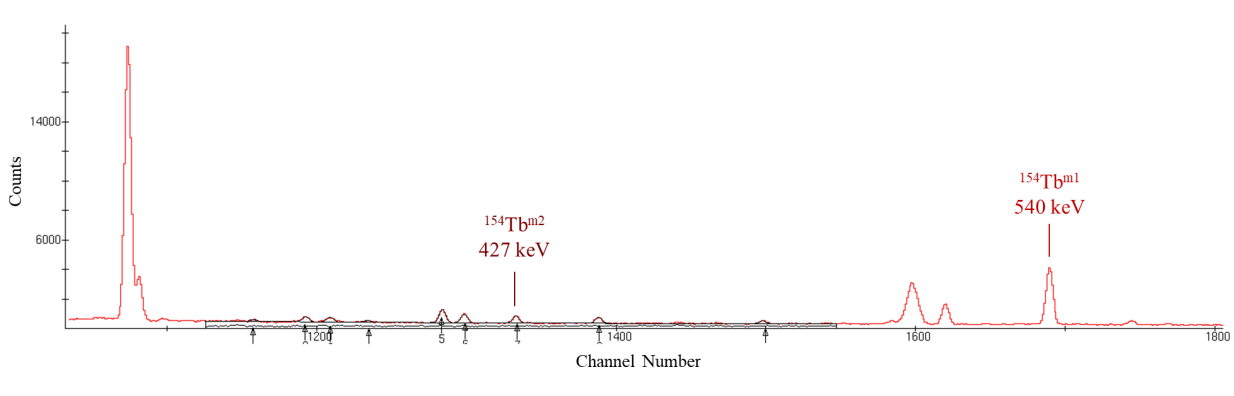

Figure 4.25: Skewed Gaussians fitted in the 350 keV to 500 keV range of a foil 1 spectrum taken on day 2. In this foil and energy range only the 427 keV $^{154}Tb^{m2}$ isomer decay peak is visible.

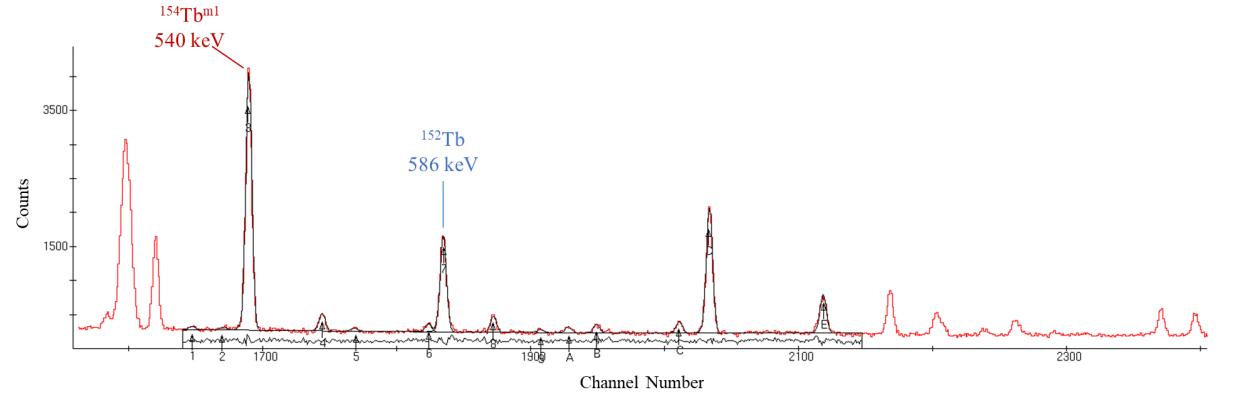

Figure 4.26: Skewed Gaussians fitted in the 520 keV to 700 keV range of a foil 1 spectrum taken on day 2. In this spectrum both the 540 and 586 keV peaks of the $^{154}Tb^{m1}$ and ^{152}Tb decays, respectively, were present.

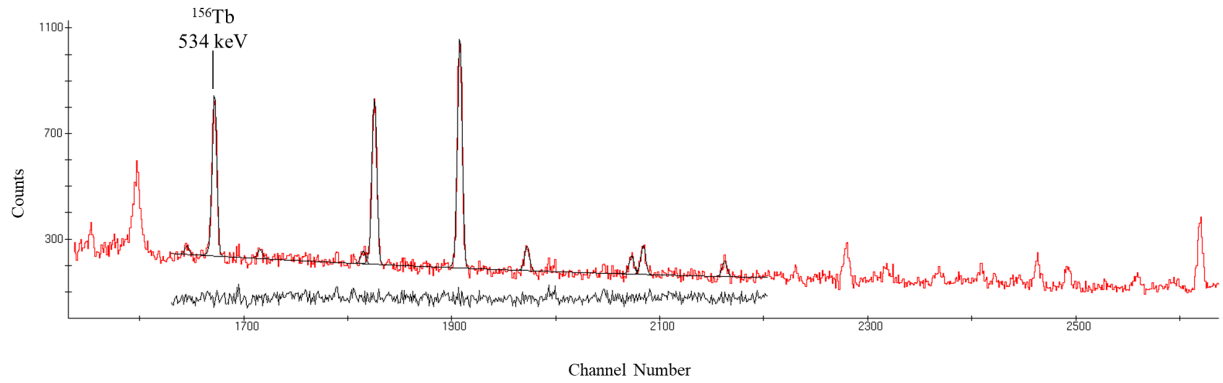

Figure 4.27: Skewed Gaussians fitted in the 520 keV to 700 keV range of a foil 9 spectrum taken on day 5. This foil was exposed to α's of lower energy thus the only peak of interest visible in this energy region was that of the 534 keV γ from the decay of the ^{156}Tb isotope. This peak was fitted along with the other surrounding peaks to obtain a good background fit.

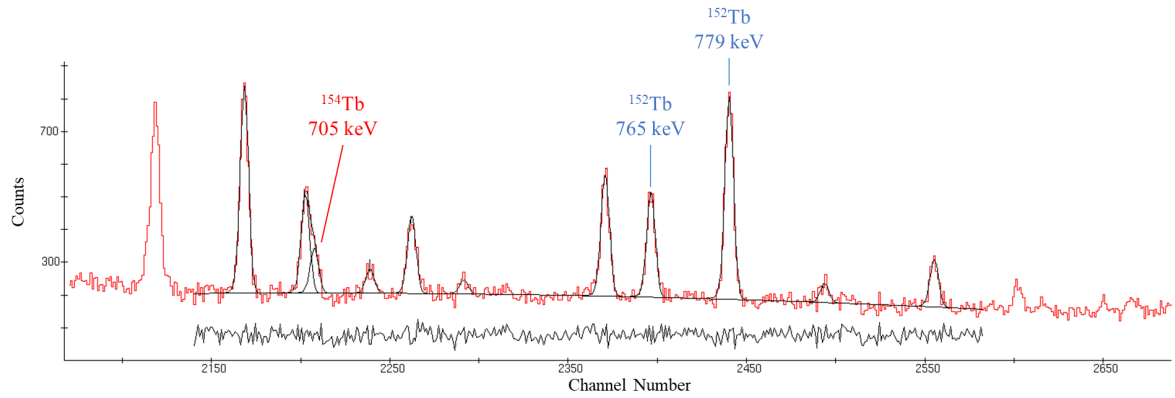

Figure 4.28: Skewed Gaussians fitted in the 700 keV to 800 keV range of a foil 1 spectrum taken on day 2. The peaks of interest are labelled with their isotopes and γ energy.

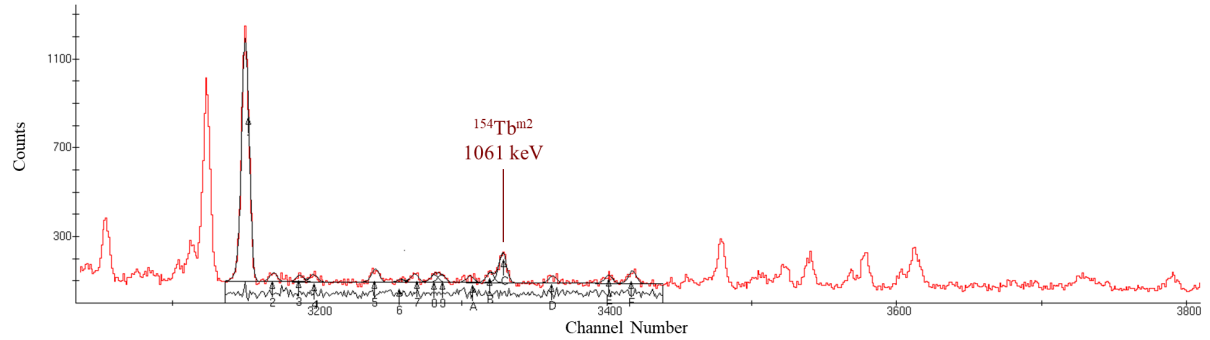

Figure 4.29: Skewed Gaussians fitted in the 900 keV to 1100 keV range of a foil 1 spectrum taken on day 2. The 1061 keV peak of interest is labelled.

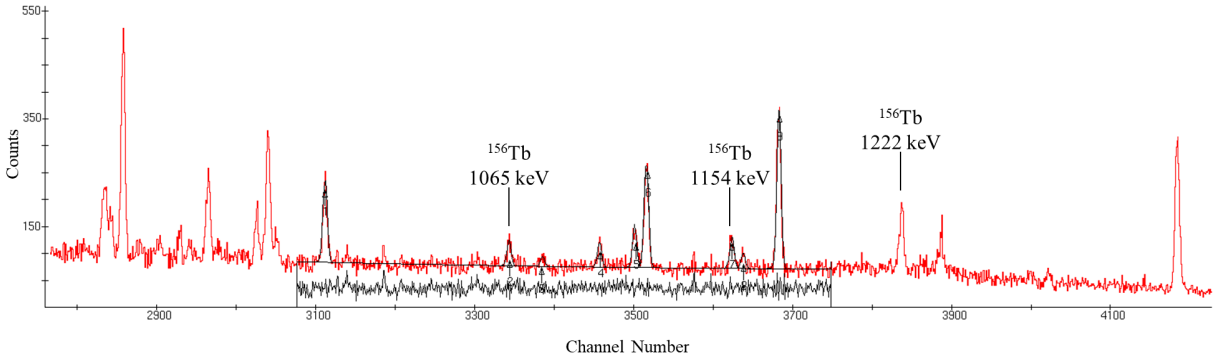

Figure 4.30: Skewed Gaussians fitted in the 1000 keV to 1200 keV range of a foil 9 spectrum taken on day 5. This foil was exposed to α's of lower energy, thus the 1065, 1154, and 1222 keV peaks produced from the decay of ^{156}Tb were visible. The first two peaks were fitted in this energy range but the third was fitted separately as shown in figure 4.31.

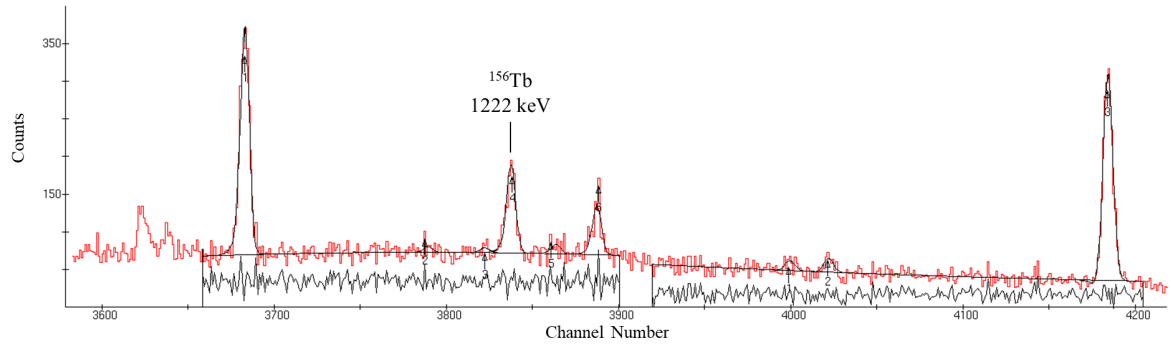

Figure 4.31: Skewed Gaussians fitted in the 1200 keV to 1300 keV range of a foil 9 spectrum taken on day 5. This foil was exposed to α's of lower energy thus the 1222 keV γ peak from the decay of ^{156}Tb was visible and fitted as shown.

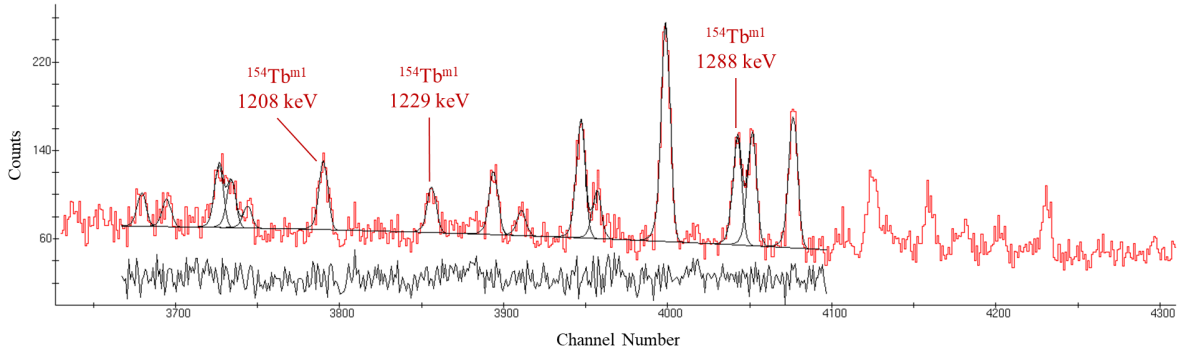

Figure 4.32: Skewed Gaussians fitted in the 1200 keV to 1300 keV range of a foil 1 spectrum taken on day 2. The three ^{154}Tb^{m1} isomer decay peaks above 1200 keV are labelled with their γ energies.

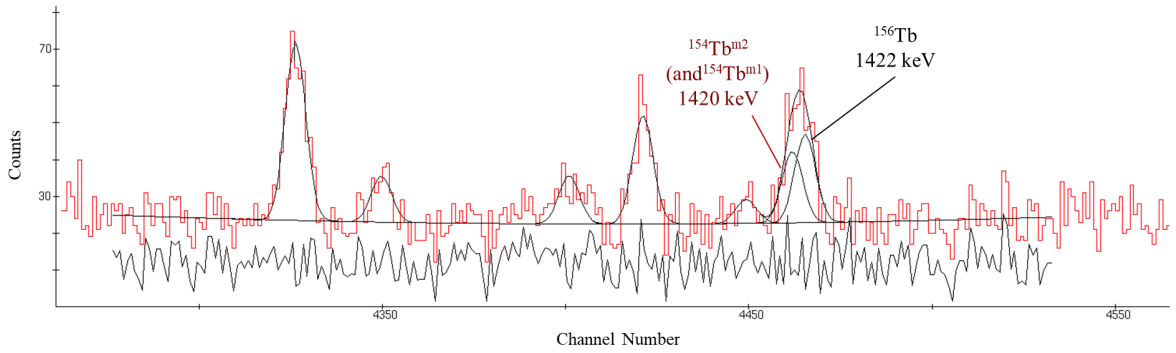

Figure 4.33: Skewed Gaussians fitted in the 1300 keV to 1450 keV range of a foil 9 spectrum taken on day 5. This foil was exposed to α's of lower energy thus the 1422 keV peak of ^{156}Tb decay was visible and fitted as shown. This was difficult to fit, especially when the statistics of the ^{156}Tb were lower. This was because there was a close neighbouring peak at 1420 keV, as labelled. This is the result of the decay of ^{154}Tb^{m2} and ^{154}Tb^{m1}. As these isomers decay, they emit a 1419.81(8) and 1419.4(7) keV γ ray with an intensity of 46% and 0.72%, respectively. In foil 9 the cross-sections for the production of ^{154}Tb isomers are relatively small but this high intensity peak from the ^{154}Tb^{m2} decay can still be seen and is much more prevalent in the lower numbered foils where the foil was exposed to α's of higher energy as demonstrated in figure 4.34.

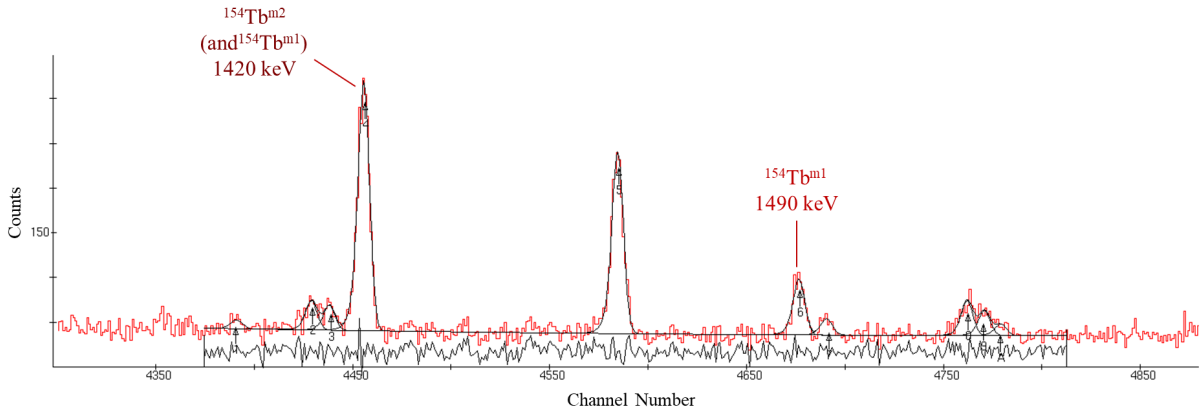

Figure 4.34: Skewed Gaussians fitted in the 1400 keV to 1500 keV range of a foil 1 spectrum taken on day 2. The 1490 keV, ^{154}Tb^{m1} isomer decay peak is labelled along with the 1420 keV produced from the decay of ^{154}Tb^{m2} and ^{154}Tb^{m1}.

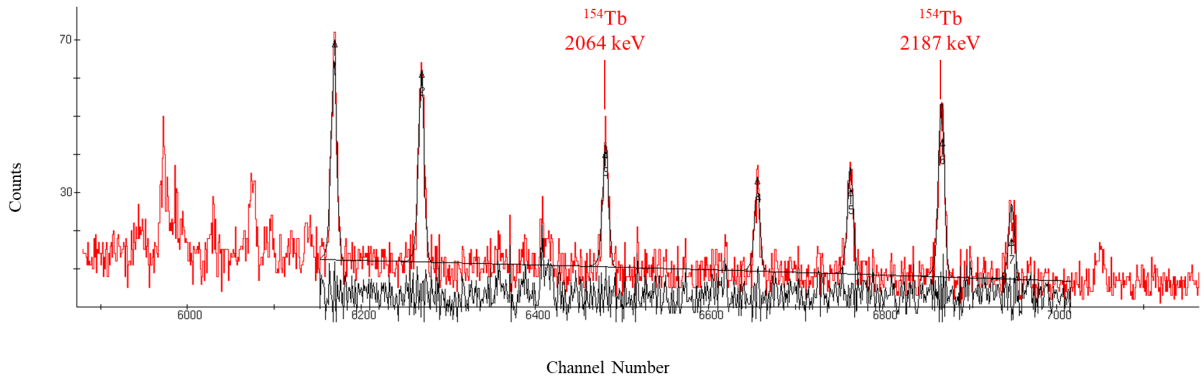

Figure 4.35: Skewed Gaussians fitted in the 2000 keV to 2200 keV range of a foil 5 spectrum taken on day 2. The 2064 and 2187 keV peaks of the ^{154}Tb ground state isotope decay are labelled.

4.7.3 Special case fits

In some spectra the fit of a peak was not appropriate or possible. For example for the spectra collected with the HPC detector while its amplifier settings were 1 μs (instead of 3 μs), the resolution was poorer. Thus, it was not possible to clearly fit Gaussians to the 161 and 163 keV peaks of ^{155}Tb isotope, the 1288 keV peak of the ^{154}Tb^{m1} isomer, or the 647 keV peak of the ^{152}Tb^{m1} isomer. Figures 4.36, 4.37 and 4.38 demonstrate why this was the case. Therefore, these data points are missing from the decay curves used to determine the activity of each isotope and isomer discussed in chapter 5.

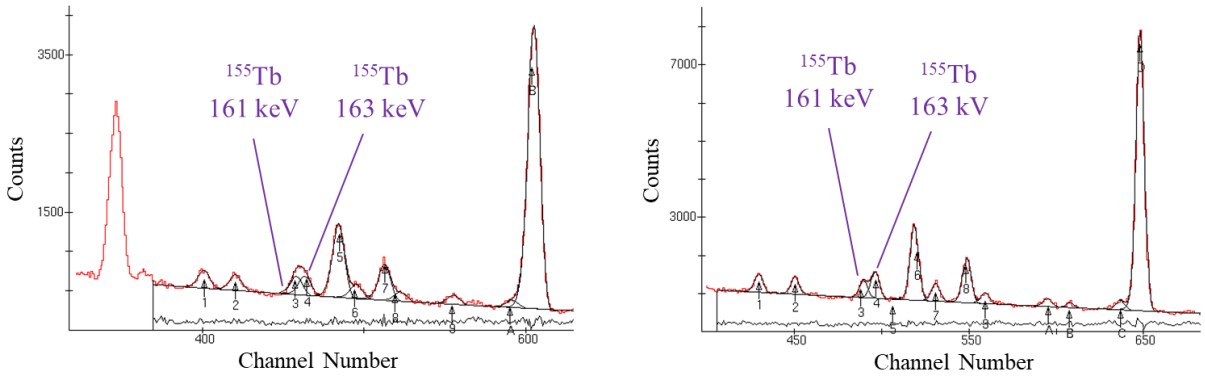

Figure 4.36: Two fitted spectra of the 161 and 163 keV peaks of ^{155}Tb isotope decay, taken using the HPC HPGe detector (a) before and (b) after the amplifier settings were changed from 1 μs to 3 μs. As the resolution improved the distinction between the two peaks became clear enough to fit robustly (i.e. the areas of the peaks had the correct ratios given their intensities).

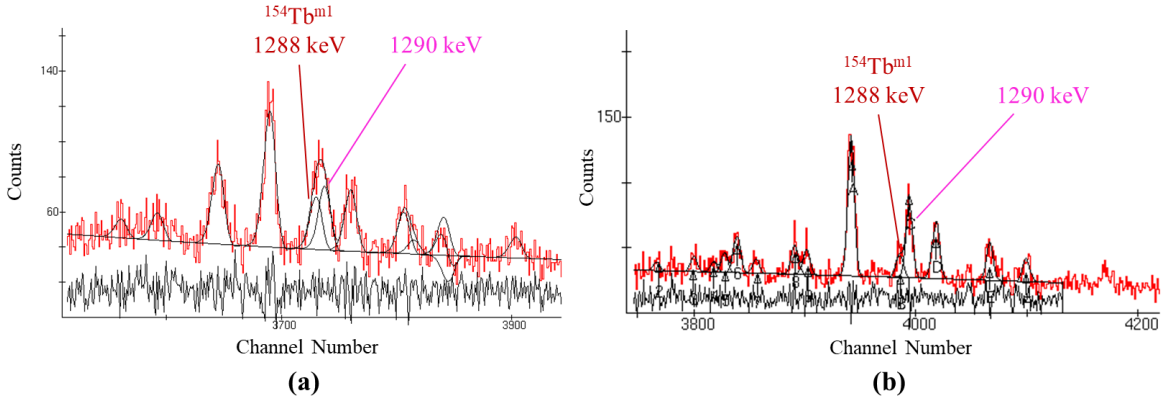

Figure 4.37: Two fitted spectra of the 1288 keV peak of the ^{154}Tb^{m1} isomer decay, taken using the HPC HPGe detector (a) before and (b) after the amplifier settings were changed from 1 μs to 3 μs. There was a peak at 1290 keV which was difficult to separately fit before the resolution was improved.

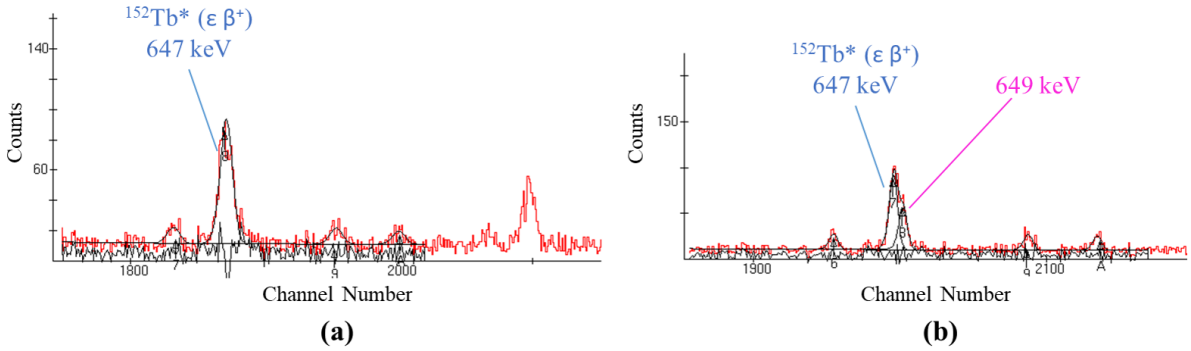

Figure 4.38: Two fitted spectra of the 647 keV peak of the ^{152}Tb^{m1} isomer decay, taken using (a) the HPC HPGe detector before the amplifier settings were changed from 1 μs to 3 μs and (b) using the G11 detector. There was a peak at 649 keV from the decay of ^{154}Tb^{m2} and ^{154}Tb^{m1} isomers which was difficult to separately fit before the resolution was improved on the HPC HPGe detector. Therefore, the 647 keV peak was not used for the half-life and cross-section analysis discussed in chapter 5.

4.8 Count correction

The collection time for each spectrum was comparable to the half-life of the isotopes measured. Therefore, the count rate for the area under the peaks taken from fitting Gaussians to the peaks was not a constant. The decay count correction can be applied to the areas under the γ peaks to find the count rate (in s^{-1}) of each peak at the start of the spectrum, A_c. The count rate at the start of each spectra (A_c) was then corrected for the efficiency of the detector and the geometry of the set-up for each spectrum taken.

4.8.1 Decay count correction

Activity (A) can be expressed in two ways,

$$A = \frac{dC}{dt} \tag{4.18}$$

and

$$A = A_c e^{-\lambda t}, \tag{4.19}$$

where C = counts, t = time and $\lambda = \frac{\ln(2)}{\text{half-life}}$. In this case A_c is the counts per second of the source at the start of the spectrum being collected. Substituting 4.19 into 4.18 gives equation 4.20

$$\frac{dC}{dt} = A_c e^{-\lambda t} \tag{4.20}$$

For the spectral data collected the total number of counts (C) was known for a particular peak and the length for which that spectrum was collected (τ) was also known. Thus, A_c was then found by standard integration between t = 0 and t = τ.

$$\begin{aligned} dC &= A_c \int_0^{\tau} e^{-\lambda t} dt \\ C &= A_c \left[-\frac{e^{-\lambda t}}{\lambda} \right]_0^{\tau} \\ C &= A_c \left[-\frac{e^{-\lambda \tau}}{\lambda} - -\frac{1}{\lambda} \right] \\ C &= A_c \left[\frac{1 - e^{-\lambda \tau}}{\lambda} \right] \end{aligned}$$

$$A_c = \frac{\lambda C}{1 - e^{-\lambda \tau}}. \tag{4.21}$$

Thus, to obtain the count per second of each peak in the spectrum at the start of the data collection (A_c) then equation 4.21 was used where C is the total number of counts under a γ peak. (The error on the A_c calculation is discussed in appendix G).

4.8.2 Efficiency count correction

The corrected counts per second under each γ peak (A_c) were then corrected for the efficiency of the set-up. As described in section 4.4, the geometric set-up of the source and detector as well as the efficiency of the detector and the intensity of the γ peak needed to be accounted for to obtain the activity, A_E, of the isotope at the start of each spectrum that was collected.

Rearranging equation 4.12 and substituting $N/time$ with A_c

$$A_E = \frac{A_c}{\epsilon_i I_\gamma f_A}. \tag{4.22}$$

As explained in section 4.4, the intrinsic efficiency (ϵ_i) for each Tb γ energy peak was calculated. Depending on the distance and physical state of the source (foil sheet or powdered form), the appropriate geometric efficiency correction value (f_A) was taken from the disk source approximation in table 4.1. The intensity of the γ peaks (I_γ) were taken from table 4.2. The error on the calculation of A_E is presented in appendix H.

By the end of these corrections, the activity of each isotope at the start of each spectrum A_E was extracted for each γ energy of interest (see table 4.2) in each spectrum. In order to calculate cross-section for the production of each isotope and isomeric state in each foil then, the activity at the end of α irradiation (A_T) needed to be determined along with accurate knowledge of the half-life of each isotope and isomeric state, and the thickness of the Eu foil. The foil thickness was previously measured and is discussed in section 3.1. The following chapter details the next stage of analysis used to extract new half-life measurements for six out of nine Tb states measured as well as cross-section measurement values calculate from the A_T values extracted from the γ spectra data.

Chapter Five

Cross-section and half-life measurements and results

After the initial stages of analysing the raw γ spectra of the irradiated ^{nat}Eu foils (discussed in chapter 4) the activity (A_E) for each γ peak of the Tb isotopes present at the start of each spectrum were extracted. The total activity of each isotope at the end of α irradiation (A_T) is required for the cross-section measurements of each isotope. In order to obtain values for A_T the next stage of analysis was to plot decay curves for each γ peak.

5.1 Decay curves

As expressed in equation 4.19, the activity of a radioactive isotope, $A = A_0 e^{-\lambda t}$ is dependent on the initial activity (A_0), time (t) and the half-life of the isotope as $\lambda = \frac{\ln(2)}{\text{half-life}}$. For each isotope peak $A_0 = A_T$ and A_E (see equation 4.22) is A. Taking the natural log of the decay equation gives,

$$\ln A_E = \ln A_T + \frac{ln(2)}{\text{half-life}} t. \tag{5.1}$$

A decay curve for each isotope peak in each of the nine foils was produced by plotting $\ln A_E$ against the start time of each spectra since the end of α irradiation of the foil. If no other isotopes or isomers were decaying into the isotope/isomer being plotted in the decay curve, then the plot would form a straight line. Therefore, a straight line was fitted to each set of data using least squares fitting. Referring to equation 5.1, the gradient and intercept of each fit could be used to extract the half-life,

$$\text{half-life} = \frac{ln(2)}{\text{gradient}}, \tag{5.2}$$

and total isotope activity at the end of the α irradiation,

$$A_T = e^{\text{intercept}}, \tag{5.3}$$

respectively. Therefore, the decay curve fits were used to extract the A_T value for each γ energy peak of interest in each foil in addition to measuring the half-life of the isotopes. The A_T values extracted from these decay curves were then used to calculated cross-sections. Moreover, for some of the isotopes, the data were sufficiently good to make new, statistically significant, half-life measurements. In these cases, the half-life measurements were compared to the currently published values that are shown in table 4.2 and are discussed in the relevant isotope section of this chapter. A summary of the new half-life measurements is given in table 6.1 in chapter 6.

For a reliable fit of the decay curves it was important to cut off low statistical data because such data were unreliable as the peaks were more likely to be affected by statistical noise. Moreover, after a length of time there appeared to be a significant jump in relative error on $\ln(A_E)$. For example, the relative errors for foil 1 ^{153}Tb $\ln(A_E)$ data were less than 2% for data taken on day 12 or before. After this time the relative error jumped to 6% or greater. This sudden increase in error was seen in many of the $\ln(A_E)$ data sets and occurred around

the time where the A_c value decreased below 0.1 counts per second. Therefore, for all of the decay curves, spectra data were not included if the peak had an A_c value of less than 0.1 counts per second. However, if this cut-off occurred where the spectra were taken over shorter time periods then subsequent longer collection time spectra data were included if the total counts under the peak was larger than that for the "cut-off" spectrum because the relative errors of these longer spectra were in-keeping with shorter spectra where A_c>0.1 s^{-1}.

5.2 Half-life measurements

For the majority of these Tb isotopes and isomers, the half-lives have not been measured since the 1970's. As part of the analysis with the Tb data collected, the half-lives of these isotopes and isomers were measured using the gradient of the decay curves as explained in equation 5.2. Each foil and γ energy monitored as part of the cross-section analysis produced a separate decay curve. Each decay curve provided a separate half-life measurement. Therefore, for many of the isotopes and isomers, multiple repeat measurements of their half-lives were made. The error of each half-life measurement was calculated from the error on the gradient of the fit and by using standard error propagation of equation 5.2. For the isotopes where a new half-life measurement was possible, a weighted average of each half-life measurement was taken to obtain a final value for the half-life of each isotope.

5.3 Cross-section measurements

Accurately knowing the half-life and initial activity of the isotope at the end of irradiation (A_T) is crucial for accurately determining the cross-section of interaction. As explained in section 3.4 the beam current was not constant throughout irradiation. Therefore, equation

5.4 (previously stated in equation 3.8 but repeated here for convenience) was used to determine the cross-section. The factor Y (see equation 3.7) depended on the beam current and the half-life of the isotope (or isomer) being produced. If new measured half-life values were produced in the decay curve analysis then these were used to calculate Y for each isotope. Otherwise, the previously established NNDC and IAEA half-life values or the were used instead.

The foil thickness (21.3±0.5 μm) was used to calculate N_{target} according to equation 2.4. Then Y and N_{target} were used to calculate the cross-section,

$$\sigma = \frac{A_T}{Y \cdot N_{target}}, \tag{5.4}$$

for each γ energy in each foil. The separate γ energy measurements of A_T within the same foil effectively acted as repeat readings of A_T. Therefore, repeat measurements of cross-sections for a particular foil (or α energy range) were achieved. For each foil a weighted average was taken of the cross-section measurements calculated from the separate γ energies and a weighted error was also calculated from each cross-section measurement for each foil.

The final cross-section measurements for each Tb isotope and isomeric state are given in tables 5.2 to 5.10 in section 5.5. The α energy range and average α energy of each foil is also given in these tables. Refer back to section 3.3 (table 3.7) for the discussion and calculation of these foil α energies.

5.4 Intrinsic efficiency correction

However, before the A_T and half-life values could be extracted from the decay curve plots, a systematic error within the data was identified and was corrected. This systematic error was

connected to the efficiency correction. Figure 5.1 shows an example decay curve of the 105 keV γ energy of the ^{155}Tb isotope before (a) and after (b) the extra correction was applied. Before the extra (intrinsic) efficiency correction was applied (figure 5.1(a)), there was a discontinuous drop in the $\ln A_E$ values with respect to time after the first four points in the data. This discontinuity was present at the same point for all energy peaks and isotopes. The point of discontinuity occurred a the time where the foil-detector separation was reduced. The foils were originally 13.5 or 15 cm from the HPC or G11 detector, respectively. However, the unplanned reduction in beam current and irradiation time profoundly affected the total activity of the foils. Therefore, after the first four measurements were taken, the foils were brought closer to the detector, between 4.45 and 5.3 cm, to increase the statistics of the spectra. It was originally assumed that the geometric efficiency correction discussed in section 4.4.2 would account for the efficiency change that would occur as foil-detector separation changed, but this was proven not to be the case. The following will discuss why this is the case and how the data were corrected to produce decay curves like that shown in figure 5.1(b).

When the source is closer to the face of the detector there is a larger range of angles for which an emitted γ ray can strike the surface and travel through some of the detector crystal. The change in incident angle will affect how much of the crystal is exposed to the γ ray and will therefore affect the efficiency of producing a photo-peak contributing interaction (i.e. affecting the intrinsic efficiency of the interaction). In short, for larger source-detector distances, the γ rays that strike the detector face are travelling "more parallel" to the detector axis than those emitted from a source placed closer to the detector, and, therefore, have a longer path length in the crystal and thus a higher interaction possibility which leads to a higher intrinsic efficiency than a simple solid angle correction would predict. The energy of the photon may also contribute to the changes of intrinsic efficiency with distance, due to the different path lengths, [63]. However, this work focused on γ energies greater than 100 keV

and a strong energy dependence was not observed in these data. The intrinsic efficiency correction used was found to work well, as detailed below.

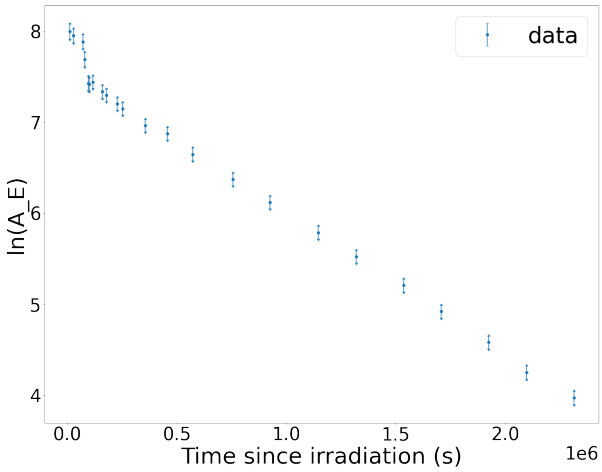

(a) Before extra intrinsic efficiency correction.

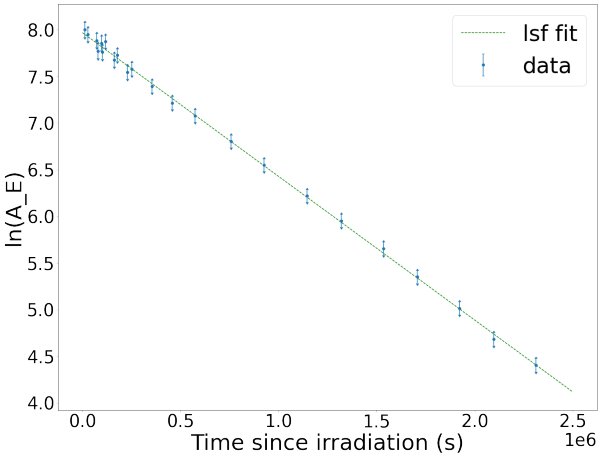

(b) After extra intrinsic efficiency correction.

Figure 5.1: Both (a) and (b) are decay curves of Foil 9 produced using the data from the 105 keV γ energy emitted by the decay of the ^{155}Tb isotope. Before the correction is applied (a) there is a clear discontinuity after the first four data points. The first three were when the foil was 15 cm from the detector face and, for point four, the foil was 13.5 cm from the detector. For all subsequent data points the foil was placed between 4.45 and 5.3 cm from the detector. After the extra intrinsic efficiency correction is applied (b) there is no discontinuity.

To determine the angle and energy dependence of intrinsic efficiency, the ^{152}Eu calibration source was placed at all of the distances given in table 4.1 (these were the same distances used when collecting the irradiated ^{nat}Eu foil spectra). A ^{152}Eu spectrum was collected for an hour at each of these distances and intrinsic efficiency was calculated for the main γ peaks in the spectrum using equation 4.12. A comparison ratio was made between the intrinsic efficiency measured for a source at each distance (d_x) to the intrinsic efficiency measured when the source was 15 cm from the detector face, such that

$$\text{ratio} = \frac{\text{Intrinsic efficiency for } \gamma_G \text{ at distance } d_x \text{ from the detector}}{\text{Intrinsic efficiency for } \gamma_G \text{ at 15 cm from the detector}}. \tag{5.5}$$

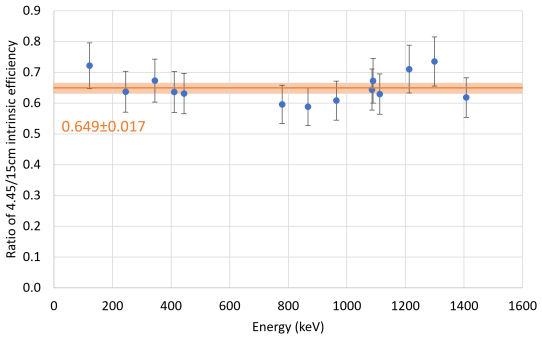

(a) 4.45 cm

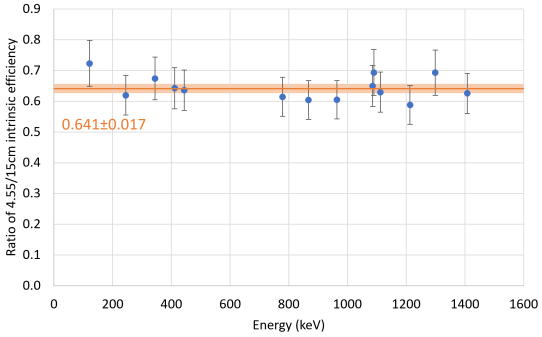

(b) 4.55 cm

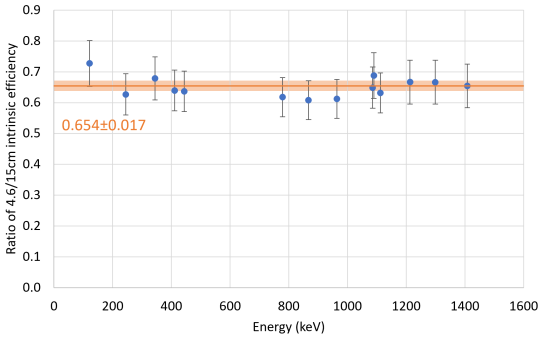

(c) 4.6 cm

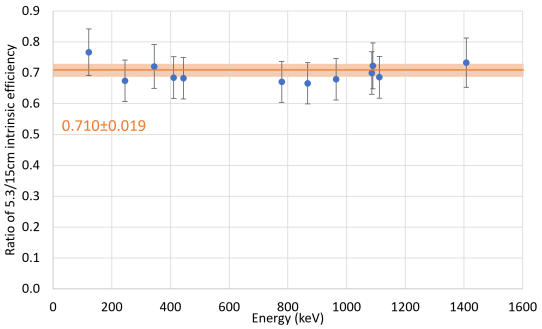

(d) 5.3 cm

Figure 5.2: Intrinsic efficiency ratio with respect to γ energy for four source distances. The ratio data points were calculated using equation 5.5. There was no significant trend with respect to γ energy, therefore a weighted average of the ratio points in each graph was taken and this can be seen by the orange line. The pale orange band represents the calculated weighted error for the weighted average ratio.

The ratios were calculated for each main γ energy in the ^{152}Eu spectra and figure 5.2 displays four example graphs of the calculated intrinsic efficiency ratios of each γ energy for four closer distances.

For each distance, there was no significant trend with respect to γ energy, therefore, a weighted average of the ratio points across all the γ energy peaks for each distance was taken and these are shown by the orange line in each graph in figure 5.2. The pale orange band represents the calculated weighted error for the weighted average ratio for each distance.

Figure 5.3 displays the weighted ratios for each distance. As expected (according to Ref [64]), the intrinsic efficiency is poorest when the source distance is comparable to the diameter of the detector (4.54-4.93 cm).

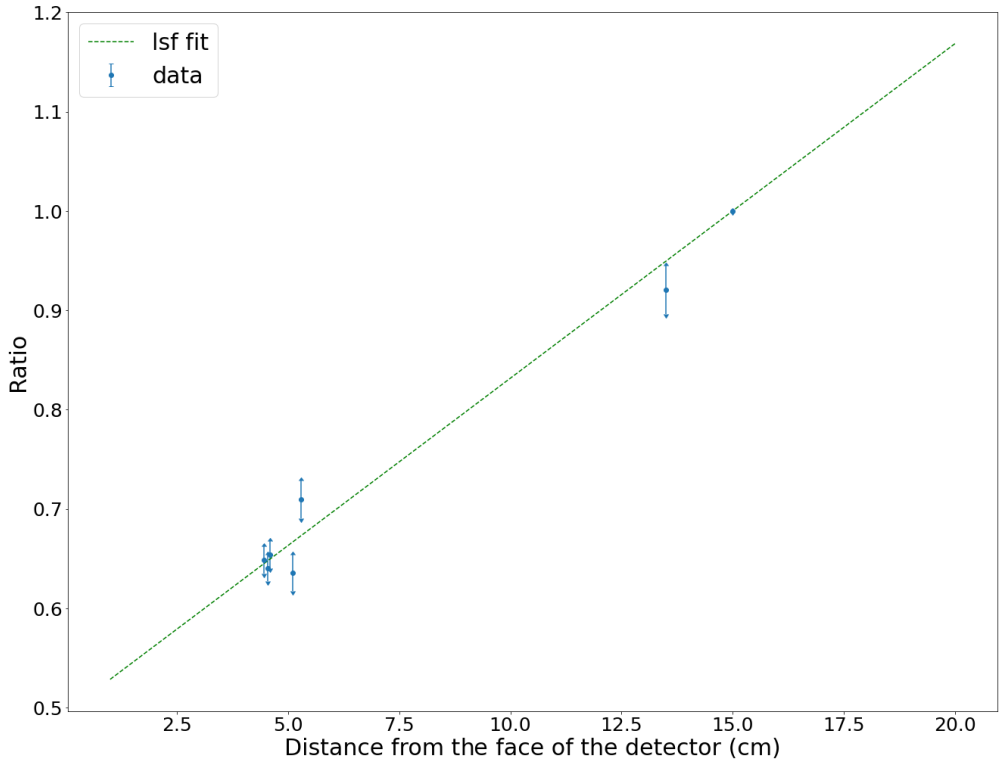

Figure 5.3: Weighted averaged intrinsic efficiency ratios (compared to a ^{152}Eu source at 15 cm from the faces of the detector) as a function of distance from the face of the detector. The LSF linear fit (dotted green line) acts only as a guide for the eye. The ratio to distance relationship is non-linear as discussed in Refs [63, 64],

The ratio data points for distances 4.45, 4.55 and 4.6 cm were all within error of each other and very close in value, therefore to simplify the correction process a weighted average of their ratios was taken to produce a correction ratio of 0.65±0.01. This correction ratio was use to correct the original A_E values for the 4.45, 4.55 and 4.6 cm foil spectra data. The correction ratios for each distance from the face of the detector are given in table 5.1. The original A_E values were corrected by

$$A_E(\text{corrected}) = \frac{A_E(\text{original})}{\text{correction ratio}}, \tag{5.6}$$

Table 5.1: The weighted average intrinsic efficiency correction ratio with respect to the intrinsic efficiency measured at 15 cm from the HPGe detector face.

Distance from HPGe detector face (cm)	Weighted average correction ratio	Weighted error on correction ration
13.5	0.92	0.02
5.3	0.71	0.02
5.1	0.64	0.02
4.45, 4.55 or 4.60	0.65	0.01

and standard error propagation methods were used to calculated the error on A_E(corrected), incorporating the error from the correction ratio.

Having corrected for the change in intrinsic efficiency with distance, the decay curves were then plotted and the gradient and intercept values extracted for half-life and cross-section analysis. Section 5.5 discusses the nuances of the analysis of each isotope half-life and cross-section result extracted from the decay curves.

5.5 Decay curve, half-life and cross-section analysis and results for each isotope

5.5.1 Terbium - 151

The cross-sections calculated using TALYS (see figure 2.3) would suggest that both the ground state and excited isomer state of ^{151}Tb are formed in $\alpha+^{nat}$Eu reactions. However, as discussed in section 4.5, the excited state decays with a half-life of only 25 seconds which was too short to be observed in any of the γ spectra collected. Therefore, only the ground state of ^{151}Tb was present in the nine irradiated foils during spectra collection. This meant that the half-life of the γ peaks measured from the decay of ^{151}Tb would only depend on the half-life of the ground state. Moreover the total activity of ^{151}Tb produced (A_T)

would effectively be the sum of the production by direct reaction and indirect (through the decay of the excited state) reaction. Because no independent information was known about the production of the ^{151}Tb^{m1} then these two ground state production paths could not be separated. Therefore, the cross-section measurement for ^{151}Tb detailed below is an effective cross-section which includes 100% of the direct reaction and 93.4% (the branching ratio of IT) of the cross-section for ^{151}Tb^{m1}.

As previously mentioned in table 4.2, two γ energies were used to study the decay of the ^{151}Tb isotope, the 252 and 287 keV peaks with I_γ values of 26.3% and 28.3%, respectively. The presence of ^{151}Tb γ peaks only occurred in the first two foils. Therefore, only four decay curves were plotted. The γ peak area statistics in the spectra used to produce the decay curves were relatively poor especially in foil 2, thus, measuring the half-life of the decay from these four decay curves was unreliable. Therefore, the NNDC half-life value (see table 4.2) was used to constrain the half-life of the decay curve fits. The gradient of the fits were allowed to vary within the quoted NNDC half-life error. An example of a decay curve produced by the 287 keV data from foil 1 is shown in figure 5.4.

The intercept values were then used in equation 5.3 to extract the A_T values for the four decay curves. Equation 5.4 was subsequently implemented (with Y calculated using the NNDC half-life value for ^{151}Tb) to obtain four cross-section measurements; two for foil 1 and two for foil 2. For each foil a weight average of the two cross-section values were taken and the final cross-section results are given in table 5.2.

Table 5.2: Cross-section values for the production of ^{151}Tb from α+^{nat}Eu reactions measured in two irradiated ^{nat}Eu foils. The α beam energy range of each foil is also given.

^{nat}Eu Foil	Lowest energy at the back of foil (MeV)	Average foil energy (MeV)	Highest energy at the front of foil (MeV)	Cross-section (mb)
1	37.62	38.34	39.04	18(1)
2	36.06	36.86	37.64	5(1)

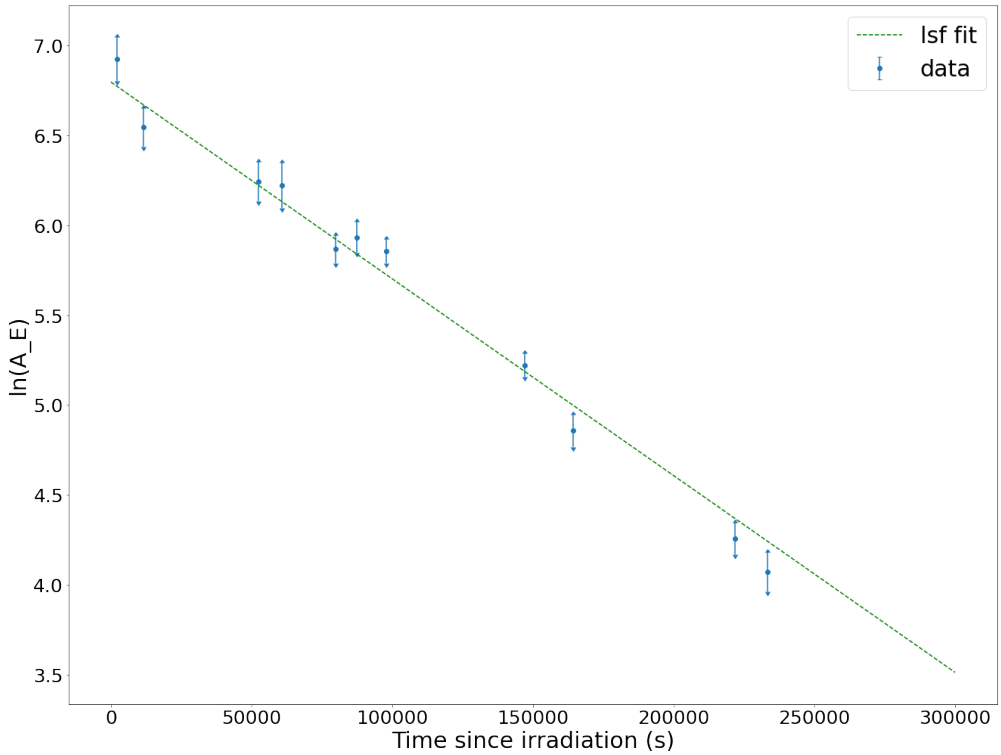

Figure 5.4: A decay curve produced using the data from the 287 keV γ energy emitted by the ^{151}Tb isotope in foil 1. The gradient of the LSF was constrained by the previously known half-life value 17.609±0.014 hours. The χ^2/ndf of the fit was 1.7.

5.5.2 Terbium 152 excited state

The excited state of ^{152}Tb (^{152}Tb^{m1}) was previously measured to decay with a half-life of 4.2±0.1 minutes [65]. Due to this state decaying much faster than the other isomers and isotopes measured in this study, the γ spectra collection process for ^{152}Tb^{m1} was limited to the first four foils in the nine foil stack (as explained in section 4.6). Only six 1 minute spectra were collected within the fist nine half-lives of the isomer from foils 2, 3, and 4. However, 20 consecutive, one minute spectra were collected of foil 1 within the first eight half-lives of the isomer. The spectra from foil 1 provided excellent quality data for the construction of decay curves, an example of which, for the 283 keV γ, is shown in figure 5.5. In each of the four foils, seven γ energy peaks produced from the decay of ^{152}Tb^{m1} were measured across

all 38 spectra to produce the decay curves. These peak energies were 160 keV (16.6%), 235 keV (4.2%), 277 keV (8.5%), 283 keV (59.8%), 386 keV (3.27%), 472 keV (11.8%) and 1167 keV (3.7%). Note that the 647 keV γ emission was also monitored, however, as explained in section 4.7.3, this peak overlapped with γ emissions from the $^{154}Tb^{m2}$ and $^{154}Tb^{m1}$ isomers. Therefore, the 647 keV data were not used.

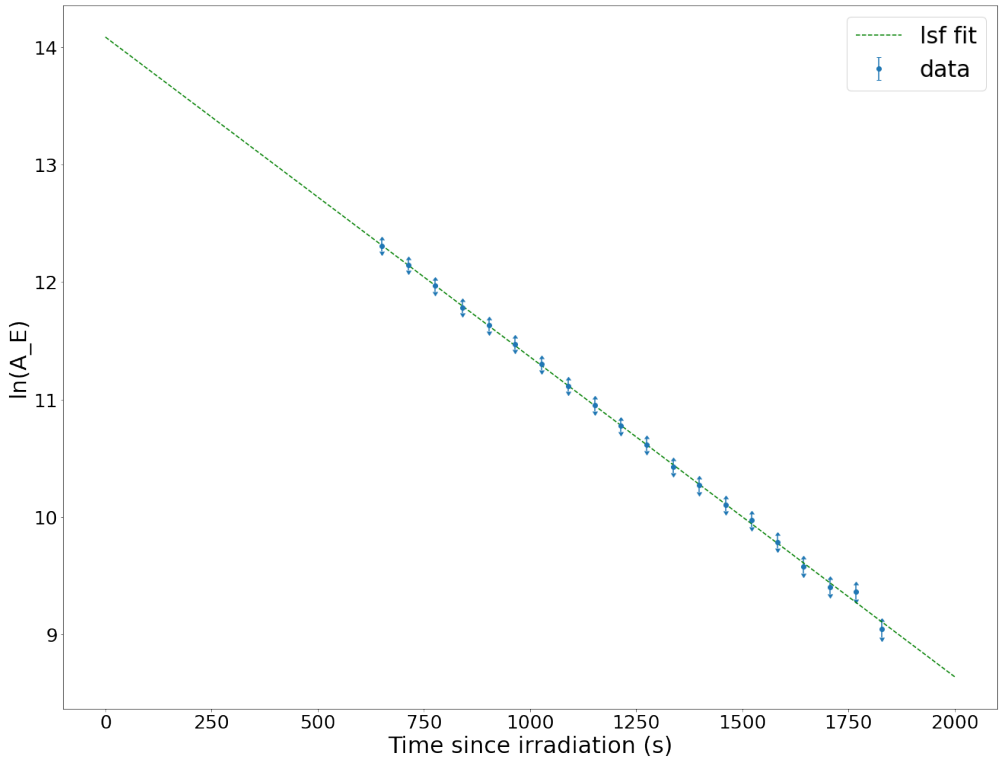

Figure 5.5: Foil 1 decay curve produced using the data from the 283 keV γ energy emitted by the decay of the $^{152}Tb^{m1}$ isomer in foil1. The χ^2/ndf of the fit was 0.2.

A weighted average of the 7 half-lives extracted from the gradient of the 7 decay curves of foil 1 was calculated to obtain a new half-life measurement of 4.22±0.02 minutes. This measurement agrees with the previously determined value but improves upon the precision of the measurement. The newly determined value was used to constrain the gradient of the decay curve fits of foils 2, 3 and 4 as there were very few (3 to 6) points in these data sets. Figure 5.6 displays a couple of example decay curves for foils 2 and 4 where the gradient was constrained within the errors of the newly measured half-life. In both of these graphs the

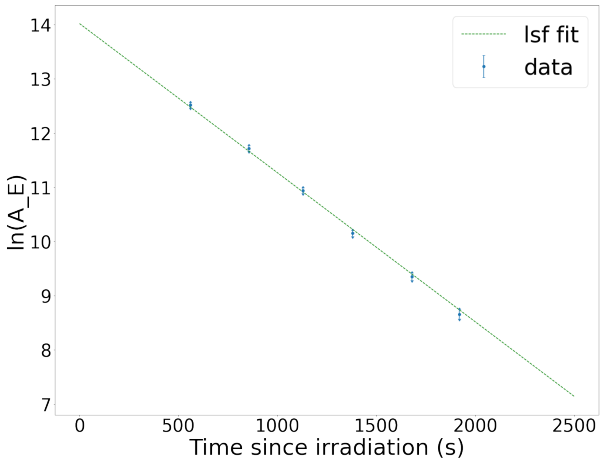

(a) Foil 2, 283 keV. The χ^2/ndf of the fit was 1.3.

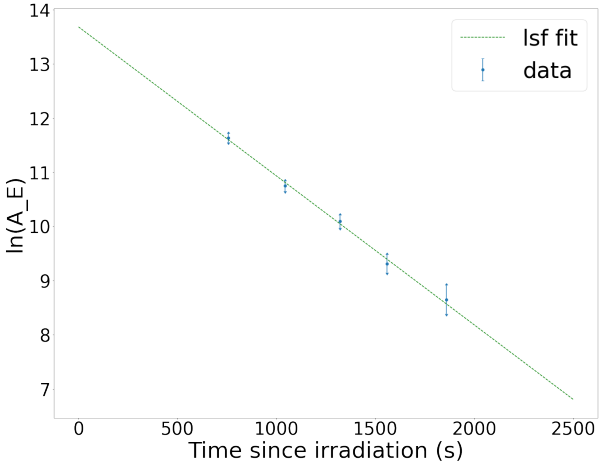

(b) Foil 4, 472 keV. The χ^2/ndf of the fit was 0.4.

Figure 5.6: Decay curves of the ^{152}Tb^{m1} isomer where the gradient of the linear LSF was constrained by the newly measured half-life of 4.22±0.02 minutes.

points aligned well with the gradient and this was true for all the other ^{152}Tb^{m1} γ energy and foil decay curves.

Table 5.3: Cross-section values for the production of ^{152}Tb^{m1} from α+^{nat}Eu reactions measured in four irradiated ^{nat}Eu foils. The α beam energy range of each foil is also given.

^{nat}Eu Foil	Lowest energy at the back of foil (MeV)	Average foil energy (MeV)	Highest energy at the front of foil (MeV)	Cross-section (mb)
1	37.62	38.34	39.04	342(7)
2	36.06	36.86	37.64	328(10)
3	34.46	35.35	36.19	282(9)
4	32.81	33.77	34.71	212(13)

The intercept value of each of decay curve was used in equation 5.3 to extract the A_T values. Equation 5.4 was then implemented (with Y calculated using the newly measured half-life value for ^{152}Tb^{m1}, 4.22±0.02 minutes) to obtain seven cross-section measurements for each of the four foils. A weighted average was taken of the seven cross-section measurements calculated for each foil to provide the final cross-section results. These are provided in table 5.3.

5.5.3 Terbium - 152

Four γ energies were used to study the decay of the ^{152}Tb isotope from the ground state, these were 271, 586, 764 and 778 keV peaks with I_γ values of 9.53%, 9.21%, 2.74% and 5.54%, respectively. The data for the 586 keV peak taken using the HPC HPGe detector when the shaping time was 1 μs (and thus the resolution was poorer) were excluded from the decay curves. This was because of the presence of a background peak with a slightly lower energy which was indistinguishable from the 586 keV peak in these specific spectra.

The ^{152}Tb γ peaks are visible in the first seven irradiated ^{nat}Eu foils and the statistics of these peaks were sufficient to produce 28 decay curves. An example decay curve produced by the 271 keV data from foil 1 is shown in figure 5.7. As mentioned in section 4.5, 78.9% of the time the ^{152}Tb^{m1} isomer state decays by internal conversion to the ground state. Therefore, the decay curve of the ^{152}Tb ground state would not be expected to be linear in time. However, the spectra data collection for the ^{152}Tb ground state did not occur until after at least nine half-lives of the isomer state had passed. Therefore, over 99.8% of the isomer state had already decayed before the ^{152}Tb ground state spectra data collection began. The impact of this was that, for all the ^{152}Tb ground state data collected, the decay of ground state was no longer dependent on the decay of the isomeric state and solely depended on its own decay. This is why a linear fit was applied to the ^{152}Tb ground state decay curves and meant that the half-life of the ground state could be accurately extracted from these plots.

The current published value for the ^{152}Tb half-life is 17.5$\pm$0.1 hours as extracted from the A=152 Nuclear Data Sheets [56]. This value is a weighted average of two experiments, however, the final value was the same as that obtained in 1967 (see Ref. [66]). In this 1967 study, the 344 keV γ transition was used to measure (with a Ge(Li) detector) the half-life in addition to using a β counter. Now, more than 50 years on, more modern, higher-resolution germanium detectors are available and were used to collect the spectra

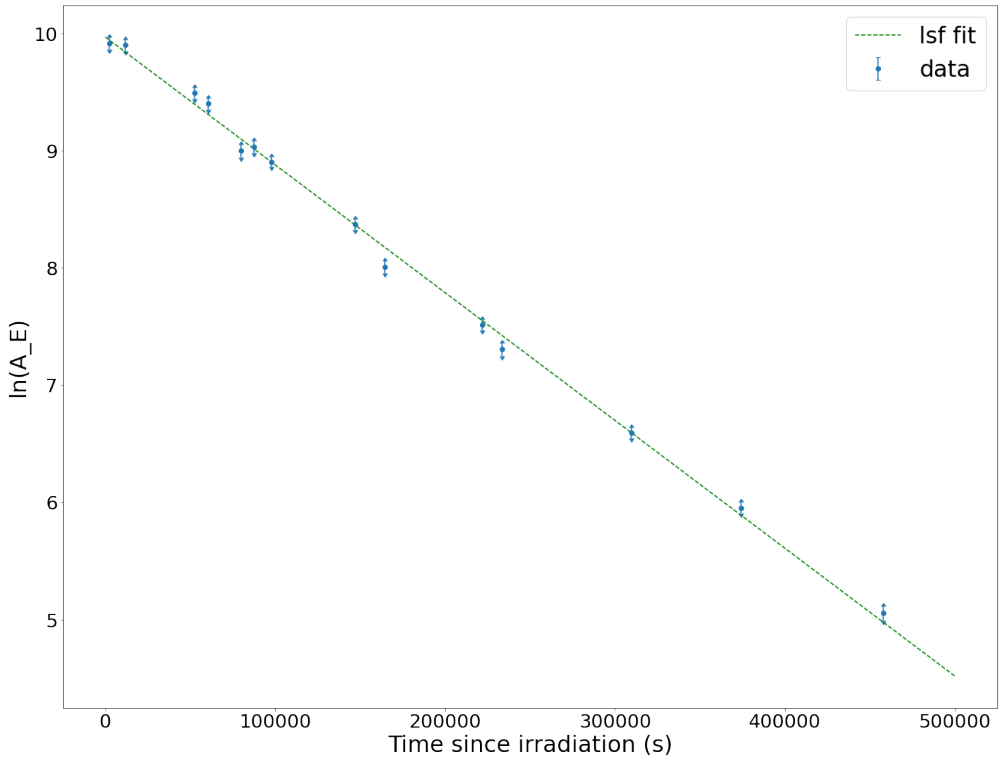

Figure 5.7: Foil 1 decay curve produced using the data from the 271 keV γ energy emitted by the ^{152}Tb isotope as it decayed. The χ^2/ndf of the fit was 2.7.

that produced the 28 independent decay curves of the ^{152}Tb ground state. Therefore, 28 independent measurements of the ^{152}Tb half-life were obtained from the gradient of the decay curves. A weighted average of these provided a new half-life measurement of 17.07±0.07 hours.

The ^{152}Tb ground state data presented in the decay curves was effectively the accumulation of the direct production and 78.9% of the ^{152}Tb^{m1} isomer production from the α+^{nat}Eu foil irradiation process. The ground state is a Tb isotope of medical interest and thus knowledge of the total production of the ground state is key for furthering this production method for medical use, and so it was not essential to measure the cross-section for solely the direct production of the ground state. For medical production, it is important to know the total production likelihood of a reaction with energy, thus extracting the cross-section for the

Table 5.4: Cross-section values for the total production of ^{152}Tb ground state from direct and indirect α+^{nat}Eu reactions. These cross-sections were measured in seven irradiated ^{nat}Eu foils. The α beam energy range of each foil is also given.

^{nat}Eu Foil	Lowest energy at the back of foil (MeV)	Average foil energy (MeV)	Highest energy at the front of foil (MeV)	Cross-section (mb)
1	37.62	38.34	39.04	409(9)
2	36.06	36.86	37.64	397(9)
3	34.46	35.35	36.19	355(8)
4	32.81	33.77	34.71	286(7)
5	31.08	32.16	33.18	201(5)
6	29.30	30.47	31.59	101(3)
7	27.45	28.72	29.97	25(1)

direct reaction accumulated with the indirect reaction was the main focus of this work. Therefore, the intercept values of each of the 28 decay curves were used in equation 5.3 to extract the effective A_T values for γ energies for the total production of the ground state in the 7 foils.

Equation 5.4 was then implemented (with Y calculated using the newly measured half-life value for ^{152}Tb, 17.07±0.07 hours) to obtain four cross-section measurements for each of the seven foils, and a weighted average of these four results yielded a final cross-section for each foil α energy range. The final results are given in table 5.4.

5.5.4 Terbium - 153

There were three γ energies (82, 110, and 212 keV) emitted by the ^{153}Tb isotope that were monitored for a total 20 days in each of the nine foils. Figure 5.8 shows an example of a ^{153}Tb isotope decay curve produced using the A_E data from the 212 keV γ ray. The 212 keV γ energy was emitted with an intensity of 28.5%. The very clear and high statistics peak meant data were collected for 6-8 half-lives, for which the literature value is 2.34±0.01 days [60]. The lower intensity peaks at 82 and 110 keV (5.4% and 6.4%, respectively) provided

usable data for 4-6 half-lives of the ^{153}Tb isotope. Unfortunately, while producing the decay curves for the 82 keV peak, it was found that this energy region was impacted by scattered lead X-rays. It was impossible to subtract the effect of this from the 82 keV peak area data and it subsequently affected the decay curve of this energy. Therefore, the data from the 82 keV peak were not included in the subsequent half-life and cross-section measurements.

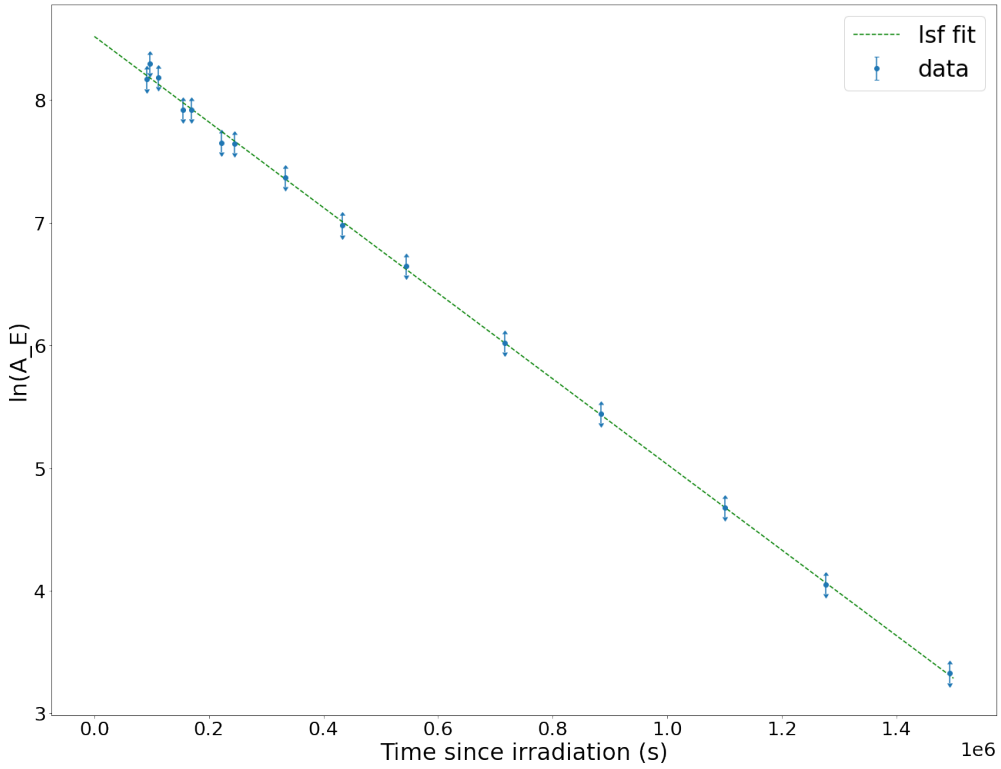

Figure 5.8: Foil 7 decay curve produced using the data from the 212 keV γ energy emitted by the ^{153}Tb isotope. The χ^2/ndf of the fit was 0.6.

The current published value for the ^{153}Tb half-life is 2.34±0.01 days as extracted from the A=153 Nuclear Data Sheets [60]. This value was 92% weighted on the measurement published in 1970 [67]. In Ref [67] the ^{153}Tb half-life was measured using the 212 keV γ peak and an unspecified Gd K X-ray for at least three half-lives. The γ ray was measured using a Ge(Li) detector and the X-ray with a 2-mm-thick NaI(Tl) detector. There were five determinations of the half-life for which a weighted average and error was calculated to obtain the final measurement.

Table 5.5: Cross-section values for the production of ^{153}Tb from α+^{nat}Eu reactions measured in nine irradiated ^{nat}Eu foils. The α beam energy range of each foil is also given.

^{nat}Eu Foil	Lowest energy at the back of foil (MeV)	Average foil energy (MeV)	Highest energy at the front of foil (MeV)	Cross-section (mb)
1	37.62	38.34	39.04	141(4)
2	36.06	36.86	37.64	124(3)
3	34.46	35.35	36.19	150(3)
4	32.81	33.77	34.71	215(5)
5	31.08	32.16	33.18	316(7)
6	29.30	30.47	31.59	395(9)
7	27.45	28.72	29.97	461(10)
8	25.48	26.90	28.25	440(10)
9	23.40	25.00	26.46	383(8)

The ^{153}Tb decay-curves produced from the α+^{nat}Eu reaction in the nine foils spanned a time range of four to eight half-lives. There were two γ energies monitored (110 and 212 keV) and there were nine foils that were separately measured. Therefore, a total of 18 decay curves were produced and thus a total of 18 half-life measurements were made. The weighted average of these 18 values produced a ^{153}Tb half-life of 2.291±0.006 days. This half-life measurement is shorter than the current value, however, it was measured using higher resolution germanium detector and multi channel analysers set-up where the FWHM of a 650 keV was 1.5 keV instead of 40 keV [67]. This improvement in resolution would ensure no other γ energies present near the selected peak were included in the measurement of the peak. Moreover, this new measurement was produced by averaging over more repeat measurements (18 instead of 10). All of these factors combines to enable the improvement in the precision of the ^{153}Tb half-life measurement. Therefore, this new value for half-life was subsequently used for the remainder of the cross-section analysis.

The intercept values for each of the 18 decay curves were used in equation 5.3 to extract the A_T values. Equation 5.4 was then implemented (with Y calculated using the newly measured half-life value for ^{153}Tb , 2.291±0.006 days) to obtain two cross-section measurements for

each of the nine foils. A weighted average was taken of the two cross-section measurements calculated for each foil to provide the final cross-section results. These are provided in table 5.5.

5.5.5 Terbium - 154

The isotope ^{154}Tb exists and was produced in a ground state and two excited, isomeric states. Numerous studies of this isotope and its isomers have been made and are cited in the NDS for A=154 [58]. Using a previous 1973 study [68] as an example, the half-life of the three states were monitored through the emission of the 2064 and 2187 keV γ from the decay of the ground state; the first excited state was measured through the 540 keV emission; and the second excited state with the 226 keV γ emission. Thus these γ energies were selected for this new measurement and additional γ energies (see table 4.2) were also monitored. The analysis and results for each of the three states of ^{154}Tb are detailed in the following subsections.

Terbium - 154m2

In addition to the 226 keV (27(3)%) γ emission previously used to measure the decay of ^{154}Tb^{m2}, the γ energies 427 keV (17.3(12)%) and 1061 keV (4.1(7)%) were also monitored. Decay curves for these three energy peaks were produced for the first seven foils in which the isomer was present. Figure 5.9 shows an example decay curve plot for each energy where a straight-line fit was applied to the data. Although the number of data points for the 1061 keV peak decay curves were limited, all three energies appear to display linear decay curve behaviour.

The average half-lives from the three energies varied and the weighted averages for each γ are

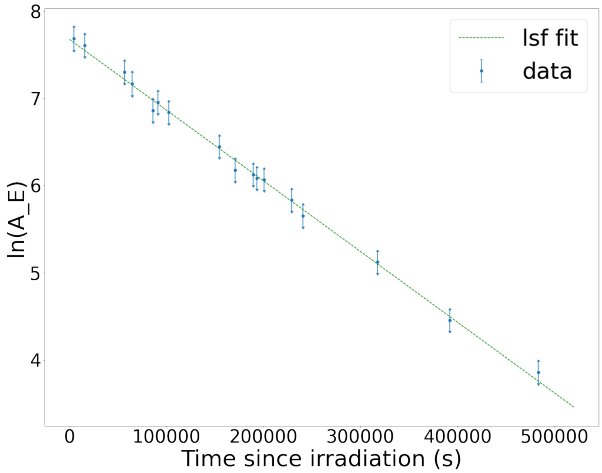

(a) **Foil 3 decay curve from the 226 keV γ emission. The χ^2/ndf of the fit was 0.3.**

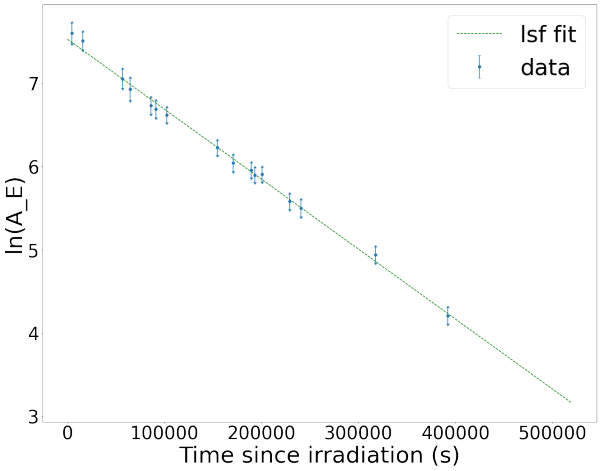

(b) **Foil 3 decay curve from the 427 keV γ emission. The χ^2/ndf of the fit was 0.4.**

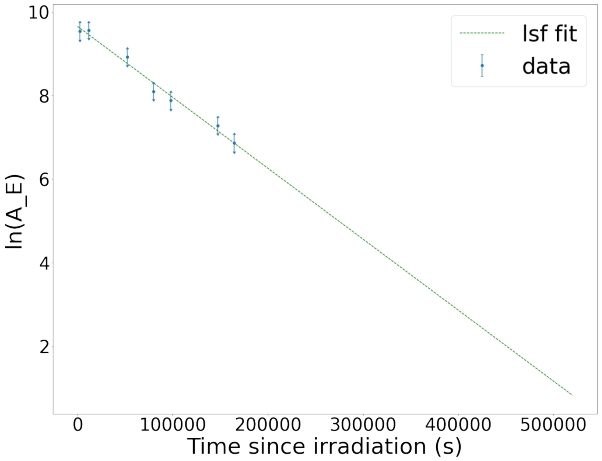

(c) **Foil 1 decay curve from the 1061 keV γ emission. The χ^2/ndf of the fit was 0.6.**

Figure 5.9: Decay curves produced from three different γ energies emitted by the ^{154}Tb^{m2} isomer state as it decays.

given and discussed here. The 226 keV produced a half-life of 24.0±0.2 hours; the 427 keV produced a half-life of 22.9±0.2 hours; and the 1061 keV produced a half-life of 11.4±0.3 hours. The published NDS half-life value [58] for the decay of ^{154}Tb^{m2} is 22.7±0.5 hours. The half-life of the decay curves produced by the 1061 keV peak data was significantly lower than this. After further investigation is was found that the ^{154}Tb^{m1} state with a half-life of 9.4 hours [58] also emitted a 1061 keV peak with an intensity of 0.14(3)%. This was initially dismissed because of the low emission intensity by ^{154}Tb^{m1} as it decays and low predicted TALYS cross-section for the production of the ^{154}Tb^{m1} isomeric state. However, during the analysis it was found that the ^{154}Tb^{m1} state was produced with 20 times the activity of the ^{154}Tb^{m2} level. Therefore, the statistics within the 1061 keV peak were significantly influenced by the half-life of the ^{154}Tb^{m1} state. Due to this additional contribution, the data from the 1061 keV peak were excluded from the half-life and cross-section results for the ^{154}Tb^{m2} state.

The half-lives produced from the 226 and 427 keV peaks agree with each other at the level of 3.8 standard deviations. They are both also within error of the published values [69, 68] used in a weighted average to obtain the NDS value of 22.7±0.5 hours [58]. A weighted average half-life from the 226 and 427 keV decay curve data collected from the α+^{nat}Eu reactions gives a value of 23.58±0.15 hours. This new half-life measurement is 1.7 standard deviations from the NDS half-life value.

To determine the cross-section measurements for the production of ^{154}Tb^{m2} in the seven foils, the intercept values for each of the seven 226 and 427 keV decay curves were used in equation 5.3 to extract the A_T values. Equation 5.4 was then implemented (with Y calculated using the newly measured half-life value of 23.58±0.15 hours) to obtain two cross-section measurements for each of the seven foils. A plot of these cross-section results as a function of α energy is shown in figure 5.10. This figure shows a distinct (more than one standard deviation) separation between four (out of the seven) cross-section results produced

by the two γ energies. Compared to the other Tb isotope and isomeric state cross-section data where the cross-sections calculated by different γ energies are within errors of each other, this greater variation between the two $^{154}Tb^{m2}$ cross-section measurements may have been due to the relatively low original activity of $^{154}Tb^{m2}$. Future experiments would be needed to verify the results given here, where a greater activity of $^{154}Tb^{m2}$ is produced. This would improve the statistics and thus reliability of the final results.

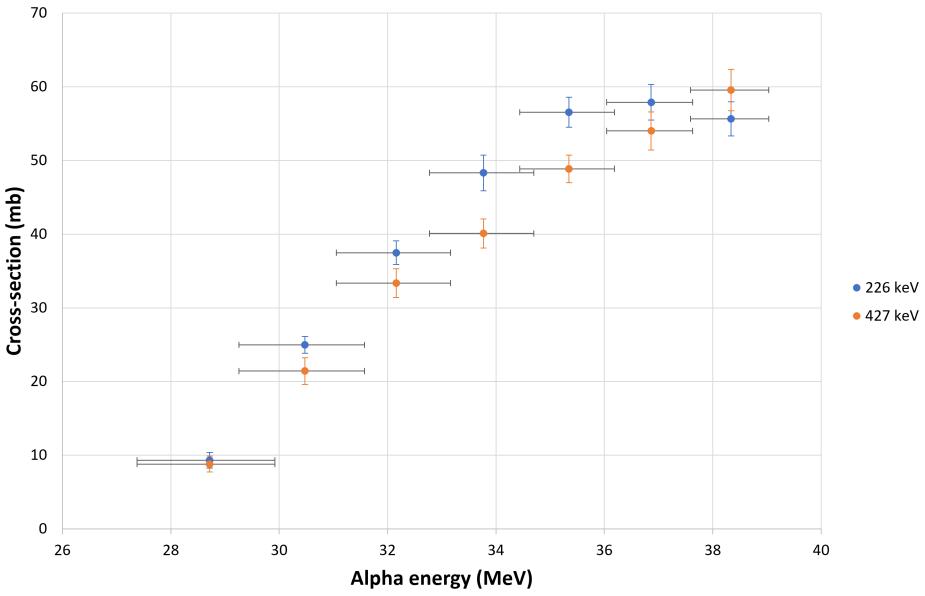

Figure 5.10: Measured cross-section results for the production of $^{154}Tb^{m2}$ using data from two γ energies, 226 (blue) and 427 (orange) keV, as a function of α energy.

Due to the lower activity and consequently greater variation in the $^{154}Tb^{m2}$ results, the final cross-section measurement for each foil was obtain by averaging the 266 and 427 keV results. The positive error margin was taken at the maximum 226 keV data error and the minimum error margin was taken as the lower 427 keV error margin (except for the highest α energy cross-section where the 266 and 427 keV data points are reversed, see figure 5.10). The final cross-section results and errors are provided in table 5.6.

Table 5.6: Cross-section values for the production of $^{154}Tb^{m2}$ from $\alpha+^{nat}Eu$ reactions measured in seven irradiated ^{nat}Eu foils. The α beam energy range of each foil is also given.

Eu Foil	Lowest energy at the back of foil (MeV)	Average foil energy (MeV)	Highest energy at the front of foil (MeV)	Cross-section (mb)
1	37.62	38.34	39.04	58^{+4}_{-5}
2	36.06	36.86	37.64	56^{+4}_{-5}
3	34.46	35.35	36.19	53^{+6}_{-6}
4	32.81	33.77	34.71	44^{+7}_{-6}
5	31.08	32.16	33.18	35^{+4}_{-4}
6	29.30	30.47	31.59	23^{+3}_{-4}
7	27.45	28.72	29.97	9^{+1}_{-1}

Terbium - 154m1

As well as looking at the universally used 540 keV γ emission, four additional γ energy emissions of the $^{154}Tb^{m1}$ isomer decay were monitored in the irradiated nine foils. However, the intensities of the other γ emissions were relatively small, 0.5-1.5% compared to the 20% intensity of the 540 keV emission. This drastically impacted the statistics of these four peaks, therefore, it was decided to only use the 540 keV data for the production of decay curves to enable reliable and precise half-life and A_T measurements.

Nine decay curves of the 540 keV γ emission were produced, one from the data of each irradiated ^{nat}Eu foil. Data used in the decay curves covered a 3-9 $^{154}Tb^{m1}$ half-life time period. The foil-3 decay curve is given as an example in figure 5.11. In a previous study of this isomer [68] there was in indication that $^{154}Tb^{m2}$ was decaying into the middle (m1) isomeric state. The data used by Jaffy et al. [68] to support this case is shown in figure 5.12. However, the decreasing gradient curvature plotted over the data relied on only two data points, both with large error bars. Moreover this curve in the data could have also been due to background that was unaccounted for. Considering these arguments for the shape of the data in figure 5.12 it would be difficult to conclude that there was definitely a component of

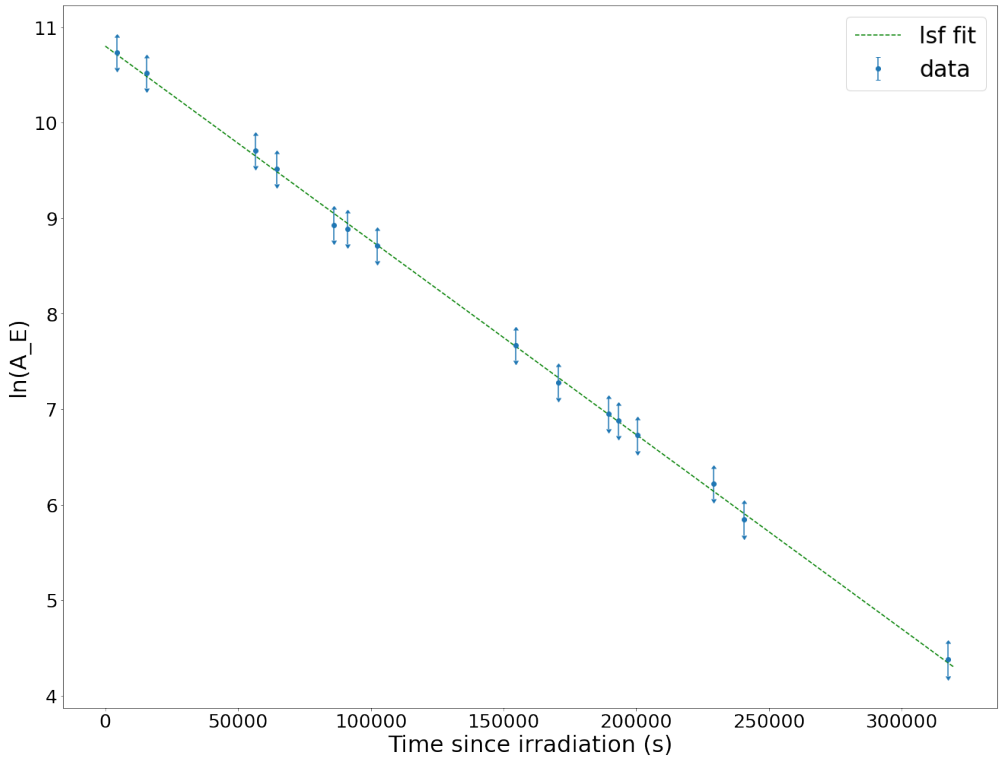

Figure 5.11: Foil 3 decay curve produced using the data from the 540 keV γ energy emitted by the ^{154}Tb^{m1} isomer. The χ^2/ndf of the fit was 0.1.

^{154}Tb^{m2} decay.

There was no observed curvature in the ^{154}Tb^{m1} decay curves produced from the α+^{nat}Eu irradiated foils. If there was a dependence on the ^{154}Tb^{m2} isomer, a reason why this may not be visible is because ^{154}Tb^{m2} decays by IT only 1.8% of the time and in these irradiated foils the production of the ^{154}Tb^{m1} state was 20 times that of the ^{154}Tb^{m2} state. Moreover, the curve in the 1973 [68] data shown in figure 5.12 was only visible after 100 hours and the data collected for this new measurement was studied for up to 85 hours. Therefore, the effect of ^{154}Tb^{m2} was assumed to be negligible and a linear LSF was applied to each graph, like that shown in figure 5.11.

The current published value for ^{154}Tb^{m1} half-life is 9.4±0.4 hours as extracted from the A=154 Nuclear Data Sheets [58]. This value is an unweighted average of several publications.

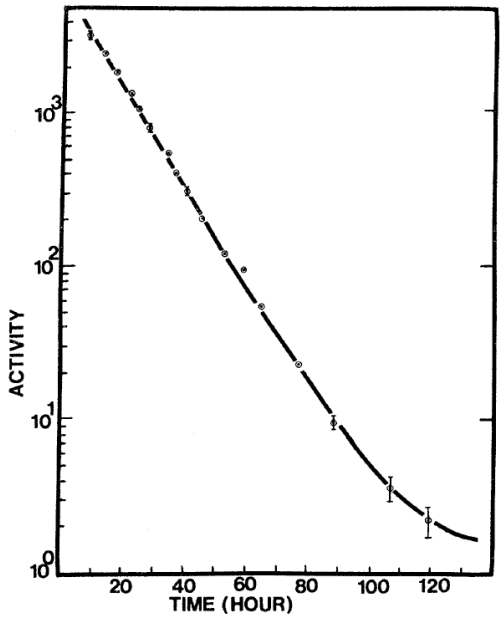

Figure 5.12: Activity (in counts per minute) of the $^{154}Tb^{m1}$ isomer produced in 1973 [68] from the 540 keV γ energy data. This decay curve was then fitted assuming the $^{154}Tb^{m1}$ isomer decay was affected by the decay of the $^{154}Tb^{m2}$ isomer.

Using the data from the nine irradiated foils discussed in this thesis, a weighted average of the nine half-life values calculated from the nine decay curve gradients produced a new half-life value of 9.43±0.04 hours. This value is in agreement with the published average value and improves upon the precision of previous work.

The intercept values for each of the 9 decay curves were used in equation 5.3 to extract the A_T values. Equation 5.4 was then implemented (with Y calculated using new half-life value of 9.43±0.04 hours) to obtain a cross-section measurement for each of the nine foils. These are provided in table 5.7.

Table 5.7: Cross-section values for the production of ^{154}Tb^{m1} from α+^{nat}Eu reactions measured in nine irradiated ^{nat}Eu foils. The α beam energy range of each foil is also given.

Eu Foil	Lowest energy at the back of foil (MeV)	Average foil energy (MeV)	Highest energy at the front of foil (MeV)	Cross-section (mb)
1	37.62	38.34	39.04	526(19)
2	36.06	36.86	37.64	540(21)
3	34.46	35.35	36.19	519(19)
4	32.81	33.77	34.71	468(19)
5	31.08	32.16	33.18	380(17)
6	29.30	30.47	31.59	236(9)
7	27.45	28.72	29.97	109(6)
8	25.48	26.90	28.25	26(3)
9	23.40	25.00	26.46	22(2)

Terbium - 154 ground state

In addition to the 2064 (7.1(3)%) and 2187 keV (9.9(8)%) γ energies, the 705 keV (4.8(3)%) γ ray was also used to monitor the decay of the ^{154}Tb ground state. However, the activity measurements from this energy did not follow the same trend as the other two energies. This needs further investigation but for the purpose of the rest of the ^{154}Tb ground-state analysis only the 2064 and 2187 keV data were used.

As stated previously in section 4.5, figure 4.15 shows how these ^{154}Tb isomeric states either decay directly to ^{154}Gd or via the ^{154}Tb ground state. As discussed above, the decay curves of the isomer states were linear with respect to time, implying only a single half-life component was present in each. This was not true for the ground state. Extracting information from the A=154 NDS [58] and the measurements made above, the ^{154}Tb ground-state decays with a half-life of 21.5 hours, the ^{154}Tb^{m1} isomer decays with a much shorter half-life of 9.43 hours and the ^{154}Tb^{m2} isomer decays with a slightly longer, 23.58 hour, half-life. The ^{154}Tb^{m2} decays by IT 1.8% of the time and the ^{154}Tb^{m1} decays by IT to the ground state 21.8% of the time. Therefore, the decay of the ^{154}Tb ground state does not follow a simple exponential

relationship time time, see figure 5.13. In this figure the 2064 keV A_E data from foil 2 have been plotted as a function of time (t). At the start, there is an increase in the activity of the ^{154}Tb grounds state. This is a feature that is expected when a shorter half-life isomer (i.e. ^{154}Tb^{m1}) feeds into the longer-lived ground state. The comparable ^{154}Tb^{m2} and ground-state half-lives makes distinguishing the effect of one on the other in the plot difficult to see. Moreover, the original activity of the ^{154}Tb^{m2} isomer was relatively low ($\sim$ 20 time less than the ^{154}Tb^{m1} state) and only 1.8% of ^{154}Tb^{m2} undergoes IT. With all of these compounding factors and the limited number of data points in each ^{154}Tb activity plot, the fitting of the curves was simplified such that the ^{154}Tb ground state only depended on the ^{154}Tb^{m1} isomer decay and its own decay. The Bateman equation [42],

$$A_E = BA_{Tm1}\frac{\lambda_g}{\lambda_g - \lambda_{m1}} \cdot (e^{-\lambda_{m1}t} - e^{-\lambda_g t}) + A_{Tg}e^{-\lambda_g t}, \tag{5.7}$$

was used to fit the curvature of the data points in the $A_E(t)$ plots for each γ energy (2064, and 2187 keV) data set in the first seven foils. The parameters λ_g and λ_{m1} are the decay constants of the ground state and $m1$ state, respectively. The half-life of the ground state was a free parameter in the fit, however, due to very few data points before the maximum of the curve, the half-life of the $m1$ state was fixed to 9.43 hours in order to constrain the fits to improve the reliability of the fitting. Moreover, because of the same data point limitations, the branching ratio of the $m1$ isomer to the ground state, B, was restricted to 0.218 [46] (the IT branching ratio of the $m1$ isomer). The initial activities of the ground (A_{Tg}) state and $m1$ isomer (A_{Tm1}) immediately after α beam irradiation stopped were also free parameters of equation 5.7.

Fourteen graphs like that displayed in figure 5.13, were produced from foils one to seven using the 2064 and 2187 keV data. (Note that the statistics of these energy peaks in foils 8 and 9 were too low or negligible, negating production of the corresponding plots.) From these 14 fits, the weighted average half-life value for the ground state was 22.7$\pm$0.5 hours

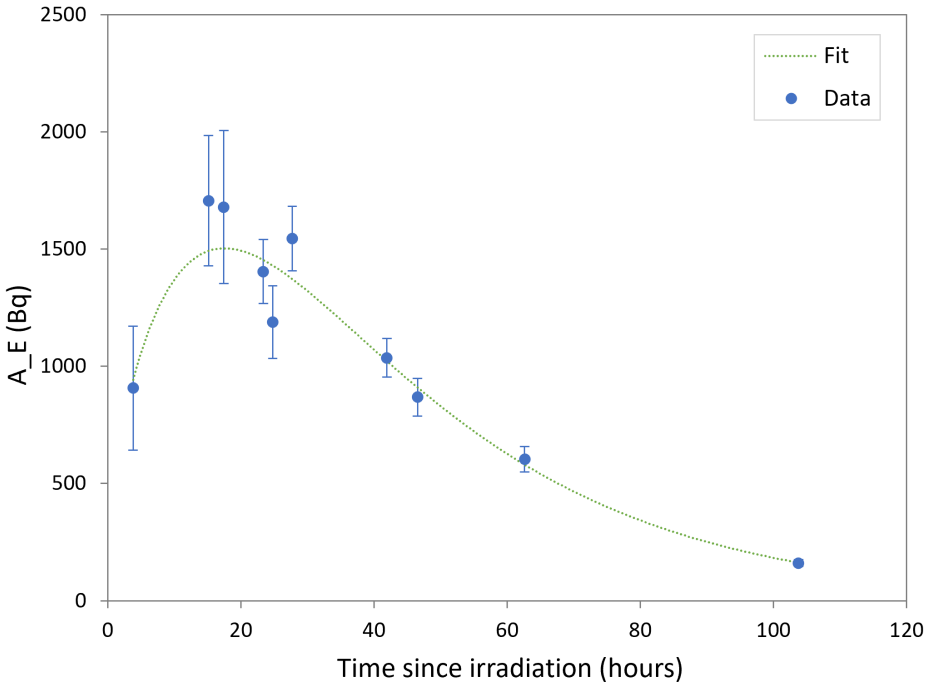

Figure 5.13: The activity, A_E, of the ^{154}Tb ground state plotted as a function of time since α-beam irradiation stopped. This was produced using the 2064 keV emission data from foil 2. The green dotted line was produced from fitting equation 5.7. The χ^2/ndf of the fit was 0.8.

from the 2064 keV data and 22.0±0.6 hours from the 2187 keV data. Both of these are in agreement with the published ^{154}Tb^{m2} half-life value of 22.7(5) hours and the 2187 keV data half-life was within errors of the published ^{154}Tb ground state half-life of 21.5(4) hours. Unfortunately, the relatively low statistics of the ground-state data and the complex nature of the internal decays meant that no improved half-life value for the ground-state could be obtained.

The output values for the A_{Tm1} parameters of the 14 fits were within 8 standard deviations or fewer of the A_T values extracted from the ^{154}Tb^{m1} decay curves in section 5.5.5 "Terbium - 154m1". This is despite the ground-state data fits being carried out with very few data points (especially before the maximum of the activity curves) in addition to a number of the data

Table 5.8: Cross-section values for the direct production of ^{154}Tb ground state from α+^{nat}Eu reactions measured in seven irradiated ^{nat}Eu foils. The α beam energy range of each foil is also given.

Eu Foil	Lowest energy at the back of foil (MeV)	Average foil energy (MeV)	Highest energy at the front of foil (MeV)	Cross-section (mb)
1	37.62	38.34	39.04	17^{+24}_{-17}
2	36.06	36.86	37.64	20^{+19}_{-18}
3	34.46	35.35	36.19	25^{+23}_{-21}
4	32.81	33.77	34.71	42^{+33}_{-31}
5	31.08	32.16	33.18	38^{+9}_{-9}
6	29.30	30.47	31.59	9^{+8}_{-8}
7	27.45	28.72	29.97	9^{+6}_{-6}

points possessing relatively large errors. The 14 A_{Tg} output values (i.e. A_T values for the direct production of the ground state) were then used in equation 5.4 (with Y calculated using the published half-life value of 21.5±0.4 hours) to obtain two cross-section measurements for each of the seven foils. Similarly to the analysis for the ^{154}Tb^{m2} state (sec section 5.5.5 "Terbium - 154m2"), an average of the two cross-sections for each foil was taken and the extreme errors of each measurement were used for the error on the average cross-section. These final cross-section results are provided in table 5.8.

5.5.6 Terbium - 155

There were four γ energies emitted by the ^{155}Tb isotope that were monitored for a total of 29 days (5-6 half-lives) in each of the nine foils. These were: 105 keV (25.1%); 149 keV (2.65%); 161 keV (3.54%); and 163 keV (4.44%). As explained in section 4.7.3, due to the poorer energy resolution of the HPC HPGe detector when the shaping time was 1 μs (FWHM of 3 keV at 160 keV instead of a FWHM of 1.4 keV for when the shaping time was 3 μs), accurately fitting Gaussians to the 161 and 163 keV peaks was not possible for these spectra. Therefore the data for these two energy peaks from these specific spectra were excluded from the decay

curves. Apart from this case, the other decay curves were produced as before. Figure 5.14 shows an example of a ^{155}Tb isotope decay curve produced using the A_E data from the 105 keV γ-ray from foil 9.

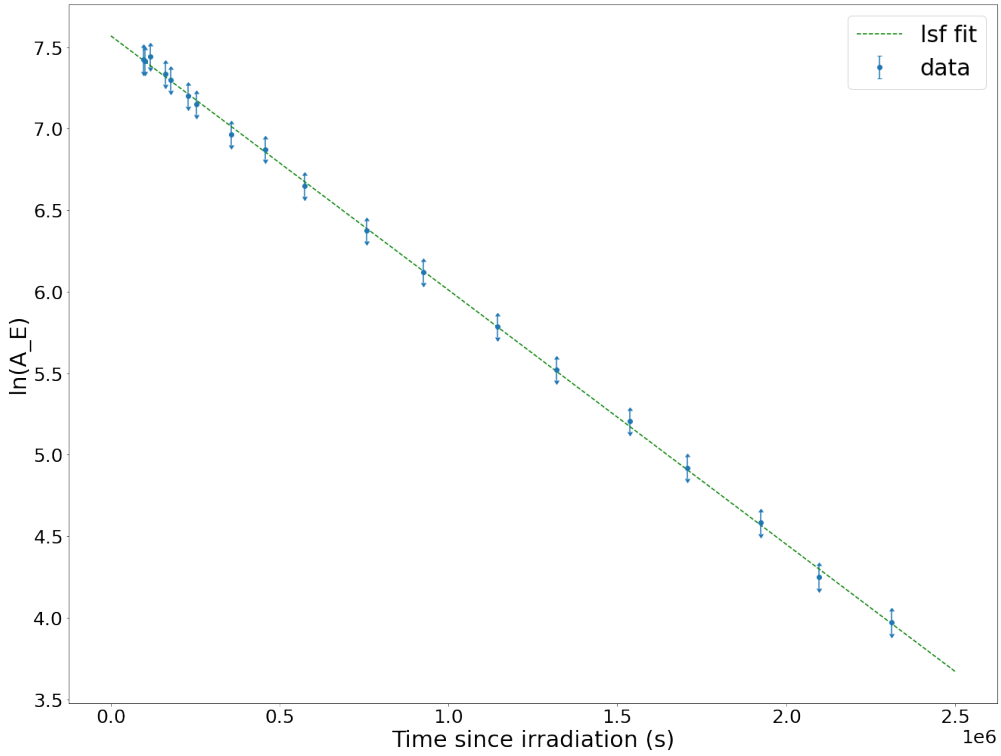

Figure 5.14: Foil 9 decay curve produced using the data from the 105 keV γ energy emitted by the ^{155}Tb isotope as it decays. The χ^2/ndf of the fit was 0.4.

The current published value for ^{155}Tb half-life is 5.32±0.06 days as extracted from the A=155 Nuclear Data Sheets [61]. This value was solely weighted on the measurement published in 1970 [67]. In Ref. [67], the ^{155}Tb isotope half-life was measured using the 87 and 105 keV peaks for at least 3 half-lives. There were four determinations of the half-life which were used to obtain the final measurement.

The ^{155}Tb decay curves produced from the α+^{nat}Eu reaction in the nine foils spanned a time range of at least 3 half-lives and, for the majority of the graphs, data spanning greater than 5 half-lives were plotted. There were four γ energies monitored (105, 149, 161 and 163

Table 5.9: Cross-section values for the production of ^{155}Tb from α+^{nat}Eu reactions measured in nine irradiated ^{nat}Eu foils. The α beam energy range of each foil is also given.

^{nat}Eu Foil	Lowest energy at the back of foil (MeV)	Average foil energy (MeV)	Highest energy at the front of foil (MeV)	Cross-section (mb)
1	37.62	38.34	39.04	53(1)
2	36.06	36.86	37.64	69(2)
3	34.46	35.35	36.19	91(2)
4	32.81	33.77	34.71	120(3)
5	31.08	32.16	33.18	188(4)
6	29.30	30.47	31.59	268(5)
7	27.45	28.72	29.97	373(6)
8	25.48	26.90	28.25	426(7)
9	23.40	25.00	26.46	371(6)

keV) and there were nine foils that were separately measured. Therefore, a total of 36 decay curves were produced and thus a total of 36 half-life measurements were made. The weighted average of these 36 values produced a ^{155}Tb half-life of 5.25±0.01 days. This value is within errors of the published value. Due to the superior detector resolution, length of study and number of repeat measurements this new value for half-life was then subsequently adopted for the remainder of the cross-section analysis.

The intercept values for each of the 36 decay curves were used in equation 5.3 to extract the A_T values. Equation 5.4 was then implemented (with Y calculated using the newly measured half-life value for ^{155}Tb, 5.25±0.01 days) to obtain four cross-section measurements for each of the nine foils. A weighted average was taken of the four cross-section measurements calculated for each foil to provide the final cross-section results. These are provided in table 5.9.

5.5.7 Terbium - 156

Although it was not mentioned in chapter 4, the TALYS calculations also included production of the two additional isomeric states of ^{156}Tb: ^{156}Tb^{m1} with a half-life of 24.4(10) hours; and ^{156}Tb^{m2} with a half-life of 5.3(2) hours. These isomeric states decay 100% by internal transitions, IT and will thus add to the ground state as they decay. Unfortunately, using the experimental set-up described in this thesis, neither states emitted a uniquely identifiable γ energy as they decayed, and thus could not be measured individually. The 49.9630 keV γ known to depopulate the m1 isomers and the 88.4 keV γ known to depopulate the m2 isomers were not resolvable using the HPGe detectors from the 49.959 keV K_β X-ray and 88.97 keV γ emissions of the ^{156}Tb ground state. Therefore, only the ground state of the isotope was measured.

Five γ energy emissions from the decay of the ^{156}Tb ground-state were monitored in the nine foils. However, the production of this isotope was very small in comparison to the other, Tb isotopes and isomers discussed above. Therefore, only the most intense peak with an energy of 534 keV and intensity of 67% yielded sufficient statistics to produce reliable decay curves.

When considering the function with which to fit the 534 keV peak decay curve, the affects of isomer states decaying should be considered. However, TALYS predicted that the cross-sections of the two isomers states would be 0 to 50% compared to that of the ground state. This, compounded with the low statistics of this isotope meant the effect of the isomers on the ground state was considered to be negligible and thus a straight line fit was used for the ground-state decay curves.

The statistics of the 534 keV peak produced by this relatively intense γ emission were not sufficient to reliably obtain an improved half-life result for this state. Therefore, the NNDC half-life value (see table 4.2) for this isotope was used to constrain the half-life in the nine

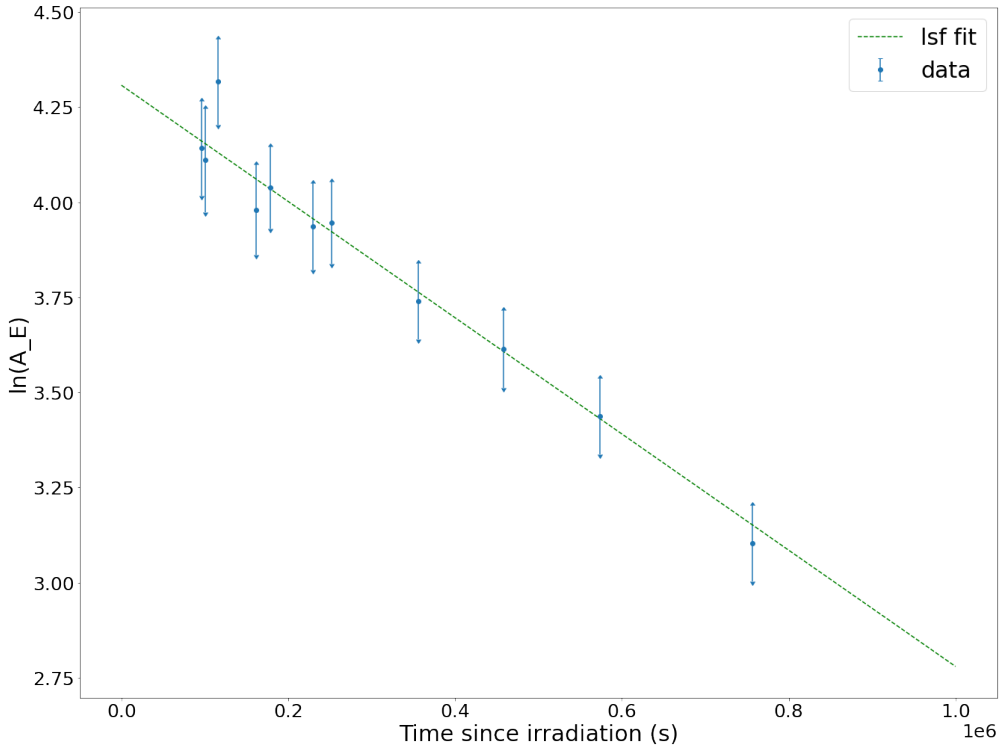

Figure 5.15: Foil 9 decay curve produced using the data from the 534 keV γ energy emitted by the decay of the ^{156}Tb isotope where the gradient of the fit was constrained by the published half-life value of 5.35±0.10 days. The χ^2/ndf of the fit was 0.4.

decay curve fits. An example of a decay curve produced from the 534 keV data from foil 9 is shown in figure 5.15 where the gradient of the LSF was constrained by the published half-life value and errors of 5.35±0.10 days [62].

The intercept values for each of the 9 decay curves were used in equation 5.3 to extract the A_T values. Equation 5.4 was then implemented (with Y calculated using the published value of 5.35±0.10 days) to obtain a cross-section measurement for each of the nine foils. These are provided in table 5.10.

Table 5.10: Cross-section values for the production of ^{156}Tb from α+^{nat}Eu reactions measured in nine irradiated ^{nat}Eu foils. The α beam energy range of each foil is also given.

^{nat}Eu Foil	Lowest energy at the back of foil (MeV)	Average foil energy (MeV)	Highest energy at the front of foil (MeV)	Cross-section (mb)
1	37.62	38.34	39.04	3.5(5)
2	36.06	36.86	37.64	4.0(5)
3	34.46	35.35	36.19	4.4(3)
4	32.81	33.77	34.71	4.9(4)
5	31.08	32.16	33.18	5.4(3)
6	29.30	30.47	31.59	6.3(3)
7	27.45	28.72	29.97	6.7(5)
8	25.48	26.90	28.25	7.7(5)
9	23.40	25.00	26.46	10.6(5)

Cross-section measurements were made for the production of ^{151}Tb, ^{152}Tb^{m1}, ^{152}Tb, ^{153}Tb, ^{154}Tb, ^{154}Tb^{m1}, ^{154}Tb^{m2}, ^{155}Tb and ^{156}Tb from the α+^{nat}Eu reactions for up to nine α energies. The statistics for the production of ^{152}Tb^{m1}, ^{152}Tb, ^{153}Tb, ^{154}Tb^{m2}, ^{154}Tb^{m1} and ^{155}Tb states were also substantial enough to draw new half-life measurements from the data as well. Although more work, with higher statistics data, is needed for some of the isotopes and isomers produced (^{154}Tb, ^{154}Tb^{m2} and ^{156}Tb) to reduce the uncertainties on the cross-sections results obtained here, the current data already provide quantitative cross-sections in these particular isotopes and isomer.

The following chapter is a summary of the Tb half-life and cross-section work and TALYS calculated cross-sections are compared to the results from this work. Measuring these cross-sections was the first step in developing this new production route for medical Tb isotopes. Therefore, chapter 6 also discusses what future measurements would be needed to further this production avenue as well as detailing how the current cross-section measurement method could be improved upon.

Chapter Six

Terbium cross-section and half-life summary, discussion, and conclusions

Medical Tb isotopes: ^{149}Tb, ^{152}Tb, ^{155}Tb, and ^{161}Tb are of great interest for the future of nuclear medicine treatment and the emerging field of theragnostics. An area that was highlighted as "needing improvement" was the ability to mass produce these isotopes using a method which was both physically and financially accessible to hospitals (and thus, patients). This was particularly true for the neutron-deficient isotopes (^{149}Tb, ^{152}Tb and ^{155}Tb). The initial production of these isotopes was limited to very high energy proton beams inducing spallation reactions in a target which then undergoes electromagnetic separation to extract the individual medical Tb isotopes. This production method is therefore limited to very few sites around the world and is extremely costly. As mentioned in chapter 1, a cost effective method for Tb separation from other lanthanides has been produced [32, 40] and a number of studies looking at alternative production methods which could utilise this separation technique have been carried out. These production methods have focused on using Gd targets and lower energy proton beams to produce Tb isotopes. Natural Gd is comprised of seven isotopes, so, to avoid the need for additional electromagnetic separation of the target after irradiation to extract the individual medical Tb isotopes, the Gd target needs to be

enriched for an individual isotope (i.e. either ^{152}Gd for ^{152}Tb production or ^{155}Gd for ^{155}Tb production). Unfortunately this is particularly difficult for ^{152}Gd, for its natural abundance is only 0.2%, and even ^{155}Gd only has a natural abundance of 14.8%. Therefore, to overcome this target enrichment issue, the work discussed in this thesis aimed towards developing a new alternative production route using Eu targets and α beams instead of Gd targets and proton beams. Europium naturally exists as only two isotopes, ^{151}Eu and ^{153}Eu, which occur in an approximate 50/50 abundance split. This would make enrichment of either isotope much easier as there is more of the individual isotope per weight of the natural Eu metal. However, there had been very limited experimental work carried out on the cross-sections of α+Eu reactions.

The cross-section information is essential to identifying if clean medical Tb isotope production is possible and what projectile energy should be used to produce the highest yield of the desired isotope. The previously established ability to separate Tb from other lanthanides [32, 40] means that, in this context, clean medical Tb production methods would be where no other Tb isotopes are produced at the same time as producing one of the medical Tb isotopes. Therefore, to measure if this α+Eu production route was viable, the aim of the experimental work and analysis discussed in chapters 2 to 5 was to measure the $\alpha+^{nat}$Eu reactions for the production of all Tb isotopes. Cross-sections calculated by the nuclear reaction code, TALYS, were used as a guide for identifying Tb isotopes produced and selecting an α energy range for the investigation. Figure 6.1 is a repeat of the $\alpha+^{nat}$Eu TALYS cross-section calculation shown in section 2.1.1.

In addition to improved target enrichment abilities, another reason why α+Eu reactions were selected for medical Tb production investigations was because of the excellent promise of clean medical Tb production predicted by TALYS cross-sections. Looking at the individual Eu isotope reactions with respect to incident α energy in figure 6.2 (a repeat of figures 2.4 and 2.5), there was a clear α energy window of 34 to 36 and 20 to 26 MeV for ^{152}Tb and

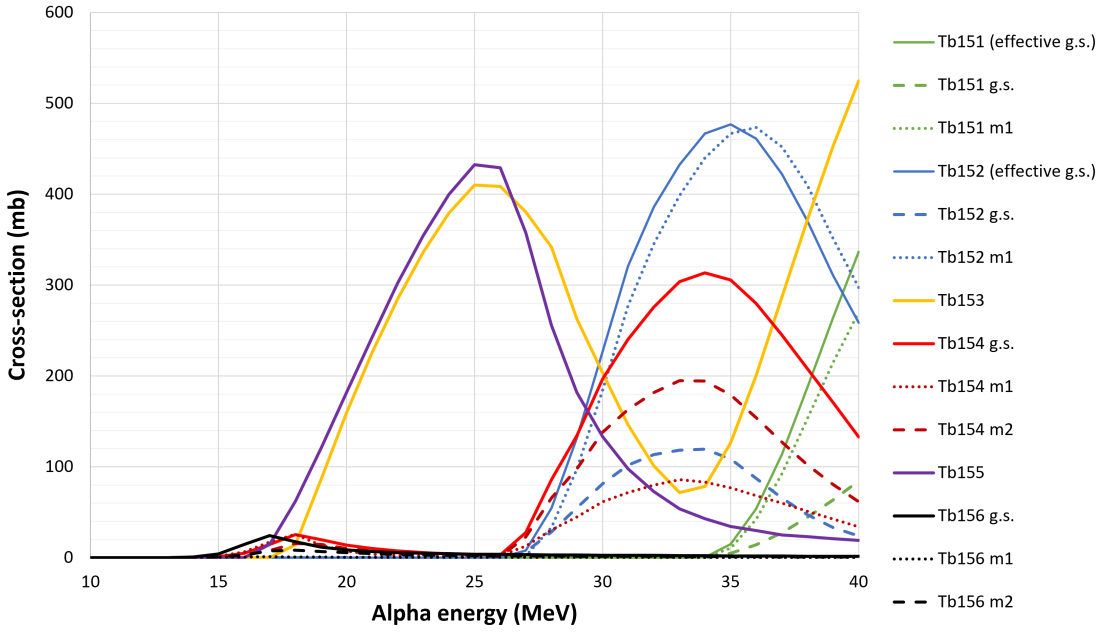

Figure 6.1: TALYS predicted cross-sections as a function of α energy for the production of Tb isotopes and isomers from α+^{nat}Eu reactions.

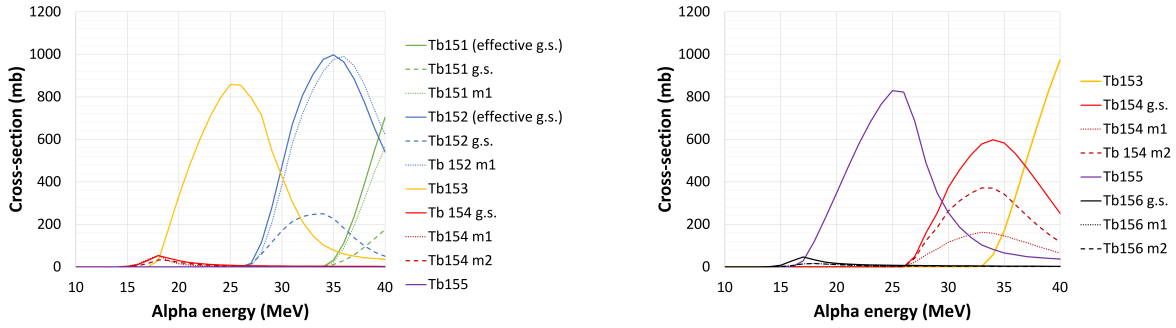

(a) ^{151}Eu target (b) ^{153}Eu target

Figure 6.2: TALYS predicted cross-sections as a function of α energy for the production of Tb isotopes and isomers using Eu isotope enriched targets.

^{155}Tb production from ^{151}Eu and ^{153}Eu targets, respectively. Therefore, if the experimentally produced cross-sections agree with TALYS cross-sections then the α+Eu production methods could be viable.

For medical isotope production isotopically enriched Eu oxide powders can be used, however, in order to measure cross-sections, very thin metal foils are needed. Europium is the most reactive lanthanide and easily oxidises. Consequently, making very thin, isotopically enriched Eu foils would be very expensive. Therefore, to measure and compare experimental cross-sections to TALYS cross-sections, natural Eu foils were used. In this work, the $\alpha+^{nat}$Eu cross-sections were measured for the production of two medical Tb isotopes ^{152}Tb and ^{155}Tb and potential contaminants: ^{151}Tb, ^{152}Tb^{m1}, ^{153}Tb, ^{154}Tb, ^{154}Tb^{m1}, ^{154}Tb^{m2} and ^{156}Tb. By irradiating a stack of nine ^{nat}Eu foils, up to nine cross-sections for different incident α energies were measured of each isotope and isomer. The individual results of these are given in tables 5.2 to 5.10 in chapter 5. Section 6.2 of this chapter compares these results to TALYS predictions.

The nature of measuring cross-sections meant that multiple decay curves of the Tb isotopes and isomers were produced. This allowed for essential information for cross-section measurements to be extracted, but also multiple repeat measurements of the half-lives of the isotopes and isomers. Many of these half-lives have not been measured since the 60's and 70's and having the most accurate and precise half-life knowledge for medical isotopes is crucial for both imaging and dosimetry. Therefore, where the isotopes were produced in larger quantities, and reliable repeat measurements of their half-lives were possible, a weighted average of the repeat measurements were calculated to produce a final half-life result for each isotope and isomer. The details of these measurements and analysis were discussed in chapter 5 and are summarised in section 6.1.

There were many stages to the cross-section measurements. These included: beam energy

and current measurement; foil thickness measurement; calculating α beam energy degradation through the target; γ spectra collection; decay and detector efficiency corrections; decay curve production and extraction of relevant parameters; and finally, half-life and cross-section extraction. The development of this experiment was detailed and considered. Emphasis was always give to improving the accuracy and precision of each stage. However, no experiment is perfect and although cross-sections of Tb production from ^{nat}Eu targets have been measured, there are still a number of stages and experiments that are needed before this method of medical Tb isotope production could be used for clinical trials or hospital treatment. Section 6.3 discusses which areas of the work detailed in this thesis could be improved upon and what steps should be taken next to test the viability of this production route further.

6.1 Terbium half-life summary

As discussed in the previous chapter, several new half-life measurements were extracted from the decay curves produced for the cross-section measurement. Table 6.1 summarises the current published NDS values and new measurements for all the Tb isotopes and isomers analysed in this cross-section work. The new measurements were produced from a weighted average of the values extracted from each decay curve for a particular isotope/isomer. Each half-life value from a decay curve acted as a repeat measurement of the half-life. The number of repeat measurements used for each final new measurement value is detailed in the determinations column of table 6.1.

In some cases — ^{152}Tb^{m1}, ^{154}Tb^{m1} and ^{155}Tb (highlighted in teal) — the new half-life measurements were in agreement (within errors) of the currently published NDS values. For these isomers and isotopes, the new measurements provided a more precise value for each half-life. The half-life results for ^{152}Tb, ^{153}Tb and ^{154}Tb^{m2} (highlighted in red) were 3.5, 4.2

Table 6.1: Currently published NDS values and new half-life measurements for the Tb isotopes and isomers measured during the cross-section measurement. The new half-life measurements which were in agreement with published values within one standard deviation are in teal and those which are within five standard deviations are in red. The number of repeat measurements used to obtain the new weighted average half-life is given in the determinations column.

Isotope or isomer	NDS published half-life	Newly measured half-life	Determinations
^{151}**Tb**	17.609(14) hours	-	-
^{152}**Tb**^{m1}	4.2(1) minutes	4.22(2) minutes	7
^{152}**Tb**	17.5(1) hours	17.07(7) hours	28
^{153}**Tb**	2.34(1) days	2.291(6) days	18
^{154}**Tb**	21.5(4) hours	-	-
^{154}**Tb**^{m1}	9.4(4) hours	9.43(4) hours	9
^{154}**Tb**^{m2}	22.7(5) hours	23.58(15) hours	14
^{155}**Tb**	5.32(6) days	5.25(1) days	36
^{156}**Tb**	5.35(10) days	-	-

and 1.7 standard deviations away from the NDS published values, respectively. Comparing the method used to extract these new half-life measurements to the methods use to obtain the previous ^{152}Tb, ^{153}Tb and ^{154}Tb^{m2} half-lives [70, 67, 68], more γ energies were monitored using the new measurement method and a greater number of repeat readings were also taken. Moreover, the new half-life measurements proposed here were recorded over a greater number of half-lives than previous measurements. Therefore, although the new measurements do vary from previous ones, the improvement in the measurement techniques could account for this.

Compared to the previous measurements taken in the 60's and 70's, all of these new half-life measurements have benefited from the much improved detector resolution and sensitivity; electronic processing; analysis software packages; and data fitting programs that have been used here. Moreover, very careful planning and execution of the measurements to minimise uncertainties have improved the data quality and parameter extraction. This coupled with with the large number of measurements over a greater half-life range led to the increased

reliability and precision of these new values.

In future half-life measurements of the ^{151}Tb and ^{154}Tb isotopes and ^{154}Tb^{m2} isomer, a higher energy α beam and longer irradiation time should be used to increase their production. This would increase the statistics of their decay peaks and thus enable a half-life measurement. Increased statistics would also enable the investigation of the half-life discrepancy discussed and seen in chapter 5, between the two γ's emitted by ^{154}Tb^{m2} as it decays. In contrast, the ^{156}Tb isotope statistics would benefit from a decrease in the incident α beam energy. However, for the ^{156}Tb isotope, future measurements would also need to consider the effects of the two isomeric states that would also likely be produced.

For future half-life measurements of the ^{151}Tb, ^{154}Tb and ^{156}Tb states, it would also be beneficial to monitor fewer foils or use more HPGe detectors. This would enable more spectra to be collected. This is especially crucial in the early hours after irradiation where the effects of shorter-lived isomeric states will be most visible. For the ^{154}Tb and ^{156}Tb isotopes this will be essential to ensure enough data points are collected for a Bateman equation function to be fitted reliably to the data.

6.2 Comparing TALYS calculations to the Cross-section results

As stated above, a comparison of the measured cross-sections and TALYS calculated cross-sections for each of the isotopes and isomers are given below. Up to nine measurements were produced from the data for the different α energies incident on each foil. In all of the cross-section graphs below, the α energy error bars represent the α energy range of each irradiated ^{nat}Eu foil and the cross-section data points are plotted at the α energy for the centre of each irradiated ^{nat}Eu foil.

6.2.1 Terbium - 151

Two γ energy emissions from the decay of the ^{151}Tb isotope were used to study its production. The ^{151}Tb ground state was produced in the first two Eu foils of the Eu/Al target stack. The isomeric state would have also have been produced, however, this decayed too quickly to be measured using the detector set-up described in chapter 4. The isomeric state decays 93.4% of the time to the ground state of ^{151}Tb, therefore, to compare TALYS to the two weighted average measured cross-sections calculations, an "effective ground state" cross-section was produced from the TALYS α+^{nat}Eu cross-sections. The "effective ground state" cross-sections in figure 6.3 is where 93.4% of the isomer cross-section was added to the ground state cross-section. The trend of the TALYS cross-section follows the trend of the two ^{151}Tb data sets but is shifted to lower α energy by 2 to 3 MeV.

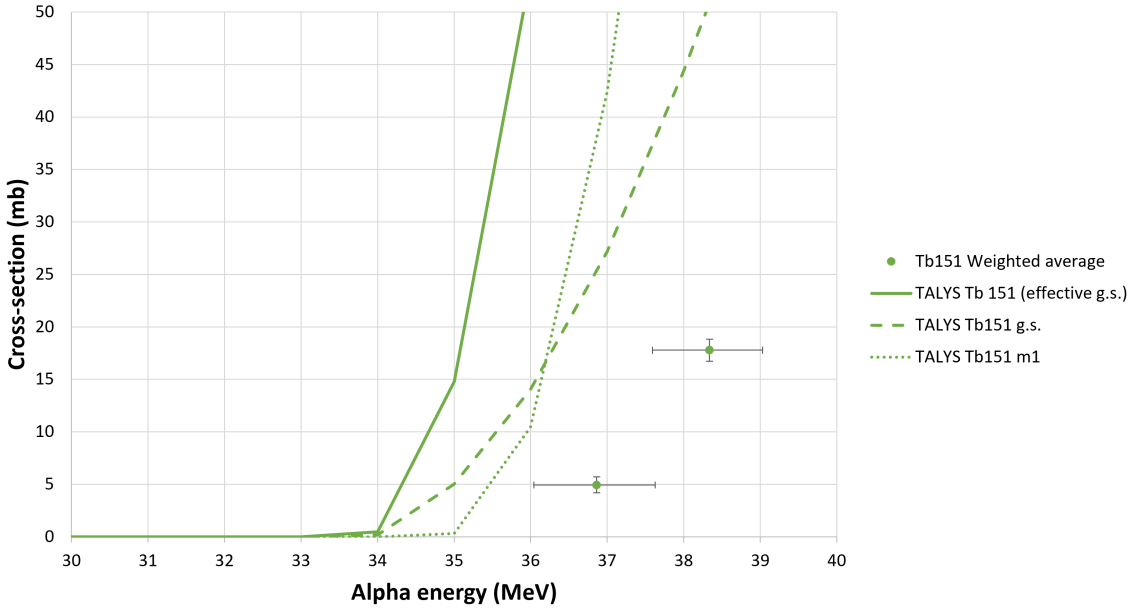

Figure 6.3: The weighted average measured cross-sections for the production of the ^{151}Tb ground state by direct and indirect channels from α+^{nat}Eu reactions as a function of α energy. The TALYS cross-sections for the ground state, excited state and effective ground state which is where 93.4% of the m1 cross-section was added to the ground state cross-section are compared to these two measured cross-sections for the ground state.

6.2.2 Terbium - 152m1

Due to detector set-up constraints and the short half-life of the ^{152}Tb^{m1} isomer, this state was only measured in the first four Eu foils of the Eu/Al target stack. The weighted average cross-section measured for each of the four foils was obtained using cross-section measurements from seven γ energy emissions following the ^{152}Tb^{m1} decay. Figure 6.4 compares TALYS calculations to the measure values. The trend of the TALYS cross-section follows that of the four measurements, however, the trend is shifted to lower α energies by 4 to 6 MeV and the maximum cross-section for the measured production of ^{152}Tb^{m1} is actually at higher α energies than predicted by TALYS. In order to determine the exact α energy needed to obtain the maximum cross-section further measurements using higher energy α beams are

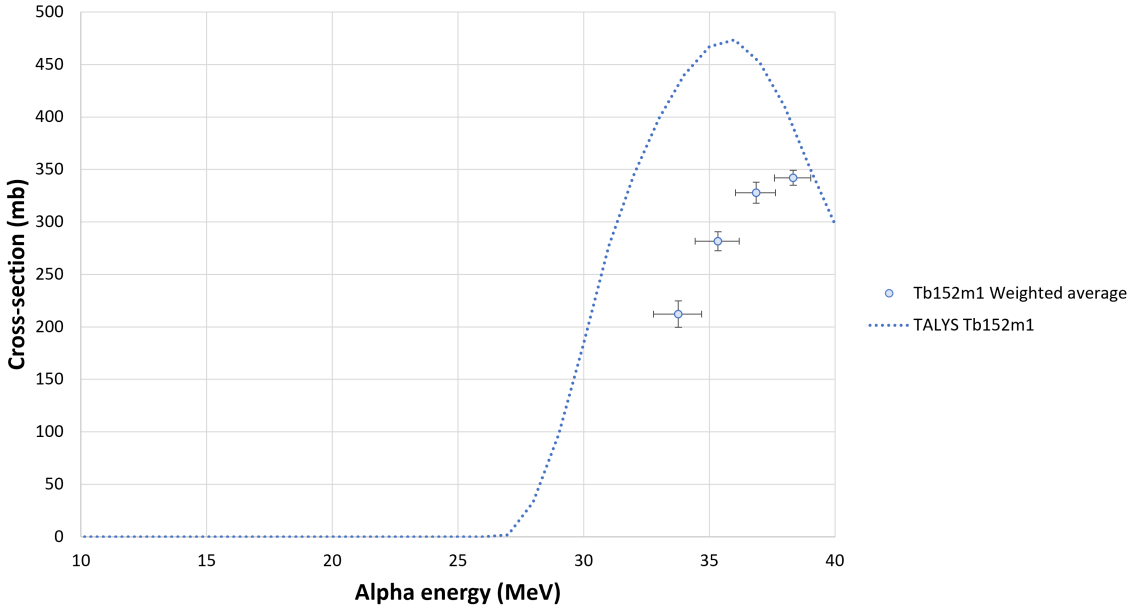

Figure 6.4: The weighted average measured cross-sections for the direct production of the ^{152}Tb^{m1} isomer state from α+^{nat}Eu reactions as a function of α energy. The TALYS calculations are compared to the data for these four measurements.

needed.

6.2.3 Terbium - 152

Four γ energy emissions of the ^{152}Tb isotope were used to study its production. The ^{152}Tb ground state was produced in the first seven Eu foils of the Eu/Al target stack. The isomeric state was also produced, however, the data taken of the ground state were collected after over 99.8% of the isomeric state had already decayed (i.e. after nine half-lives). Therefore, the ground state weighted average cross-sections measured here were from both direct and indirect α+^{nat}Eu reactions. In other words, the measured cross-sections consisted of 100% direct reactions and 78.9% of the cross-section for the isomeric state as the branching ratio of IT is 78.9%. To compare TALYS calculations to these data, an "effective ground state" cross-

section calculation was produced from the TALYS α+^{nat}Eu cross-sections. The "effective ground state" cross-sections in figure 6.5 is where 78.9% of the isomeric cross-section was added to the ground state cross-section. The trend of the TALYS cross-sections follows that of the seven measurement for ^{152}Tb, but is shifted to lower α energies by 2 to 3 MeV and the maximum cross-section for the measured production of ^{152}Tb occurs at a higher α energy than TALYS predicts. In order to determine the exact α energy needed to obtain the maximum cross-section, further measurements using higher energy α beams are needed.

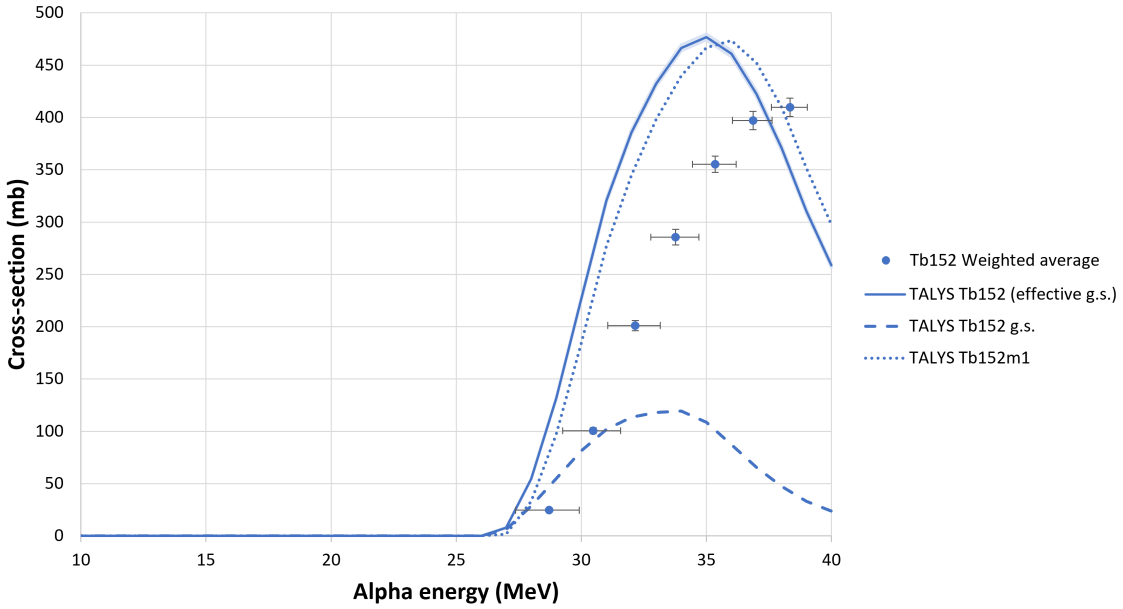

Figure 6.5: The weighted average measured cross-sections for the production of the ^{152}Tb ground state by direct and indirect channels from α+^{nat}Eu reactions as a function of α energy. The TALYS cross-sections are compared to the seven measurements where the effective g.s. TALYS curve is formed from 78.92% of the m1 cross-section added to the ground state cross-section.

6.2.4 Terbium - 153

Weighted average cross-sections were measured for the production of ^{153}Tb from α+^{nat}Eu reaction for all nine Eu foils of the Eu/Al target stack. Each weighted average was calculated using cross-section measurements from two γ energy emissions that followed from the ^{153}Tb decay. The TALYS calculated cross-sections in figure 6.6 are compared to the weighted average measured cross-sections of these nine points and the trends are the same. However, the TALYS trend is shifted to lower α energies by 2 to 3 MeV and the cross-section values are also smaller by approximately 50 mb compared to the measured values.

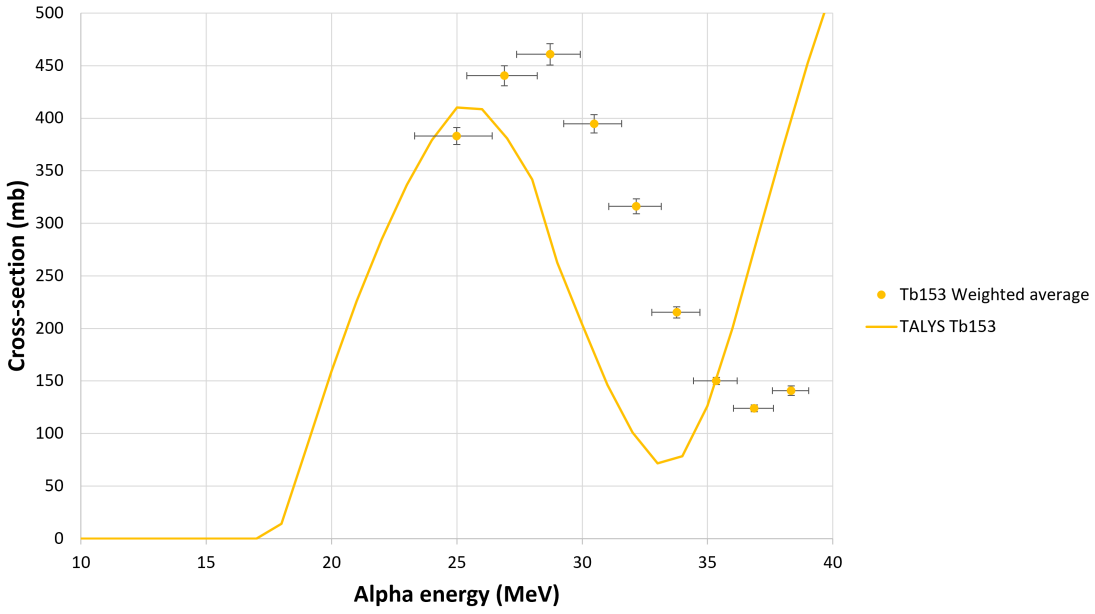

Figure 6.6: The weighted average measured cross-sections for the production of the ^{153}Tb isotope from α+^{nat}Eu reactions as a function of α energy. The TALYS calculations are compared to the nine measured cross-section data points for this isotope.

6.2.5 Terbium - 154m2

The $^{154}Tb^{m2}$ isomer was produced in lower quantities in the $\alpha+^{nat}Eu$ reactions. As mentioned previously, there was also a slightly larger variation in the half-lives extracted from the two γ energies used to measure the cross-section. This led to larger errors (compared to other isotopes and isomers) for the average $^{154}Tb^{m2}$ cross-section measurements as shown in figure 6.7. The TALYS calculated cross-sections were approximately four times higher than the seven measured cross-sections. However, the trend of increasing cross-section from 25 to 33 MeV of TALYS matched the data, although beyond 33 MeV the TALYS cross-sections decrease, unlike the data, which continue increasing towards a maximum cross-section between 38 and 40 MeV.

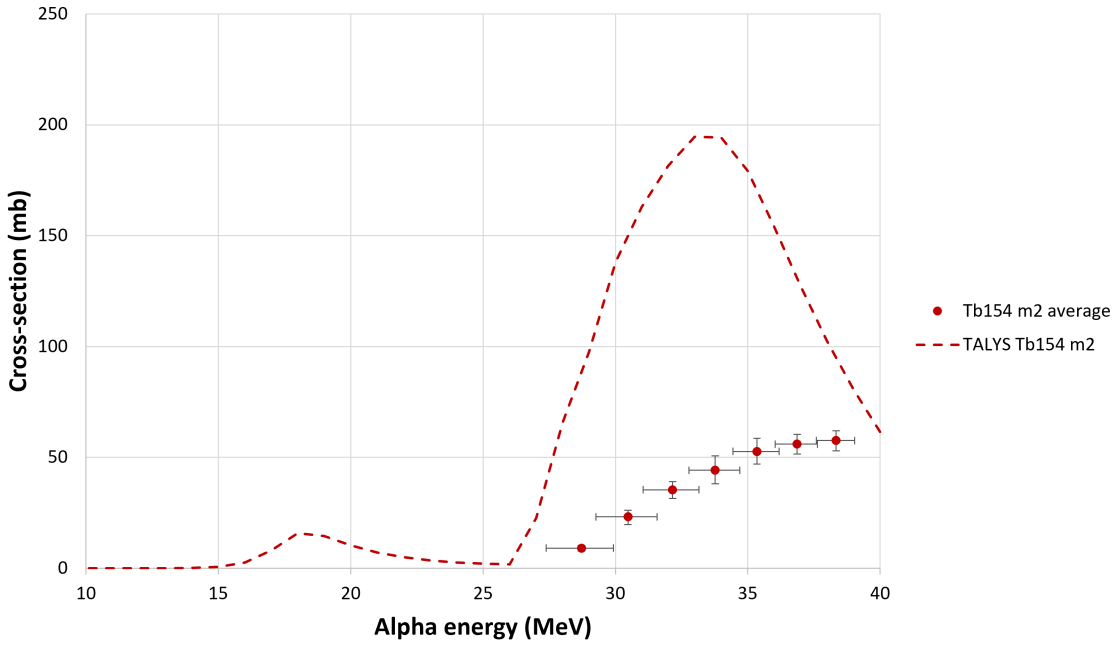

Figure 6.7: The average measured cross-sections for the direct production of the $^{154}Tb^{m2}$ isomer from $\alpha+^{nat}Eu$ reactions as a function of α energy. The TALYS calculated cross-sections are compared to these seven measured values for this isomer.

To improve or verify these cross-section results a future repeat of this measurement where a

>40 MeV α beam and longer irradiation period is used would be advised. This would increase the production of this isomeric state and thus increase the statistics for the individual γ measurements which would improve both the cross-section and half-life measurements of this isomer by constraining the errors and improving the decay curve fits.

6.2.6 Terbium - 154m1

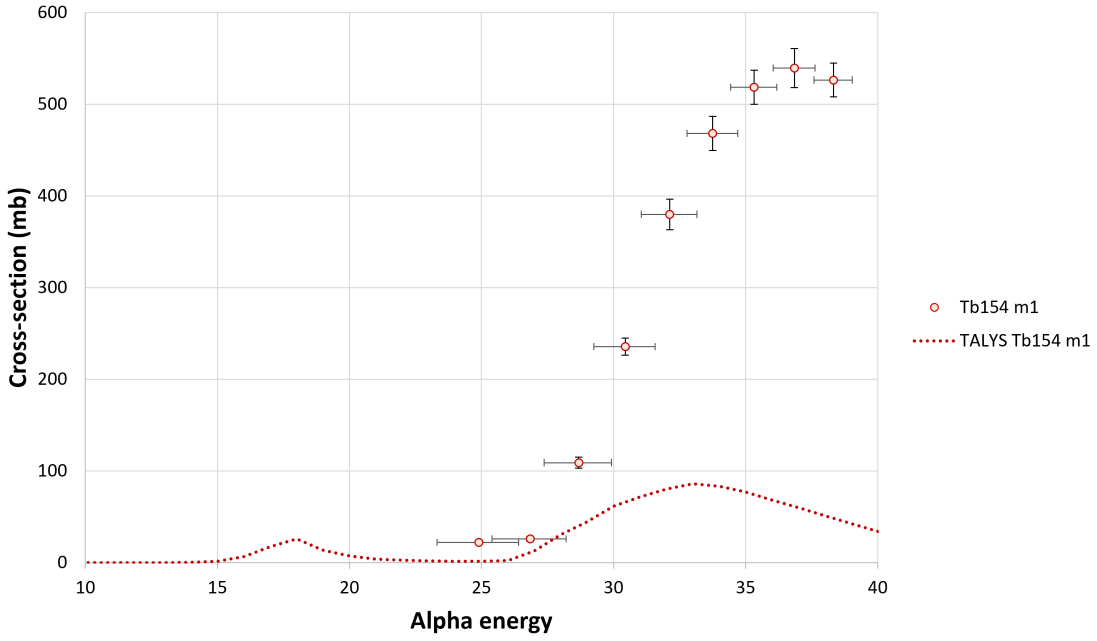

Figure 6.8: Measured cross-sections for the direct production of the ^{154}Tb^{m1} isomer from α+^{nat}Eu reactions as a function of α energy, measured using the 540 keV γ emission. The TALYS calculated cross-sections are compared to these nine measurements.

The 540 keV emission was used to measure the cross-section for the production of ^{154}Tb^{m1} from α+^{nat}Eu reactions in all nine Eu foils of the Eu/Al target stack. An important point of note regarding the decay curves was that there was no evidence observed in the present work that the ^{154}Tb^{m2} isomer had a decay component feeding the ^{154}Tb^{m1} isomer. Therefore, the cross-section measurements calculated from the parameters of the ^{154}Tb^{m1} decay curves were

assumed to be from only direct population via $\alpha+^{nat}$Eu reactions. The TALYS calculated cross-sections are compared to the nine measured values in figure 6.8. The trend is reproduced by TALYS, however, the maximum calculated cross-section occurs for an incident α energy 2.8 MeV lower than the data points. Additionally, the TALYS calculated values are six times lower than the measured quantities.

6.2.7 Terbium - 154

Measuring the cross-section for the production of ^{154}Tb in the ground state from $\alpha+^{nat}$Eu reactions proved more complex than the other Tb isotopes and isomers. This was firstly due to two isomeric states decaying into the ground state which had an observable effect on the decay of the γ's emitted by ^{154}Tb as it decayed. As the isomers had half-lives of similar order to that of the ground state, the standard process (used for ^{151}Tb and ^{152}Tb) of measuring the compound cross-section of both direct and indirect production of the ground state could not be performed using the decay curve of ^{154}Tb . This meant that, rather than using straight line decay curves for the extraction of activity immediately after irradiation, a Bateman equation was fitted to the activity data of the ground state as a function of time to extract the initial ground-state activity produced directly by $\alpha+^{nat}$Eu reactions.

Secondly, too few spectra were collected for each foil in the early hours after irradiation. This would be where the effect of the 9.43 hour half-life of the ^{154}Tb^{m1} isomer decay would be most visible in the activity curves of the ^{154}Tb ground state. More data points in this time window would have improved the fitting of the Bateman function to the ^{154}Tb data and thus improved the cross-section measurement for the ground state.

Finally, the activity and thus statistics of the ^{154}Tb ground state were low, making it more difficult to fit and leading to an increased the error margin for the average cross-sections.

Despite these difficulties, average cross-section measurements from the 2064 and 2187 keV emissions were produced from the activity data of the ^{154}Tb ground state. Similarly to ^{154}Tb^{m2}, the two cross-sections for each α energy were averaged and the maximum and minimum cross-section error margins from each γ energy were used as the error on the average, instead of using a weighted average and error. This was chosen as it better reflected the uncertainty in these data due to the poor statistics and lack of constraining data points in the activity-curve fitting.

Due to low statistics in foils 8 and 9 only seven cross-section measurements were made. TALYS predictions are compared to these final cross-section results for ^{154}Tb in figure 6.9. It can be seen that the TALYS values are five to six times higher than the measured data although the predictions do appear to follow the correct trend.

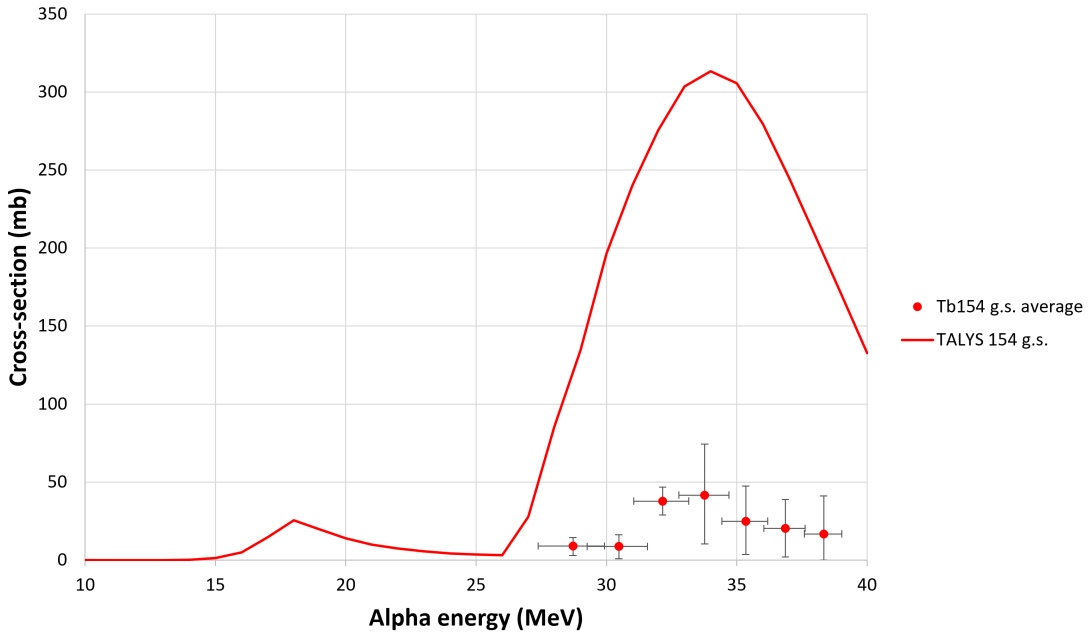

Figure 6.9: The average measured cross-sections for the direct production of the ^{154}Tb isotope in the ground state from α+^{nat}Eu reactions as a function of α energy. The TALYS calculated cross-sections are compared to these seven measurements for the ^{154}Tb ground state.

Due to the low γ statistics from the decay of both the ^{154}Tb ground state and the ^{154}Tb^{m2} isomer, the decay of the ^{154}Tb^{m2} state was not included in the Bateman equation used to fit the ground-state activity data. Future cross-section measurements with high activity production of all three ^{154}Tb states should include the effects of both the ^{154}Tb^{m1} and ^{154}Tb^{m2} states on the decay of the ground state.

6.2.8 Terbium - 155

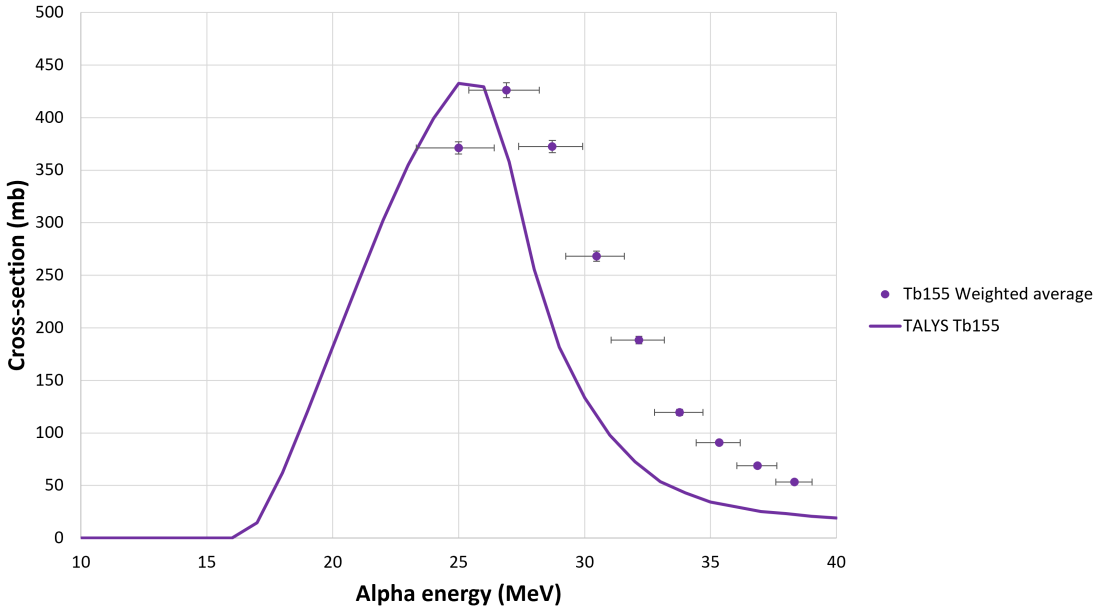

Figure 6.10: The weighted average measured cross-sections for the direct production of the ^{155}Tb isotope from α+^{nat}Eu reactions as a function of α energy. TALYS calculations are compared to these nine measurements.

Weighted average cross-sections were measured for the production of ^{155}Tb from α+^{nat}Eu reactions for all nine Eu foils of the Eu/Al target stack. Each weighted average was calculated using cross-section measurements from four γ energy emissions following the ^{155}Tb decay. TALYS calculated cross-sections are compared to the weighted average measurements of the

nine foils in figure 6.10. The trend of the TALYS calculated values follows that of these nine measured values for ^{155}Tb, including a comparable maximum cross-section value of approximately 425 mb. However, the TALYS points are shifted to lower α energies by 1.5 to 2 MeV and the TALYS values are lower than measured for higher α energies, i.e. those above the cross-section peak maximum.

6.2.9 Terbium - 156

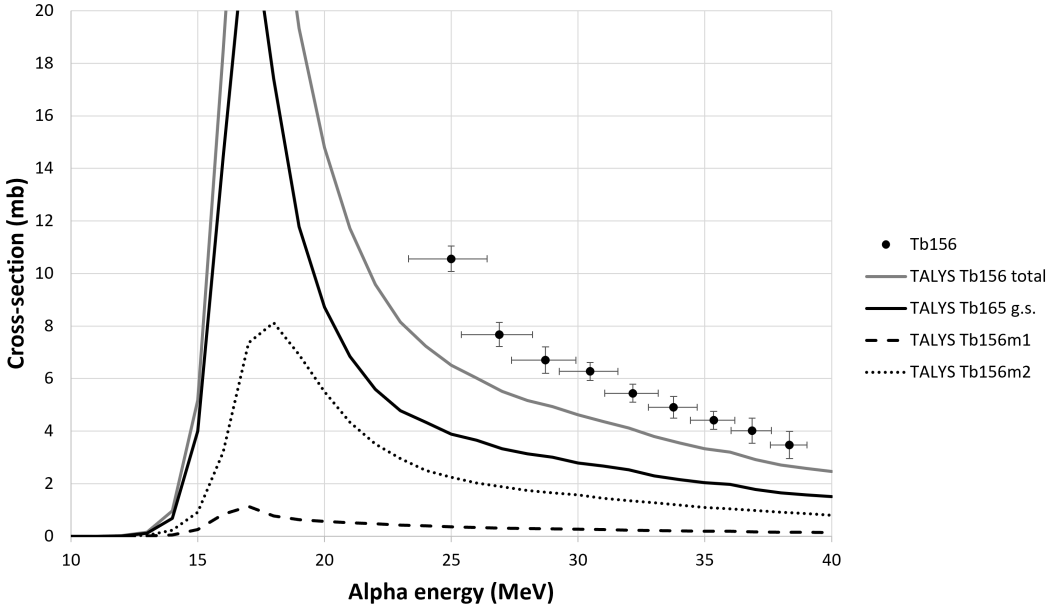

Figure 6.11: Terbium-156 ground-state cross-sections measured using the 534 keV γ emission as a function of α energy. TALYS cross-sections, for the ground state, two excited states and the sum of all three, are compared to these nine measurements.

The final cross-section results for the ^{156}Tb isotope in the ground state were measured using data from one γ energy and the production and effects of the ^{156}Tb isomeric states were not able to be separated. Therefore, when TALYS calculations are compared to the data in figure 6.11, the total production including both isomer states is considered. The experimental

results were summarised in chapter 5, table 5.10.

Similarly to the other isotopes, the TALYS calculations follow the same trend as the measured cross-sections for ^{156}Tb. As with the previous comparisons made above, the cross-section values of the TALYS predictions appear shifted to lower α energies by 2-5 MeV compared to the established data points.

6.2.10 Summary

To enable a view of the bigger Tb production cross-section picture, figure 6.12 collates all the cross-section measurements made from the α+^{nat}Eu reaction data. Comparing figure 6.12 to the TALYS cross-sections in figure 6.1, it is clear that similar trends are followed. However, there are some key differences. For all of the isotopes and isomers measured (except for the ground state of ^{154}Tb) a general shift in the TALYS calculated values can be seen towards lower α energies compared to the data. Using the incident α energy for maxima (and minimum for ^{153}Tb) cross-section turning points for both the TALYS and measured cross-section graphs, the α energy shift was measured to be 1.5 to 5 MeV, where the maxima of the TALYS calculated cross-sections occur at lower α energies than measured for each isotope and isomer.

The other notable difference is the scale of ^{154}Tb^{m1} cross-sections. Out of the three states of ^{154}Tb , TALYS calculations predicted the ground state to have the highest cross-section values (maximum of 313 mb), followed by the most excited ^{154}Tb^{m2} state (maximum of 195 mb), and then only a maximum of 86 mb for the production of ^{154}Tb^{m1}. However, upon measuring these cross-sections, ^{154}Tb^{m1} possessed the highest maximum cross-section of all Tb isotopes and isomeric states, reaching 540(20) mb at 36.86 MeV. In contrast, the measured cross-sections for the ground state and ^{154}Tb^{m2} isomer were comparably low, with

neither surpassing a cross-section of 60 mb in the α energy range measured here.

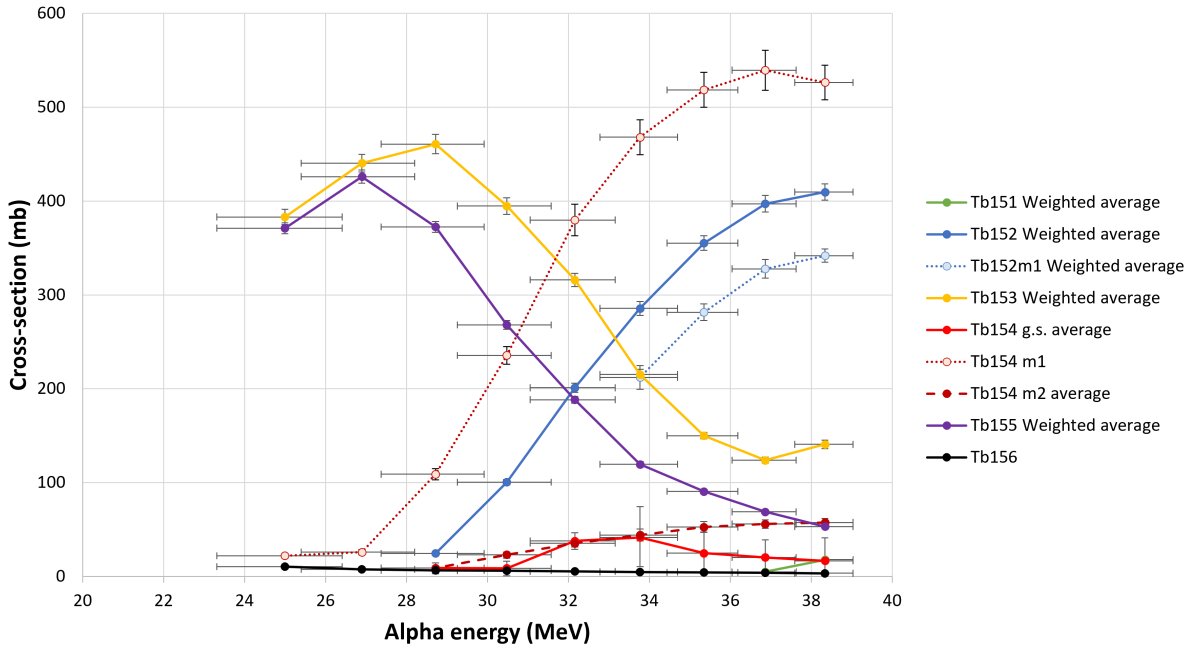

Figure 6.12: Measured cross-sections for the production of Tb isotopes and isomers from α+^{nat}Eu reactions as a function of α energy. The lines between the data points only act as guides for the eye.

As the measured results in figure 6.12, in general, follow a similar trend to TALYS calculations, it is likely that (as initially assessed purely from TALYS predictions prior to the measurements), clean, separate production of medical isotopes ^{152}Tb and ^{155}Tb could be possible using isotopes enriched Eu targets. From the measured cross-section data here, an α energy production window for ^{155}Tb would be between 24.97 and 28.72 MeV. However a slightly lower maximum energy of 26.90 MeV may be better to avoid the production of contaminant ^{154}Tb^{m1}. For maximum, clean production of ^{152}Tb a higher α energy is needed of greater than 36.86 MeV. The upper limit is unknown using these measured data, as the ^{152}Tb cross-section would need to be measured for higher α energies, however, 40 MeV would be a reasonable suggestion from extrapolating using the curvature of the ^{152}Tb data.

6.3 Experimental improvements and future work

As a whole, the foil preparation, irradiation, spectrum collection and data analysis were performed well, with precision and accuracy. However, some aspects of the work could be improved upon. One of the main issues which impacted the data statistics was the unplanned reduction in beam current and irradiation time. The consequence of this was that the irradiated foils need to be moved closer to the HPGe detectors for spectra collection to ensure high enough γ statistics were recorded. This in turn then introduced other variables such as changes in geometric efficiency and the nonlinear effect of intrinsic efficiency with respect to source-detector distance. Although these were able to be corrected for, all of these correction factors have added to the errors of the final results. At the time this was unavoidable due to the ion source filament in the cyclotron breaking. However, if this experiment was repeated, a higher current and longer beam time would be used to ensure that the position of the foils could remain at a fixed distance from the detector for all spectra collection and that the statistics of all the Tb isotopes and isomers were higher.

In future cross-section measurements of $\alpha+^{nat}$Eu reactions, a greater focus should be placed on the measurement of the ^{151}Tb, ^{154}Tb and ^{156}Tb isotopes and their isomeric states. All of these states (apart from ^{154}Tb^{m1}) suffered from low activities and thus low statistics. Moreover, more spectra need to be collected in the early hours after α irradiation has stopped to enable accurate Bateman functions to be fitted to the activity curves of ^{154}Tb and ^{156}Tb ground states.

Due to poor statistics of the ground state and no information on the isomers of ^{156}Tb, the influence of the isomeric states on the ground state were not able to be separated for the purpose of the cross-section measurements made here. Therefore, future measurements should focus on developing a detector set-up capable of measuring the ^{156}Tb isomers and use a Bateman equation to fit the ground-state activity data.

The isomeric state of ^{151}Tb has a 25 second half-life. Therefore, the γ detector set-up used in this work would be inadequate to measure this isomer. For future ^{151}Tb^{m1} cross-section measurements, an on-line γ detector should be used to take very short spectra (less than 25 seconds in length) of a Eu foil immediately after α irradiation has stopped.

With longer irradiation times and a higher α beam current, the absolute production of ^{154}Tb(g.s) and ^{154}Tb^{m2} should be increased and additional cross-section measurements are recommended to verify the cross-section results measured here. With increased initial activities, and thus improved statistics, the effect of the ^{154}Tb^{m2} isomer on the decay of the ground state would be more evident and future analysis of the ^{154}Tb ground state should also include these potential effects.

Despite the improvements mentioned above and potential future work needed on α+^{nat}Eu reaction cross-sections for the production of some contaminant Tb isotopes and isomers, precise and reliable cross-sections have been measured for the medical ^{152}Tb and ^{155}Tb isotopes and the main contaminant isotopes ^{153}Tb and ^{154}Tb^{m1}. This knowledge will enable refinements to the production calculations of the medical isotopes and provides key information to develop this production method further. The next steps to verifying α+Eu production routes for medical Tb are discusses in the following subsection.

6.3.1 Future work to develop medical Tb isotope production using α beams and Eu targets.

Given the calculated TALYS cross-sections follow similar trends to the measured data, with a 1.5 to 5 MeV shift in incident α energy, it could be assumed that the same α energy shift would be present when comparing TALYS calculations of α beams and separate Eu isotopes targets (see figure 6.2) to measured (or actual) cross-sections of α beams and isotopically

enriched Eu target reactions. Therefore, following the same principles for clean isotopes production discussed in chapter 2 where for 151 and 153 isotope enriched Eu targets the cleanest production is possible round the maximum cross-section of the ^{152}Tb and ^{155}Tb isotopes, respectively, then looking at figure 6.12, clean ^{152}Tb isotope production would be achieved been 36.86 and 40 MeV using a ^{151}Eu target and clean ^{155}Tb isotope production would be achieved been 24.97 and 28.72 MeV using a ^{153}Eu target. However, one of the key differences between the measured and TALYS cross-sections is the ^{154}Tb^{m1} cross-section. According to TALYS calculations this isomer would be produced by the α+^{153}Eu reactions. Therefore, to ensure that ^{155}Tb production is not heavily contaminated by the ^{154}Tb^{m1} isomer production then the maximum energy of α+^{153}Eu reactions for ^{155}Tb production should be lowered to 26.90 MeV.

The next experimental measurements needed to develop the α+Eu production route further would be to perform separate α irradiations of both 151- and 153-Eu enriched targets. Because of the reactive nature of Eu, these enriched targets will either be much thicker foils than those used for the ^{nat}Eu cross-section measurements or, most likely, a compressed oxide powder target. Care should be taken to calculate α beam energy degradation though these targets to ensure that the α energy range through the targets does not result in α energies where the cross-section for contaminants are high. Due to the use of thicker targets, these enriched targets should be irradiated with an α beam energy at the top of the ideal productions range. Therefore, the ^{151}Eu target should be irradiated with a 40 MeV beam and the ^{153}Eu targets should be irradiated with 26.90 MeV beam.

The same target thickness, beam energy and current measurement methods should be used as discussed in chapter 3 and the same γ data collection and analyses processes explained in chapters 4 and 5 should be used to ascertain the activity of all Tb isotopes produced. From these results the level of Tb contamination using α+^{151}Eu and α+^{153}Eu reactions will be known. If Tb contamination isotopes are low enough for medical use then a batch of each

enriched irradiated target could be sent to NPL collaborators for chemical target separation [32]. If the yield of the medical isotopes following all these process is high enough then α+Eu reactions could be a valid production method for medical isotopes ^{152}Tb and ^{155}Tb.

If the ^{154}Tb^{m1} does prove to be a substantial contaminant, then calculations and further experiments could be performed to determine if using lowering beam current and longer beam irradiation times would reduce the proportion of the shorter lived, 9.43 hour, ^{154}Tb^{m1} compared to the longer lived, 17.07 hours and 5.25 days, medical isotopes ^{152}Tb and ^{155}Tb, respectively.

6.4 Final thoughts

In the end, the main aim of this work was to measure the $\alpha+^{nat}$Eu cross-sections using the MC40 cyclotron, which was achieved for the production of ^{151}Tb, ^{152}Tb^{m1}, ^{152}Tb, ^{153}Tb, ^{154}Tb^{m2}, ^{154}Tb^{m1}, ^{154}Tb, ^{155}Tb and ^{156}Tb. However, this experiment was also successful on a more general scale. Measuring absolute nuclear reaction cross-sections is a highly sensitive and detailed process, and the method discussed in this thesis had not been previously established at the Birmingham Cyclotron Facility.

In most cross-section measurements, cross-section-calibration foils are often used in between layers of the foil of interest. The cross-sections of these calibration foils have been previously measured. These previous measurements are then used to help determine the beam energy and degradation as the beam travels through the foil stack, to then calculate the beam energy in the foils of interest for the cross-section measurements. The activity of these calibration foils are also used to help measure beam current delivered to the target. This dependence on previous cross-section measurements of other isotopes (e.g. ^{nat}Ti(α,x)^{51}Cr or ^{nat}Cu(α,x)^{66}Ga [71]) would automatically introduce a systematic error if these "known"

calibration cross-sections were incorrect. Moreover, in cross-section measurement publications, the thickness of the foils are either not measured independently from the manufacture value, which are often supplied with a quoted error of 25%, or, if the thickness of the foil is independently measured, it is determined by weighing the foil. The use of weighing scales can be very accurate as long as the scales are level and regularly calibrated with a secondary or primary standard and the mass of the foil is not comparable to the precision of the weighing scale. This method also relies on the need for accurate foil area measurement which will add an additional level of error to the final thickness measurement. Designing a cross-section measurement method from scratch provided the opportunity find new ways of measuring and improving on current techniques commonly used in the cross-section measuring field. Therefore, when designing the cross-section experiment, discussed in this thesis, great emphasis was placed on ensuring the beam energy, beam current and foil thickness were accurately and precisely measured and did not depend on other cross-section measurements or ill calibrated equipment.

The nuclear group at the University of Birmingham run a diverse range of nuclear experiments and one of the benefits of this is the ability to easily share knowledge and equipment. For example, the beam energy and foil thickness measurement techniques used in this thesis were tailored and developed for the purpose of cross-section measurement from techniques used in fundamental nuclear physics experiments. The consequence of this was that, instead of relying on knowledge of the cyclotron deflector position and its calibration to provide a beam energy, typically with an error of at 0.5 MeV, the gold foil and DSSD detector set-up enabled an accurate and precise reading of 39.06±0.21 MeV. This method relied solely on fundamental kinematic physics, precisely known α calibration source energies and well understood light particle energy degradation through materials. Similarly, the triple α energy degradation measurement of Eu and Al foil thicknesses also only relied on well known and understood light particle energy degradation through materials. This enabled a Eu foil

thickness measurement of 21.3±0.5 μm, which was a vast improvement on the precision of the manufacture's value of 25 μm ± 25%. Moreover, the 3.7 μm difference between the manufactured and measured thickness values would have made a significant difference in the cross-section calculation which relies on foil thickness as one of its parameters, and the drastic reduction in the relative error on the thickness value also reduced the percentage errors on the final cross-section results. For fundamental nuclear physics experiments, the MC40 cyclotron beam current is measurement from a plate at the end of the beam line. However, for cross-section measurements this was improved upon by the addition of a Faraday cup at the end of the beam-line containing the target. This was isolated from the rest of the beam line using an insulator and increased the accuracy of the beam-current measurement.

Using information learnt from preliminary $\alpha+^{nat}$Eu reaction experiments and developing techniques from other areas of nuclear physics, accurate and precise measurements of the initial incident α beam energy, foil thickness and beam current were developed for the purpose of nuclear reaction cross-section measurements at the University of Birmingham. The subsequent γ spectroscopy and data analysis techniques developed and discussed in chapters 4 and 5 are also now available for others to use for future cross-section measurements at the University of Birmingham.

The cross-section method and data analysis developed enabled the successful cross-section measurements of the medical and contaminant Tb isotopes production from the $\alpha+^{nat}$Eu reactions. These cross-sections results will play an important role in the next stages of developing this route of medical Tb production. Moreover, the relative ease of producing isotopically enriched Eu targets compared to Gd targets could prove to be a key factor in the future of α+Eu, Tb production.

A final but important point to end this Tb work on is the revised, new half-life measurements made during the cross-section measurement process. Accurate and precise nuclear half-lives

are crucial for imaging and dosimetry in nuclear medicine. Therefore, the more precise ^{152}Tb and ^{155}Tb half-life measurements of 17.07(7) hours and 5.25(1) days, respectively, are of importance for future medical work with these isotopes.

Chapter Seven

Industrial PET imaging motivations and theory

7.1 Introduction

As mentioned in the introduction to chapter 1, over the last few decades positron emitting isotopes have been used to study flow inside industrial machinery. The method commonly used is Positron Emission Particle Tracking (PEPT). Particles ranging in material and size (tens of microns to several millimetres) are either exposed to a particle beam to become radioactive (emitting positrons) or are imbued with radioactive nuclei such as ^{18}F. One or more of these particles are placed into pieces of machinery under investigation and are tracked through the machine using γ detectors in coincidence. The position and velocity of these particles are recorded and from this, the manufacturers can improve their machinery.

However, standard PEPT only observes one or a few particles at a time and this information is extrapolated to infer the behaviour of all the particles in the system. In medical PET imaging, fluid positron tracers are used and this provides collective movement information. The distribution of radioactive fluid can be seen and the collective flow observed. However,

the potential benefits of this information have rarely been explored for industrial purposes.

This chapter will discuss the motivations behind the use of PET for industrial imaging in more detail as well as explain the how PET images are produced: from 511 keV photon production and detection, to image reconstruction.

7.2 Motivation

Many machines are contained within opaque (often metal) walls. This limits the ways one can see what is happening inside the device. Commonly, the understanding of the internal workings comes from changing and measuring what goes into the machine and measuring how this affects what comes out. Some monitoring methods (e.g. visual or electronic) can provide 1D or sometimes 2D information. However, PET and PEPT provide highly useful 3D information on the distribution and movement of material within a machine. The ability of the 511 keV photons (emitted by PET/PEPT tracers in the machine) to pass though many types of industrial casing and be detected allows industrial partners to gain details and specific information about the inner workings, so improvements to the devices can be made.

A highly relevant topic of today is climate change. Over the past few decades great focus has been placed on reducing greenhouse gas emissions. Atmospheric improvement devices such as carbon absorbers and catalytic converters can be used for this purpose (see appendices I and J for more details). The effectiveness of these devices is studied by measuring the output gases and comparing them to the input gases. However, if the internal movement of the gases were measured there is potential to understand the processes more and further improve these devices. PET imaging could be used to elucidate the inner workings of carbon absorbers and catalytic converters.

Table 7.1: A selection of positron emitting radioactive isotopes suitable for producing gaseous or liquid tracers for PET imaging, and their half-lives [15] and production reaction carried out by the MC40 cyclotron [72].

Isotope	Half-life (minutes)	Production reaction
^{11}C	20.364 ±0.014	^{14}N(p,α)^{11}C
^{13}N	9.965 ±0.004	^{16}O(p,α)^{14}N
^{15}O	2.037 ± 0.003	^{14}N(d,n)^{15}O
^{18}F	109.77 ± 0.05	^{16}O(^{3}He,p)^{18}F ^{18}O(p,n)^{18}F

The ability to observe the collective movement using PET rather than PEPT is particularly relevant when studying the movement of liquids and especially gases. This is because PEPT is limited to solid tracers which can not always accurately mimic the movement of the surrounding liquids and gases which are under study. However, PET imaging traces can be made in a variety of liquid and gaseous forms (see table 7.1 for details on a selection of PET isotopes that can be made using the MC40 cyclotron at the University of Birmingham). Due to this advantage, PET imaging could be used to study the movement of both liquids and gases in industrial devices.

There are currently no published papers looking at PET imaging used to study the movement of the gases inside carbon capture devices, however, there was work carried out by a previous Master's student at the University of Birmingham (see appendix I for more details) [73]. As well as clearly seeing the geometrical distribution of the gases within the system, this study could provide evidence to support current gas distribution models. There was a study carried out in 1992 [74] on the gas distribution in catalytic converters using PET imaging (see appendix J for more details). One dimensional PET images were produced at the time, however, PET imaging has improved greatly since the NeuroECAT PET machine used in this study. Currently, no follow-up studies have been carried out, thus one of the aims of using the GE discovery PET/CT scanner is to improve on the work previously done utilising the 3D imaging of modern medical PET scanners.

Similarly, the investigation into the inner workings of some industrial machinery requires the study of liquid flow through fine mesh which can prove problematic for solid PEPT imaging tracers. Therefore, PET imaging would provide an appropriate solution to study these devices. A company, CALGAVIN [75], produce stationary mixers. These are specifically designed and made pipe inserts consisting of metal spirals and loops which generate the appropriate vortexes within the fluid to mix or move it to where is necessary to provide optimal heat transfer for the application. In the study presented in section 8.2, CALGAVIN wished to determine whether fluid flowed through the centre of two insert designs. They had previously used dye to determine the rate of flow and the 2D distribution by observing the outside of the pipe, however, they needed a method which would allow a cross-sectional view through the pipe. PET could provide this.

Before new research using the PET scanner could take place, the GE Discovery ST PET scanner needed to be calibrated and quality assurance tests needed to be carried out to find the position and energy resolution, as well as timing resolution. These tests provided vital information on the limitations of experimental work and the best imaging settings to use. Moreover, it was important to know how much activity will be needed to image a device as well as the physical dimension limits of a device to avoid distortion of images at the edges of the field of view. Therefore, initial investigations were carried out to determine these properties of the scanner. These are discussed in section 8.1.

7.3 Theory of PET imaging

This section of the chapter discusses how positron emission is used to form a PET image. The basic principles of coincidence detection, and contributions to background through random and scattered events are explained. An overview of image reconstruction methods used

by the GE Discovery ST PET/CT scanner which are Filtered Back Projection (FBP) and Ordered Subset Expectation Maximisation (OSEM) is also included.

7.3.1 Positron production and detection

PET images are formed using positron emitters which undergo β^+ decay. This occurs when a nucleus has more protons (Z) than is stable for the nucleus (N) of atomic mass (A),

$$ {}^{A}_{Z}N \rightarrow \quad {}^{A}_{Z-1}N' + \beta^+ + \nu_e \tag{7.1} $$

(where ν_e is an electron neutrino). These are not common, naturally occurring nuclei, so for PET scans to be possible the radioactive tracers (sources) must be made by cyclotrons. ^{18}F was the radioactive nuclide used for all the work discussed here and was produced using either one of the two methods described in equations 7.2 and 7.3. The ^{3}He or proton beams produced by the MC40 cyclotron were 35 MeV and 10.8 MeV, respectively.

$$ {}^{3}He + H_2^{16}O \quad \rightarrow \quad H_2^{18}F + p \tag{7.2} $$

$$ p + H_2^{18}O \quad \rightarrow \quad H_2^{18}F + n \tag{7.3} $$

A PET scanner does not detect the positron (β^+) directly. Once the positron is emitted it slows down in the medium and once it reaches rest (or near rest) it briefly forms positronium with an electron from its surroundings and they then annihilate one another. To conserve momentum and energy, the electron and positron form two photons travelling back-to-back, each with energy equal to the mass of the electron (and positron), 511 keV. These two photons are detected in coincidence by the γ detectors of the PET scanner.

Often the detectors used in PET scanners are scintillating detectors either BGO (bismuth

germinate, $Bi_4Ge_3O_{12}$) or LSO (lutetium oxyorthosilicate, Lu_2SiO_5) due to their high densities (7.13 and 7.40 g/cm^3, respectively [76]) and thus greater efficiency at absorbing high energy 511 keV photons. Unfortunately, greater efficiency comes at the cost of energy resolution. Compared to NaI scintillator crystals (often used in SPECT imaging) BGO and LSO crystals have relatively poor energy resolution. For example, BGO possesses a 16% energy resolution at 511 keV [77] whereas the energy resolution for NaI is approximately 8% at 511 keV.

When a 511 keV photon strikes the crystal of these scintillating detectors the photon can interact with an electron within the crystal via any of the pathways discussed in section 4.1. This electron then causes other electrons within the crystal to become excited from the valence band to the conduction band. The crystal structure of BGO and LSO crystals are such that the crystal is transparent to the energy of the optical photons emitted as the electron de-excites back to the valance band. The total number of optical photons produced is proportional to the number of electrons that were excited which is proportional to the initial energy deposited by the 511 keV photon in to the crystal.

[53][78] The optical photons produced in the scintillation crystal are then guided via the design of the crystal and its casing to the Photo-Multiplier Tube (PMT) which is optically connected to the crystal. The optical photons are absorbed by the initial structure in a PMT, the photocathode. The number of electrons produced by the photocathode is proportional to the energy deposited by the 511 keV photon. To amplify the signal, the electrons emitted by the photocathode are accelerated by a potential difference to a series of dynodes, as shown in figure 7.1. At each dynode the electrons strike the surface and release 8-10 times more electrons. If, for example, there are 10 dynodes in a PMT then there will be an increase of up to 10^{10} electrons. This amplified signal is collected at the anode and processed by the preamplifier. The electronic signal is then passed on to the subsequent signal processing electronics. However, the preamplifier also acts as a barrier to prevent changes in the signal

processing units to affect the detector electronics.

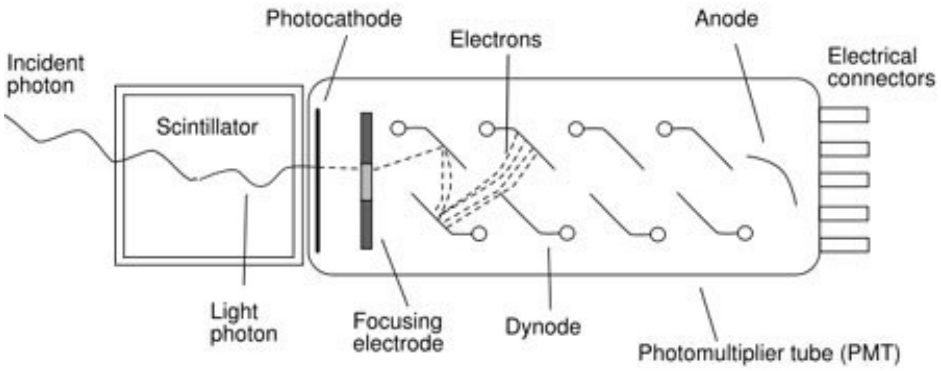

Figure 7.1: A simplified diagram of a scintillating crystal and PMT, showing its main features [79].

In most medical PET scanner systems a large number of these detector units (crystals, PMTs and preamplifiers) are typically arranged in a ring structure. To provide improved spacial resolution of the PET images, the scintillator crystal blocks are usually segmented. A grid is cut into the crystal, but cuts do not go through the entire crystal. The rear of the block (coupled to the PMTs) is uniform (uncut). In many systems, the each crystal is attached to 4 PMTs (an example of these is shown later in figure 7.8 which depicts a GE Discovery ST PET scanner crystal block and PMTs). When an interaction of a γ-photon occurs in the crystal, the optical photons produced not only inform the energy deposited by the γ-photon, but, the optical light distribution between the 4 PMTs changes depending on which segment of crystal the original γ-photon interacted. This enables a more precise location of the 511 keV photon interaction in the crystal, thus improving the spacial resolution. It is important to note that one of the most crucial calibrations a PET scanner must perform is to ensure that the detector and electronic settings are able to used the intensity information form each set of 4 PMTs to accurately locate which segment of the crystal the 511 keV interacted with. This is known as crystal mapping.

Several sets of scintillating crystals attached the 4 PMTs (detector blocks) are groups together

in a module. Each module has its own set of preamplifiers and electronics, controlled by a microprocessor. Several modules are then arranged in the traditional medical PET scanner ring structure which will encircle the body of a patient. The specific detector ring structure of the GE Discovery ST PET scanner is described in detail in section 7.4.

A coincidence processor compares arrival times of signals from all the modules in the ring, and identifies prompt coincidences where the two signals arrive within a specified resolving time, τ. The length of time for each PET image and the number of image frames are pre-set in a protocol before the scan. As the data arrives during the scan the coincidence events are stored either as sinograms (which are explained in appendix K) or in listmode which records each coincidence with a time stamp of when it occurred in the data collection process. Sinograms reduce the memory required to store the data collected, however, listmode allows greater flexibility when reconstructing data, enabling the duration of each image frame to be changed from the original pre-set data collection protocol.

While a scan is being collected, delayed coincidences are also stored. This are used to measure the rate of random coincidences. This is explained in more detail in section 7.3.2 and is useful to measure when establishing the optimal tracer activity to use when imaging an object (see section 7.4.2 for more detail).

The coincidence data collected during a scan enables tracer location and image production. The details of this and how scattered and random coincidences occur are discussed in section 7.3.2.

7.3.2 Identifying a point source

As previously discussed, medical PET scanners consist of adjacent rings of detectors working together to detect coincident photon signals. This enables the tracking and imaging of the

whereabouts of a radioactive source placed within the subject.

Figure 7.2 demonstrates how PET source location works for a point source where a large number of positron emitters are located in a single point. In figure 7.2a, a positron is emitted from the source and a set of back-to-back photons are detected in “coincidence" by two detectors in the scanner. A line can then be drawn between these two detectors, known as a line of response (LOR), see figure 7.2b. It can be deduced that the source lies somewhere on this line. The source will emit more than one positron so more LORs are made (figure 7.2c). Where the LORs overlap is the location of the source.

It is important to note that in order for two photons to be recorded as “coincidence" photons, they must arrive at each detector within a pre-set coincidence time window, τ, of each other. However, sometimes “coincidence" photons are not from useful events. For example a coincidence signal can be caused by a scattered photon as shown in figure 7.3 (a) where the LOR from this event would misplace the actual location of the source. In other instances (see figure 7.3 (b)) photons from separate annihilations may arrive in coincidence with each other also providing misinformation - this is referred to as a random coincidence.

Scatter events are more common in more dense and larger volumes of material and can be corrected for using attenuation information from CT images in PET reconstruction as well as by gating on the energy of the photon. Lead collimating septa placed in between detector crystals also reduces the proportion of scattered coincidence events [80]. However, accurate scatter correction is difficult to completely achieve.

To reduce the time needed to obtain an acceptable PET image, higher tracer activities should be used, however, the number of random events increases with activity. Therefore, a balance must be found for how much activity should be used for an image before random events become too great a problem. This is discussed in more detail in section 7.4.2. Although not relevant for the GE Discover ST PET/CT scanner, more modern PET scanners also use

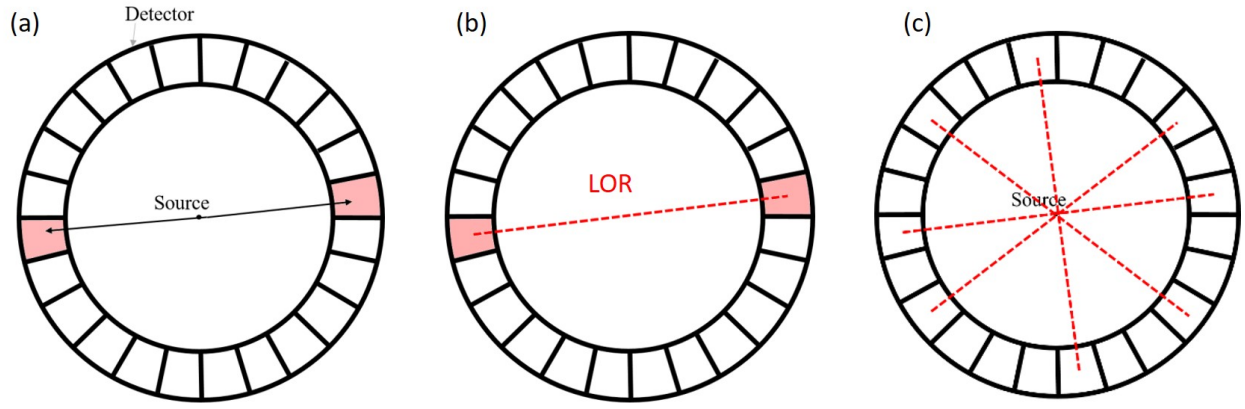

Figure 7.2: (a) A positron being emitted at the source and two back to back photons being released when it annihilates with an electron. The two photons are detected (by the highlighted detectors). (b) From these two photons an LOR (shown by a red dashed line) is drawn. (c) More positrons are emitted, further LORs are drawn and an image region where the source lies is produced from the back projected LORs.

time of flight (TOF) [81] [82] information to improve image resolution as well as decrease noise from random and scatter events (i.e. increasing signal to noise ratios (SNR)).

This simple example of locating a single point source can be extrapolated when imaging more complex objects such as the distribution of a tracer in a body or the distribution of fluid within a machine. Standard tomographic approaches are used to reconstruct the image from the measured projections which are stored in either sinogram or list form. The two basic approaches are analytical, based on filtered back projection (FBP), or iterative.

In its simplest form, backprojection consists of projecting the coincidence data back along the LORs. In the same way as for the point source in figure 7.2, this results in an image of the object having the correct features but blurred due to the tails of the LORs (see figure 7.4). This blurring can also be understood as an imbalance of sampling between low and high spatial frequencies. To remove the blurring a filter is applied during backprojection - this is "filtered backprojection" (FBP). More details of all this are given in appendix K.

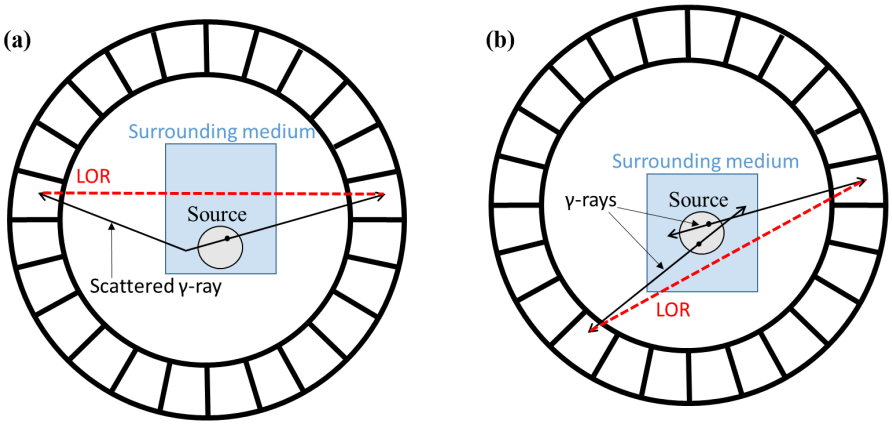

Figure 7.3: (a) A demonstration of a scatter coincidence event. A positron being emitted at the source and two back to back photons being released. One of the photons is scattered before it reaches the detector causing an LOR which does not pass through the location of the source. (b) A demonstration of a random coincidence event. Two sets of back to back photons emitted at the same time. One photon from each pair cause a coincidence event to be recorded and the LOR from this does not pass through the location of the source.

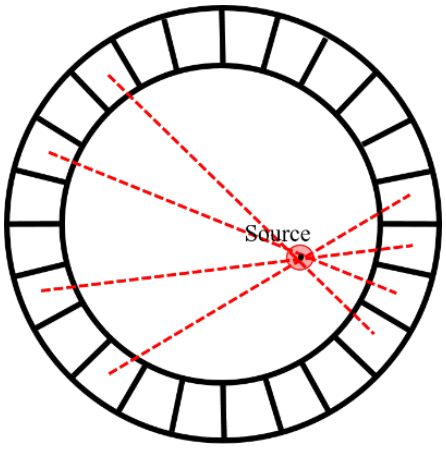

Figure 7.4: The tails of the LOR back projections cause the spreading out of the image, shown as a larger red circle around the black point source.

The second method of reconstruction, by iteration, is commonly used and is explained in more detail in section 7.3.3. The type of iterative reconstruction used by the GE Discovery PET scanner, OSEM, is also discussed.

How the data is collected can also affect the data processing, section 7.3.4 briefly explains the difference between "2D" and "3D" PET data collection. The section also informs the reader about the types of PET image slices that are used when looking at the PET data. The names of positions within the PET scanner are often used when explaining features within the images and describing the image slice being used, therefore, these are also include in this section.

7.3.3 Iteration method

Rather than simply back projecting the data collected (with or without filters), iterative reconstruction methods start with an initial guess of the image, for example, a uniform image of the average count rate. The "guess" is then projected forward and these projections are compared with the collected data projections and the prediction is adjusted [83] (page 278). This process is repeated until the forward projections of the predicted image and the collected projection data converge.

This can be a powerful reconstruction tool as attenuation and detector specific effects on the collected data can be accounted for in the iterative process. For example, FBP makes the false assumption that the PET detector system has perfect spatial resolution. Iterative algorithms can be constructed to account for real detector response. However, it should be noted that the non-linear nature of some iterative processes may cause the signal to noise ratio (SNR) and the spatial resolution to vary through an image. The consequences of this should be investigated ([83] pages 312-312). In addition to attenuation and detector corrections,

the blurring effects cause by the variation in positron range and depth of interaction could be accounted for in an iterative algorithm.

OSEM

The Maximum likelihood (ML) method of iterative reconstruction was developed by Rockmore and Macovski [84] and includes the statistical Poisson nature of the emitted signal and detection capabilities [85]. Shepp and Vardi [86] produced the Expectation Maximisation (EM) algorithm to solve ML reconstruction. EM proved to be a desirable way to solve ML reconstruction as it guarantees non-negativity, convergence and preserves data count between iterations, however, the process is slow and requires multiple iterations to converge [85] .

Hudson and Larkin aimed to improve the speed of EM and developed Ordered Subset EM (OSEM) reconstruction, the details of which are discussed in [87]. In its simplest terms, the data are split into ordered subsets, the EM algorithm is carried out on the first subset of data and the result from this is carried forward to the next subset for which the EM algorithm is used again, and so on. One full iteration is considered to be when each subset has been processed once. In OSEM, increasing the number of ordered subsets reduces the number of iterations and inter speeds up the EM reconstruction process. Figure 7.5 is taken from Hutton's and Hudson's [88] paper and demonstrates the power of OSEM by reconstructing the same image of a brain using three methods. Here the 2 iterations OSEM image (right) is comparable in quality to the 190 iterations EM reconstruction (centre) for which both are clearly far superior to the 10 iteration EM image.

Although OSEM does not always exactly converge to ML solutions, its speed means that it is often used for iterative reconstruction across many PET scanner systems. The GE Discovery ST PET/CT scanner used for industrial PET investigations could perform either FBP or

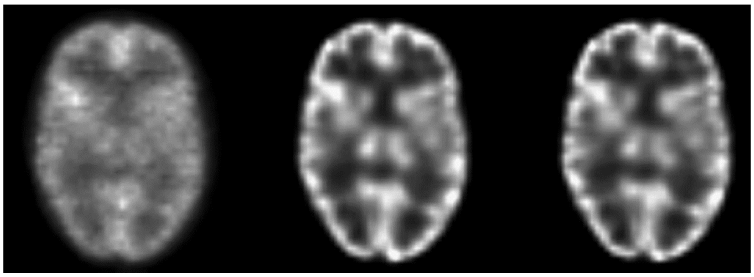

Figure 7.5: Left: EM reconstruction (10 iterations) modelling attenuation only. Centre: EM reconstruction (190 iterations) with model of attenuation, 3D distance-dependent collimator response and 3D object shape-dependent scatter. Right: dual matrix OS (2 iterations) using same model as in the centre. (This figure and caption are copied from Fig.6 in Ref. [88]).

OSEM image reconstruction.

7.3.4 2D and 3D PET imaging

All modern medical PET scanners produce multiple 2D cross-sectional slices of the object being imaged. The slices can then be stacked to form 3D images of the object. There are three points of view these images can be dissected through: axial, sagittal, and coronal. Figure 7.6 provides an explanation of these imaging planes as well as the three directions an object can be viewed from: Left to Right (LtoR); Superior to Inferior (StoI); and Anterior to Posterior (AtoP).

[78] However, in this instance "2D" and "3D" PET imaging has a different meaning. A standard circular array PET scanner will have rings of detectors. In "2D" PET imaging lead collimating septa are used in between separate detector rings. In this mode the scanner records coincidences only between detectors which lie on the same ring as one another and half the ring either side. This reduces the number of false coincidence detections from random and scattered. However, if the collimating septa are removed and the PET scanner records coincidence data between detectors regardless of the rings they belong to then the images

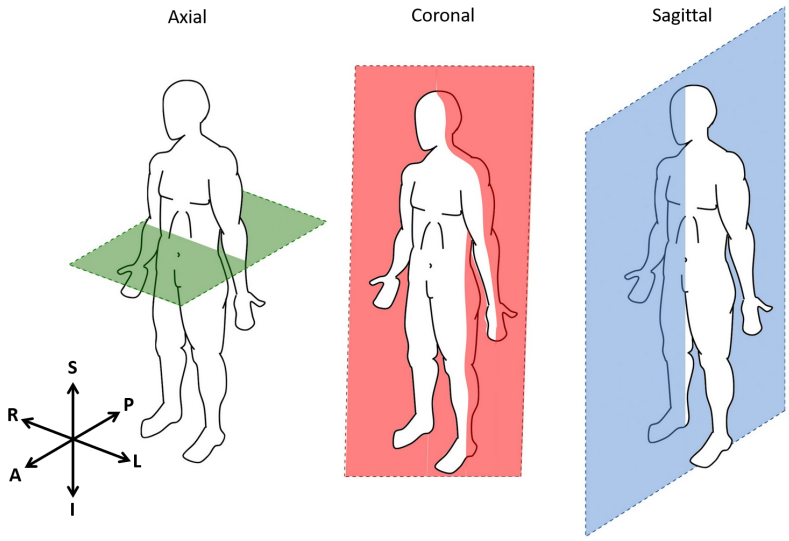

Figure 7.6: The three planes of imaging taken from [89]. Axial slices are perpendicular to the superior, S, to the inferior, I, (head to feet) direction of the object. Coronal slices are perpendicular from Anterior, A, to Posterior, P, (front to back) direction. Sagittal slices are perpendicular from the left, L, to right, R, direction.

produced are known as "3D" PET images. This "3D" method increases the efficiency of the detector 4-5 times that of the "2D" method [90] . However, "3D" imaging requires more computing power to reduce noise from false (random and scatter) coincidences which are no longer removed by lead collimating septa. The GE Discovery ST scanner at the University of Birmingham uses removable collimating septa between each ring to transform from a "2D" PET scanner to "3D" scanning capabilities.

For all the research and calibration carried out and discussed in this thesis, the collimating septa were left in between the PET rings. Thus all the images were taken in a "2D" PET imaging format.

7.4 GE Discovery ST PET scanner

[78] The GE Discovery ST PET/CT scanner consists of a CT (x-ray computerised tomography) scanner on the front and a set of PET detection rings at the rear. Figure 7.7 shows a photograph of the scanner. It was released on the market in 2003 and the specific scanner at the University of Birmingham was originally bought by the Queen Elizabeth hospital, Birmingham in 2005 and transferred to the Positron Imaging Centre (PIC) in late 2015.

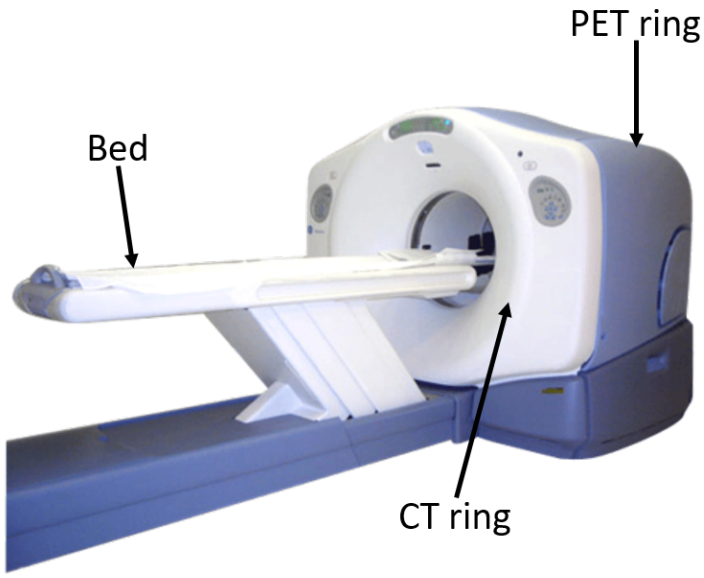

Figure 7.7: GE Discovery ST PET scanner [91].

PET imaging is the main focus of the scanner's use, therefore, the CT part of the scanner was not used due to the health and safety risk it poses without the correct infrastructure (e.g. a lead lined shield wall for the operators to stand behind). However, it is important to note that for larger objects with varying density, where attenuation effects can have a significant impact on the image quality, attenuation corrections obtained by CT images are required for quantitative PET imaging. Fortunately, for the initial study with CALGAVIN, the device

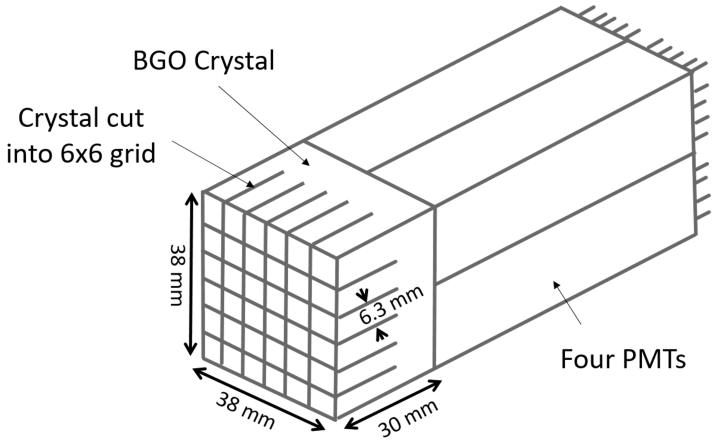

Figure 7.8: BGO crystal block attached to four PMTs.

under investigation was well localised to a known pipe (of 30 mm interior diameter) and had roughly uniform attenuation.

The PET detector section of the scanner was constructed such that 35 modules are arranged in a ringed structure and there are 2 sets of module rings. Each module consisted of 8 BGO crystal blocks in a 2 × 4 matrix. Each of these crystal blocks was cut into a 6 × 6 crystal grid attached to 4 PMTs as shown in figure 7.8. There are four crystal blocks arranged next to each other to form the 15 cm length of the Axial Field Of View (AFOV), see figure 7.9.

As mentioned in section 7.3.4, the "2D" imaging format was used for all data collection. This means that each 6.3 × 6.3 mm crystal forms coincidences with the crystals on the same 6.3 mm ring and half the crystals on either side. There are 24 of these crystals along the AFOV. As each crystal forms coincidences with a total of 2 crystals this would produce 48 axial slices. However, as the end crystals each miss a half crystal to form coincidences with, then the total number of axial slices in a PET image is 47. Therefore, as labelled in figure 7.9, each axial slice covers a physics length of 3.27 mm. However, due to the nature of the detectors and the interaction of positrons in matter, the axial resolution would be poorer than this and needed to be measured. The number of coronal and sagittal slices of the final

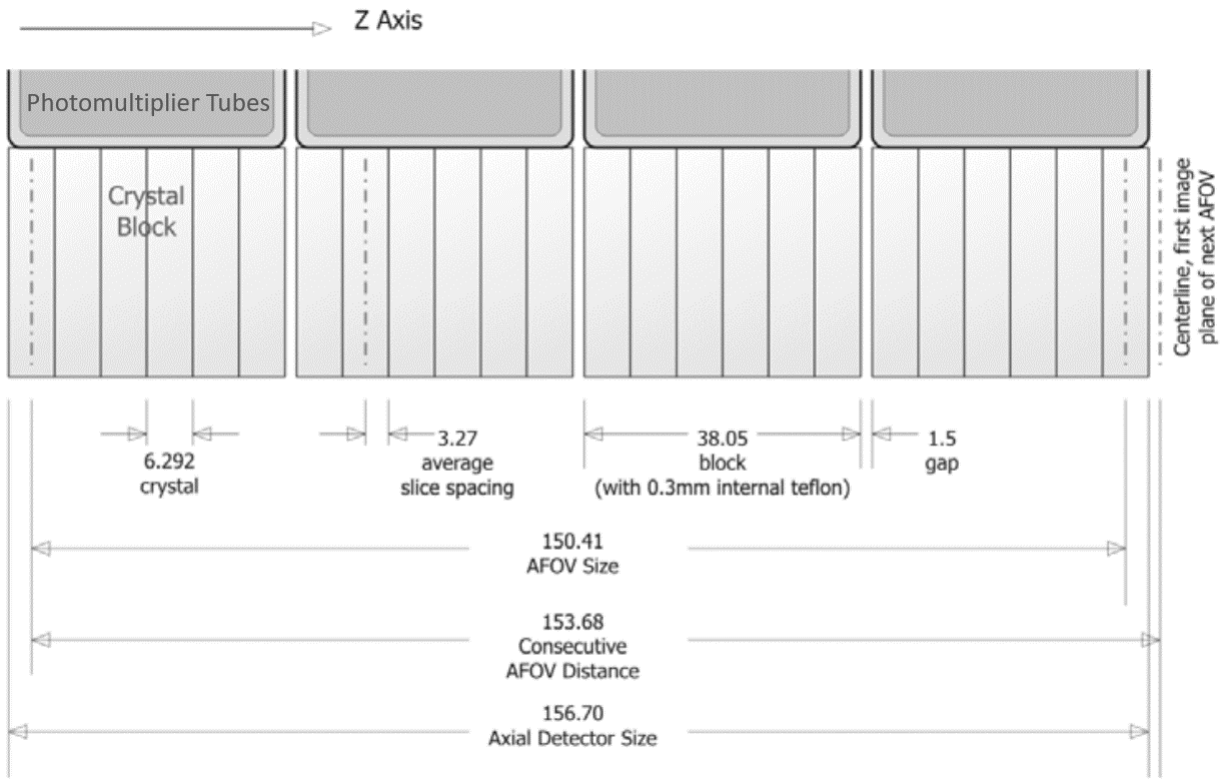

Figure 7.9: Diagram of the PET detector arrangement parallel to the axis of the scanner. The length of the AFOV is given for the image reconstruction and the physical detector AFOV are labelled. This diagram was taken from [92](page 308).

PET image depends on the size of the reconstruction matrix used. For example a 256 × 256 reconstruction matrix produces 256 coronal and 256 sagittal slices.

7.4.1 Calibration and quality assurance of PET scanner

[78] In order for any information to be gained from images produced by the PET scanner, images of known objects must be taken and analysed to check that investigative images are reliable. In addition to this it is important to know with what precision the information gleamed from the images can be trusted.

[78] These assessments are commonplace for all medical scanners and NEMA guide lines [93]

are often used as a reference for quality assurance testing methods. The variation in image resolution and quality needed to be ascertained before being able to draw conclusions about unknown systems. These investigations and their results are described in section 8.1.

7.4.2 Noise Equivalent Counts

Before investigative PET imaging of industrial devices could occur, the amount of activity to be used in the images needed to be established. Increasing the activity improves the quality of the images to a point, after this the number of random coincidences become too prevalent and increasing activity no longer improves the image and may cause a decrease in image quality. By detecting delayed coincidence events, the contribution of random coincidences can be determined and subtracted from the image, but this subtraction causes an increase in statistical noise. Measuring the Noise Equivalent Counts (NEC) provides a good way to address this.

[78] NEC are the "number of counts which would give the same signal to noise ratio on the basis of simple Poisson statistics" [94]. To obtain this value, the number of random counts being produced needs to be known. The prompt counts from a scanner are formed of random (R) and true (T) coincident counts collected when a γ rays starts the coincidence window timer and a second γ is detected within the time frame τ (as discussed in section 7.3.2). If the starting of the coincidence window was delayed by a time longer than τ then the only counts collected are random coincidence.

The following are definitions of the types of counts [94]:

$$\text{Prompt (P)} = \text{T+R} \tag{7.4}$$

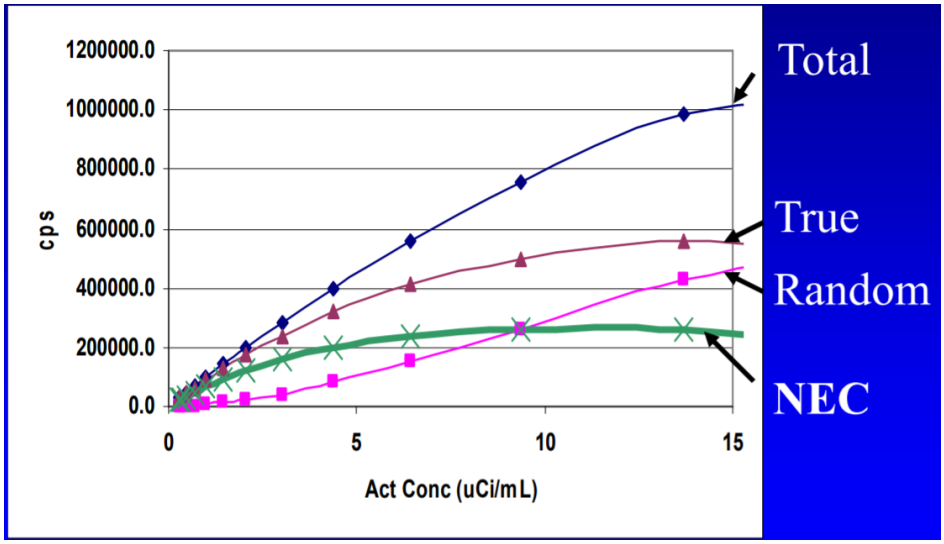

Figure 7.10: An example total true, random and NEC counts against activity. This graph was taken from [95].

and

$$\text{Delay (D)} = \text{R}, \tag{7.5}$$

therefore,

$$\text{T} = \text{P} - \text{D}. \tag{7.6}$$

NEC is defined as,

$$NEC = \frac{(P-D)^2}{(P+D)}, \tag{7.7}$$

which can be written as

$$\rightarrow NEC = \frac{T^2}{(T+2R)}. \tag{7.8}$$

As mentioned previously, increasing the activity improves the quality of the image. However, because rate of random counts increases non-linearly, there comes a point where there is limited/no improvement in image quality with increase in activity. This is reflected in the plateauing of the NEC shown in the example graph in figure 7.10.

[78] A graph, like the one in figure 7.10, showing total, true, random and noise equivalent

counts is a common assessment made of PET scanners. It can be carried out by taking a short lived positron emitter such as ^{18}F and allowing it to decay in the scanners FOV while recording the prompt and delayed (random) counts. This information is used in equations 7.6 and 7.8 to form the NEC data points.

To establish the optimal activity for imaging using the GE Discovery ST PET/CT scanner, the data for a NEC graph was collected and the results are discussed in section 8.1.4.

Chapter Eight

Industrial PET imaging experimental work

In this chapter the practical elements of the PET investigation and the analysis and results of these are discussed.

Before, the PET scanner could be used to investigate machinery, a full calibration of the scanner was needed. This included energy calibration, timing calibration between detectors and crystal position calibration. Moreover, investigations into capabilities of the scanner were required to understand imaging limits and enable optimisation of the resultant images. For example, determining the NEC variation with activity allows the identification of the optimal activity range of tracer to be used in a future investigation. It was also important to know the types of information that could be extracted from the images, therefore, how the spatial resolution of images changed depending on the position of the sources within the field of view was measured as well as the how image quality changed depending on the reconstruction methods used and length of data collection. All of these preliminary investigations along with the work carried out to fix the initial faults within the scanner system are described in detail in section 8.1.

After the scanner was calibrated and parameterised, a heat transfer solutions company, CALGAVIN, approached with a question about the flow of fluid through two different designs of their stationary mixers; the Bubble Bursting (BB) insert and the Harris insert. The main question posed was – is there any fluid stuck or flowing through the centre of the pipe with either insert? Section 8.2 discusses, in more detail, the reasoning behind why it was important to know this information as well as the results found. Other types of information that could be obtained from these data were also investigated and discussed. From this work a lot was learnt on how to improve future investigations of this type and the variety of information PET imaging could bring to industrial investigations.

8.1 Preliminary work

8.1.1 Initial faults

The GE Discovery ST PET/CT scanner currently at the University of Birmingham's PIC originally came from the Queen Elisabeth Hospital, Birmingham in 2015. Until 2017 it had not been used regularly and was no longer in a working state. From October 2017 till April 2018 work was focused on finding and solving the various problems that had arisen. Initially the computer operating system would not boot up fully. One of the DARC (data and reconstruction computer) discs had become faulty and required replacing. Once the system turned on fully, two more faults were identified. One of the crystal block preamplifiers had broken and was short circuiting the detector ring. The offending module this block belonged to was found by measuring the potential difference across half of the detector ring to assess which half of the ring the break had occurred. Then half of the half was tested and so on till the module was identified and the electronics board of this module including the broken preamplifier was replaced. Furthermore, one of the data control modules had developed a

fault and was identified by rotating the modules around and seeing how the error messages changed. Once identified, the module was replaced.

These were the major faults with the scanner that were resolved. However, due to the age of the scanner, the system would often freeze and require rebooting. In addition, one of the RAM cards was replaced in the main computer. Once the scanner displayed no faults, calibration and quality assurance testing began.

8.1.2 Scanner calibration

The scanner has built in calibration steps and protocols as well as monthly, weekly and daily quality assurance tests. The calibration steps mentioned in the service manual [92] (pages 76-93) were followed. This included energy calibration, timing calibration between detectors, and crystal position calibration. However, one of the main issues that arose when calibrating the scanner was that the processes relied on a inbuilt ^{68}Ge pin source. This should be replaced every year [96] as ^{68}Ge has a half-life of 270.93 $\pm$ 0.13 days [15]. The pin source was last replaced in 2015. The original activity was 55 MBq therefore, the activity of the pin source was less than 4 MBq when the PET scanner needed to be re-calibrated.

The calibration pin source was no longer active enough for accurate calibration. Therefore, to resolve this, a cylindrical phantom, 15 cm long and 5 cm in diameter, was filled with a positron source (^{18}F-water). The cylindrical phantom was used in addition to the pin source and was placed on the bed in the middle of the detector rings to provide a uniform irradiation of the PET detectors when calibrating.

One of the main problems of working with a former medical PET scanner was that many of its inner workings are not publicly available. Although the calibration steps in the manual were followed the scanner calibration did not improve when using the supplementary cylindrical

phantom placed continuously in the centre of the scanner. The missing step was that the pin source (which is always concealed within the PET scanner casing) is not continuously exposed to the detectors during the calibration process. When the calibration processes are running there are periods where the pin source is out of its lead lined case and in the FOV of the scanner and there are times when the pin source is store in a lead lined case, outside the FOV of the scanner. This allowed the electronics to compare the difference with and without a source present and adjust itself correctly from this. Once this was realised the supplementary cylindrical phantom was placed in and out of the FOV in time with the pin source. After this realisation, the energy, detector coincidence, and crystal position mapping calibrations greatly improved with each calibration iteration.

Unfortunately, the original calibration was lost during the early calibration attempts performed without removing the phantom, so the subsequent calibration of the scanner took many iterations. The crystal mapping which allows the scanner to identify the centre of each crystal block took a particularly long time to recover.

For some aspects of the calibration the supplementary cylindrical phantom filled with ^{18}F-water was not optimal but these are discussed in section 9.1.1. However, once the scanner was calibrated to a usable state spatial and timing resolution investigations were carried out.

8.1.3 Resolutions assessments with active point sources

To establish the spacial resolution of the scanner a source smaller than the spacial resolution should be used. Two 1mm glass beads were soaked in ^{18}F water and baked under a heater. After the beads were dry the activities of the beads were measured in a well counter. Bead A had an activity of 0.2 MBq and bead B had and activity of 0.3 MBq. Bead B was then placed in the centre of the scanner (position 1 in figure 8.1) and image data were collected

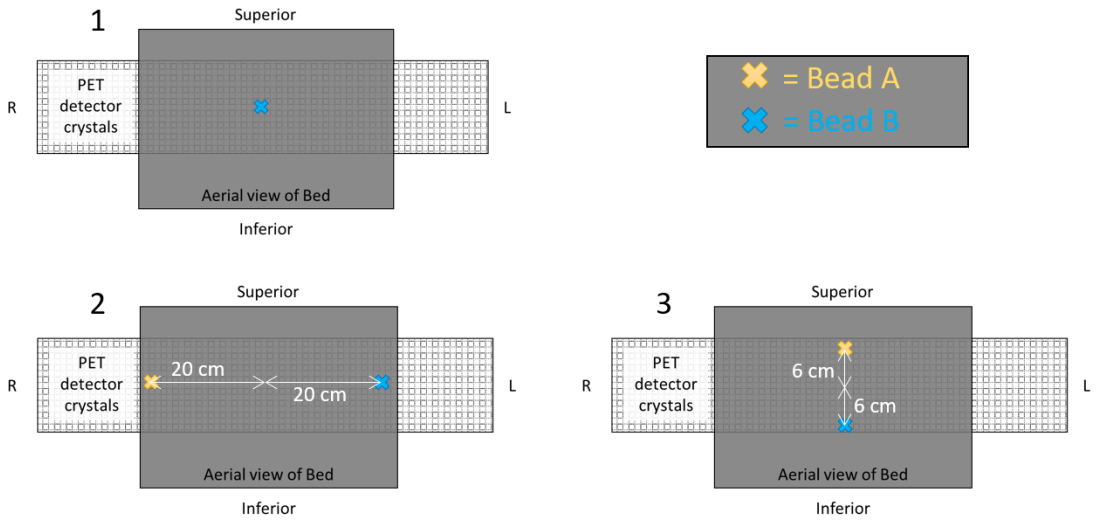

Figure 8.1: The positions of active beads A (yellow) and B (blue) during three different 120 second scans. The measurements of each bead's position were measured from the centre of the scanner.

for 120 seconds. Beads A and B were then placed near the edges of the AFOV and the edges of the scanner bed as shown by positions 2 and 3 in figure 8.1, respectively.

The three data sets were reconstructed using FBP. The reconstructed data were then transferred from the PET scanner to an external computer where the images were processed and analysed using Mango [97], a Digital Imaging and Communications in Medicine (DICOM) software package. In addition to viewing the axial, coronal, and sagittal slices of the PET images taken, Mango was used to extract image intensity cross-section (profile) and volume data. Tools in Mango allow lines to be drawn on individual slices of an image. The profile of the intensity along this line was extracted as a csv file. Regions of interest (ROI) can also be drawn on the images and the intensity of each image voxel (3D pixel) within that ROI was extracted in the form of a histogram csv file.

Intensity profiles were taken of each bead from the: left to right (L to R); anterior to posterior (A to P); and superior to inferior (S to I) directions. These intensity profile measurements

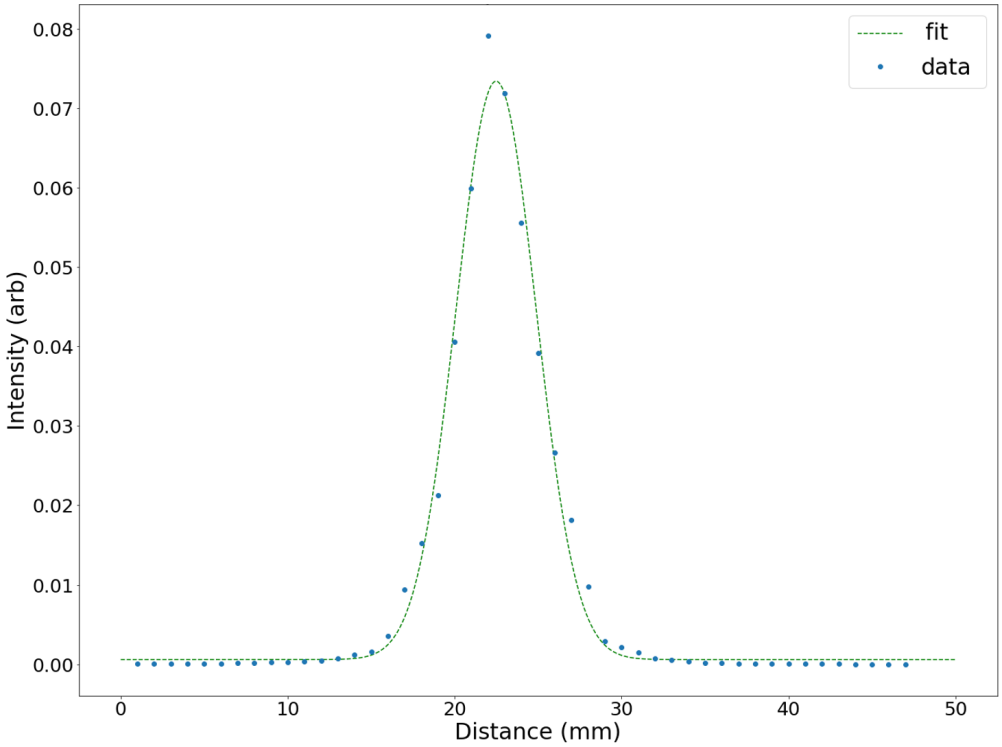

Figure 8.2: An intensity profile through the centre of bead B. The line cutting though the image from the superior to the inferior direction looking at a coronal slice of the bead. The intensity (in arbitrary units) of the image along this line was measured every millimetre and the data points are presented in blue. The spread of the point source was fitted with a Gaussian as shown by the dotted green line.

were carried out for each perpendicular (axial, coronal, and sagittal) slice through the centre of each bead. For each intensity profile a Gaussian was fitted to the intensity data. An example of this is demonstrated in figure 8.2.

The FWHM values were calculated from the Gaussian fit parameters of each intensity profile. Beads A and B were of comparable size and activity, within errors, therefore, their FWHM values for a particular direction (L to R, or A to P, or S to I) were averaged. A sample standard deviation divided by the square root of the number of FWHM values averaged was used for the error on the average FWHM for a particular bead position within the scanner. Figure 8.3 shows how the FWHM values of a point source vary with the direction of measurement, depending on the position of the bead within the scanner.

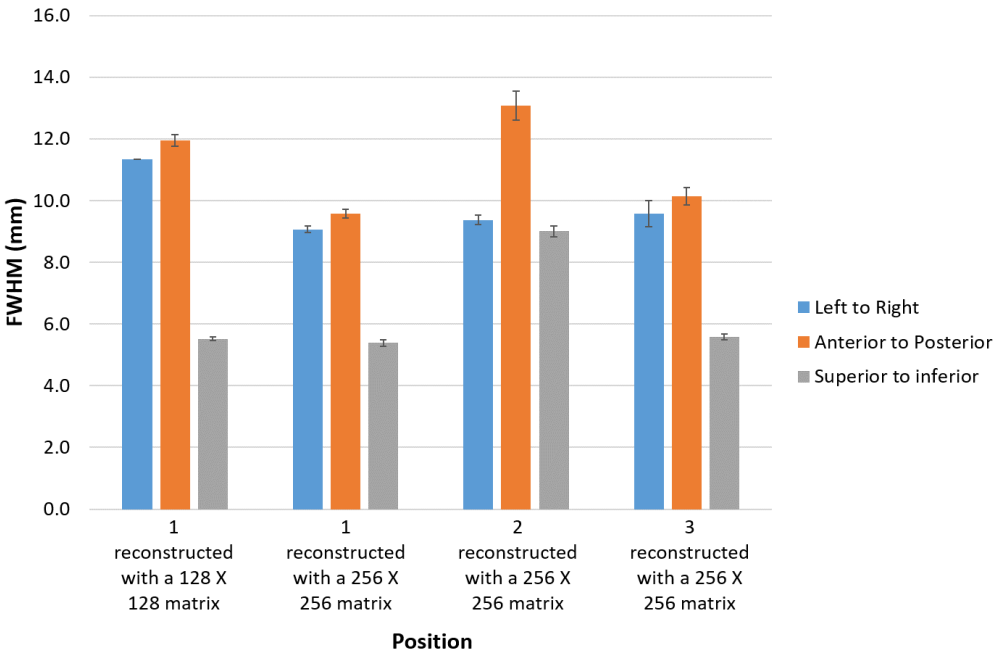

Figure 8.3: The average FWHM measurement of a point source (1 mm beads, A and B) in three directions of a 120 second PET image: left to right (blue); anterior to posterior (orange); and superior to inferior(grey). Positions of beads A and B are denoted by a number 1, 2 or 3 and these correspond to the positions in figure 8.1. The reconstruction of each image was through the FBP method and the size of the reconstruction matrix used is also given under each set of data.

Initially, a comparison was made between reconstructing FBP images using either a 128 $\times$ 128 matrix or a 256 $\times$ 256 matrix. The FWHM values for these two scenarios are given by the first two data sets in figure 8.3. Increasing the reconstruction matrix significantly improves the spatial resolution (decreases FWHM) in the transaxial directions (R to L and A to P). An improvement in spatial resolution with matrix size was to be expected as a larger reconstruction matrix allows for greater detail. Thus the 256 $\times$ 256 matrix was used for all subsequent FBP reconstructions.

When the beads were placed in position 2 (see figure 8.1), 20 cm away from the central line

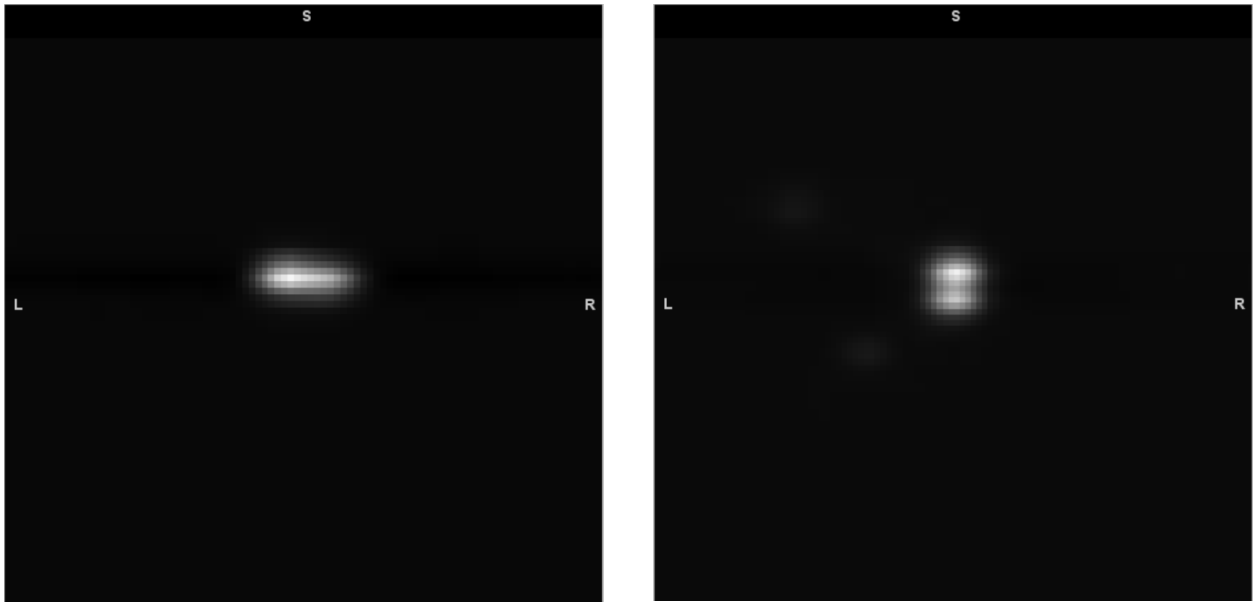

(a) Beads A and B placed 8.5 ± 0.5 mm apart in the L to R direction.

(b) Beads A and B placed 8.0 ± 0.5 mm apart in the S to I direction.

Figure 8.4: 120 second PET images of two beads reconstructed using a 256 × 256 FBP matrix. The images are coronal slices through the centre of the two beads.

of the scanner, the resolution in the A to P and S to I directions became poorer, i.e. the FWHM values significantly increased. In this case the beads are much closer to one set of detectors than another. However, as the beads were placed along the axis but at the edges of the AFOV, 6 cm from the centre of the scanner (position 3) then there was very little to no significant impact on the image resolution. From this data it was concluded that for objects placed centrally along the axis of the scanner, the imaging resolution was approximately independent of axial position, as expected when using the scanner in 2D mode.

The axial (S to I) direction consistently has the best resolution with a point source presenting a FWHM of 5.5 ± 0.2 mm when positioned on the axis of the scanner. The transaxial resolution values, 9.1 ± 0.1 and 9.6 ± 0.1 mm in the R to L and A to P directions, respectively, are significantly poorer for a point source placed centrally within the scanner. The impact of this can be seen in figure 8.4 (a) and (b) where beads A and B were placed in the centre

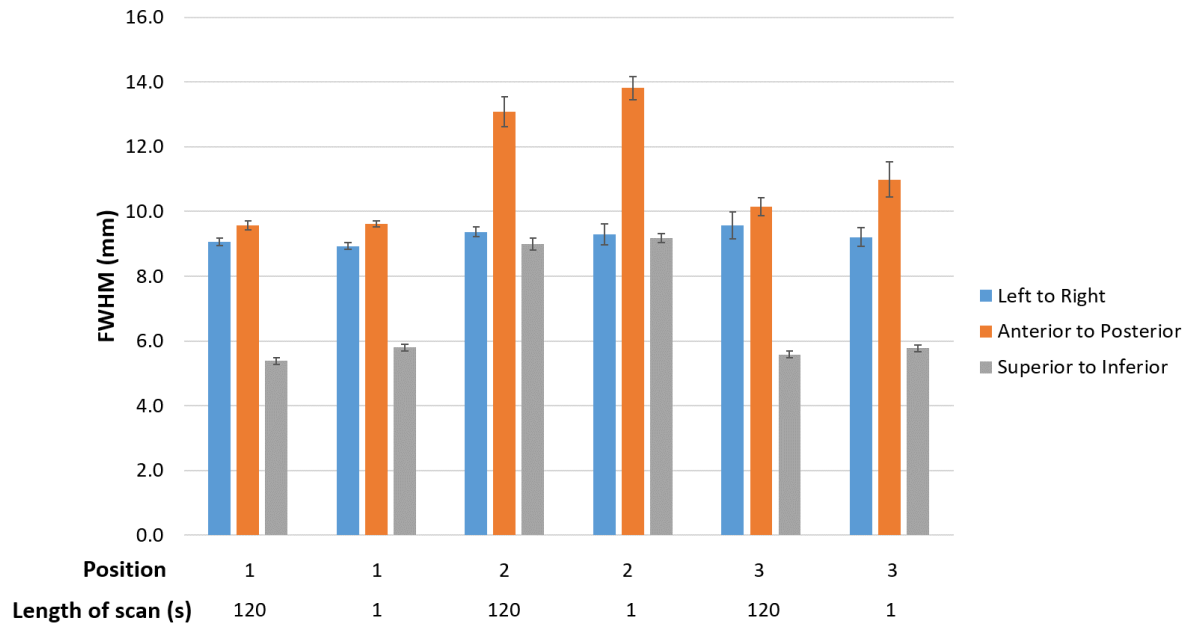

Figure 8.5: The average FWHM measurement of point sources (beads A and B) in three directions of a 1 and 120 second PET image: left to right (blue); anterior to posterior (orange); and superior to inferior (grey). Positions of beads A and B are denoted by a number 1, 2 or 3 and these correspond to the positions in figure 8.1. Each image was reconstructed using a 256 × 256 FBP matrix.

of the scanner but 8.5 ± 0.5 mm apart in the L to R direction and 8.0 ± 0.5 mm apart in the S to I direction, respectively. 120 second image frames were taken. It is clear that at this close proximity, the beads separated in the L to R direction could not be resolved from each other, whereas the beads separated in the S to I direction could clearly be distinguished from one another.

The impact of the length of time data was collected for on the image resolution was also studied. When the 120 second frames images of beads A and B were taken, as described above, additional one second frame images of the beads were also collected. These short frame images were also reconstructed using a 256 × 256 matrix FBP and the intensity profile process to determine the FWHM in the three directions was carried out in the same

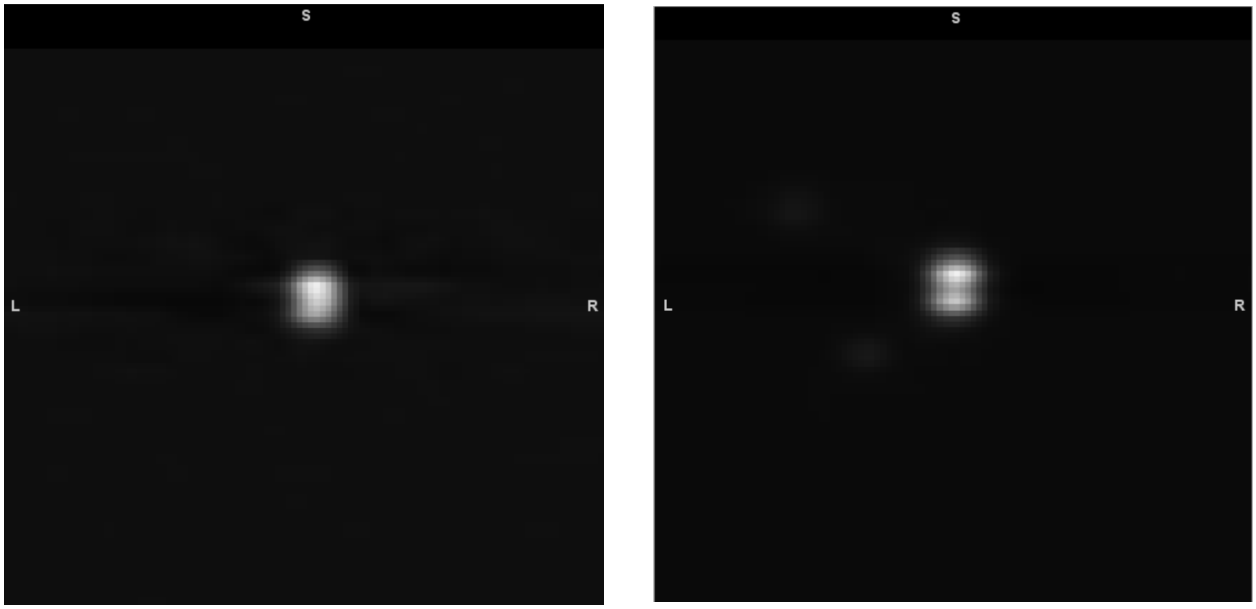

(a) Image data collected for 1 second. **(b) Image data collected for 120 seconds.**

Figure 8.6: PET images of two beads (A and B) separated by 8.0 ± 0.5 mm in the S to I direction and reconstructed using a 256 × 256 FBP matrix. The images are coronal slices through the centre of the two beads and the data for each image was collected for different lengths of time.

way. A comparison of the two data sets (1 and 120 second images) is shown in figure 8.5.

Apart from a small improvement (0.2 mm) for resolution with increased data collection in the S to I directions when the bead was placed centrally (position 1), there was no significant impact on image resolution of a point source with decreasing the time the image data was collected for. Therefore, the spatial information data from axial image slices taken for different durations can be compared.

The slight improvement in spatial resolution in the S to I direction can be seen in figure 8.6 by comparing a 1 and 120 second image taken of beads A and B spaced 8.0 ± 0.5 mm apart in the S to I direction. Figure 8.6 demonstrated that the longer data collection time enabled the differentiation of the two beads when they were placed so close together.

Including 256 × 256 reconstruction FWHM data from both the 120 and 1 second frame

images, point source resolution (FWHM) values along the central axis of the scanner vary from 8.8 to 10.0 mm in the L to R direction, 9.5 to 11.5 mm in the A to P direction, and 5.3 to 5.9 mm in the S to I direction depending on the source position along the AFOV. However is it also important to know how clearly an area with no activity (a cold spot) can be seen in an otherwise uniform activity background. This was investigated and is discussed below. Moreover, the data discussed till now was of point sources for which reconstruction is relatively simple. The effect of changing the image frame length would become clearer when imaging a more complex object. This is the point of discussion in section 8.1.5.

8.1.4 NEC

As discussed in section 7.4.2, NEC is an important measurement used to determine the optimal activity for taking an image. For health and safety reasons, it is best to use less activity. In addition, too high an activity causes random events to occur too often. NEC graphs allow the determination of activity needed for a good quality image before random counts become a too prominent a feature.

To calculate the NEC values for a range of activities, a small 50 ml phantom was filled with 345 MBq (measured using a well counter) of ^{18}F water and placed centrally within the bore of the scanner. While collecting a scan, the GE discovery ST scanner outputs "Delayed Events Subtraction" true and random counts. Over the subsequent 400 minutes, a total of 20 one minute scans were recorded, until the activity was 29 MBq. The true and random event counts were recorded for each minute. Equation 7.8 was used to calculate the NEC value for each scan and the activity of the phantom was calculated using equation 4.19 where the half-life of ^{18}F is 109.77 minutes [15]. The total, true, random and NEC are plotted in figure 8.7. However, there was a large range of activities between 70 and 140 MBq where data points were missing. Therefore, the measurements were repeated the next day, but starting

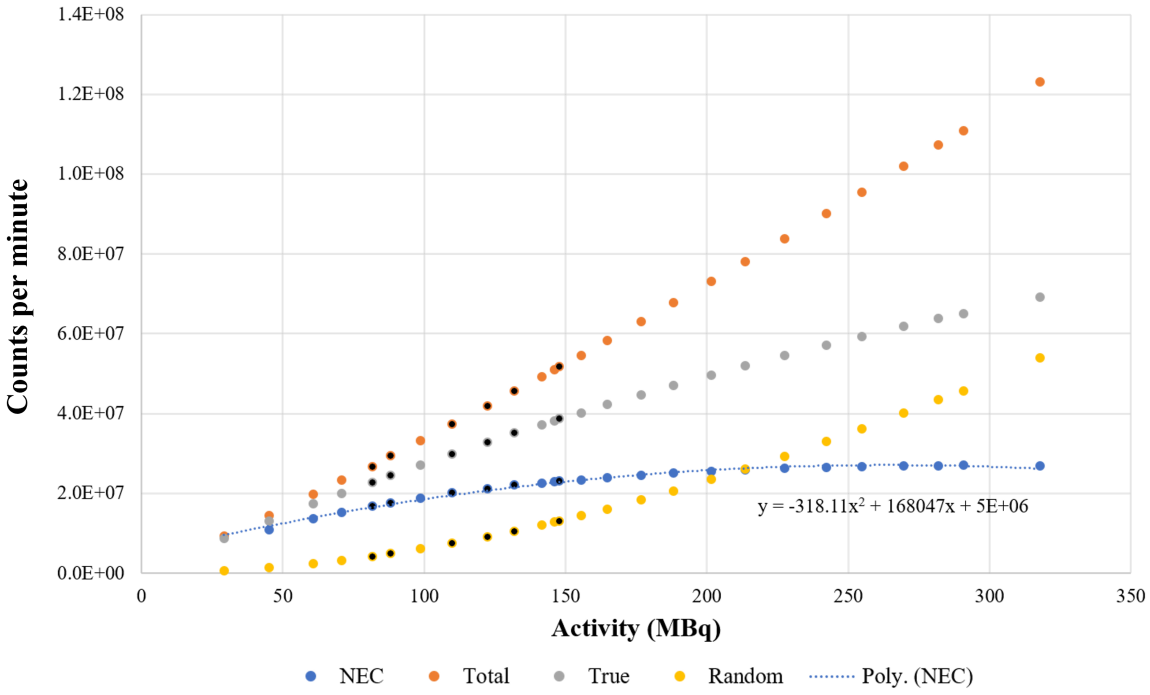

Figure 8.7: NEC (blue) calculated by measuring true (grey) and random (orange) counts recorded within a minute using a 50ml phantom of different activities. The points with the black centres were taken on the next day. A polynomial line of best fit was applied to the NEC data and the equation for this is displayed in the graph.

with a phantom of lower activity, 170 MBq. These are represented in figure 8.7 with the black centred data points. This second set of data confirmed the trend of the previous data set.

A polynomial was fitted to the NEC data and the maximum of the NEC was found to correspond with an activity of 264 MBq. Due to the increased health risks of using higher activities it is not necessarily beneficial to use 264 MBq of activity. Moreover, the NEC does not change much with activity over a wide range: there is only a 22% increase increase in NEC from 140 MBq to 264 MBq. Therefore, activities ranging from 140 to 240 MBq were used in subsequent work with CALGAVIN.

8.1.5 The effect of data frame length on image quality

Often, the purpose of taking PET images of industrial machinery will be to look at the change in movement of something inside. Therefore, it is important to know how short an image frame can be and still provide useful, accurate and precise information. As seen in section 8.1.3, seeing the change in image quality is not always obvious when using point sources. In addition, the objects being imaged in industrial machinery are more complex in shape. Sometimes the object of interest is actually not radioactively labelled but is surrounded by activity. The ability to be able to see this cold spot and measure its dimensions is therefore important. As discussed in section 8.1.3, the scanner resolution (FWHM of a point source) in the L to R and A to P directions was approximately 1 cm. To test if a 1 cm cold spot could be seen against a uniform activity background, a 10.14 $\pm$ 0.09 mm glass bead was submerged in a 50 ml phantom containing ^{18}F water. This also provides a more complex shape to image and compare how changing frame length affects the image quality.

The 50 ml phantom was filled with ^{18}F water and placed in the centre of the scanner. When the total activity of phantom was approximately 250 MBq (near the maximum of the NEC curve in section 8.1.4) a selection of images were taken of varying lengths, 1, 2, 3, 5, 10, and 120 second frames. Each frame was reconstructed using a 256 $\times$ 256 FBP matrix. An axial slice through the centre of the bead in the phantom is displayed in figure 8.8 for each frame.

Though the images increase in quality with duration of data collection the cold spot is clearly visible in all of the images. Comparing the images to the 120 second frame (bottom right of figure 8.8), the image quality of this phantom at 3 and 5 second frame images are reasonably similar to that of a 120 second frame.

A second set of images was taken in the same way when the total activity of the phantom reached approximately 150 MBq. This activity was chosen as it was at the bottom of the

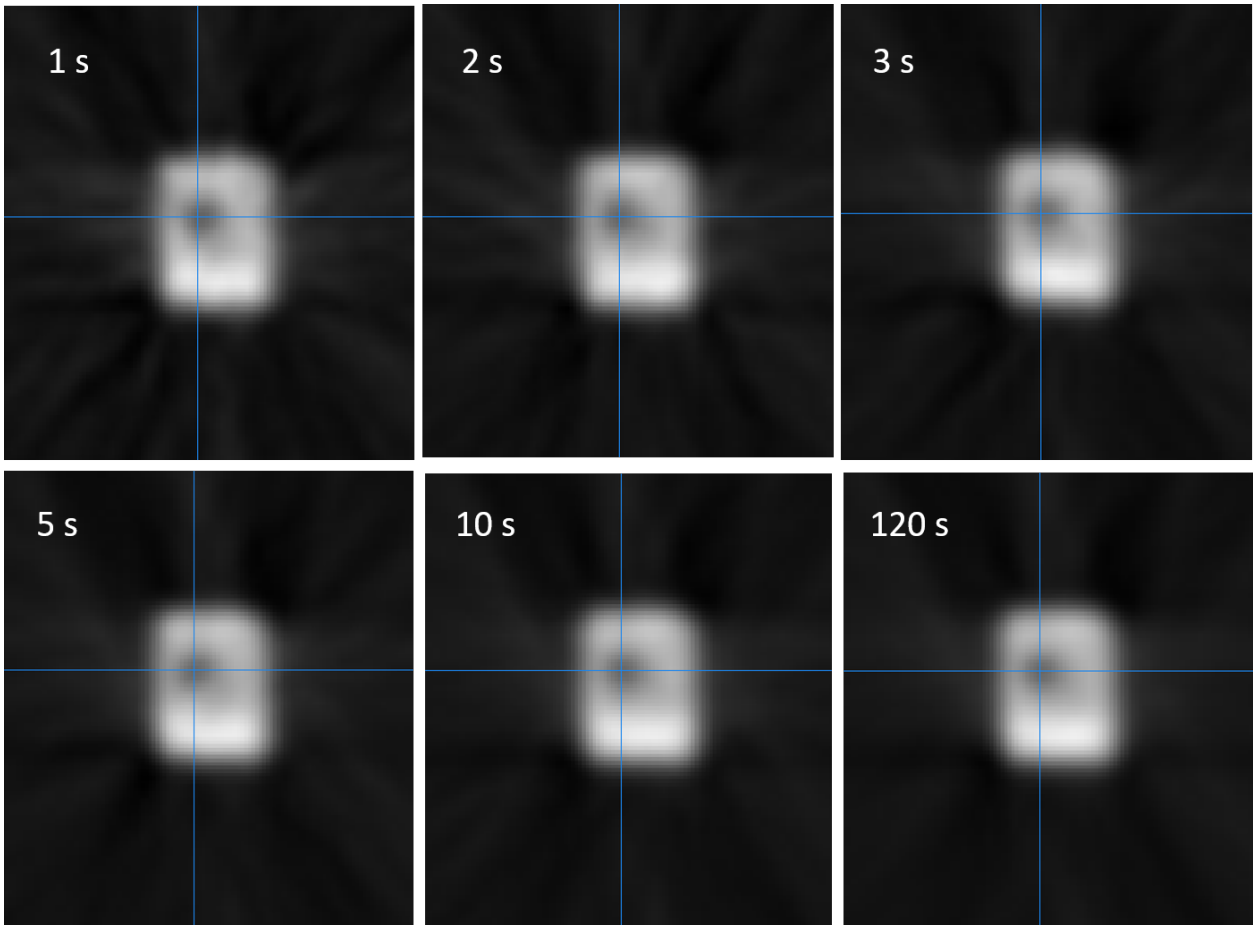

Figure 8.8: **A 50 ml phantom filled with approximately 250 MBq of ^{18}F water, containing a 10.14 $\pm$ 0.09 mm glass bead (cold spot) was placed in the centre of the scanner and six frames were taken of differing lengths: 1, 2, 3, 5, 10, and 120 seconds. Each frame was reconstructed using a 256 $\times$ 256 FBP matrix. An axial slice through the centre of the bead is shown in each image and the frame length the data was collected for is also displayed on each image. The 50 ml phantom is denoted by the lighter areas and the bead by the dark areas withing the light. The length of each frame is indicated in the top left of each image and the blue cross-hairs pass through the centre of the bead.**

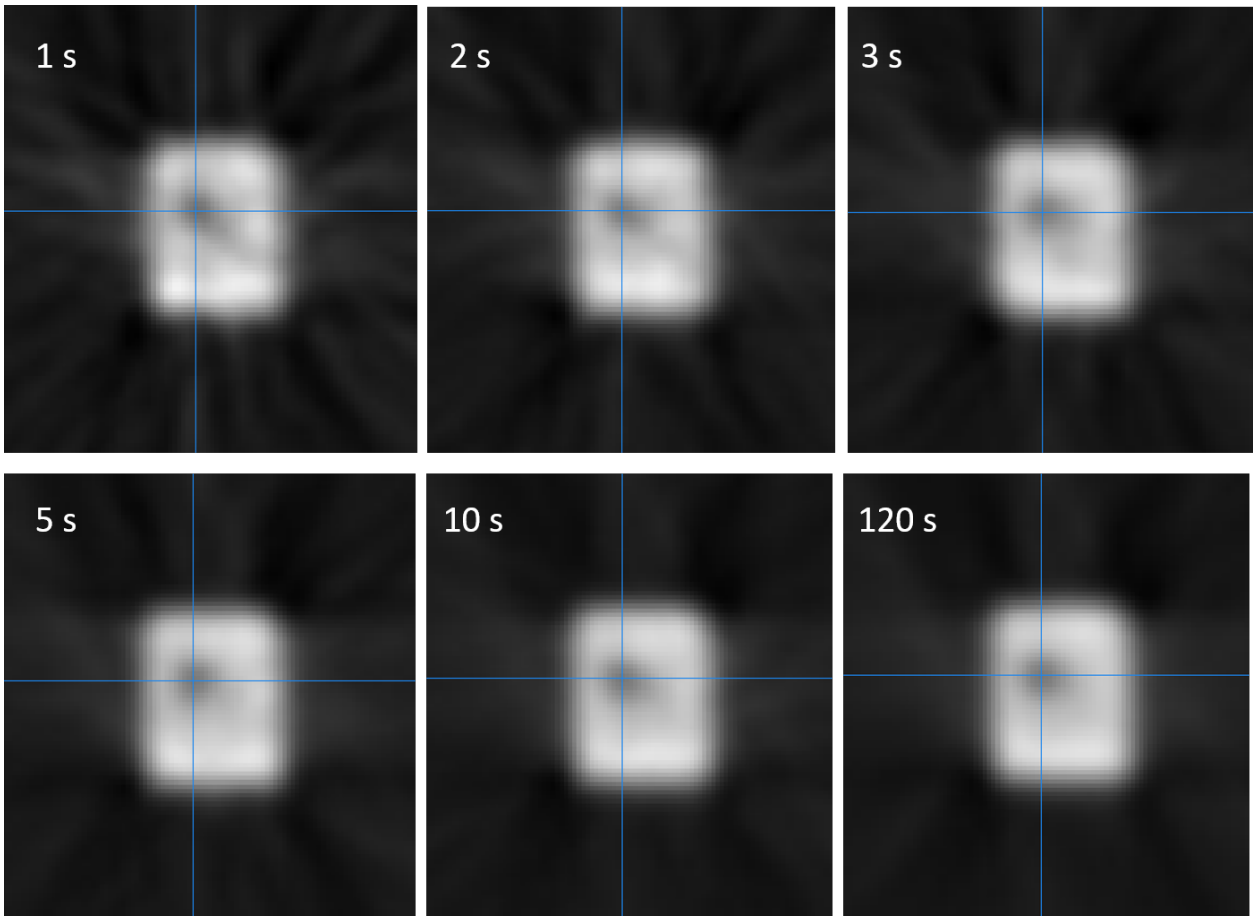

Figure 8.9: **A 50 ml phantom filled with approximately 150 MBq of ^{18}F water, containing a 10.14 $\pm$ 0.09 mm glass bead (cold spot) was placed in the centre of the scanner and six frames were taken of differing lengths: 1, 2, 3, 5, 10, and 120 seconds. Each frame was reconstructed using a 256 $\times$ 256 FBP matrix. An axial slice through the centre of the bead is shown in each image and the frame length the data was collected for is also displayed on each image. The 50 ml phantom is denoted by the lighter areas and the bead by the dark areas withing the light. The length of each frame is indicated in the top left of each image and the blue cross-hairs pass through the centre of the bead.**

usable range of activities according to the NEC values in section 8.1.4 . These six images were processed in the same way as before and are shown in figure 8.9.

Comparing figures 8.8 and 8.9, the use of a lower activity decreased the quality of the image. For this lower activity, a 5 second frame would be the limit of reconstruction to obtain a image of quality comparable to a 120 second image. Therefore, depending on the activity used in the experiment a minimum of a 3 or 5 second frame length should be used.

Moving point source

Imaging a point source source is less demanding for reconstruction. Therefore, 1 second frame images can be used to image point sources moving. To test this a 3 mm glass bead was imbued with 6 MBq of ^{18}F and placed 5.8 $\pm$ 0.5 cm from the centre of a spinning arm, in the FOV of the PET scanner. Sets of 1 second frame images were taken of the bead spinning in 5.8 cm radius circles at 3 different speeds; 2.9 $\pm$ 0.3 cms^{-1}; 5.4 $\pm$ 0.5 cms^{-1}; and 29.6 $\pm$ 2.6 cms^{-1}. The beads rotation speeds were determined by measuring the time taken for 10 full rotations of the spinning arm. The circumference of the circle the bead at radius 5.8 cm makes was divided by the time taken for one rotation. Figures 8.10, 8.11, and 8.12 show the series of 1 second frame images of the bead rotating at the three different speeds.

In a single 1 second frame it would be expected that the image of the point source would show the length that the bead travels in one second. For each speed, an intensity cross section was taken along the trajectory of the bead. The intensity profile was a hat function convoluted with a Gaussian function, therefore, the distance between the start and end of the beads movements was taken between the half maximum values of the full intensity. These were measured to be 2.8, 5.4, and 27.8 cm for each speed respectively. These results were within errors of the speed values thus proving the 1 second images of point sources can be useful in providing movement information if the bead does not move back on itself within a single

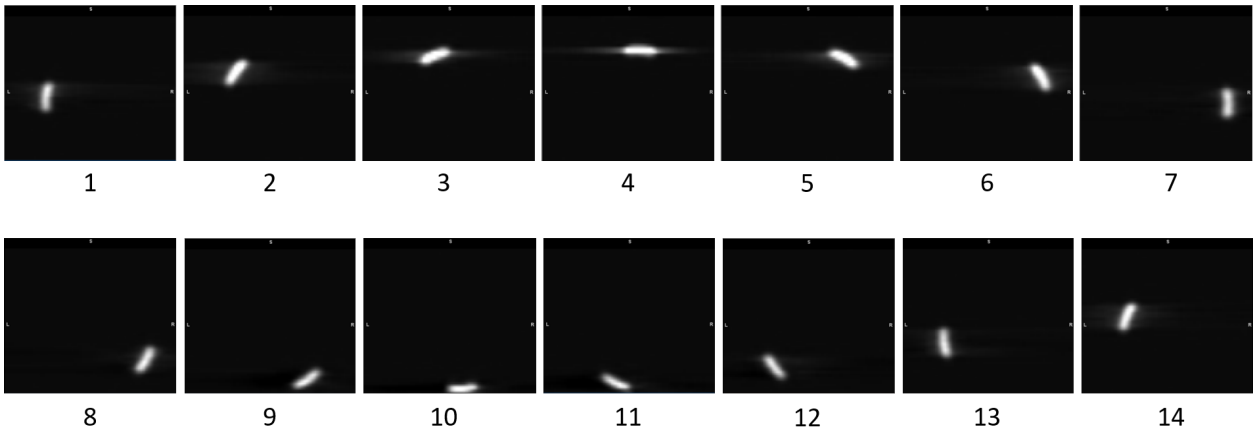

Figure 8.10: A 3 mm, ^{18}F active, glass bead placed 5.8 ± 0.5 cm from the centre of a spinning arm. The bead is travelling at 2.9 ± 0.3 cms^{-1}. Each image is a coronal slice of a 1 second frame reconstructed using a 256 × 256 FBP matrix. Data was taken for 14 seconds. The number under each image is the frame number.

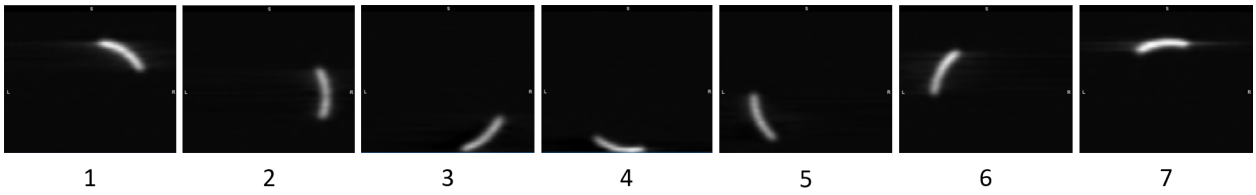

Figure 8.11: A 3 mm, ^{18}F active, glass bead placed 5.8 ± 0.5 cm from the centre of a spinning arm. The bead is travelling at 5.4 ± 0.5 cms^{-1}. Each image is a coronal slice of a 1 second frame reconstructed using a 256 × 256 FBP matrix. Data was taken for 7 seconds. The number under each image is the frame number.

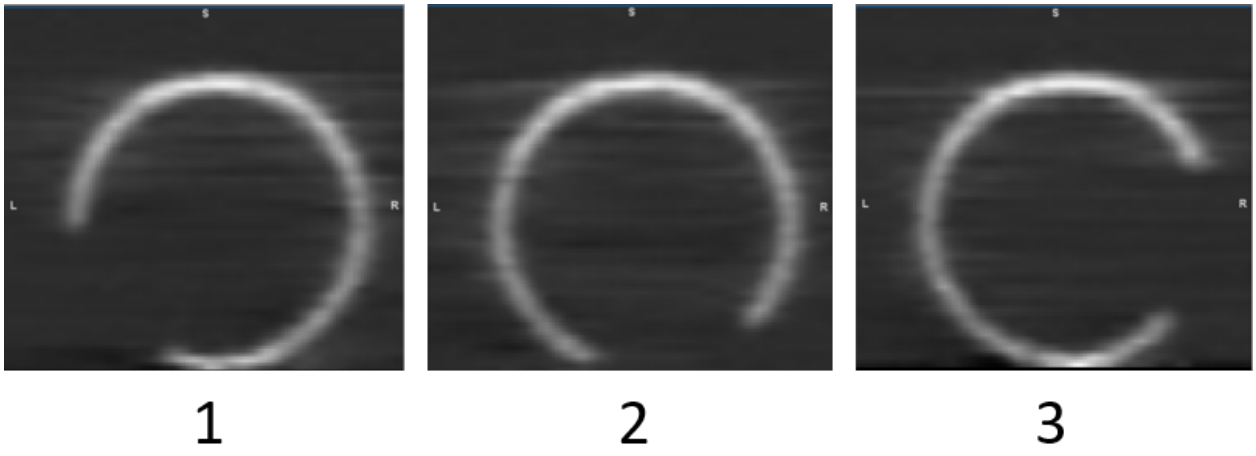

Figure 8.12: A 3 mm, ^{18}F active, glass bead placed 5.8 ± 0.5 cm from the centre of a spinning arm. The bead is travelling at 29.6 ± 2.6 cms^{-1}. Each image is a coronal slice of a 1 second frame reconstructed using a 256 × 256 FBP matrix. Data was taken for 3 seconds. The number under each image is the frame number.

frame. Also the bead should be high enough activity to enable good tracking images. This is especially true if the bead is to be moving quickly as increasing speed effectively reduces the activity per length travelled. The effect of this can be seen in figure 8.12 where the image quality of this fast moving bead is poorer compared to figures 8.10 and 8.11 where bead is moving much slower.

Re-framing data

When the data is being collected, the length of each frame and the number of frames the data were collected for is specified in a preset "image protocol". There is an option to also record the data in list mode (ViP mode), where each coincidence interaction is recorded with a time stamp. This enables the data to be retrospectively re-framed into different length frames to the originally collected data. However, this type of data collection requires much more storage memory. It was determined that the re-framing of a single long frame into short frames did not affect the image quality and the images produced were comparable to

those taken directly as multiple shorter frames. However, the effect on total image intensity was not initially measured and the effects of this were discovered during the analysis of the CALGAVIN data and are discussed in the latter part of section 8.2.2.

8.1.6 Resolution assessment of cold spots and the use of different reconstruction methods

As mentioned in section 7.4, the GE Discovery ST PET scanner can reconstruct images using either FBP or OSEM. Using FBP enables the ability to see if there are any image artefacts caused by poor calibration. This may not be as clear using OSEM because of the nature of iterative reconstruction, where a guess of the image is made and then adjusted rather than simply back projecting the original data. This was why FBP was originally used to establish the resolution and assess the initial calibrated state of the scanner.

However, OSEM is most commonly used for image reconstruction (for the reasons discussed in section 7.3.3), therefore, it was important to assess how the image quality changed from FBP to OSEM. The same 50 ml phantom containing a 10.14 $\pm$ 0.09 mm glass bead was filled with approximatly 250 MBq of ^{18}F water. A 5 second frame of data was collected and then reconstructed using the OSEM method. The data were divided into 21 subsets and 2 iterations were carried out to form the final images. A 256 $\times$ 256 reconstruction matrix was used. An axial slice through the centre of the bead is displayed in figure 8.13 for both the OSEM and FBP reconstructed images. The FBP image is the 5 second frame image originally shown in figure 8.8.

Comparing the two reconstruction methods: the cold spot (bead) is still clearly visible when reconstructing with OSEM; the edges of the object are clearer; and the background less noisy. Therefore, OSEM was also used for reconstruction of the industrial imaging investigations

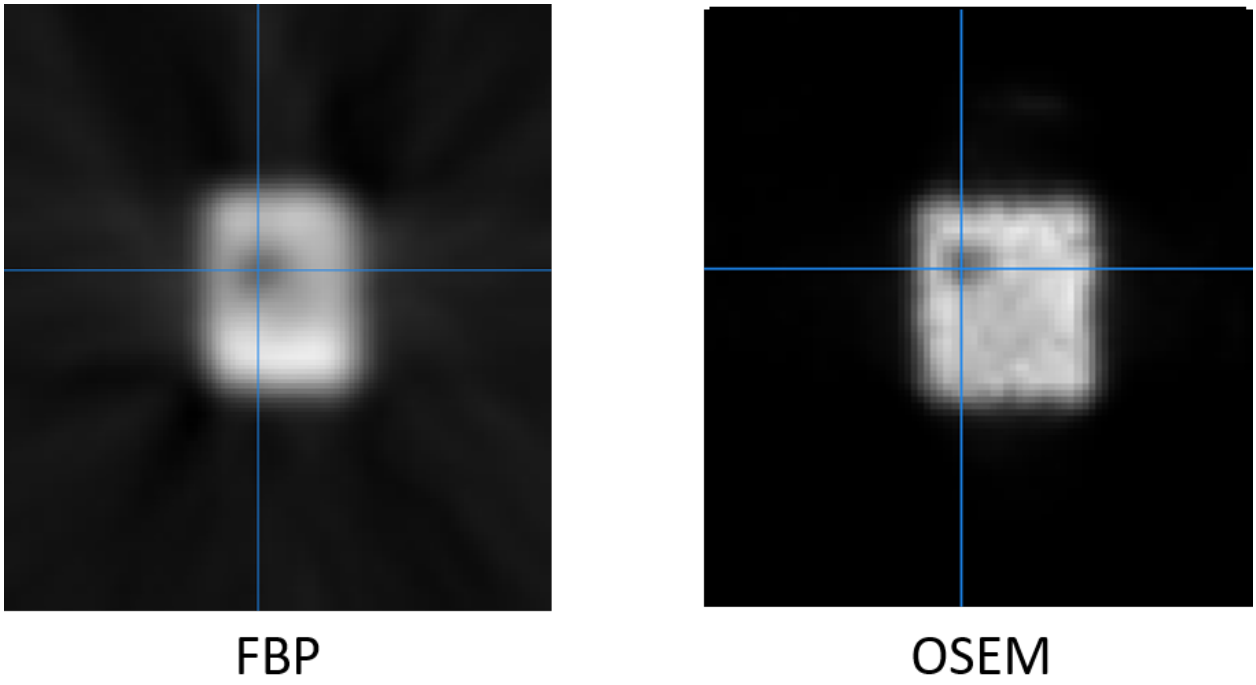

Figure 8.13: A 50 ml phantom filled with approximately 250 MBq of ^{18}F water, containing a 10.14 ± 0.09 mm glass bead (cold spot) was placed in the centre of the scanner. The right hand image show a 5 second frame image was taken and reconstructed using the OSEM method. The data were divided into 21 subsets and 2 iterations were carried out to form the final images. A 256 × 256 reconstruction matrix was used. This is compared to the 5 second frame, FBP image on the left taken from figure 8.8. An axial slice through the centre of the bead is shown in each image. The 50 ml phantom is denoted by the lighter areas and the bead by the dark areas within the light.

with CALGAVIN which are the topic of the next section.

8.2 CALGAVIN

Among the products designed and produced by CALGAVIN are "stationary mixers" [98]. These are specially-designed inserts for piping that exert forces on the fluid to mix it and force it to the edges of the pipe. This enables greater and faster transfer of heat to or from

the system. Figure 8.14 is an image of a sample insert. The metallic loops and twists are specifically designed for the needs of the customers.

Figure 8.14: A sample of a hiTRAN Thermal Systems stationary mixer produced by CALGAVIN.

A customer of CALGAVIN commissioned an insert to be produced for their system. The brief for the insert was that it must provide high heat transfer, disturbance and high pressure drop. Two designs for the insert were put forward by CALGAVIN. The first was a more dense version of their traditional insert (shown in the sample in figure 8.14). This more dense design was called the 'Bubble-Bursting" (BB) insert, an image of which is shown in figure 8.15 (a). The second proposed insert was named the Harris insert (an image is displayed in figure 8.15 (b)) and was a completely new design, with a denser and twisting core.

CALGAVIN wished to investigate how the two different insert designs affected the fluid flow in a pipe. Along with their own measurements (including pressure drop, heat transfer and time spent in the pipe with an insert, known as residence time) they needed a method of measuring if there was any fluid hold-up through the centre of the pipe with the insert. If fluid was trapped or moved too slowly through the centre, this would be problematic for the processes the insert would be used for. The cross-sectional information PET can produce was an ideal solution to this and an initial experiment was carried out to determine how the fluid flowed through the pipe. PEPT was also considered. However, there were concerns that the beads used to trace fluid motion would become stuck in the dense wiring of the inserts and would not reflect the true fluid motion.

Therefore, an experiment using PET imaging was designed to look at the fluid flow through

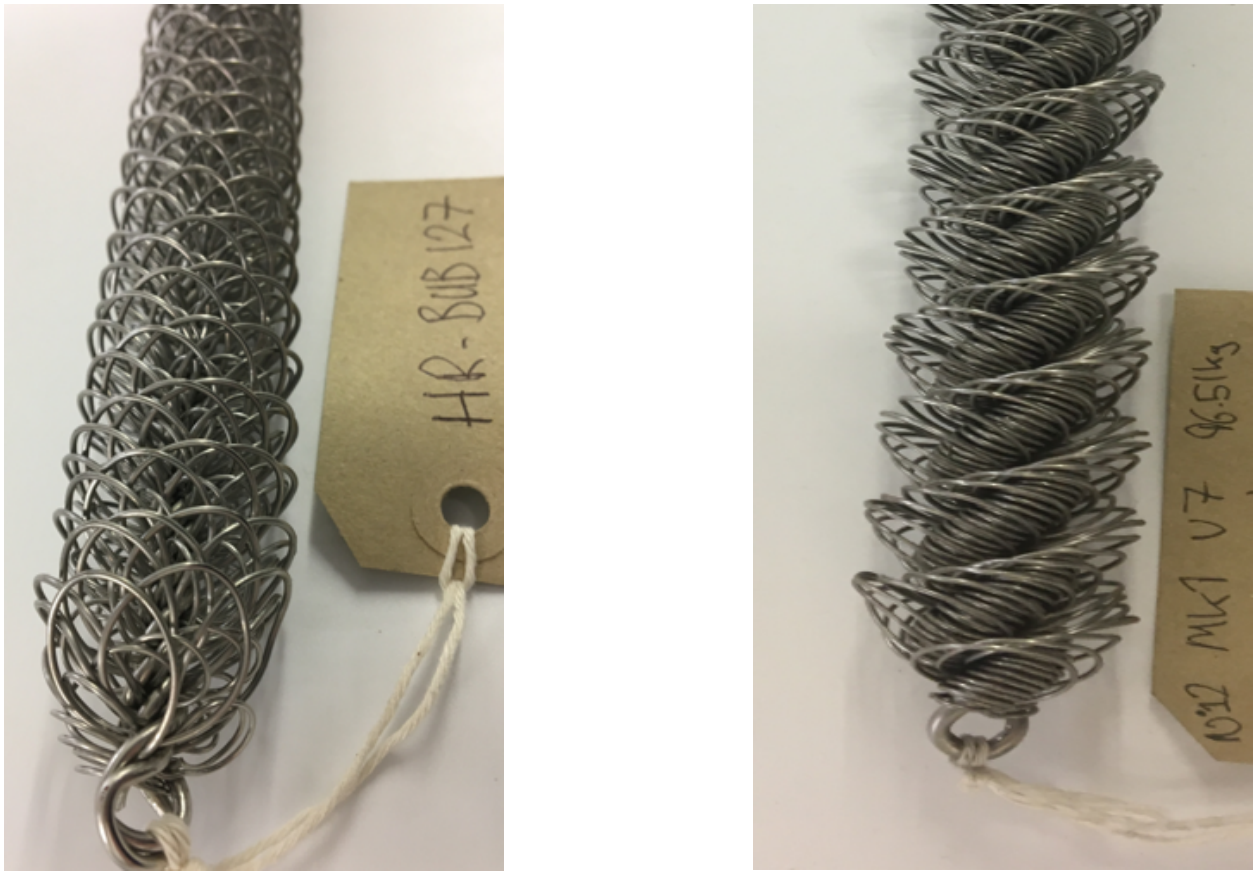

(a) Bubble-Bursting insert (BB). **(b) Harris insert.**

Figure 8.15: Two insert designs proposed by CALGAVIN for one of their clients.

the two inserts and compare to the flow through a blank pipe. The following subsection will describe the experimental set-up used to investigate this and the type of data collected.

8.2.1 Experimental set-up and data collection method

The experimental set-up consisted of a pipe with a 30 mm interior diameter, inside which the appropriate insert would be placed. The pipe was connected in a closed circuit with a reservoir; pump; flow meter and controller; four point injection inlet; and an outlet valve. A diagram of the set-up is shown in figure 8.16 and an annotated image of the set-up is provided in figure 8.17. The system was operated in a closed loop while it was filled with a

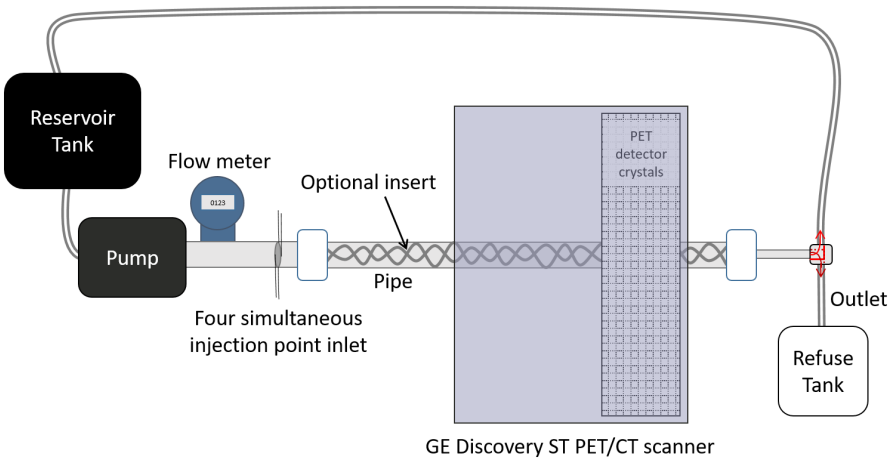

Figure 8.16: Diagram of the CALGAVIN insert fluid flow investigation experiment.

4:1 ratio of glycerol:water mix. This fluid combination was used to mimic the viscosity of the fluids that would be moving in the complete system of the client who requested these inserts. During PET tracer injection and data collection, the system was switched to the refuse outlet to ensure the PET tracer did not loop back through the system. If the active fluid did loop back through, this would prevent further measurements that day because the first injection would spread-out through the system and no longer give a sharp and relatively short increase in activity within the FOV of the PET scanner as it looped back round. Therefore, an additional injection would be needed anyway and this next image would be of lower contrast because the background activity in the scanner would be higher.

For optimal image quality, the pipe was positioned to run centrally through the bore of the scanner, as shown in figure 8.17. Between the pump and the start of the pipe was the injection system, consisting of a single syringe feeding four injection points, as shown in figure 8.18. The aim of this was to provide a simultaneous and uniform injection of activity round the circumference of the pipe.

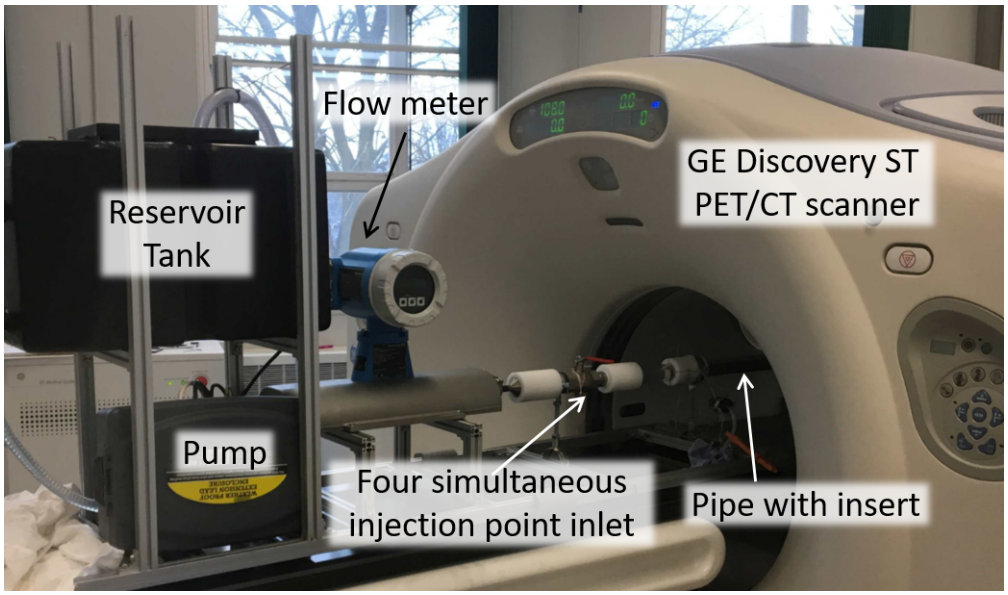

Figure 8.17: An annotated image of the CALGAVIN insert fluid flow investigation experimental set-up.

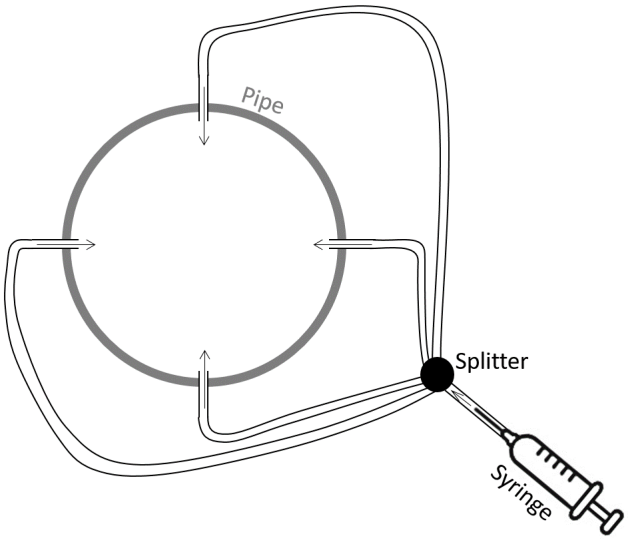

Figure 8.18: A diagram of the activity injection point where a single syringe input is split into four injection points evenly distributed, 90° from one another around the circumference of the pipe. Note that this diagram is not to scale and the four pipes were of equal length.

PET data was collected firstly for the Harris insert, then for a blank tube and then for the BB insert. In each instance several PET data sets were collected. However, the inserts take up volume within the pipe, therefore the fluid passes more quickly through a pipe with either insert. The slower fluid movement in the blank tube affected how the PET data was taken the details of which are specified below.

A small volume of water containing between 140 and 236 MBq of ^{18}F was drawn up into a syringe. Additional glycerol-water mix was drawn up to the 3 ml marker of the syringe. The syringe was then shaken to mix the fluids before injecting into the four point inlet just after the start of PET data collection. PET data was collected for a total of 10 minutes for each injection. The data was originally collected in ten 1 minute frames but ViP mode was turned on to enable the re-framing of the data later. For the blank tube a second set of 10 minute data collection occurred, to ensure the full flow of activity past through the PET scanner was recorded. Some of the activity remained in the inlet tubes thus an additional 10 ml of glycerol-water mix was drawn up into a syringe and injected into the system just after the start of an additional 10 minute PET scan. A further 10 minute PET scan was then taken after this for the blank tube. During each 10 minute PET scan the start and end time of the injection (if this occurred) was recorded along with the maximum kilo-counts per second (kcps) within the scanner (displayed on the scanner) and the time at which this occurred within the scan.

8.2.2 Data analysis, results and discussion

Before each data set was reconstructed, the ten 1 minute PET data set was re-framed. Initially, the Harris and Blank tube data sets were re-framed into 200 three second frames and each frame was reconstructed using 256 $\times$ 256 matrix FBP. However, because the activity in the tube was less than the initial activity in the syringe the image quality for a three second

frame was too poor for the Harris insert data and the Harris and BB insert data were then re-framed into 120 five second frames. Each re-framed Harris and BB insert data set was reconstructed using 256 × 256 matrix OSEM (divided into 21 subsets where two iterations were performed) as this provided crisp edges and less background noise. Unfortunately, before the blank tube data could be re-framed into 120 five second frames and reconstructed with OSEM, the scanner computer developed a major fault and re-framing and reconstruction could not take place. Therefore, the blank tube data only existed in 200 three second frames reconstructed with FBP.

Figure 8.19 displays three orthogonal views of cross-sections through the centre of the pipe for one set of images produced of the blank pipe (b), Harris (a) and BB (c) insert. Though the reconstruction method used for the blank tube was different to the insert images, the blank pipe data still provided information on the evolving distribution of the injected tracer through a pipe with no insert. It was expected that the activity would be distributed fairly evenly through the fluid running through the pipe due to the four point injection system. However, the activity can be seen to be moving along the top of the pipe. This would indicate that the active fluid injected into the pipe was less dense than the fluid in the pipe - this is most likely due to the slightly higher water content in the injected fluid - something that should be reassessed on any future experiment. This aside, by comparing the blank pipe distribution, figure 8.19 (b), to the Harris (a) and BB (c) insert images, it is clear that the inserts have an impact on the active fluid distribution. The active fluid is no longed floating along the top the pipe but is more evenly distributed about the edges of the pipe. It was then inferred from the movement of the active fluid that all the fluid in the pipe followed a similar distribution. However, the difference in density was a point that needed to be considered when analysing the data.

Examining each OSEM reconstructed data set of the Harris and BB insert provided enough qualitative evidence to prove that no (or very little) fluid flowed through the centre of the

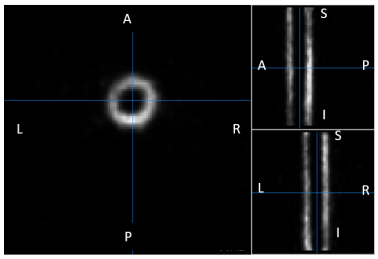

(a) Harris insert, OSEM reconstructed image of the 1:25-1:30 frame where the scanner maximum count rate was 178 kcps.

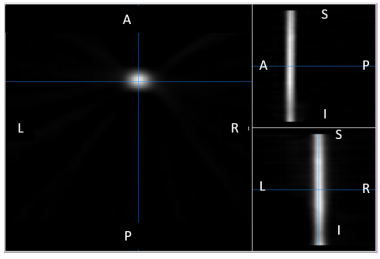

(b) Blank pipe FBP reconstructed image of the 6:27-6:30 frame where the scanner maximum count rate was 178 kcps.

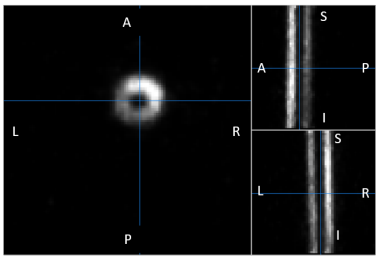

(c) Bubble-Bursting insert, OSEM reconstructed image of the 1:55-2:00 frame where the scanner maximum count rate was 176 kcps

Figure 8.19: Cross-sections through the centre of the pipe when the activity in the scanner was at its highest. (The blue lines are image slice navigation cross-hairs).

pipe. An example data set for each insert is displayed in figures 8.20 and 8.21 where a series of axial, coronal, and sagittal slices progress with time. These images provided CALGAVIN with the evidence they needed to conclude that no fluid became stuck or flowed through the centre of the pipes with either insert. Therefore, either pipe was suitable for their customer. For CALGAVIN, the aim of this experiment was complete. However, using these CALGAVIN data sets, a further aim was to determine what other, more quantitative, information could be extracted using the PET scanner.

The initial and simplest quantitative information that could be extracted was the dimensions of flow of the fluid. Figures 8.19, 8.20 and 8.21 qualitatively show that the Harris insert produces a thinner ring of flow compared to the BB insert. To establish this for certain, the intensity profiles along cross-sections of different image slices were used to measure the difference between fluid flow ring radius and thickness for each insert.

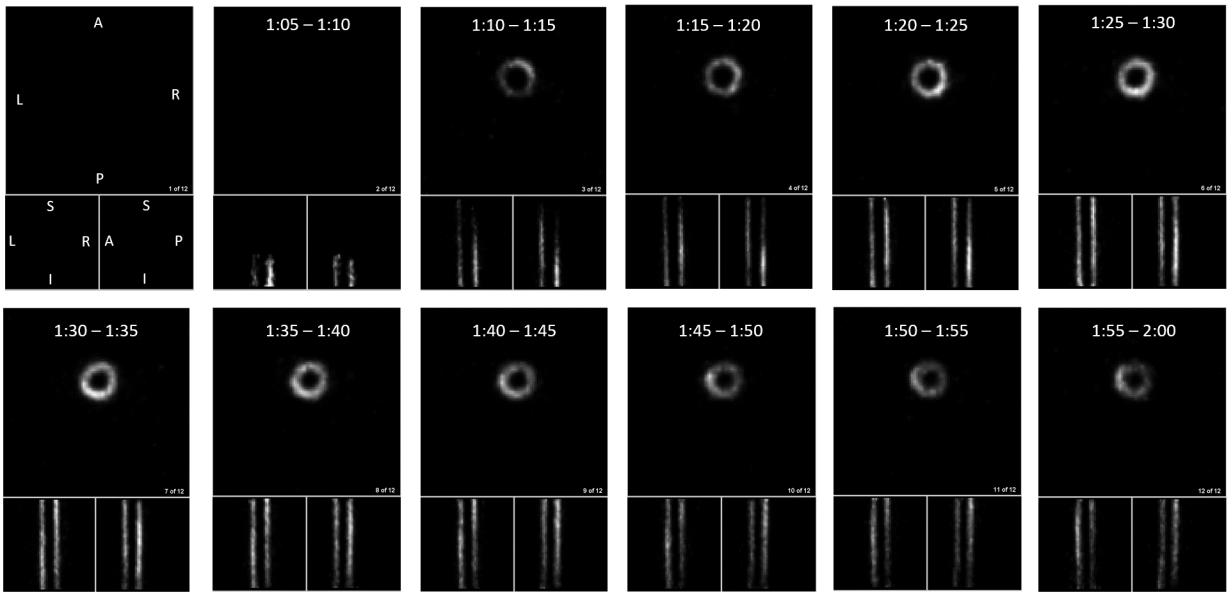

Figure 8.20: Five second frames of the Harris insert between 1:00 and 2:00 minutes of this particular scan. The maximum count rate recorded in the scanner for this data set was 178 kcps. The images are OSEM reconstruction and the axial slice (largest image in each frame) is through the centre of the AFOV of the scanner. The coronal and sagittal slices (left and right, respectively, directly underneath each axial slice) were taken through the centre of the pipe. The time of each frame is given at the top of each axial slice.

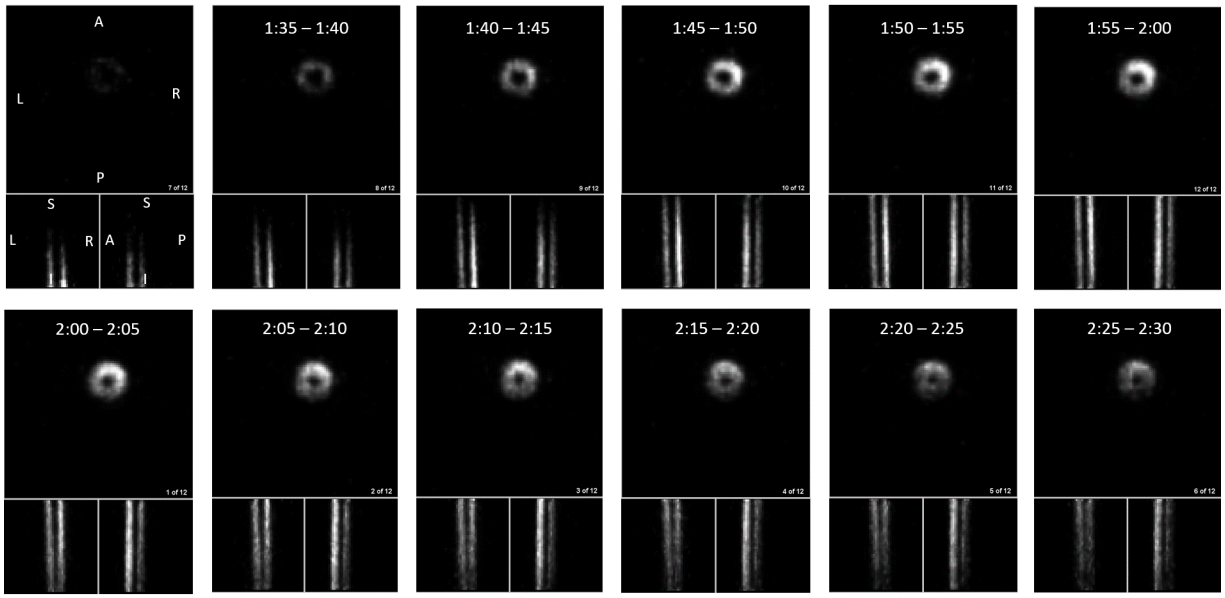

Figure 8.21: Five second frames of the BB insert between 1:30 and 2:30 minutes of this particular scan. The maximum count rate recorded in the scanner for this data set was 176 kcps. The images are OSEM reconstruction and the axial slice (largest image in each frame) is through the centre of the AFOV of the scanner. The coronal and sagittal slices (left and right, respectively, directly underneath each axial slice) were taken through the centre of the pipe. The time of each frame is given at the top of each axial slice.

Measuring how the width of fluid flow changes with time.

For both the Harris and BB insert image data, a coronal slice through the centre of the pipe was selected for each time frame and a line was drawn from left to right through the central point of the AFOV. The intensity profile along the cross-section line was extracted and two Gaussian peaks were fitted as shown in figure 8.22. The central point (μ) and σ values for each peak were extracted from the fitting parameters. The FWHM of each peak in the fit were calculated using $2\sqrt{(2\log(2))}\sigma$ and the inner and outer diameters of the rings of fluid flow were calculated using

$$\text{inner diameter} = \left(\mu_2 - \frac{\text{FWHM}_2}{2}\right) - \left(\mu_1 + \frac{\text{FWHM}_1}{2}\right) \tag{8.1}$$

and

$$\text{outer diameter} = \left(\mu_2 + \frac{\text{FWHM}_2}{2}\right) - \left(\mu_1 - \frac{\text{FWHM}_1}{2}\right), \tag{8.2}$$

where 1 and 2 denote the first and second peak in the fit.

The inner and outer diameter measurements were calculated for the same position on the pipe for each five second frame between 1 and 3 minutes where the intensity of the tracer was highest. Figure 8.23 shows two plots of the these diameters for the Harris (a) and BB (b) insert against time. The error bars of each point were calculated using the errors on the fit parameters. However, given the diameter fluctuations are much larger than these error bar more investigation is needed to establish if these are true fluctuations in diameter of flow or if the error margins on each measurement were too small.

For both the Harris and BB insert the outer diameter measurements were relatively stable

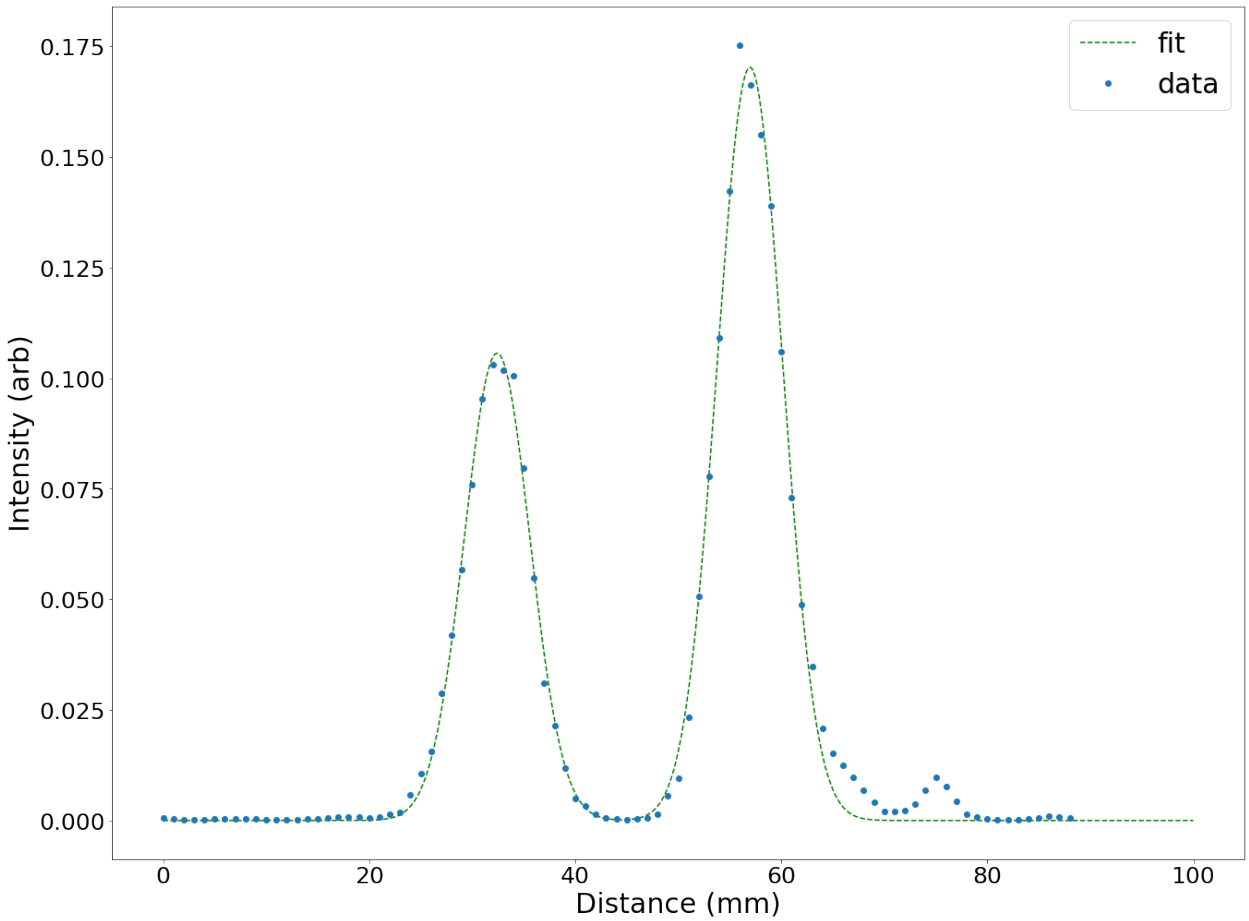

Figure 8.22: Intensity profile of a cross-section line taken from left to right across a coronal slice through the centre of the a pipe with a Harris insert. The intensity measurements every millimetre along the cross-section line (blue dots) were fitted using two Gaussians (green line).

with time. However, for the inner diameter of flow there appears to be a decease in diameter. This is especially true for the BB insert. The change in trend and more sporadic nature of the later data points is most likely due to there being less activity in the scanner at this time. A cut-off on intensity peak height was considered to remove some data points which have poorer statistics. However, even the last data points produced peaks that were at least 10% that of the highest intensity peak of the earlier data points. Therefore, the change in inner diameter seen may be a genuine product of the fluid movement, but further investigation is needed.

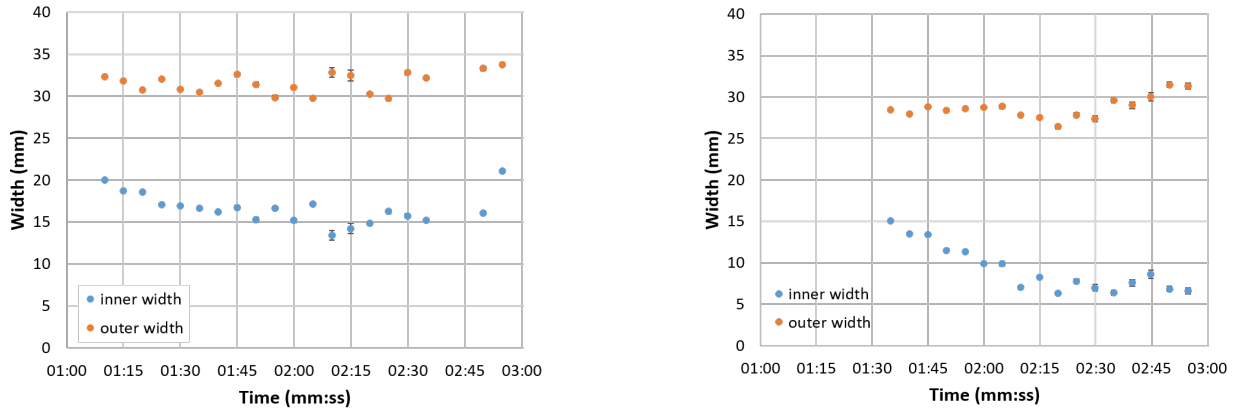

(a) Harris

(b) BB

Figure 8.23: The inner and outer diameter measurements of the flow of fluid through the Harris and BB inserts against time. The diameters were measured using left to right cross-sections of a coronal slice through the centre of the pipe. The measurements were taken at the centre of the AFOV.

Ignoring these fluctuations in diameters, the data points were averaged for each instance and the outer diameters of the Harris and BB inserts were 31.6 ± 0.3 and 28.7 ± 0.3 mm, respectively. The inner diameters were and 16.6 ± 0.4 , 9.2 ± 0.7 mm respectively. The error margins were the $\frac{\text{standard deviation}}{\sqrt{\text{number of data points}}}$. The outer diameter of the Harris fluid flow is slightly larger than the interior diameter of the pipe (30 mm). However, if the fluid is being pushed close to the edges of the pipe walls then this is to be expected due to the Gaussian blurring of the PET spatial resolution. From these diameter measurements it can be definitively stated that the Harris insert forces the fluid flow towards the walls of the pipe more than the BB insert. Therefore, the Harris insert may cause better heat transfer rates than the BB insert. Moreover, there is a larger area of the inner pipe for which there is no fluid flow in a pipe with a Harris insert compared to a BB insert.

It is important to note that the intensity profiles through sagittal slices were also taken in the A to P direction. However, due to the density bias of the active fluid to float to the top of the pipe, the intensity profiles of these cross-sections were more asymmetric and

skewed the width measurements. Therefore, only L to R cross-sections were used for width measurements as these were more symmetric and unaffected by density difference between the active and inactive fluid.

Measuring the width of fluid flow along the length of the pipe within the AFOV.

Rather than looking at how the diameter of the fluid flow in the pipe changes with time, the same coronal (L to R) diameter measurements were taken at different points along the AFOV (i.e. along the pipe) within the same image frame. The image frame selected was that with the highest activity present in the FOV. This measurement was to determine if the diameter of fluid flow changed along the pipe. These results are displayed in the graphs in figure 8.24. The fluid flowed from the inferior to the superior direction. The lower axial slice value is the superior end of the PET scanner. The diameter measurements showed small fluctuations along the axis, however, the error margins of the measurement may be underestimates, as discussed previously. To determine if this were true, the data could be re-framed into longer time frames to improve the image quality and statistics. A better measurement of the diameter widths could be made using this data. Unfortunately, due to the technical difficulties with the scanner this was not possible.

The data points were averaged for each instance and the outer diameters of the Harris and BB inserts were 31.3 ± 0.4 and 27.9 ± 0.4 mm, respectively. The inner diameters were 16.9 ± 0.2 and 11.1 ± 0.3 mm, respectively. The error margins were the $\frac{\text{standard deviation}}{\sqrt{\text{number of data points}}}$. The Harris insert diameter averages for the variation along the length of the pipe and variation with time are within error of each other. However, this is not true for the BB insert where the difference between the average diameter against time and the average diameter along the pipe is within two standard deviations for the outer diameter and within 3 standard deviations for the inner diameters.

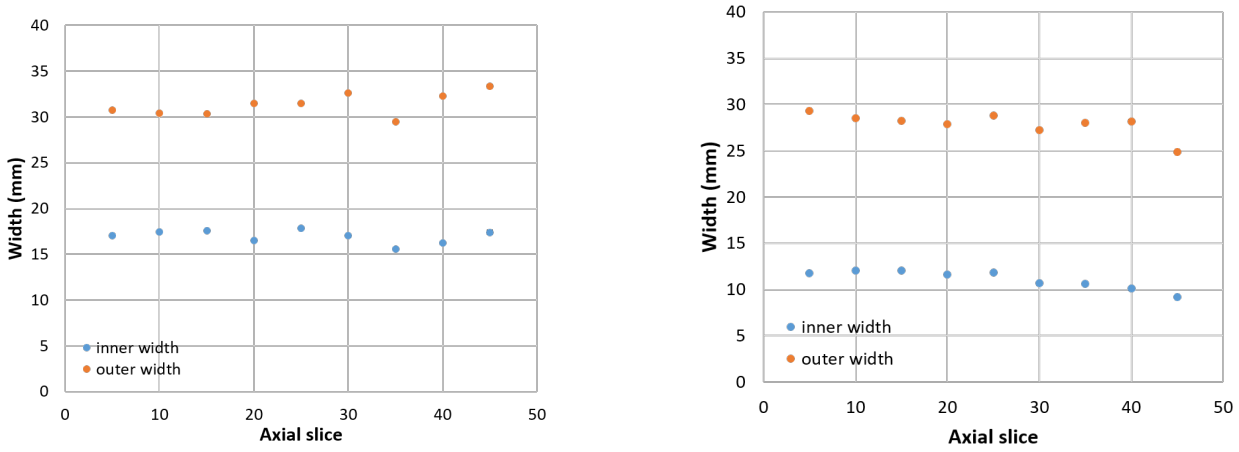

(a) Harris

(b) BB

Figure 8.24: The inner and outer diameter measurements of the flow of fluid through the Harris and BB inserts at different axial slices along the pipe. The intensity profiles used to measure the widths were taken left to right across a coronal slice through the centre of the pipe.

In conclusion the Harris insert produces the most consistent fluid flow with time and spatial position along the pipe. It also forces the fluid to the edges of the pipe more than the BB insert and there is clear area of no fluid flow in the centre of the pipe. From this information is was suggested that the Harris insert would be the most appropriate insert to use for the client of CALGAVIN. However, the pressure change caused by the Harris insert compared to the BB insert was too great and the BB insert was selected for the client.

Residence time

One of the measurements performed by CALGAVIN to quantify the rate of motion within a pipe with a particular insert is residence time. CALGAVIN originally investigated this by injecting a solution which conducts electricity before the start of the pipe with the insert. A voltage measurement is take at the start (top) and end (bottom) of the pipe. The time taken to travel the distance separating these points, the residence time, is then extracted from these data and the spread of the injected fluid can also be measured. An example of

this type of data is shown in figure 8.25 where three data sets are overlaid. In this example, a residence time of about 180 seconds was measured for this particular fluid flow rate.

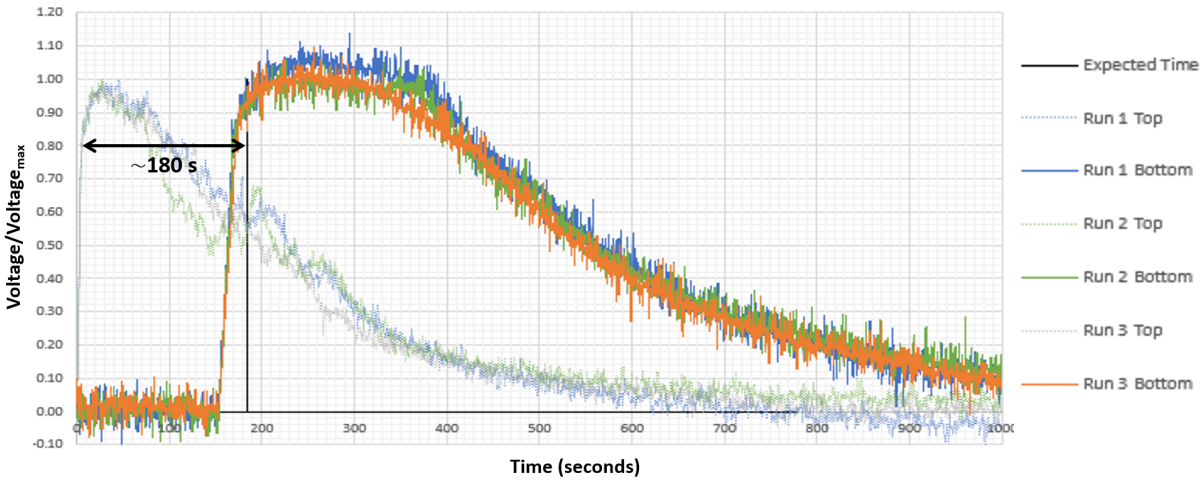

Figure 8.25: The voltage measurement at the start (Top) and end (Bottom) of the pipe after a solution which conducts electricity was injected before the start of the pipe with an insert. There are three data set shown. These data were collected and this image was produced by CALGAVIN [75]. The residence time for these data sets was measured to be approximately 180 seconds as indicated on the graph.

The aims of these PET investigations were not only to provide CALGAVIN information on fluid flow through the centre of the pipe but to also establish what other useful parameters could be quantitatively measured using these images. The measurement of residence time, previously performed using an electrically conducting solution, could usefully be achieved using the PET images previously collected for establishing the dimensions of fluid flow. In this instance the electrically conducting solution is replaced by a PET tracer.

An example of how this would be achieved was carried out using a set of Harris insert data. This was because the Harris insert was originally seen as the better insert when looking at fluid flow dimensions alone (see previous subsection). To provide the residence time using the PET data, the total intensity of a single (3.3 mm thick) axial slice was measured for each 5 second frame between 1 and 4 minutes. This was achieved by using the following steps.

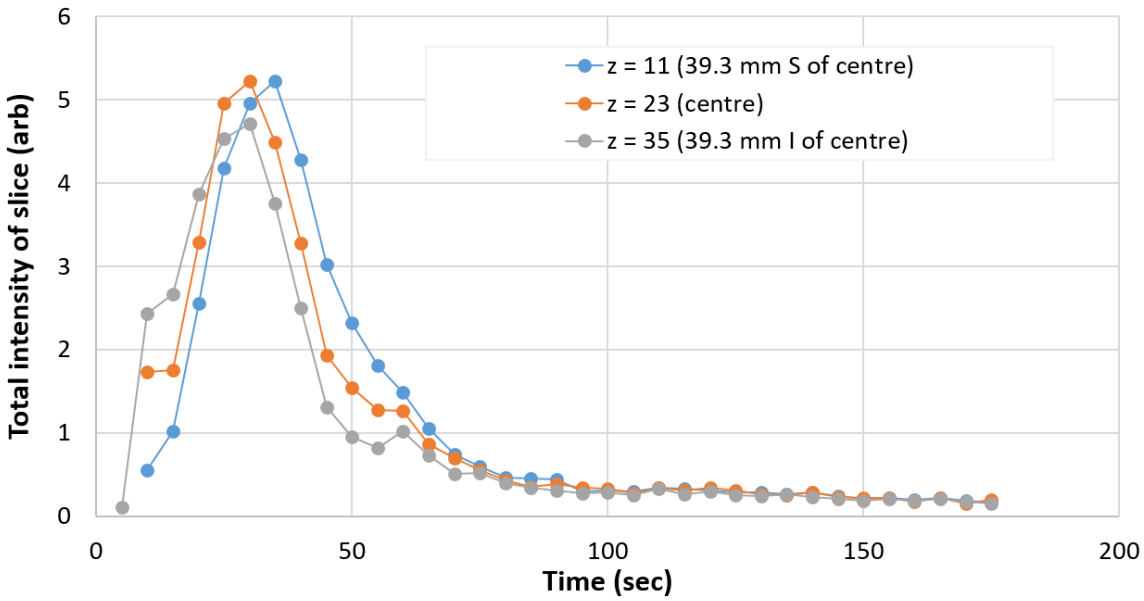

Figure 8.26: The data points are the total intensity of the volume of a single axial slice measurement as a function of time for three different axial (z) slices, 39.3 mm apart from one another. The z = 23 slice is the central slice in the AFOV. The lines between the points are a guide for the eye.

For each frame, a volume of interest, one axial slice thick, was drawn on the image. A histogram of the voxel intensities within this volume was extracted (excluding zero value voxels). The intensity range of the histogram was from 0 to 0.3 arb. intensity units and was split into 300 bins. The number of counts in each bin was then multiplied by the intensity value midway between the value of the bin the counts were in and the next bin up (i.e. the bin value + 0.0005). These 300 intensity values were then summated to produce the total intensity value of the volume in one PET axial slice. The total intensity measurement variation with time were carried out for 3 different axial (z) slices, z = 35, z = 23 (the axially central slice), and z = 11. The z = 11 and z = 35 slices were 39.3 mm superior and inferior to the central slice, respectively. The variation with time of these total slice intensity values are displayed in figure 8.26.

As the fluid flowed from I to S then, as expected, the intensity of the z = 35 slice increased first, followed by the central slice (z = 23) and then the z = 11 slice. The width of the intensity peak also broadens slightly as the active fluid flows through the pipe. Moreover, the small fluctuations in intensity, which are potentially due to how the tracer was injected, smooth out farther along the pipe as the insert mixed the fluid. Taking into account the flow rate and the distance between the measurements along the pipe, a residence time could be calculated.

Further analysis was carried out to examine the small bump that occurred at 60 seconds in figure 8.26. The potential non-uniformity of the injection of the tracer might explain this bump. However, a 5 second image of a single slice possessed too low a level of statistics to draw a definite conclusion. To examine the cause of this bump at 60 seconds using more statistics the total intensity extraction steps were repeated for the whole FOV of this data set, not just one axial slice. When the total intensity value for the whole FOV of each 5 second frame was plotted against time a clear pattern emerged of discontinuous intensity behaviour every minute as seen in figure 8.27. This was traced back to how the data were original collected, in ten 1 minute sections. Towards the end of each minute frame there appears to be an adjustment of image intensity where the intensity levels out. Then at the start of the next frame the intensity appears to resume its decrease, following the original pattern at the start of the previous minute. This jump in behaviour every minute caused the intensity discontinuity between each minute frame. The reason for this discontinuous behaviour is most likely due to an in-built feature of the scanner to optimise the image quality between frames. It is known that medical PET scanners will adjust perceived activity of an object with time, adjusting the data in accordance with the half-life of the tracer being used. Due to the tracer being pushed through the pipe much faster than the half-life of ^{18}F this may cause conflict in the data handling within the scanner between each image frame. However, in future experiments this discontinuous intensity behaviour between separate frames can be

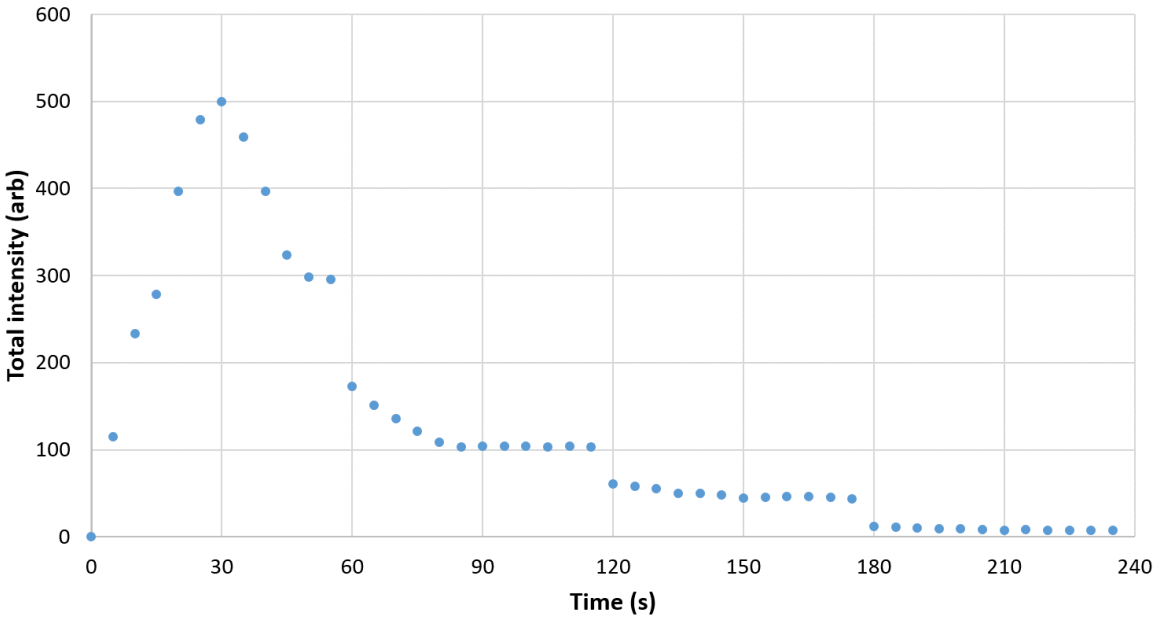

Figure 8.27: The time evolution of the total intensity measurement of the total volume inside the FOV of the PET scanner. The data points were taken for each 5 second frame of a Harris insert data set. Every minute there are clear discontinuities in the intensity data most likely due to how the data was originally collected in ten 1 minute frames.

avoided by collecting a set of data as one image frame and then later re-framing the data into smaller time frames.

This easily correctable mistake in PET data collection aside, PET has a clear advantage over previous methods of residence time measurement, for PET measurements can occur at multiple points (up to 47, as this is the number of axial slices) along the pipe. Therefore, the effect of the length of the insert on the residence time could be measured more easily in this form of data collection. Moreover, in one PET measurement multiple parameters can be measured at once, for example, the dimensions of flow with time as well as volume intensity profiles. Unfortunately, to produce usable quality images the time resolution of each frame is limited to 1 second for simple point sources and 3 or 5 seconds for more complex images.

Unfortunately, the PET scanner continued to have faults. It was problematic when turning the machine on and attempting to take and process data. Thus, to due to the pressures of time, further investigations using this scanner were terminated. However, with more time, more research could and should be carried out using PET imaging for industrial images including the extraction of more quantitative information from the CALGAVIN PET data already collected. This will be discussed in chapter 9.

More information on potential future measurements using the PET scanner and improvements to measurements already discussed are detailed in the following chapter, along with a summary of the benefits PET imaging has to offer the industrial community.

Chapter Nine

Conclusion and future work

The main aim of these PET studies using the GE Discovery ST PET/CT scanner was to devise novel techniques of using a former medical PET scanner to explore the breadth of information that could be extracted from PET images taken of industrial machinery. Moreover, the niche advantages of PET over PEPT imaging needed to be qualified by extracting industrially useful information from PET images which would otherwise not be obtainable by PEPT or other non-positron techniques. Both of these aims were achieved during the PET work carried out with industrial partner, CALGAVIN and are discussed in more detail below. However, the work with CALGAVIN would not have been possible without the preliminary studies which tested the spatial and time resolution limits of the PET scanner. From preliminary studies, the spatial resolution of a point source placed centrally within the FOV of the PET detector rings was established to be 5.5±0.2 mm in the superior to inferior direction; 9.6±0.1 mm in the anterior to posterior direction; and 9.1±0.1 mm in the left to right direction. It was also established that the resolution capabilities did not change significantly when moving the point source along the axis through the centre of the bore. However, the resolution became slightly poorer if the source was placed away from the central axis. This information was useful in understanding that the systems under investigation should be placed along the central axis of the scanner and that the image spatial quality is fairly

uniform along the axis, thus spatial measurements made along this direction are comparable.

One of the most important features investigated was how the image quality was affected by duration of data collection and activity of tracer used. These were imperative to establishing the limits of how quickly a PET image of useful quality can be taken and to set boundaries on the types of machinery mechanism that can be followed. For a point source tracer, usable PET images could be produced within 1 second. However, one of the main advantages of PET over PEPT is the potential to study collective fluid flow in liquid or gas form. For these more complex images, with enough activity (between 140 - 260 MBq) good quality three second PET images were producible for the liquid studies. Further preliminary work would be needed to determine the effect of imaging gases instead.

The work with industrial partner, CALGAVIN, was successful in providing information about the fluid flow distribution through the centre of pipe with two different inserts designed by them. More importantly, the work with CALGAVIN allowed for exploration of the PET scanner capabilities and the types of information that could be extracted in future investigations either with the stationary mixer produced by CALGAVIN or measuring other mechanisms. It was clear that the dimensions of fluid flow was an obvious quantitative measurement that could be and was made. The cross-sectional information PET provides is a useful tool to extract interior motion which would not be possible otherwise. However, a potentially more interesting and powerful measurement that was initially investigated with these CALGAVIN data was that of measuring total intensity of image slices over time. In these initial investigations the 3D image intensity (measured in arbitrary units) was monitored over several frames. Within a single set of data several measurements can be compared. This would allow companies to study the duration fluid stays within a machine and also look at the mixing capabilities as the intensity profile of the tracer changes over time (e.g. how the width of the injected activity peak widens over time). Unfortunately, the way the CALGAVIN data was collected impacted the intensity profile and is discussed

in more detail in section 9.1.2. The improvements to volume intensity measurements are also discussed in section 9.1.2 where further quantification of intensity measurements are explained which would allow the intensity information of different data sets to be comparable.

This initial work has highlighted a few new opportunities that PET imaging can provide for industry. However, in order to carry out impactful research using the GE Discovery ST PET scanner into the interior workings of machines like carbon absorbers and catalytic converters (discussed previously and in appendices I and J) improvements in detector calibration and data collection are needed. Future improvement to these are the main discussion points of this chapter.

9.1 Future improvements

For some of the PET work carried out using the GE Discovery ST PET scanner, there were clear areas where improvements could be made and would be advised for future work. However, there are also other aspects that are more subtle and would need future investigations to establish if changing the current method slightly would have an positive impact on the end results. The obvious and less obvious potential improvements are present at both the scanner calibration stage and the data collection and analysis stage. Addressing these would be a great start to the next steps in using the PET scanner for more industrial applications.

9.1.1 PET calibration improvements

As discussed in section 8.1.2, the calibration of the scanner was not as simplistic as following the manual. Due to an old and relatively inactive ^{68}Ge calibration pin source, a cylindrical phantom filled with ^{18}F-water was used instead for energy calibration, timing calibration

between detectors, and crystal position calibration. Once it was realised that the phantom must be placed in and out of the FOV of the scanner in time with the pin source, the calibrations began to improve such that the PET images produced were accurate spatially and gave resolutions of usable quality. However, a cylindrical phantom filled with ^{18}F-water and placed centrally within the bore of the PET scanner was not necessarily the optimal solution and may have caused problems with the calibration.

The reason for the uncertainty in using this supplementary cylindrical phantom is because many of the finer details of how the GE scanner uses the calibration data are not public knowledge due to industrial secrecy. One issue to consider is that the supplementary phantom filled with ^{18}F decays much quicker than ^{68}Ge. This means that during a day of calibration, the activity of the calibration source is drastically lower at the end of the day than at the start. This inconsistency may be a factor which the PET scanner was attempting to correct as it is expecting a much longer lived calibration source and thus more consistency in the calibration data statistics. The activity originally placed inside the supplementary phantom also changed from day-to-day. Hence, this change in calibration source may confuse the calibration system. However, at the time, ^{18}F was readily available and these potential affects were less of a concern as the calibration of the scanner did eventually improve.

The central position and stationary nature of the supplementary cylindrical phantom may have also impacted calibration, especially the coincidence timing calibration between detectors. The original ^{68}Ge pin source moves in circles around the edge of the PET scanner when in the FOV of the detectors. This means at any one time the source is much closer to one set of detectors than another. This not only subtly effects the timing of coincidence photons (because one photon will reach a detector faster than the other compared to when the calibration source is placed central in the bore of the scanner) but it also affects which detectors are involved in a single coincidence measurement, as figure 9.1 highlights. In figure 9.1, each coloured arrow represents a back to back pair of 511 keV photons emitted at the

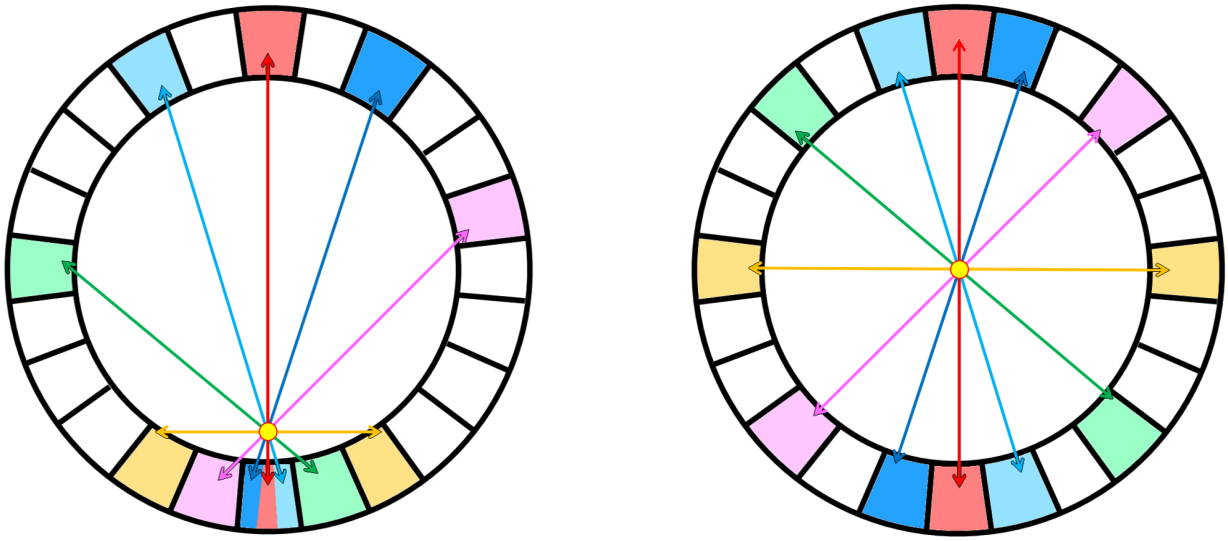

(a) **Calibration source near the detectors**

(b) **Calibration source placed centrally in FOV**

Figure 9.1: A simplified diagram of a ring of PET detector modules with a calibration source place within the FOV. Back-to-back photons from positron emission and annihilation within the calibration source are shown as arrows. Each coloured arrow represents a different angle of emission (i.e. the same colour between (a) and (b) means the same angle). The colour of the PET modules are to help the eye identify which modules are paired in coincidence depending on the angle of the photon emission.

same angle in each scenario where the source is either at the edge of the detectors (a) or centrally withing the scanner (b). It is clear from these simplified diagrams that there are differences in detector pairs when the source is placed centrally and when placed on the edge, near the detectors. What is also apparent is that as the pin source moves around the edge of circle, different pairs of detectors will occur. As the supplementary calibration source (the cylindrical phantom) was placed centrally within the bore and did not move round the edge of the detectors, these changes in detector pairs did not occur. If the undisclosed details of the timing calibration incorporates the pin source position with the data that are expected then it is clear that a supplementary source placed centrally and unmoving may cause a

problem, as the calibration process is not expecting a uniform field of activity exposure. Moreover, the size of the supplementary cylindrical phantom is very different to the pin source and this too will affect the detector coincidence pairs.

Fortunately, using this ^{18}F supplementary cylindrical phantom was unlikely to have inhibited accuracy of the detector energy calibration. However, it may have impeded the crystal position mapping calibration as well as most definitely affecting coincidence timing calibration. Ideally a new ^{68}Ge pin source would be bought to replace the old source each year, however, this is very costly. An alternative solution could be to design and produce a holder for the phantom which mimics the motion of the pin source. The difference this could make may be insignificant but should be investigated to ensure the best calibration of the PET scanner in future work.

9.1.2 CALGAVIN

As mentioned previously, the PET investigations into imaging fluid flow through stationary mixers designed by CALGAVIN were successful. The original question of determining if fluid flowed through the centre of either of the two inserts provided was qualitatively answered to a standard which satisfied CALGAVIN. Moreover, these data were very useful for investigating the types of quantitative information that can be extracted from the PET images, including fluid flow dimensions and the length of time it takes for fluid to flow through a system (residence time). However, there were areas of the experimental set-up and data collection that could be improved upon. These are discussed below along with suggestions of other quantitative information that could be extracted in future PET work using the GE Discovery ST PET/CT scanner.

Experimental set-up improvements

The main area that needed improving in the experimental set-up was the method of injecting activity into the system. There are two facets to this. The first is ensuring that the injected active fluid was exactly the same density as the fluid in the pipe, for it was seen that, in the empty pipe CALGAVIN data, the tracer did not mix uniformly with the system fluid and floated on top. The second part of the injection process that needed improvement was the method of injection to provide a uniform activity through the cross-section of the pipe.

The total activity of the ^{18}F-water made each day varied and this changed how much active water was used in each batch that was injected into the pipe. The original set-up only topped up the injected batch with a premix 4:1, glycerol:water fluid that flowed through the system. Therefore, the glycerol to water ratio that was injected into the system for imaging contained a greater ratio of water and was thus less dense than the rest of the fluid in the pipe. The effects of this were discussed in section 8.2.2. However, in the future, greater care would be taken to ensure that the volumes of water and glycerol added to the activated water were adjusted on an individual basis to achieve the same ratio as the original fluid in the system.

Once the density of the injected fluid is the same as the rest of the system then the uniformity of the injection method can be more easily seen. Although the original design with four injection points shown in figure 8.18 was made to attempt a more even distribution of fluid around the pipe, the effectiveness of this needed to be established. The four pipes leading from the syringe into the injection points were all flexible plastic tubes. These tubes move with the syringe. Therefore, the position of the injecting syringe relative to the main pipe will change how bent each injection tube is. The curvature of the injection tubes will change how much pressure is need to force fluid through it and thus more fluid might be injected through one injection tube more than others. Potentially rigid injection tubes would be used in the future to ensure repeatable injections. Moreover, the inlet tubes only protrude

a small distance into the main pipe, therefore it is not clear if any of the active fluid reaches the centre of the pipe in an empty pipe. However, this may become clearer once a tracer of density equal to the system is used.

Finally, if the method of injection could be automated such that the injection force applied to the syringe was consistent and took the same length of time and injected exactly the same volume of fluid each time, then all the repeated image data sets would be directly comparable. This would allow repeat measurements to be taken and averaged for all parameters extracted from the PET images.

Data collection and analysis improvements

Reflecting on the PET residence time measurement discussed in the last part of section 8.2, the most obvious improvement to be made in the data collection method is to collect a set of data as one image frame and then later re-frame the data into smaller time frames. This would resolve the intensity discontinuity effects seen in figure 8.27.

At the moment, the data presented in section 8.2 was mostly qualitative (with the measured thickness of fluid flow and residence time as exceptions). The thickness of the ring of fluid was measured for each insert and this was used by CALGAVIN in their product pitches to their clients. However, more information than residence time could be gleamed from the intensity data in these images. The image intensity could be calibrated to known activities of ^{18}F in a glycerol/water mix of a fixed ratio. Vessels of similar dimensions to the pipes used by CALGAVIN could be injected with known activities. Then, the image intensity could be measured as the ^{18}F decays. This calibration data could then be used to provide more detailed information of the fluid distribution in the pipes and convert the arbitrary intensity units into units of activity. Moreover, this data would be essential to confirm if the intensity of the images are linear with activity. This is of particular interest for OSEM reconstructed

images as linearity can be lost during iterative reconstruction.

Once the intensity of the images is calibrated to activity in the image, then direct quantitative comparisons of volume or pressure of fluid flow could be made between the two CALGAVIN inserts. This could be achieved by knowing the total activity injected into the system, measuring the total voxel volume occupied by the active fluid in the image and then measuring the intensity of the images to know the total activity per unit volume.

Unfortunately, after the CALGAVIN data were taken the PET scanner broke down. Therefore, the activity-image intensity calibration never took place as the machine required recalibrating once turned back on. The scanner recalibration may have affected the efficiency of coincidence data collection in the scanner and thus affected the intensity calibration data. Therefore, the intensity data collected after recalibration would not necessarily reflect the CALGAVIN data taken beforehand. However, in the future the CALGAVIN work could be repeated including all of the improvements mentioned above.

9.2 PET for industrial imaging conclusions

Working with an older medical PET scanner presented various challenges. Due to its age, multiple mechanical faults required identifying and fixing as well as the computer processing time taking much longer than more modern computers and possessing a tendency to crash. Moreover, because the machine was produced for hospital use, many of its functions and processes were not fully disclosed in accessible literature. This posed practical and data collection problems that needed to be resolved. In addition, more time was dedicated to optimising the scanner for industrial use and calibration without a purpose designed calibration pin source. However, through the calibration processes and the initial work with CALGAVIN discussed in chapter 8 and above, the foundational information was extracted

and novel techniques explored to begin a future of more detailed industrial PET investigations.

With more time, the GE Discovery ST PET/CT scanner could have been used to provide dynamic information of fluid flow in other industry machinery and investigations. The intensity information extracted from the data in the work discussed here could not be provided for these CALGAVIN insert using PEPT, for the bead tracers used in PEPT would become caught in the inserts. In addition, the collective fluid flow would not have been achievable using PEPT traces in one data collection pass, only by averaging it over many passes through the system. Moreover, the broadening of the fluid tracer intensity in PET can be used to look as the mixing effect of the insert in a unique way from PEPT. Depending of the complexity of the fluid flow, frames 3 seconds in length are possible with this model of PET scanner. With more modern scanners this could be improved. These novel techniques PET provides over PEPT can also be applied to gaseous studies which is current not achievable using PEPT. The use of gas tracers would be the next area to focus on to develop industrially applied PET imaging further.

The work carried out to date using the GE Discovery ST PET/CT scanner solely used ^{18}F as the PET tracer but, as mentioned in the motivation for industrial PET imaging (section 7.2), other positron emitting tracer elements could be used. This would widen the application of PET imaging to look at chemical reaction distribution within machinery. Although previously work has been carried out using one dimensional PET imaging [74], the added 3D information from using modern PET scanners could provide invaluable information. Therefore, along with the improvements and additional analytical steps discussed in this chapter and chapters 7 and 8, the future of industrial PET image lies with incorporating chemical reaction monitoring.

Appendices

A Minimum energy of Beam calculated using closest approach

For nuclei to interact they must overcome the Coulomb force of repulsion between them. To find the minimum energy required to overcome this force between an α particle and a europium nucleus the distance of closest approach (d) can be calculated (see figure 2).

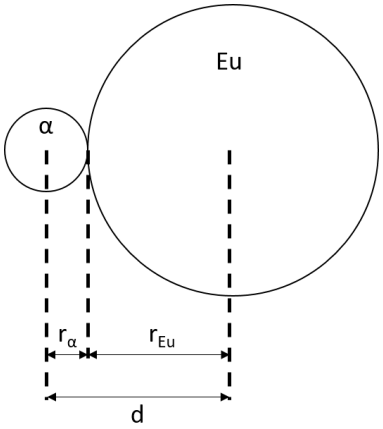

Figure 2: An α particle and Eu nuclei at the point of closest approach separated by a distance, d.

Using the assumption that the radius (r) of a nuclei is:

$$r = (1.4A^{1/3})\text{fm}$$

where A is the atomic number, the distance between an α particle and ^{151}Eu nucleus is:

$$d_{151} = 1.4(4^{1/3} + 151^{1/3}) = 9.677465... = 9.7\text{fm (2s.f.)}$$

and the distance between an α particle and ^{153}Eu nucleus is:

$$d_{153} = 1.4(4^{1/3} + 153^{1/3}) = 9.710235... = 9.7\text{fm (2s.f.)}$$

$$\Rightarrow \text{the average } d = 9.7\text{fm} = 9.7 \times 10^{-15}m$$

The Coulomb Force between the α particle and europium nuclei is given by:

$$F = \left[\frac{(Z_\alpha Z_{Eu})e^2}{4\pi\epsilon_0 d^2}\right] \div 1.6 \times 10^{-19}eV$$

where Z_α=2 , Z_{Eu}=63 , e=1.6×10^{-19}C and ϵ_0= $8.85 \times 10^{-12}Fm^{-1}$. The energy (E) required to cause the nuclei to touch, ie when d=9.7fm is given by:

$$E = Fd$$

$$\Rightarrow E = \left[\frac{(Z_\alpha Z_{Eu})e^2}{4\pi\epsilon_0 d}\right] \div 1.6 \times 10^{-19}eV$$

$$\Rightarrow E = 1.86881... \times 10^7 eV$$

$$\Rightarrow E = 19MeV.$$

Therefore 19MeV is the minimum energy required to cause a nuclear reaction.

B Calculating the production of isotopes during irradiation

The production of isotopes in an α beam depends on two factors:

1. the rate of decay of the isotope;
2. the rate of production (R) of the isotope.

The rate of change in the number of nuclei of a particular isotope is governed by

$$\frac{dN}{dt} = R - \lambda N, \tag{1}$$

where λN is the rate of decay of the isotope produced. By integrate equation 1, an expression governing the change in activity (A) can be obtained (equation 14) as follows.

Equation 1 can be rearranging to give

$$\frac{dN}{dt} + \lambda N = R. \tag{2}$$

The integrating factor (IF)

$$IF = e^{\int \lambda dt} \tag{3}$$

$$IF = e^{\lambda t} \tag{4}$$

is then used as a multiplication factor on both sides of equation 2 and then integrated over

time as follows:

$$e^{\lambda t}\frac{dN}{dt} + \lambda e^{\lambda t}N = Re^{\lambda t} \tag{5}$$

$$\frac{d}{dt}\left(Ne^{\lambda t}\right) = Re^{\lambda t} \tag{6}$$

$$Ne^{\lambda t} = R\int e^{\lambda t}dt \tag{7}$$

$$= R\left[\frac{e^{\lambda t}}{\lambda}\right] + C. \tag{8}$$

At t=0, N=0. Therefore, substituting this in:

$$Ne^{\lambda t} = R\left[\frac{e^{\lambda t}}{\lambda}\right] + C \tag{9}$$

$$0 = \frac{R}{\lambda} + C \tag{10}$$

$$-\frac{R}{\lambda} = C \tag{11}$$

$$Ne^{\lambda t} = R\left[\frac{e^{\lambda t}}{\lambda}\right] - \frac{R}{\lambda} \tag{12}$$

$$N\lambda = R - Re^{-\lambda t}. \tag{13}$$

Activity, $A = N\lambda$, therefore,

$$A = R\left(1 - e^{-\lambda t}\right). \tag{14}$$

The rate of isotope production, R, depends on the beam intensity, i.e., how many α particles are striking the target per second (I_{pps}). It also depends on the likely-hood (i.e. probability)

that the α particle will interact with the target (P). Therfore,

$$R = I_{pps}P. \tag{15}$$

$$P = N_{target}(cm^{-2})\sigma(mb) \tag{16}$$

where σ is the cross-section (likelihood) of interaction and N_{target} is given by

$$N_{target} = \frac{\rho N_A}{A_r}x \ , \tag{2.4}$$

where ρ is the density of the target in gcm^{-3}, N_A is Avogadro's number, A_r is the atomic weight of the target and x is the target thickness in cm.

The number of α particle striking the target, I_{pps}, is governed by the current of the beam, I. If I (measured in μA) is constant then

$$I_{pps} = IN_\alpha \tag{17}$$

where

$$N_\alpha = \frac{1 \times 10^{-6}}{2 \times 1.60218 \times 10^{-19}} = 3.12075 \times 10^{12} \tag{2.5}$$

is the number of α particle per 1 μA. Substituting equations 16 and 17 into equation 15 and subsequently equation 14, then

$$A = N_\alpha I N_{target} \sigma \left(1 - e^{-\lambda t}\right). \tag{18}$$

Therefore, the total activity of an isotope at the end of irradiation time, t_{irrad}, is

$$A_T = N_\alpha I N_{target} \sigma \left(1 - e^{-\lambda t_{irrad}}\right). \tag{2.2}$$

However, if the beam current is not constant then an alternative method of calculating beam intensity is needed. This is discussed in appendix C.

C Calculating cross-section with inconsistent current

As derived in appendix B, the activity of an isotope in the target at the end of irradiation is given by:

$$A_T = N_\alpha I N_{target} \sigma \left(1 - e^{-\lambda t_{irrad}}\right) \tag{2.2}$$

where:

- A_T = total activity of the isotope at the end of irradiation
- N_a = the number of α particles per μA of beam current
- I = beam current (in μA)
- σ = cross-section (cm^2)
- N_{target} = the number of target particles (cm^{-2})
- $\lambda = \frac{ln2}{T_{1/2}}$
- t_{irrad} = time irradiated for

This is true for a constant current. However, if the current varies over the time period of irradiation and the length of irradiation is less than or comparable to the half-life of the isotope then the activity of the isotope produced can be given by equation 2.7 [47]

$$A_T = \sigma N_{target} \sum_{i=1}^{n} \Phi_i \left(1 - e^{-\lambda\tau}\right) \cdot e^{\lambda\tau(n-i)} \tag{2.7}$$

where $\tau = t_{irrad}/n$ is the length of the time for a short period of irradiation and $\Phi_i (= N_\alpha I)_i$ is the beam flux for the ith period of irradiation time.

While the Eu and Al stack was irradiated, the counts in the Faraday cup were recorded approximately every minute by a Brookhaven model 1000c on the 60 nC setting. The conversion to current is given by,

$$I(nA) = \frac{counts \times 60nC}{time(minutes) \times 60} \tag{2.6}$$

therefore, the number of counts recorded in each minute is the average current (in nA) for that minute.

The total irradiation time was 25 minutes 33 seconds = 1533s. Following equation 2.7 the irradiation time can be split into 1533 segments (i.e. n = 1533 and $\tau = 1$). Therefore the summation part of equation 2.7 can be simplified to

$$Y = \sum_{i=1}^{n=1533} \Phi_i \left(1 - e^{-\lambda}\right) \cdot e^{\lambda(n-i)} \tag{19}$$

where λ has units, s^{-1}. For each segment the average current for the time period that segment resides (in μA) is used and is multiplied by N_α (3.12×10^{12} per μA, see equation 2.5). Multiplying these gives Φ for each second.

C.1 The error on the sum, Y

The error on the sum (equation 19) is the sum in quadrature of the errors for each of the 1533 components of the sum. The following will explain how the error for each of the i components were calculated.

Error on Φ

As $\Phi = N_\alpha I$, the error on Φ (σ_Φ) is thus given by $\sigma_\Phi = N_\alpha \sigma_I$ where σ_I is the error on the current. Given I (in nA) is proportional to the counts in the Faraday cup the error would be Poisson error. Therefore $\sigma_I = \sqrt{(I)}$. This must be scaled to μA.

Summarising, for each component of the sum the error on Φ_i is given as

$$\sigma_{\Phi_i} = N_\alpha \frac{\sqrt{I_i}}{1000}. \tag{20}$$

Error on each segment in the sum

The error on each component, y, of the sum was calculated by the partial differentiation of

$$y = \Phi \left(1 - e^{-\lambda}\right) \cdot e^{\lambda(n-i)}. \tag{21}$$

In equation 21 there are only two parameter with errors to consider, Φ and λ. By partially differentiating with respect to each you obtain the following:

$$\frac{\partial y}{\partial \Phi} = \frac{y}{\Phi} \tag{22}$$

and

$$\frac{\partial y}{\partial \lambda} = y \left(i - n + \frac{e^{-\lambda}}{1 - e^{-\lambda}} \right). \tag{23}$$

Therefore, the error on each y component (σ_y) can be calculated by

$$\sigma_y = \sqrt{\left(\frac{\partial y}{\partial \Phi}\sigma_\Phi\right)^2 + \left(\frac{\partial y}{\partial \lambda}\sigma_\lambda\right)^2} \tag{24}$$

which in other words is

$$\sigma_y = \sqrt{\left(\frac{y}{\Phi}\sigma_\Phi\right)^2 + \left(y\left(i - n + \frac{e^{-\lambda}}{1-e^{-\lambda}},\right)\sigma_\lambda\right)^2} \tag{25}$$

$$\sigma_y = y\sqrt{\left(\frac{\sigma_\Phi}{\Phi}\right)^2 + \left(\left(i - n + \frac{e^{-\lambda}}{1-e^{-\lambda}}\right)\sigma_\lambda\right)^2} \tag{26}$$

where $\sigma_\lambda = \frac{ln(2)\sigma_{T_{1/2}}}{T_{1/2}^2}$ ($T_{1/2}$ is the half-life of the product and $\sigma_{T_{1/2}}$ the error on half-life).

C.2 Total error on sum, Y

The total error on Y (σ_Y) is the sum in quadrature of the σ_{y_i}

The cross-section and error on cross-section calculation

The cross-section for each isotope is

$$\sigma = \frac{A_T \times 10^{27}}{N_{target} Y} mb \tag{27}$$

by substituting equation 19 into 2.7 and rearranging. Therefore, by standard partial differential error propagation, the error on cross-section is

$$\sigma_\sigma = \sigma \sqrt{\left(\frac{\sigma_{A_T}}{A_T}\right)^2 + \left(\frac{\sigma_Y}{Y}\right)^2 + \left(\frac{\sigma_{N_{target}}}{N_{target}}\right)^2}. \tag{28}$$

D Calculated Beam energy from scattered alpha energy

To find the energy of the α beam which irradiated the Eu foils the beam is initially directed into the scattering chamber in figure 3. The α beam scatters off the thin gold foil target as shown in figure 4. The energy of the scattered α particles are detected by the DSSD detectors in the chamber. By conservation of energy and moment the original α beam energy can be calculated.

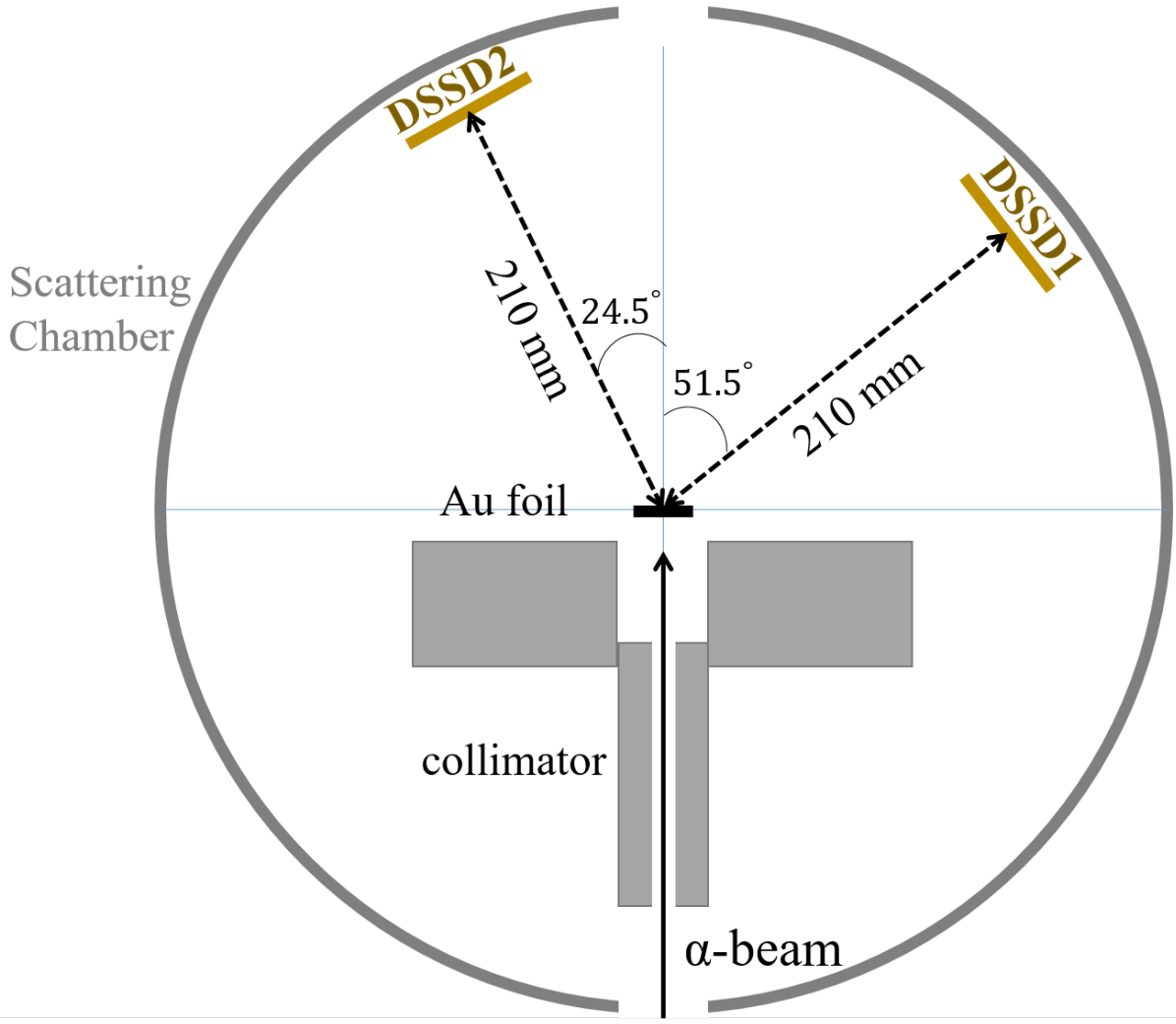

Figure 3: Diagram showing the scattering chamber α beam and DSSD detector set-up.

The following is a derivation of the equation to calculated the beam energy from the scattered

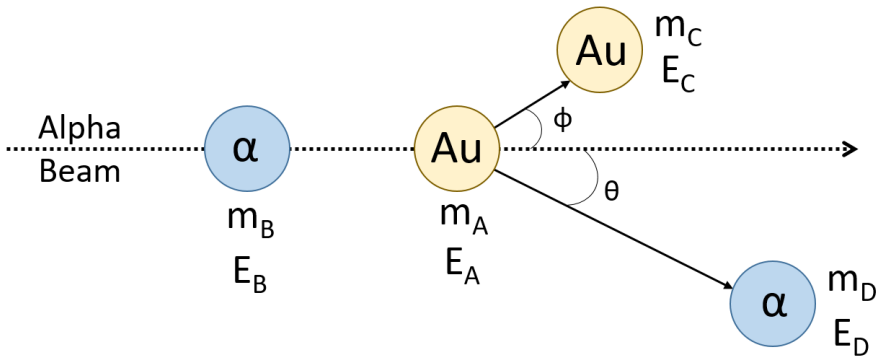

Figure 4: Diagram showing the α beam scattering off a gold target.

α energy.

In general, as the beam particle of mass, m_B, and energy, E_B, strikes the stationary target nucleus of mass, m_A (energy, $E_A = 0$), a reaction may occur with a Q-value and the new particle mass, m_C can be excited to energy level E_X will scatter at angle ϕ and the other scattered product of mass, m_D at angle θ

Therefore, by energy conservation,

$$E_B + Q = E_C + E_D + E_X,$$

which is

$$E_C = E_B + Q - E_D - E_X, \tag{29}$$

and by momentum conservation,

$$P_B = P_D \cos(\theta) + P_C \cos(\phi) \tag{30}$$

$$0 = P_D \sin(\theta) - P_C \sin(\phi). \tag{31}$$

From equation 30,

$$P_B - P_D \cos(\theta) = P_C \cos(\phi)$$

$$(P_B - P_D \cos(\theta))^2 = P_C^2 \cos^2(\phi), \tag{32}$$

and from equation 31

$$P_C \sin(\phi) = P_D \sin(\theta)$$

$$P_C^2 \sin^2(\phi) = P_D^2 \sin^2(\theta)$$

$$P_C^2(1 - \cos^2(\phi)) = P_D^2 \sin^2(\theta)$$

$$P_C^2 - P_C^2 \cos^2(\phi) = P_D^2 \sin^2(\theta)$$

$$P_C^2 - P_D^2 sin^2(\theta) = P_C^2 cos^2(\phi). \tag{33}$$

Equating eq. 32 and eq. 33

$$(P_B - P_D cos(\theta))^2 = P_C^2 - P_D^2 sin^2(\theta)$$

$$P_B^2 - 2P_B P_D cos(\theta) + P_D^2 cos^2(\theta) = P_C^2 - P_D^2 sin^2(\theta)$$

$$P_B^2 - 2P_B P_D cos(\theta) + P_D^2 = P_C^2. \tag{34}$$

Using the kinetic energy relationship, $P^2 = 2mE$ in equation 34 and then substituting for E_C using equation 29

$$2m_BE_B + 2m_DE_D - 2\sqrt{2m_BE_B2m_DE_D}cos(\theta) = 2m_CE_C$$

$$2m_BE_B + 2m_DE_D - 4\sqrt{m_BE_Bm_DE_D}cos(\theta) = 2m_C(E_B + Q - E_D - E_X)$$

$$m_BE_B + m_DE_D - 2\sqrt{m_BE_Bm_DE_D}cos(\theta) = m_C(E_B + Q - E_D - E_X)$$

$$E_B + \frac{m_D}{m_B}E_D - 2\sqrt{\frac{m_D}{m_B}E_D}cos(\theta)\sqrt{E_B} = \frac{m_C}{m_B}(E_B + Q - E_D - E_X)$$

$$\left(1 - \frac{m_C}{m_B}\right)E_B - 2\sqrt{\frac{m_D}{m_B}E_D}cos(\theta)\sqrt{E_B} + \left(\frac{m_D}{m_B} + \frac{m_C}{m_B}\right)E_D + \frac{m_C}{m_B}(E_X - Q) = 0. \quad (35)$$

To find the energy of the α beam, the beam is scattered off a thin gold target. In this reaction there is no excitation of the gold atoms, $E_X = 0$, and $Q = 0$. In addition, the beam particle (B) and the scatter particle (D) are both α particles so $m_B = m_D$. This simplifies the equation 35 to equation 36. This is a quadratic equation for $\sqrt{E_B}$

$$\left(1 - \frac{m_C}{m_B}\right)E_B - 2cos(\theta)\sqrt{E_D}\sqrt{E_B} + \left(1 + \frac{m_C}{m_B}\right)E_D = 0 \quad (36)$$

In the quadratic equation,

$$x = \frac{-b \pm \sqrt{b^2 - 4ac}}{2a} \quad (37)$$

$$x = \sqrt{E_B}$$

$$a = 1 - \frac{m_C}{m_B}$$

$$b = -2cos(\theta)\sqrt{E_D}$$

$$c = \left(1 + \frac{m_C}{m_B}\right)E_D$$

Using equation 37 solve equation 36 for $\sqrt{E_B}$ and square to obtain the energy of the beam. The beam energy is thus positive value of

$$E_B = \left[\frac{-2cos(\theta)\sqrt{E_D} \pm \sqrt{(2cos(\theta)\sqrt{E_D})^2 - 4(1 - \frac{m_C}{m_B}) \left(1 + \frac{m_C}{m_B}\right) E_D}}{2(1 - \frac{m_C}{m_B})} \right]^2 . \quad (38)$$

E HPGe detector dimensions

E.1 G11

The HPGe detector G11 used for obtaining γ spectra had the manufacture dimension shown in figure 5.

33-TN20036

End Cap = 70 mm Diameter

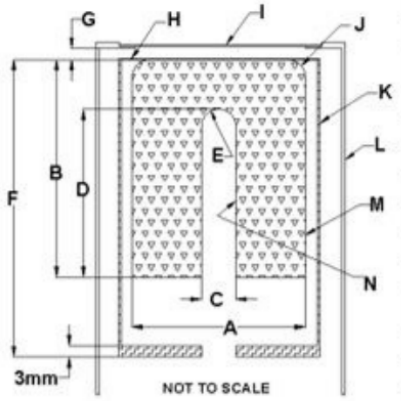

E: NOMINAL 5-mm RADIUS				
F: 94-mm CUP LENGTH				
G: 3-mm SPACE	A=	49.3	mm	Crystal Diameter
H: 0.03-mm/0.03-mm Al/Mylar				
	B=	52.9	mm	Crystal Length
I: 0.5-mm Be				
J: NOMINAL 8-mm RADIUS	C=	11.9	mm	Hole Diameter
K: 0.8-mm Al				
	D=	45.8	mm	Hole Depth
L: 1-mm Al				
M: 0.3-micron Ge/B DEAD				
N: 700-micron Ge/Li DEAD LAYER				

Figure 5: The manufacture dimensions of the G11 HPGe detector used.

Other images of this detector are shown in figures 6 and 7.

E.2 HPC

The dimensions of the HPC HPGe detector used are given in the spec sheet in figure 8

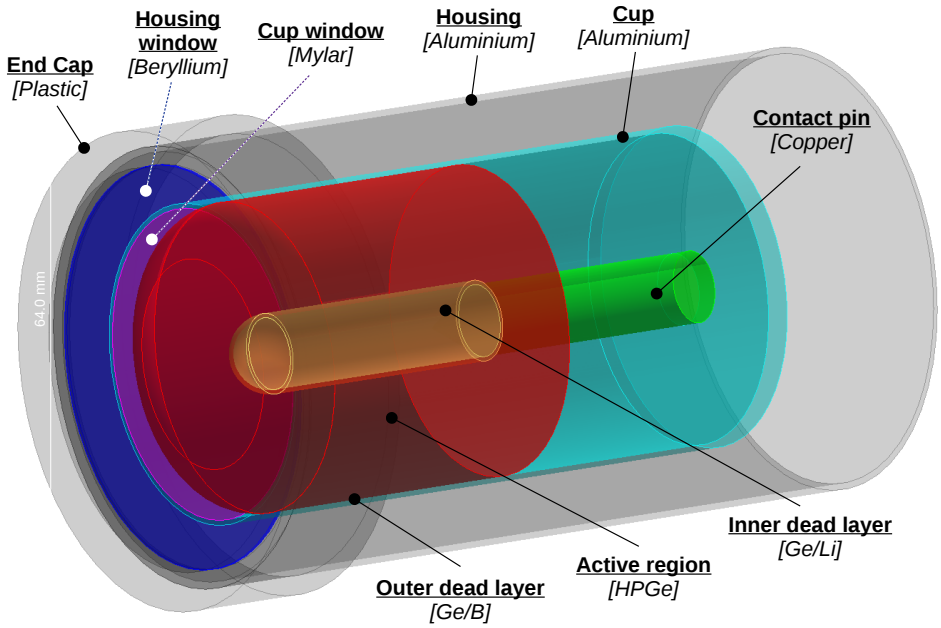

Figure 6: G11 HPGe detector used.

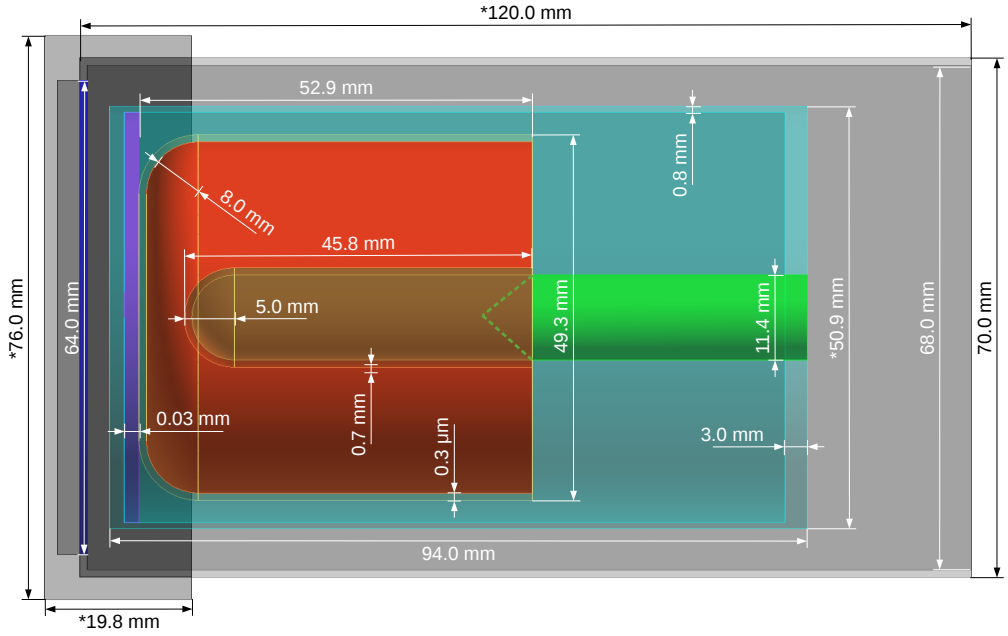

Figure 7: G11 HPGe detector dimensions.

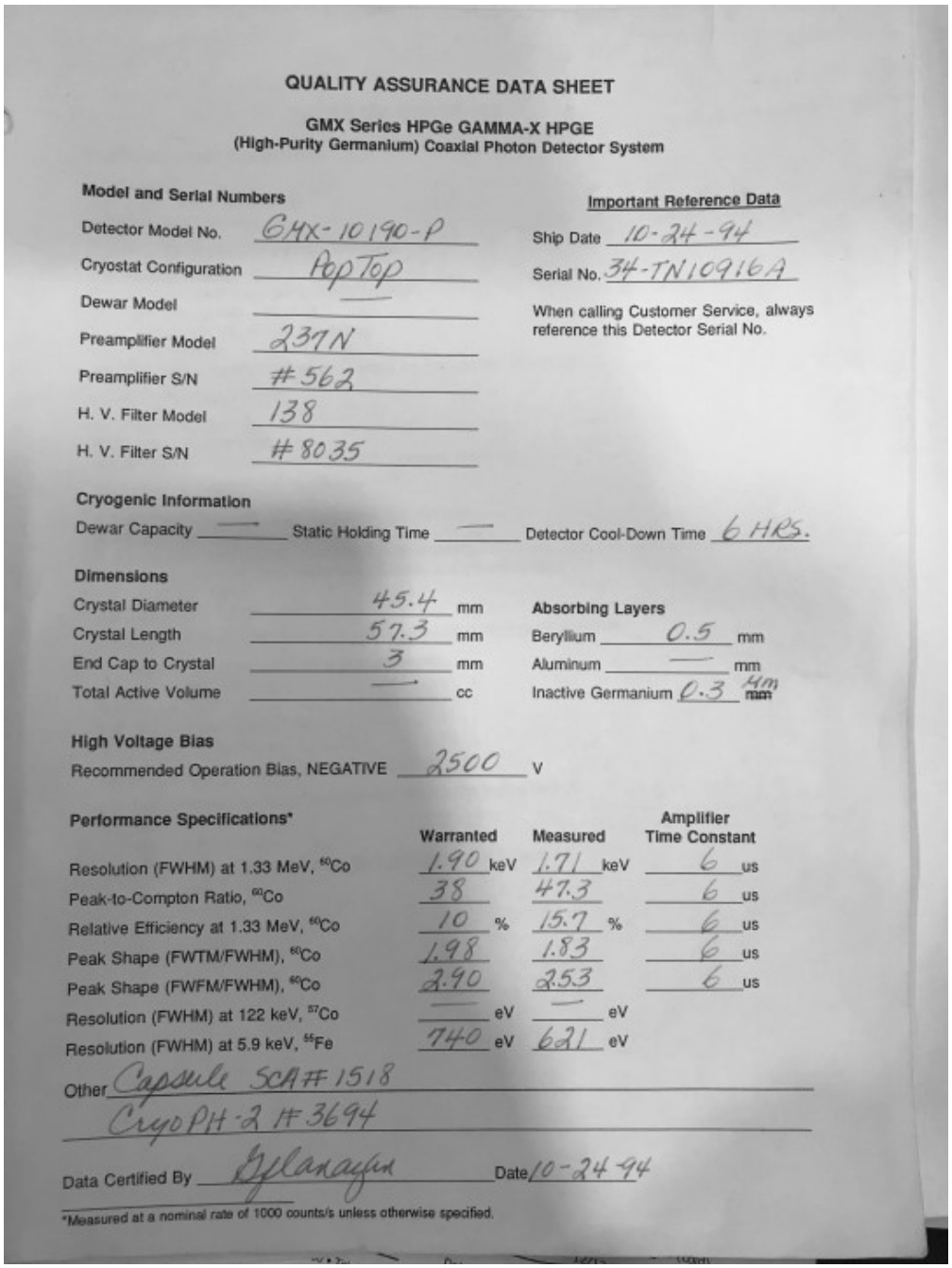

QUALITY ASSURANCE DATA SHEET

GMX Series HPGe GAMMA-X HPGE
(High-Purity Germanium) Coaxial Photon Detector System

Model and Serial Numbers

Detector Model No. GMX-10190-P
Cryostat Configuration PopTop
Dewar Model —
Preamplifier Model 237N
Preamplifier S/N #562
H. V. Filter Model 138
H. V. Filter S/N #8035

Important Reference Data

Ship Date 10-24-94
Serial No. 34-TN10916A

When calling Customer Service, always reference this Detector Serial No.

Cryogenic Information

Dewar Capacity — Static Holding Time — Detector Cool-Down Time 6 HRS.

Dimensions

Crystal Diameter 45.4 mm
Crystal Length 57.3 mm
End Cap to Crystal 3 mm
Total Active Volume — cc

Absorbing Layers

Beryllium 0.5 mm
Aluminum — mm
Inactive Germanium 0.3 ~~mm~~ μm

High Voltage Bias

Recommended Operation Bias, NEGATIVE 2500 V

Performance Specifications*

	Warranted	Measured	Amplifier Time Constant
Resolution (FWHM) at 1.33 MeV, ^{60}Co	1.90 keV	1.71 keV	6 us
Peak-to-Compton Ratio, ^{60}Co	38	47.3	6 us
Relative Efficiency at 1.33 MeV, ^{60}Co	10 %	15.7 %	6 us
Peak Shape (FWTM/FWHM), ^{60}Co	1.98	1.83	6 us
Peak Shape (FWFM/FWHM), ^{60}Co	2.40	2.53	6 us
Resolution (FWHM) at 122 keV, ^{57}Co	— eV	— eV	
Resolution (FWHM) at 5.9 keV, ^{55}Fe	740 eV	621 eV	

Other Capsule SCA# 1518
CryoPH-2 # 3694

Data Certified By Glanaghan Date 10-24-94

*Measured at a nominal rate of 1000 counts/s unless otherwise specified.

Figure 8: HPC HPGe detector dimensions.

F Obtaining and scaling Radware relative efficiency fit and error calculation and propagation.

F.1 RadWare relative efficiency fit and scaling

The equation which defined in section 4.4 for the RadWare relative efficiency fit for HPGe detectors is,

$$\text{RRE} = e^{\left[(A+Bx+Cx^2)^{-G}+(D+Ex+Fx^2)^{-G}\right]^{-1/G}} \tag{39}$$

where A, B, C, D, E, F and G are fitting parameters. RadWare relative efficiency is a function of γ energy (E_γ) and in equation 39 x and y are defined as,

$$x = ln\left(\frac{E_\gamma}{E_1}\right) \tag{40}$$

$$y = ln\left(\frac{E_\gamma}{E_2}\right) \tag{41}$$

where $E_1 = 100$ keV and $E_2 = 1$ MeV.

This RadWare relative efficiency was then scaled to intrinsic efficiency as discussed in section 4.4 by multiplying by a scaling ratio, S_R.

RadWare efficiency error

Equation 39 contains 9 parameters with errors. Differentiating w.r.t. each of these is used to obtain the overall error on RRE.

To simplify set RRE $= n = e^{m^{-1/G}}$ where $m = [(A + Bx + Cx^2)^{-G} + (D + Ex + Fx^2)^{-G}]$ so $\frac{\partial n}{\partial ?} = \frac{\partial n}{\partial m}\frac{\partial m}{\partial ?}$ where ? is parameters A $\rightarrow$ F, x and y.

$$\frac{dn}{dm} = -\frac{1}{G} m^{\frac{-1-G}{G}} e^{m^{-1/G}}.$$

The partial differentials $\frac{\partial m}{\partial ?}$ for parameters A $\rightarrow$ F, x and y are

$$\frac{\partial m}{\partial A} = -G(A + Bx + Cx^2)^{-G-1} \quad \frac{\partial m}{\partial B} = -Gx(A + Bx + Cx^2)^{-G-1}$$
$$\frac{\partial m}{\partial C} = -Gx^2(A + Bx + Cx^2)^{-G-1} \quad \frac{\partial m}{\partial D} = -G(A + Bx + Cx^2)^{-G-1}$$
$$\frac{\partial m}{\partial E} = -Gy(A + Bx + Cx^2)^{-G-1} \quad \frac{\partial m}{\partial F} = -Gy^2(A + Bx + Cx^2)^{-G-1}$$
$$\frac{\partial m}{\partial x} = -G(A + Bx + Cx^2)^{-G-1}(B + 2Cx) \quad \frac{\partial m}{\partial y} = -G(A + Bx + Cx^2)^{-G-1}(E + 2Fy).$$

Differentiating n w.r.t. G gives,

$$\frac{\partial n}{\partial G} = -Gm\frac{dn}{dm}\left[\begin{array}{l} \frac{ln(m)}{G^2} - \\ \frac{-(A + Bx + Cx^2)^{-G} ln(A + Bx + Cx^2)}{Gm} - \\ \frac{(D + Ex + Fx^2)^{-G} ln(D + Ex + Fx^2)}{Gm} \end{array}\right], \tag{42}$$

which can be simplified to

$$\frac{\partial n}{\partial G} = -Gm\frac{dn}{dm}\left[\frac{ln(m)}{G^2} - \frac{-a^{-G}ln(a) - b^{-G}ln(b)}{Gm}\right], \tag{43}$$

where $a = A + Bx + Cx^2$ and $b = D + Ex + Fx^2$.

Therefore, the error on RRE (σ_{RRE}) is given by,

$$\sigma_{\mathrm{RRE}} = \left|\frac{dn}{dm}\right| \sqrt{\begin{aligned}&\left(\frac{\partial m}{\partial A}\sigma_A\right)^2 + \left(\frac{\partial m}{\partial B}\sigma_B\right)^2 + \left(\frac{\partial m}{\partial C}\sigma_C\right)^2 + \left(\frac{\partial m}{\partial D}\sigma_D\right)^2 + \left(\frac{\partial m}{\partial E}\sigma_E\right)^2 \\ &+ \left(\frac{\partial m}{\partial F}\sigma_F\right)^2 + \left(\frac{\partial m}{\partial x}\sigma_x\right)^2 + \left(\frac{\partial m}{\partial y}\sigma_y\right)^2 \\ &+ \left(-Gm\left[\frac{ln(m)}{G^2} - \frac{-a^{-G}ln(a) - b^{-G}ln(b)}{Gm}\right]\sigma_G\right)^2\end{aligned}}, \tag{44}$$

where the appropriate equations from above are substituted in. The errors on parameters A $\rightarrow$ G are given by the RadWare fit and the error x and y (σx and σy)) are the same,

$$\sigma x = \sigma y = \frac{\sigma E_\gamma}{E_\gamma}$$

Error on intrinsic efficiency

The intrinsic efficiency for a particular E_γ Was calculated by RRE$\times S_R$. Therefore, the error on the intrinsic efficiency, σ_{ϵ_i} was calculated using

$$\sigma_{\epsilon_i} = \sqrt{\left(S_R\sigma_{\mathrm{RRE}}\right)^2 + \left(RRE\sigma_{S_R}\right)^2}. \tag{45}$$

G Area under each γ peak correction for isotope decay

A spectrum is taken over a period of time and the activity of the isotopes will change over that time period. It the half-life is long with respect to the time the spectrum was taken for a count correction may not be required as the activity of the source will not change that dramatically over this spectrum collection period. However if the time the spectrum was collected for a comparable or longer length than that of the half-life of the isotope understudy then the effects of the isotope's activity decreasing will have to be taken in to account.

Activity (A) can be expressed in two ways,

$$A = \frac{dC}{dt} \tag{46}$$

and

$$A = A_c e^{-\lambda t} \tag{47}$$

Where C = counts, t = time and $\lambda = \frac{ln(2)}{half\text{-}life}$. I this case A_c is the activity of the source at the start of the spectrum being collected. Substituting 47 in to 46 gives equation 48

$$\frac{dC}{dt} = A_c e^{-\lambda t} \tag{48}$$

For the spectral data collected the total number of counts (C) is know for a particular peak. and the length for which that spectrum was collect (τ) is also know. Thus, A_c can them be found by standard integration between t = 0 and t = τ.

$$
\begin{aligned}
dC &= A_c \int_0^{\tau} e^{-\lambda t} dt \\
C &= A_c \left[-\frac{e^{-\lambda t}}{\lambda} \right]_0^{\tau} \\
C &= A_c \left[-\frac{e^{-\lambda \tau}}{\lambda} - -\frac{e^{-\lambda 0}}{\lambda} \right] \\
C &= A_c \left[\frac{1 - e^{-\lambda \tau}}{\lambda} \right]
\end{aligned}
$$

Thus, to obtain the count per second of each peak in the spectrum at the start of the data collection (A_c) then equation 49 should be used

$$A_c = \frac{\lambda C}{1 - e^{-\lambda \tau}}, \tag{49}$$

which was defined in equation 4.21 in chapter 4. A_c can then be corrected for the efficiency of the detector for the energy of each isotope peak as well as the intensity if the γ energy of that isotope peak and geometric efficiency of the set up.

The error on the calculation of A_c is given by equation 51 where the contributing errors come from C, the error on C (σ_C), λ and the error on λ (σ_λ). The decay constant (λ) and the error on λ are dictated by the half-life ($T_{1/2}$) and the error on the half-life ($\sigma_{T_{1/2}}$) as shown in equation 50.

$$\lambda = \frac{ln(2)}{T_{1/2}} \implies \sigma_\lambda = \frac{ln(2)}{T_{1/2}^2} \sigma_{T_{1/2}} \tag{50}$$

By partially differentiating A_c (equation 49) with respect to C and λ then

$$\frac{\partial A_c}{\partial C} = \frac{\lambda}{1 - e^{-\lambda\tau}} \qquad \text{and} \qquad \frac{\partial A_c}{\partial \lambda} = C\frac{1 - (1+\lambda^2)e^{-\lambda\tau}}{(1 - e^{-\lambda\tau})^2}.$$

Therefore, the error on A_c is

$$\sigma_{A_c} = \sqrt{\left(\frac{\lambda\sigma_C}{1 - e^{-\lambda\tau}}\right)^2 + \left(C\frac{1 - (1+\lambda^2)e^{-\lambda\tau}}{(1 - e^{-\lambda\tau})^2}\sigma_\lambda\right)^2}. \tag{51}$$

H Error calculation for A_E

The error on the efficiency corrected activity of an isotopes for each peak in the spectra, A_E, was calculated using standard differentiating by parts. The following explicitly shows the steps of this process.

$$A_E = \frac{A_c}{\epsilon_i I_\gamma f_A}, \tag{52}$$

where this equation is equation 4.22 from chapter 4.

Firstly, A_E in equation 52 is differentiated with respect to each parameter which contributes error: A_c, ϵ_i, I_γ and f_A.

$$\frac{\partial A_E}{\partial A_c} = \frac{1}{\epsilon_i I_\gamma f_A} \qquad \frac{\partial A_E}{\partial \epsilon_i} = -\frac{A_c}{\epsilon_i^2 I_\gamma f_A} \qquad \frac{\partial A_E}{\partial I_\gamma} = -\frac{A_c}{\epsilon_i I_\gamma^2 f_A} \qquad \frac{\partial A_E}{\partial f_A} = -\frac{A_c}{\epsilon_i I_\gamma f_A^2}$$

These are then substituted into

$$\sigma_{A_E} = \sqrt{\left(\frac{\partial A_E}{\partial A_c}\cdot\sigma_{A_c}\right)^2 + \left(\frac{\partial A_E}{\partial \epsilon_i}\cdot\sigma_{\epsilon_i}\right)^2 + \left(\frac{\partial A_E}{\partial I_\gamma}\cdot\sigma_{I_\gamma}\right)^2 + \left(\frac{\partial A_E}{\partial f_A}\cdot\sigma_{f_A}\right)^2}. \tag{53}$$

To find the error on A_E which is denoted by σ_{A_E} and the errors on the parameters A_c, ϵ_i, I_γ and f_A are given by σ_{A_c}, σ_{ϵ_i}, σ_{I_γ} and σ_{f_A}, respectively, are used. A common factor of $A_E = \frac{A_c}{\epsilon_i I_\gamma f_A}$ can be extracted from the square root and the finally equation for the error on A_E used was

$$\sigma_{A_E} = A_E \sqrt{\left(\frac{\sigma_{A_c}}{A_c}\right)^2 + \left(\frac{\sigma_{\epsilon_i}}{\epsilon_i}\right)^2 + \left(\frac{\sigma_{I_\gamma}}{I_\gamma}\right)^2 + \left(\frac{\sigma_{f_A}}{f_A}\right)^2}. \tag{54}$$

I Carbon capture devise and previous PET studies

I.1 What are they?

Gas capture devices have multiple purposes such a gas separation and purification. Carbon capture devices are being designed mainly for the purpose of collecting waste CO_2 from factories and power plants. The CO_2 can then be stored rather than adding to the greenhouse gas emission. A common carbon capturing material used is activated carbon. The surface of activated carbon is covered in pores and is particular favoured towards absorbing CO_2.

Breakthrough is often used to investigate adsorbants, like activated carbon. It is the measure of the point where any adsorbates, such as CO_2, exit the adsorbant column because there was no available surface to bind to. Carbon analysers are often used to measure the outlet of a carbon capture device to determine the breakthrough point.

I.2 Previous PET studies

Bell [73] in 2015 used radioactive $^{11}CO_2$ produced at the MC40 Cyclotron at the University of Birmingham to investigate the gas distribution in a carbon capture device using PET (specifically using a Concorde Microsystems MicroPET P4 scanner). Both activated carbon and Zeolite 13X (another carbon capture substance) were imaged as $^{11}CO_2$ was passed through the devices. The time frame of each image was once every minute. The PET information about breakthrough for carbon absorption was compared with standard measurement methods using a carbon analyser which was also included in the experimental set-up. For the imaging of the activated carbon, the PET imaging data agreed with the breakthrough data taken using a carbon analyser. However there were discrepancies between the PET image data and carbon analyser for the Zeolite 13X material.

By carrying out a similar experiment using the GE Discovery ST PET scanner (which has a larger FOV and is a more modern detector), the potential discrepancies between the traditional methods and using a PET scanner could be solved. The image details of the flow of the CO_2 in the device could be used to justify current mathematical models.

J Catalysts and Catalytic converters and previous PET studies

J.1 What are they?

Catalysts are substances used to speed up reactions without being used in the reaction themselves. Catalytic converters are used in car exhausts to remove unreacted combustion elements from the car's emissions.

In the engine of a hydrocarbon fuelled machines, incomplete combustion produces CO, hydrocarbon particulates (small unburnt chains of fuel) and due to the high temperature of the engine the nitrogen and oxygen in the air react to form NO and NO_2. Carbon monoxide and hydrocarbon particulates are toxic to human health and nitrous oxides contribute to acid rain, a pollutant to the environment.

Catalytic converters have a honeycomb structure coated with two different catalytic agents. As the exhaust gas passes through, the initial coating reduces the nitrous oxides by,

$$2NO \rightarrow N_2 + O_2$$

$$2NO_2 \rightarrow N_2 + 2O_2$$

After the reduction stage, the second coating used is an oxidative catalyst which completes the unfinished combustion,

$$2CO + O_2 \rightarrow 2CO_2$$

$$2C_xH_{4y} + (x+y)O_2 \rightarrow xCO_2 + 2yH_2O$$

The functionality of the catalysts are commonly known by studying the input reactants and output products. However, in situ imaging of reactants inside catalysts is not common place.

J.2 Previous PET studies

A previous study was carried out in 1992 by Jonkers et al [74] where it was demonstrated that PET could be used to image catalytic converters. A Pt-CeO_2/γ-Al_2O_3 exhaust catalyst was used in the investigation. The radioactive gases; ^{11}CO, $C^{15}O$, ^{15}OO, $^{11}CO_2$, $C^{15}OO$ and ^{13}NN were used for positron imaging on the catalyst. The concentration of positron emitters could be measured for a specific time and location within the catalyst providing valuable in situ information on the inner workings of catalyst reactions required for full comprehension and modelling of catalytic theory.

The details of the original investigation are given in the Nature paper [74]. The main premise consisted of a Pt-CeO_2/γ-Al_2O_3 catalyst being contained and imaged within a Neuro ECAT PET scanner (technology from around 1980), see figure 9. The catalyst was maintained in a steady state with a continuous flow of synthetic exhaust gas passing through the catalyst. Pulses of each different radioactive gas were sent through the system. The positron images were recorded in time intervals of 1.2 seconds. 22 detectors (11 on each side) of the Neuro ECAT PET scanner worked in coincidence (and adjacent coincidence) to produce a 1 dimensional image along the length of the reactor tube. The position resolution on this set up was 1.1cm.

The strength of the radiation signal record by the detectors was recorded with position and time to form the plots displayed in figure 10. The time which reactants stayed in the catalyst supported the reactions thought to take place (see equations above). Further explanation of the graph's meaning can be found in the Nature paper [74].

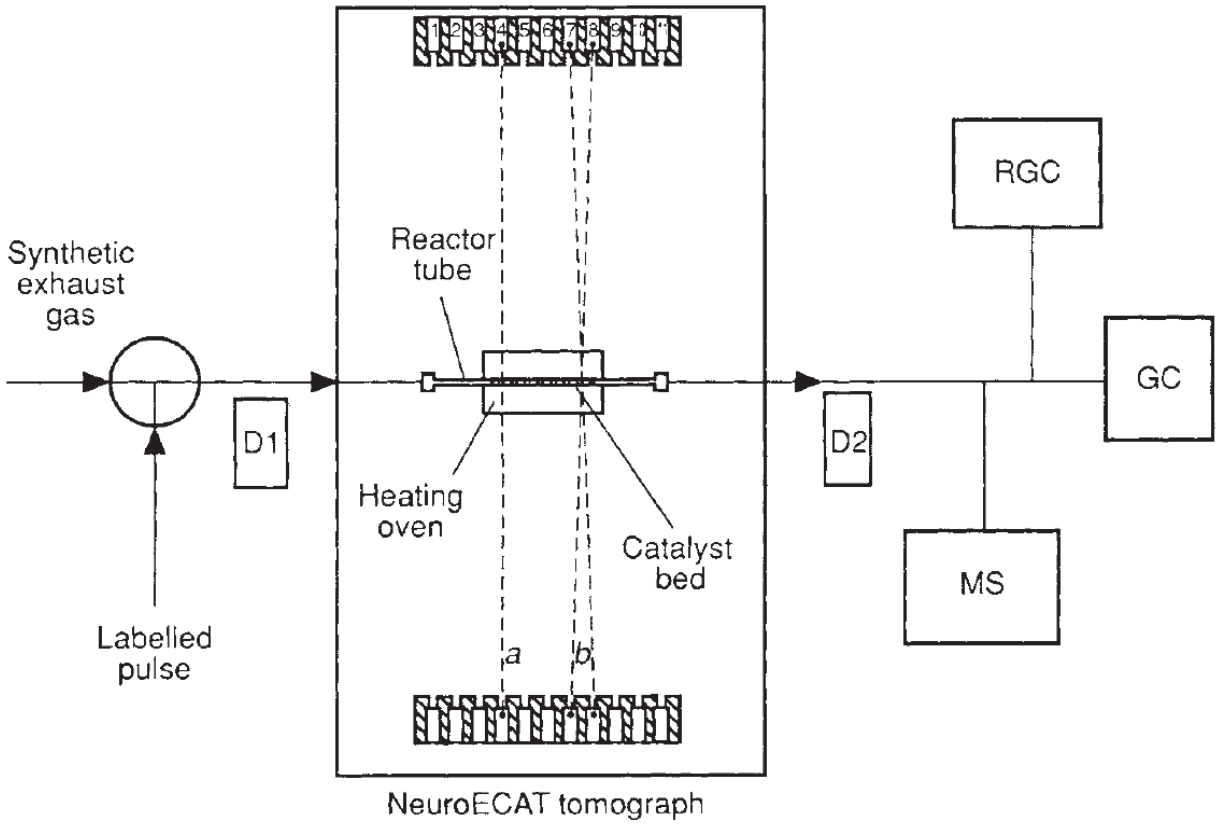

Figure 9: The experimental set up used by Jonkers et al. Inside the exhaust fume system, a diagram of the linear Neuro ECAT PET scanner is displayed [74].

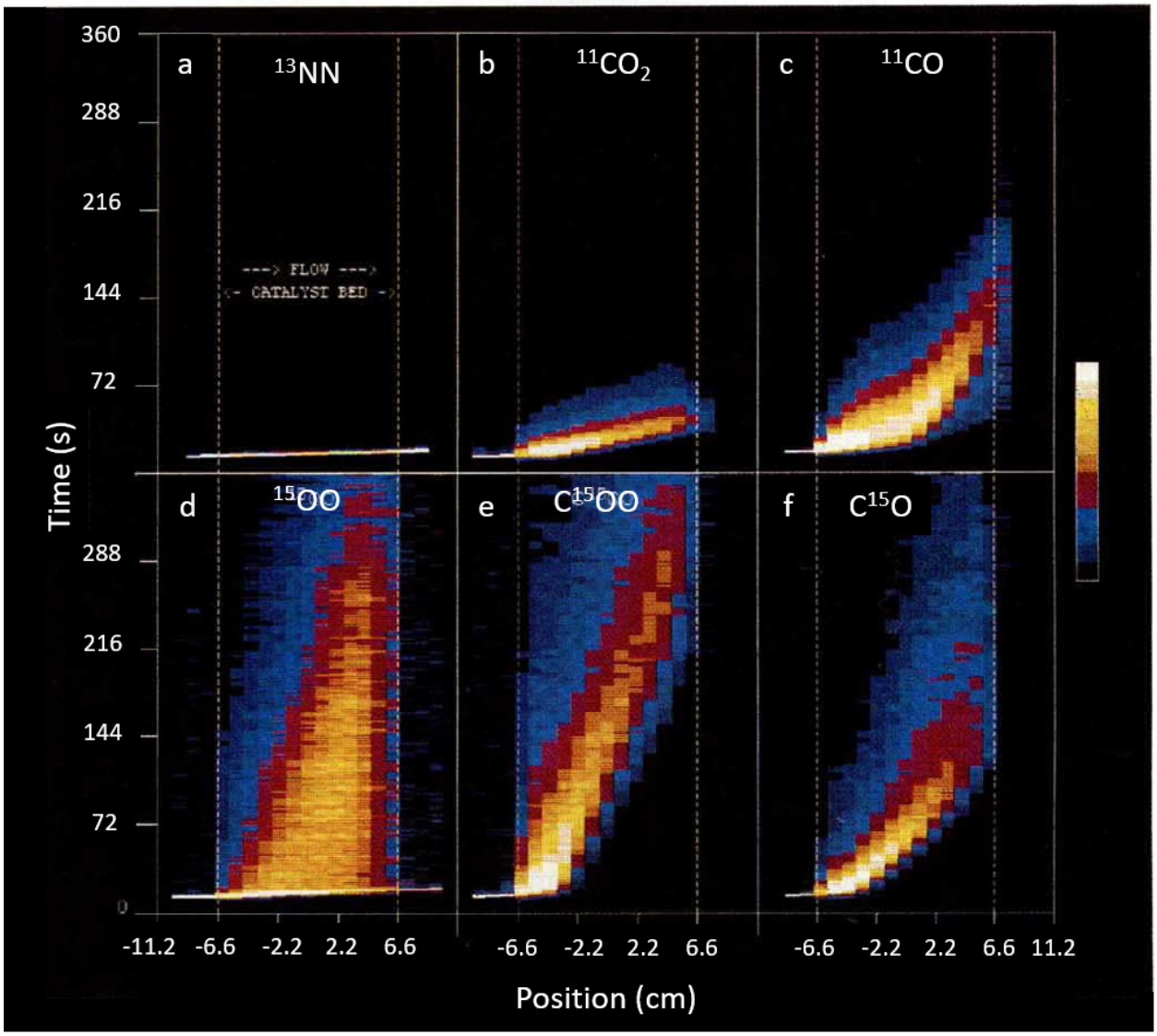

Figure 10: The experimental PET image results obtained by Jonkers et al. The x axis is the position along the catalyst for which radiation was detected. The y axis informs how long radiation was detected in that area for. The different radioactive gases imaged were; (a) ^{13}NN (b) $^{11}CO_2$ (c) ^{11}CO (d) ^{15}OO (e) C^{15}OO (f) C^{15}O [74].

One of the main benefits of repeating this work now is because of the improvements in PET detector technology. Current PET scanners have increased position resolution down to 1mm. Most scanners now also image in 2D if not 3D. Therefore, more information on the reactions happening along the cross-section of the catalysts can now be determined. Continuation of this work was suggested by the original researchers, as well as branching this method out to look at other catalysts, intrinsic kinetics and transport phenomena.

K Basic PET image theory

As briefly explained in chapter 7 the data collected from PET scanner stored either as sinograms or in list mode can be analytically reconstructed using FPB. The following is a more detailed explanation of sinogram, back projections, central slice theorem and FBP.

K.1 Sinograms

[78] Sinograms are the first step of image processing. Figure 11 shows a point source in a body. The line for which the source lies on is defined by $xcos\theta + ysin\theta = x'$ where x and y are the coordinates of the source. The parameter x' is the offset of the line from the origin and θ is the angle between the x axis and the perpendicular line to the line the LOR. The parameters, x' and θ are the polar coordinates used to define the LOR of a source.

[78] Figure 12a gives the Cartesian positions of two point sources. A plot of x' (offset) against θ (angle) produces the graphs shown in figure 12b, this is a sinogram.

[78] For each angle interval, the PET scanner detectors are coupled in parallel pairs as shown in figure 13. The pairings are then rotated by θ' and this rotation of pairings is repeated π/θ' times. For each angle, the LORs of coincident γ ray detections are recorded as functions of angle and offset to form sinograms. This process is repeated for every time frame of the PET image.

[78] Storing LORs in sinogram form uses less memory than storing individual LOR's which is why this imaging method is used in commercial PET scanners.

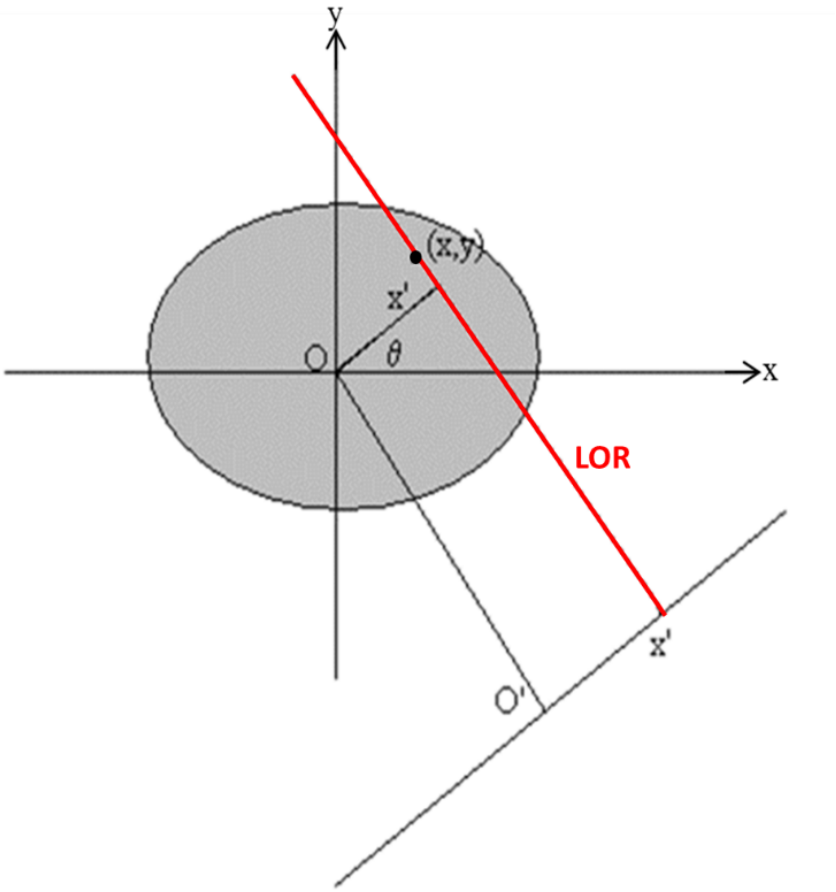

Figure 11: Labelling the LOR in polar coordinates of a point source within an object [94].

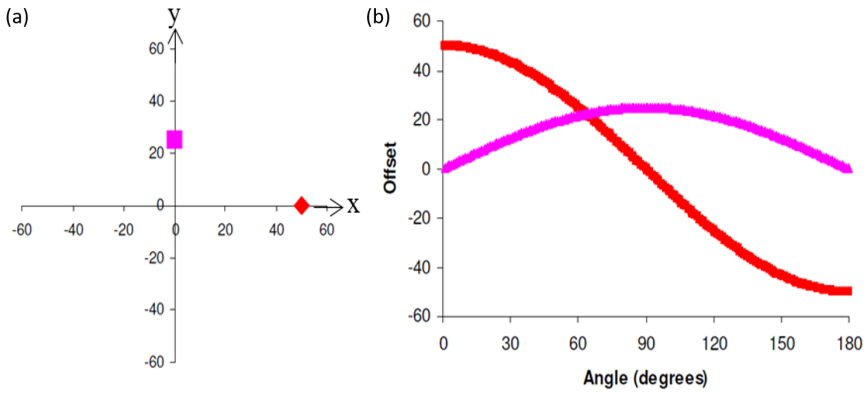

Figure 12: (a) The Cartesian coordinates of two point sources within the detector rings. (b) A plot of x' (offset) against θ (angle) producing the sinogram for each point source [94].

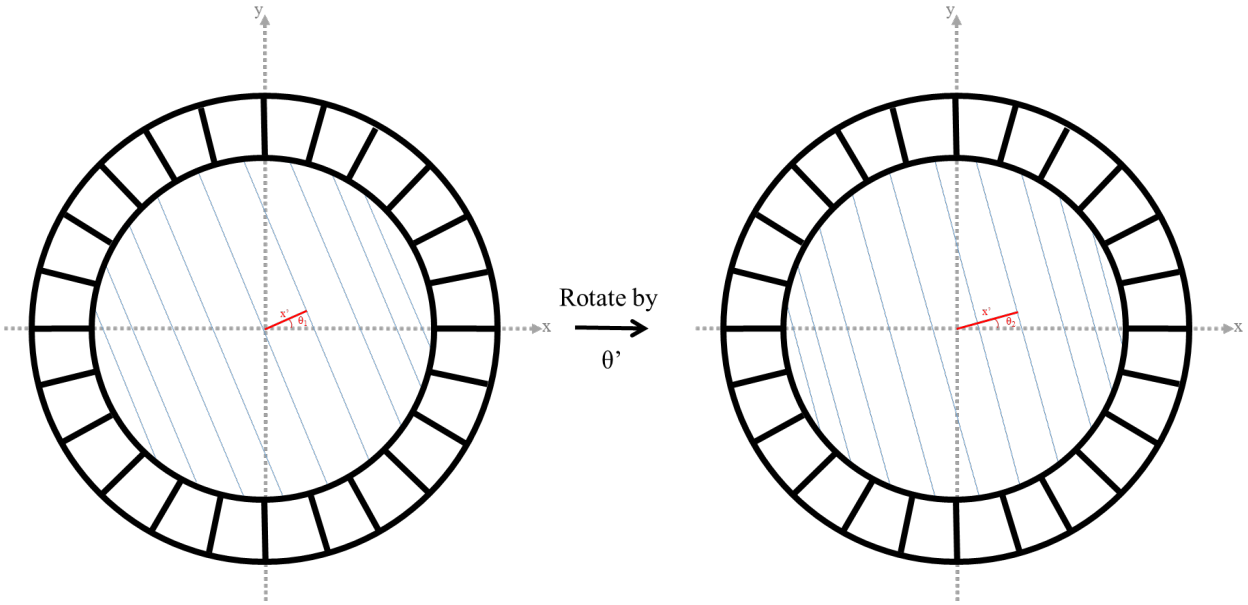

Figure 13: The PET detectors are coupled in parallel pairs. To produce sinograms the parallel parings rotates by θ' and process is repeated π/θ' times.

K.2 Back projection and filtered back projection

[78] Projection profiles are produced using the information stored in the sinograms. For each offset, the detected images are projected back uniformly along the line of measurement (the LOR). However, the image of the source, shown as a red circular area in figure 14, is a blurred form of the original object. The image is a convolution of the original object and a kernel that has a 1/r(radius) shape [73]. A filter is required to the back projection method in order to correct the blurring. In order to remove the convoluted blurring, the image information must be transposed into Fourier space where the blurring effects can be separated more easily and removed by the addition of a filter. The central slice theorem explains how the Fourier plane is used for imaging purposes.

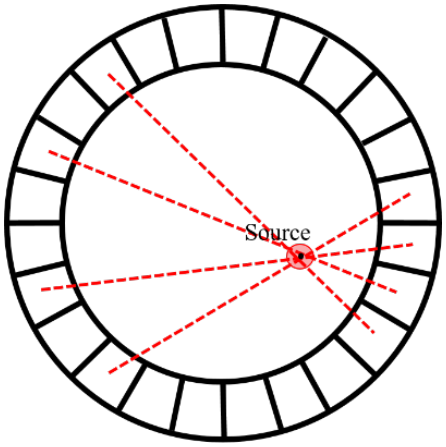

Figure 14: The tails of the LOR back projection cause the spreading out of the image, shown as a larger red circle around the black source point.

Central slice theorem

[78] For a 2D object of shape f(x,y) (see figure 15a) it is very difficult to directly take a 2D Fourier Transform (FT), however, to remove the blurring function, the 2D FT of f(x,y) is required. The central slice theorem can be used to solve this problem. If a parallel projection of an object (tracer) with a shape of f(x,y) is taken at an angle θ, the reading from the detectors will be $p_\theta(t)$ (see figure 15a). The central slice theorem states that the 1D FT of the parallel projection taken at angle θ (see figure 15a) is a slice through the centre of the 2D FT of f(x,y) at the angle θ (see figure 15b). Thus, if you repeat taking FTs of parallel projections for many different angles (between 0 and π) the 2D FT of the original object, $F(k_x,k_y)$, is produced (see figure 15c)

[78] An inverse FT can then be taken of the multiple 1D FTs to obtain the image of the object. However, studying figure 15c, it can be seen that the quality of the 2D FT, and thus the final image, is limited by the number of angles for which 1D FTs are taken from. Therefore a balance between image quality, computing power and time is required.

[78] An additional problem is that the central slice theorem samples information in a circular pattern in the Fourier domain (see figure 16a). In order to produce the image of f(x,y) a Fast

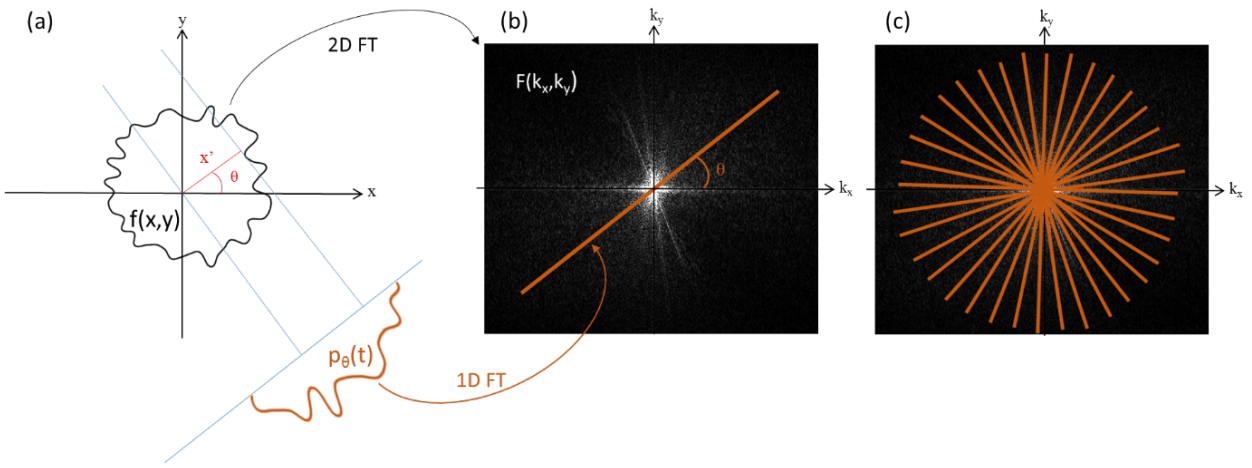

Figure 15: (a) A source (a positron emitting distribution) of shape f(x,y) is imaged at angle θ to produce the parallel projection $p_\theta(t)$. (b) $F(k_x,k_y)$ is the background image [99], which is the direct 2D FT of the function f(x,y). In the foreground is the 1D FT of the parallel projection, $p_\theta(t)$. (c) Overlay of 1D FT of parallel projections from many angles to reproduce $F(k_x,k_y)$.

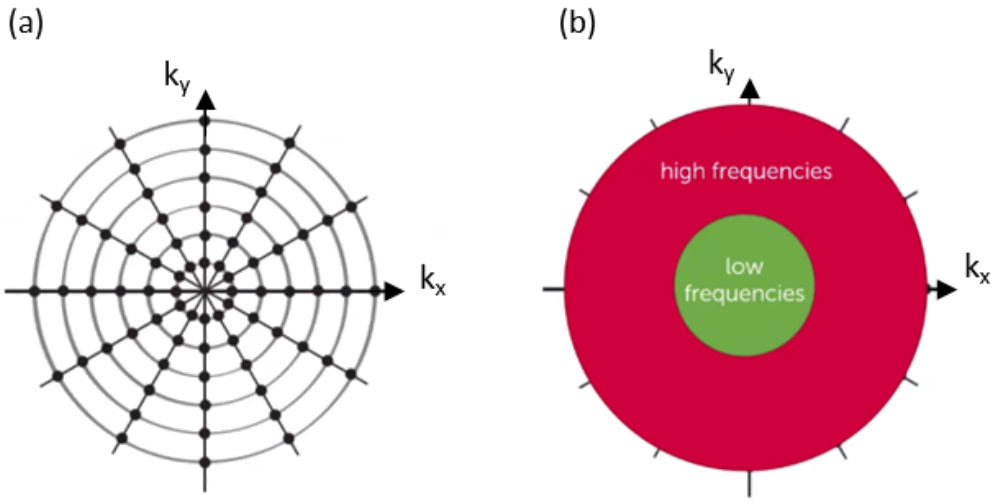

Figure 16: (a) The information in the Fourier domain when using the central slice theorem method is given in a circular array. (b) A simplified separation of low frequency space and high frequency space in the Fourier domain [100].

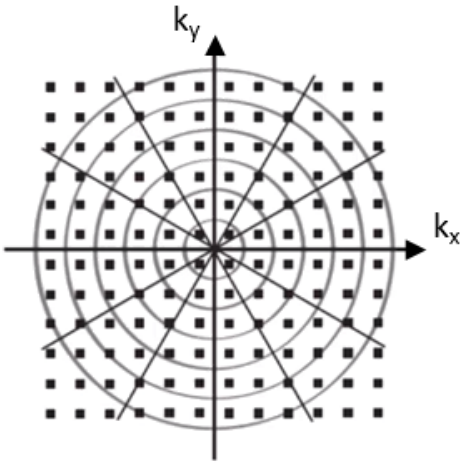

Figure 17: The circular data pattern of information collected when imaging imposed over the square data pattern required to perform a Fast Fourier Transform image reconstruction [100].

Fourier Transform (FFT) must be performed. However the FFT requires a square grid, see figure 17. So interpolation of data is then required which is difficult in the Fourier domain.

[78] Moreover, the sampling distribution of the data in the Fourier domain is more concentrated near the origin (i.e. at lower spatial frequencies) and less information is collected at higher spatial frequencies, this can be seen by comparing figure 16a and 16b. Lower spatial frequencies are responsible for the smoothing of the image and high spatial frequencies are responsible for the details and sharp edges of the image. It is this imbalance of information which gives rise to the blurring effect when back projection without a filter.

Filtered Back Projection

[78] The Filtered Back Projection (FBP) process adds a filter to improve the ratio of low frequency data points to high frequency data points. The filter, known as a ramp filter, is applied to the parallel projections after they have been Fourier transformed. This is done for

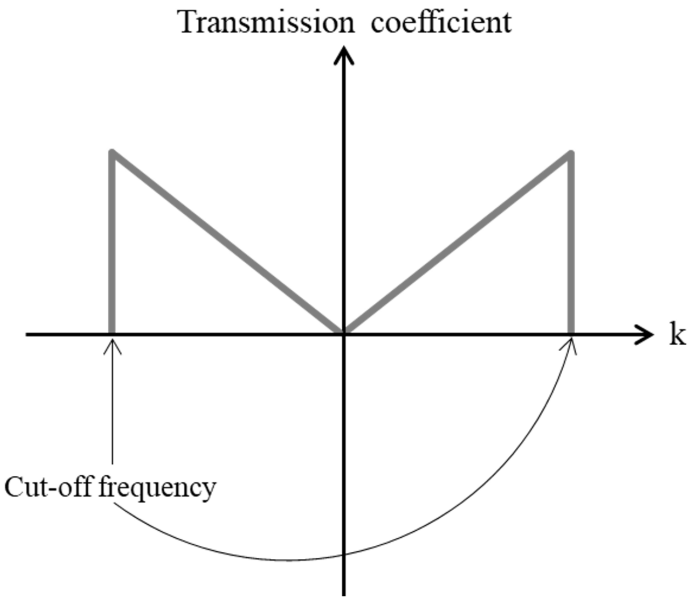

Figure 18: Ramp filter.

each angle the data was collected and then the inverse FT is taken to produce a reconstructed image. The ramp filter can have a shape similar to that shown in figure 18.

Bibliography

[1] Cancer Research UK. *Cancer incidence statistics*. https://www.cancerresearchuk.org/health-professional/cancer-statistics/. Accessed May 2021.

[2] Public Health England National Cancer Registration & Analysis Service. *Chemotherapy, Radiotherapy and Surgical Tumour Resections in England*. https://www.cancerdata.nhs.uk/treatments. Accessed May 2021.

[3] Bruno Rojas et al. "Eighty per cent more patients in 10 years of UK molecular radiotherapy". In: *Nuclear Medicine Communications* 40.7 (July 2019).

[4] J.Buscombe. "Therapeutic Nuclear Medicine in the UK". In: *A History of Radionuclide Studies in the UK*. Ed. by Bomanji J. McCready R. Gnanasegaran G. Springer, 2016, pp. 121–128.

[5] Gy Gyürk et al. "Alpha-induced reaction cross section measurements on 151Eu for the astrophysical γ-process". In: *J. Phys. G: Nucl. Part. Phys.* 37.11 (2010).

[6] Eriksson L. Conti M. "Physics of pure and non-pure positron emitters for PET: a review and a discussion." In: *EJNMMI Phys.* 3.8 (Dec. 2016). DOI: 10.1186/s40658-016-0144-5. URL: https://www.ncbi.nlm.nih.gov/pmc/articles/PMC4894854/.

[7] Powell Richards, Walter D. Tucker, and Suresh C. Srivastava. "Technetium-99m: An historical perspective". In: *The International Journal of Applied Radiation and Isotopes* 33.10 (1982), pp. 793–799. ISSN: 0020-708X. DOI: https://doi.org/10.1016/

0020-708X(82)90120-X. URL: https://www.sciencedirect.com/science/article/pii/0020708X8290120X.

[8] National Research Council (US) Committee on. *Medical Isotope Production Without Highly Enriched Uranium:2, Molybdenum-99/Technetium-99m Production and Use.* Washington (DC): National Academies Press (US); 2009. Available from: https://www.ncbi.nlm.nih.gov/books/NBK215133/ accessed Dec 2021.

[9] S Kouider, F E Kolb, and R Lippmann. "Behavior of various blood constituents (glucose, fructose, insulin, lactate, pyruvate, free fatty acids, inorganic phosphate) and the half-life of monosaccharides in plasma after i.v infusion of glucose, fructose, galactose and invert sugar solutions in ruminants. 3. Studies in sheep". In: *PubMed* 32.5 (1978). German. PMID: 736717.

[10] Clemens Kratochwil et al. "PSMA-Targeted Radionuclide Therapy of Metastatic Castration-Resistant Prostate Cancer with 177Lu-Labeled PSMA-617". In: *The Journal of Nuclear Medicine* 57.8 (2016).

[11] L W M van Kalmthout et al. "Lutetium-177-PSMA therapy for prostate cancer patients—a brief overview of the literature". In: *Tijdschr Urol* 10 (2020).

[12] Mathias J Zacherl et al. "First clinical results for PSMA targeted alpha therapy using 225Ac-PSMA-I&T in advanced mCRPC patients". In: *The Journal of Nuclear Medicine* 61.10 (2020).

[13] Clemens Kratochwil et al. "^{225}Ac-PSMA-617 for PSMA-Targeted α-Radiation Therapy of Metastatic Castration-Resistant Prostate Cancer". In: *The Journal of Nuclear Medicine* 57.12 (2016).

[14] R. Formento Cavaier et al. *Terbium Radionuclides for Theranostics Applications: A Focus On MEDICIS-PROMEDg.* Elsevier B. V., 2016.

[15] T.D. Johnson. *NNDC, Brookhaven National Laboratory.* https://www.nndc.bnl.gov/ accessed 18/08/2021. accessed 18/08/2021.

[16] Cristina Müller et al. "Alpha-PET with terbium-149: evidence and perspectives for radiotheragnostics". In: *EJNMMI Radiopharmacy and Chemistry* (2016). Letter to the editor.

[17] G J Beyer et al. "Production routes of the alpha emitting 149Tb for medical application". In: *Radiochim Acta* 90 (2002).

[18] B J Allen et al. "Production of terbium-152 by heavy ion reactions and proton induced spallation". In: *Appl RadiatI Isot.* 54 (2001).

[19] S Lehenberger et al. "The low-energy beta- and electron emitter 161Tb as an alternative to 177Lu for targeted radionuclide therapy". In: *Nucl Med Biol* 38 (2011), pp. 917–924.

[20] M de Jong et al. "Evaluation in vitro and in rats of 161Tb-DTPA-octreotide, a somatostatin analogue with potential for intraoperative scanning and radiotherapy". In: *Eur J Nucl Med* 22 (1995), pp. 608–616.

[21] C Vermeulen et al. "Cross sections of proton-induced reactions on natGd with special emphasis on the production possibilities of 152Tb and 155Tb". In: *Nucl Instrum Methods Phys Res B* 275 (2012), pp. 24–32.

[22] G J Beyerand M Miederer, S Vranjes-Duric, and et al. "Targeted alpha therapy in vivo: direct evidence for single cancer cell kill using 149Tb-rituximab". In: *Eur J Nucl Med Mol Imaging* 31 (2004).

[23] S M Rizvi et al. "In vitro and preclinical studies of targeted alpha therapy (TAT) for colorectal cancer". In: *Colorectal Dis* 3 (2001), pp. 345–353.

[24] B J Allen et al. "In vitro and preclinical targeted alpha therapy for melanoma, breast, prostate and colorectal cancers". In: *Crit Rev Oncol Hematol.* 39 (2001).

[25] Cristina Müller et al. *A Unique Matched Quadruplet of Terbium radioisotopes for PET and SPECT and for a- and b2-Radionuclide Therapy: An In Vivo Proof-of-Concept Study with a New Receptor-Targeted Folate Derivative*. The Journal of Nuclear Medicine, 2012.

[26] Cristina Müller et al. *Future prospects for SPECT imaging using the radiolanthanide terbium-155 — production and preclinical evaluation in tumor-bearing mice*. Nuclear Medicine and Biology 41, 2014.

[27] Cristina Müller et al. *Preclinical in vivo application of ^{152}Tb-DOTANOC: a radiolanthanide for PET imaging*. EJNMMI Research, 2016.

[28] Cristina Müller et al. "Direct in vitro and in vivo comparison of ^{161}Tb and ^{177}Lu using a tumour-targeting folate conjugate". In: *EJNMMI Research* 41 (2014), pp. 476–485.

[29] Cristina Müller et al. "Terbium-161 for PSMA-targeted radionuclide therapy of prostate cancer". In: *EJNMMI Research* 46 (2019), pp. 1919–1930.

[30] Zeynep Talip et al. "A Step-by-Step Guide for the Novel Radiometal Production for Medical Applications: Case Studies with 68Ga, 44Sc, 177Lu and 161Tb". In: *Molecules* 25.4 (2020). ISSN: 1420-3049. URL: https://www.mdpi.com/1420-3049/25/4/966.

[31] Ricardo Manuel dos Santos Augusto et al. "CERN-MEDICIS (Medical Isotopes Collected from ISOLDE): A New Facility". In: *Appl. Sci.* 4 (2014), pp. 265–281.

[32] B Webster et al. "Chemical Purification of Terbium-155 from Pseudo-Isobaric Impurities in a Mass Separated Source Produced at CERN". In: *Nature Scientific Reports* 9 (2019). article 10884.

[33] Freddy Poirier et al. "THE C70 ARRONAX AND BEAM LINES STATUS". In: *IPAC11* (Sept. 2011). San Sabastian, Spain. hal-01378849.

[34] A J Koning and D Rochman. "Modern Nuclear Data Evaluation with the TALYS Code System". In: *Nuclear Data Sheets* 113.12 (2012), pp. 2841–2934.

[35] C H M Broeders et al. *ALICE/ASH - Pre-compound and evaporation model code system for calculation of excitation functions, energy and angular distributions of emitted particles in nuclear reactions at intermediate energies.* (FZKA–7183). Germany, 2006.

[36] M Herman et al. "EMPIRE: Nuclear Reaction Model Code System for Data Evaluation". In: *Nuclear Data Sheets* 108.12 (2007), pp. 2655–2715.

[37] C Vermeulen et al. "Cross sections of proton-induced reactions on natGd with special emphasis on the production possibilities of ^{152}Tb and ^{155}Tb". In: *Nuclear Instruments and Methods in Physics Research B* 275 (2012), pp. 24–32.

[38] G F Steyn et al. "Cross sections of proton-induced reactions on ^{152}Gd, ^{155}Gd and ^{159}Tb with emphasis on the production of selected Tb radionuclides". In: *Nuclear Instruments and Methods in Physics Research B* 319 (2014), pp. 128–140.

[39] Ulli Köstera et al. "Electromagnetic isotope separation of gadolinium isotopes for the production of ^{152,155}Tb for radiopharmaceutical applications". In: *Nuclear Instruments and Methods in Physics Research B* 463 (2020), pp. 111–114.

[40] P. Ivanov et al B. Webster. "LN extraction chromatography resin, a method developed at NPL". (work yet to be published).

[41] Antonio M. Moro. *Nuclear Reaction Theory.* https://stfc.ukri.org/files/a-moro-nuclear-reaction-theory/. Part of the UK Nuclear Physics Summer School Belfast, 18th-21st August 2017 lecture course. Accessed September 2021.

[42] Kenneth S Krane. *Introductory nuclear physics.* New York, NY: Wiley, 1988.

[43] Simon Fraser University. *Direct and compound nucleus reaction - Introduction to Nuclear Science.* https://web-docs.gsi.de/~wolle/TELEKOLLEG/KERN/LECTURE/Fraser/L24.pdf. NUCS 342 (Lecture 24) March 21, 2011. Accessed September 2021.

[44] R.A.M. Allen et al. "'UoB-TIP (University of Birmingham - Tool for Isotope Production): Python based tool for the automation of nuclear reaction modelling and calculation of isotope production yields'". To be published 2022.

[45] R.A.M. Allen. "Thesis". PhD thesis. School of Physics and Astronomy, University of Birmingham, 2022.

[46] IAEA Nuclear Data Section. *Live Chart of Nuclides, nuclear structure and decay data*. https://www-nds.iaea.org/relnsd/vcharthtml/VChartHTML.html. accessed 18/08/2021.

[47] Gy Gyürky et al. "The activation method for cross section measurements in nuclear astrophysics". In: *Eur. Phys. J. A* 55.41 (2019).

[48] J F Ziegler, J P Biersack, and M D Ziegler. *SRIM: the Stopping and Range of Ions in Matter*. http://www.srim.org. 2008.

[49] H. Bethe and J. Ashkin. *Experimental Nuclear Physics*. E Segrè. Vol. 1. J. Wiley, New York, 1953, p. 253.

[50] ESPI Metals. *Europium Foil .001" 3N*. https://espimetals.com/shop/knd5928-europium-foil.html. Last accessed March 2022.

[51] *STFC technology* Nuclear Physics Group. *MIDAS*. https://www.aapm.org/meetings/08SS/documents/fahey.pdf. used 2020.

[52] Material Properties. *Thermal Conductivity of Chemical Elements*. https://material-properties.org/thermal-conductivity-of-chemical-elements/. used 30/06/2021.

[53] Glenn F. Knoll. *Radiation Detection and Measurement*. 4. ed. John Wiley & Sons, Inc., 2010.

[54] ORTEC. *MAESTRO Multichannel Analyzer Emulation Software*. https://www.ortec-online.com/products/application-software/maestro-mca. Version 7.01.

[55] David Radford. *RadWare software*. https://radware.phy.ornl.gov/. accessed 2018.

[56] M.J. Martin. "Nuclear Data Sheets for A = 152". In: *Nuclear Data Sheets* 114.11 (2013), pp. 1497–1847. ISSN: 0090-3752. DOI: https://doi.org/10.1016/j.nds.2013.11.001. URL: https://www.sciencedirect.com/science/article/pii/S0090375213000744.

[57] L Ruby. "A simpler approach to the geometrical efficiency of a parallel-disk source and detector system". In: *Nucl. Instr. and Meth. A 337* 531 (1994).

[58] C.W. Reich. "Nuclear Data Sheets for A = 154". In: *Nuclear Data Sheets* 110.10 (2009), pp. 2257–2532. ISSN: 0090-3752. DOI: https://doi.org/10.1016/j.nds.2009.09.001. URL: https://www.sciencedirect.com/science/article/pii/S0090375209000805.

[59] Balraj Singh. "Nuclear Data Sheets for A = 151". In: *Nuclear Data Sheets* 110.1 (2009), pp. 1–264. ISSN: 0090-3752. DOI: https://doi.org/10.1016/j.nds.2008.11.035. URL: https://www.sciencedirect.com/science/article/pii/S0090375208001300.

[60] N. Nica. "Nuclear Data Sheets for A=153". In: *Nuclear Data Sheets* 170 (2020), pp. 1–498. ISSN: 0090-3752. DOI: https://doi.org/10.1016/j.nds.2020.11.001. URL: https://www.sciencedirect.com/science/article/pii/S0090375220300508.

[61] N. Nica. "Nuclear Data Sheets for A=155". In: *Nuclear Data Sheets* 160 (2019), pp. 1–404. ISSN: 0090-3752. DOI: https://doi.org/10.1016/j.nds.2019.100523. URL: https://www.sciencedirect.com/science/article/pii/S0090375219300493.

[62] C.W. Reich. "Nuclear Data Sheets for A = 156". In: *Nuclear Data Sheets* 113.11 (2012), pp. 2537–2840. ISSN: 0090-3752. DOI: https://doi.org/10.1016/j.nds.2012.10.003. URL: https://www.sciencedirect.com/science/article/pii/S0090375212000798.

[63] D.L. Smith. "Variation of the intrinsic efficiency of a cylindrical planar Ge(Li) gamma-ray detector with source distance". In: *Nuclear Instruments and Methods* 94.1 (1971), pp. 157–163. ISSN: 0029-554X. DOI: https://doi.org/10.1016/0029-554X(71)90354-5. URL: https://www.sciencedirect.com/science/article/pii/0029554X71903545.

[64] Jehouani A, Ichaoui R, and Boulkheir M. "Study of the NaI(Tl) efficiency by Monte Carlo method." In: *Applied Radiation and Isotopes* 53 (4-5 Oct. 2000), pp. 887–91. DOI: 10.1016/s0969-8043(00)00254-2..

[65] W. W. Bowman, T. T. Sugihara, and F. R. Hamiter. "Quasirotational Levels in ^{152}Gd and Excited Levels of ^{152}Tb from the Decay of 4.2-min ^{152m}Tb". In: *Phys. Rev. C* 3 (3 Mar. 1971), pp. 1275–1287. DOI: 10.1103/PhysRevC.3.1275. URL: https://link.aps.org/doi/10.1103/PhysRevC.3.1275.

[66] K Ya Gromov et al. "INVESTIGATION OF ^{152}Tb RADIATION." In: *Izv. Akad. Nauk SSSR, Ser. Fiz., 31: 154-70(Jan. 1967).* (Jan. 1967). URL: https://www.osti.gov/biblio/4554397.

[67] Y. Y. Chu, E. M. Franz, and G. Friedlander. "Half-Lives and Gamma-Ray Abundances of Several Rare-Earth Nuclides". In: *Phys. Rev. C* 1 (5 May 1970), pp. 1826–1828. DOI: 10.1103/PhysRevC.1.1826. URL: https://link.aps.org/doi/10.1103/PhysRevC.1.1826.

[68] Jaffy C. F. Lau and James J. Hogan. "Investigation of Branching Ratios Between Isomeric States of ^{154}Tb". In: *Phys. Rev. C* 8 (2 Aug. 1973), pp. 715–717. DOI: 10.1103/PhysRevC.8.715. URL: https://link.aps.org/doi/10.1103/PhysRevC.8.715.

[69] T.Vylov et al. "Investigation of Branching Ratios Between Isomeric States of ^{154}Tb". In: *Izv.Akad.Nauk SSSR Ser.Fiz.* 36 (1972), p. 718.

[70] W. W. Bowman, T. T. Sugihara, and F. R. Hamiter. "Quasirotational Levels in ^{152}Gd and Excited Levels of ^{152}Tb from the Decay of 4.2-min ^{152m}Tb". In: *Phys. Rev. C* 3 (3 Mar. 1971), pp. 1275–1287. DOI: 10.1103/PhysRevC.3.1275. URL: https://link.aps.org/doi/10.1103/PhysRevC.3.1275.

[71] A. Hermanne et al. "Reference Cross Sections for Charged-particle Monitor Reactions". In: *Nuclear Data Sheets* 148 (2018). Special Issue on Nuclear Reaction Data,

pp. 338–382. ISSN: 0090-3752. DOI: https://doi.org/10.1016/j.nds.2018.02.009. URL: https://www.sciencedirect.com/science/article/pii/S0090375218300280.

[72] SCANDITRONIX. *MC40 Manual, Volume 9*. SCANDITRONIX, 1993.

[73] Sarah D. Bell. *The development of radioactive gas imaging for the study of chemical flow processes*. School of Chemical Engineering, University of Birmingham, 2015.

[74] G. Jonkers et al. *Surface Catalyst studied by in situ positron emission*. Nature, 1992.

[75] CALGAVIN. *CALGAVIN Homepage*. https://www.calgavin.com/. Accessed September 2021.

[76] F. Hueso-González et al. "Comparison of LSO and BGO block detectors for prompt gamma imaging in ion beam therapy". In: *IOP Publishing* 10.09 (Sept. 2015), P09015–P09015. DOI: 10.1088/1748-0221/10/09/p09015. URL: https://doi.org/10.1088/1748-0221/10/09/p09015.

[77] Omaga Piezo. *BGO AND LYSO CRYSTALS*. http://www.omegapiezo.com/crystal-scintillators/. accessed 2018.

[78] R R Trinder. *The search for new PET applications and the production of relevant radionuclides at the Birmingham (MC40) cyclotron - Midterm Assessment*. unpublished assessment report at University of Birmingham. Sepember 2018.

[79] Scintillator Materials Group (2009). *What are scintillator materials?, Stanford University*. http://web.stanford.edu/group/scintillators/scintillators.html. accessed 2016.

[80] Zaidi H and Montandon ML. "Scatter Compensation Techniques in PET." In: *PET Clin.* 2.219-34 (2007).

[81] Karp JS et al. "Benefit of time-of-flight in PET: experimental and clinical results." In: *J Nucl Med.* 49(3).462-470 (2008).

[82] Surti S. "pdate on time-of-flight PET imaging." In: *J Nucl Med.* 56(1).98-105 (2015).

[83] *Webb's physics of medical imaging / edited by M.A. Flower.* eng. Boca Raton ; London, 2012.

[84] A. J. Rockmore and Albert Macovski. "A Maximum Likelihood Approach to Emission Image Reconstruction from Projections". In: *IEEE Transactions on Nuclear Science* 23.4 (1976), pp. 1428–1432. DOI: 10.1109/TNS.1976.4328496.

[85] Jinyi Qi and Richard M Leahy. "Iterative reconstruction techniques in emission computed tomography". In: *Physics in Medicine and Biology* 51.15 (July 2006), R541–R578. DOI: 10.1088/0031-9155/51/15/r01. URL: https://doi.org/10.1088/0031-9155/51/15/r01.

[86] L. A. Shepp and Y. Vardi. "Maximum Likelihood Reconstruction for Emission Tomography". In: *IEEE Transactions on Medical Imaging* 1.2 (1982), pp. 113–122. DOI: 10.1109/TMI.1982.4307558.

[87] H.M. Hudson and R.S. Larkin. "Accelerated image reconstruction using ordered subsets of projection data". In: *IEEE Transactions on Medical Imaging* 13.4 (1994), pp. 601–609. DOI: 10.1109/42.363108.

[88] Brian Hutton, H. Hudson, and Freek Beekman. "A clinical perspective of accelerated statistical reconstruction". In: *European journal of nuclear medicine and molecular imaging* 24 (July 1997), pp. 797–808. DOI: 10.1007/BF00879671.

[89] D. Lee. *I Like to Move it, Move it...Out of the Sagittal Plane.* https://www.precisionpt.org/single-post/2016/09/30/I-Like-to-Move-it-Move-itOut-of-the-Sagittal-Plane. accessed 2018.

[90] B. Bendriem and D. W. Townsend. *The Theory and Practice of 3D PET.* Springer Science + Business Media Dordrecht, 1998.

[91] Indiamart. *GE Discovery St 8 Slice PET/CT.* https://www.indiamart.com/proddetail/ge-discovery-st-8-slice-pet-ct-18800490688.html. accessed 2018.

[92] General Electrics. *GE Medical Systems Discovery ST Service Manual - General*. Electric Company, Inc., 2004.

[93] National Electrical Manufacturers Association. *Performance Measurements of Positron Emission Tomographs, NEMA NU 2-2012*. NEMA, 2012.

[94] D. J. Parker. *PET imaging lecture notes*. School of Physics and Astronomy, University of Birmingham, 2017.

[95] *Children's Hospital Boston Harvard Medical School* Frederic H Fahey DS. *PET Basics*. https://www.aapm.org/meetings/08SS/documents/fahey.pdf. accessed 2018.

[96] Sanders Medical Products. *GE Healthcare PET Sources*. https://www.sandersmedical.com/PDF/ge.pdf accessed October 2021.

[97] UTHSCSA University of Texas Research Imaging Institute. *Mango*. http://ric.uthscsa.edu/mango/mango.html. used 2018.

[98] CALGAVIN. *hiTRAN Thermal Systems*. https://www.calgavin.com/products-and-software/hitran-thermal-systems. Accessed September 2021.

[99] E. Verner. *How to Do a 2-D Fourier Transform in Matlab*. https://matlabgeeks.com/tips-tutorials/how-to-do-a-2-d-fourier-transform-in-matlab/. accessed 2018.

[100] Youtube. *What are scintillator materials?, Stanford University*. http://web.stanford.edu/group/scintillators/scintillators.html. accessed 2016.